

Optical Studies on Two-Dimensional Organic Conductors under High Pressure

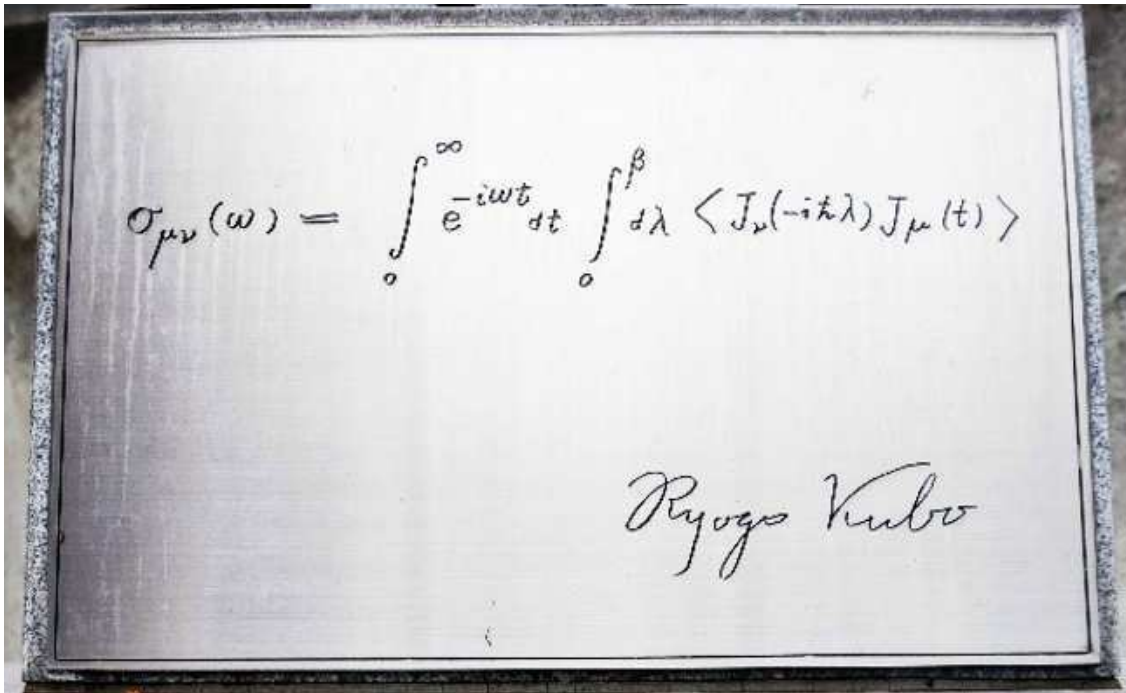
Von der Fakultät Mathematik und Physik
der Universität Stuttgart zur Erlangung der Würde eines Doktors
der Naturwissenschaften (Dr. rer. nat.) genehmigte Abhandlung

vorgelegt von
Weiwu Li
aus Zhejiang, China

Hauptberichter: Prof. Dr. Martin Dressel
Mitberichter: Jun.-Prof. Dr. Stefan Kaiser

Tag der mündlichen Prüfung: 27.06.2019
Prüfungsvorsitzende: Prof. Dr. Hans Peter Büchler

1. Physikalisches Institut der Universität Stuttgart
2019



Kubo formula

Courtesy of Prof. Yamaguchi from Kyoto University

天地有大美而不言
四時有明法而不議
萬物有成理而不說
聖人者原天地之美
而達萬物之理是故
至人無為大聖不作
觀於天地之謂也

^ 莊子·知北遊 ^

Knowledge Rambling in the North

List of Abbreviations

- 1D** one-dimensional
2D two-dimensional
3D three-dimensional
TMTTF tetramethyltetrathiafulvalene
TMTSF tetramethyltetraselenafulvalene
TTF tetrathiafulvalene
STF diselenadithiafulvalene
BEDT-TTF, ET bis(ethylenedithio)-tetrathiafulvalene
Pd(dmit)₂ bis-(ethylenedithio)tetrathiafulvalene
DW density wave
SDW spin density wave
CDW charge density wave
SC superconductivity
AFI, AFM antiferromagnetic (insulator)
QSL quantum spin liquid **CO** charge order, charge ordered or charge ordering
SP spin-Peierls
ZGS zero-gap state
VBS valence bond state
DOS density of state
PDOS partial density of state
HOMO highest occupied molecular orbital
LUMO lowest occupied molecular orbital
DAC diamond anvil cell
RA ring-over-atom
RB ring-over-bond
ac alternating current
dc direct current

NMR nuclear magnetic resonance
ESR electron spin resonance
SQUID superconducting quantum interference device
ARPES angle-resolved photoemission spectroscopy
STM scanning tunneling microscope
FTIR Fourier-transform infrared spectroscopy
THz Terahertz
K-K Kramers-Kronig
EMV electron-molecular vibration
MIR Mott-Ioffe-Regel
BCS Bardeen, Cooper and Schrieffer (theory)
DMFT dynamical mean field theory
MDF massive Dirac fermion
DFT density functional theory
SW spectral weight

Abstract

The prosperity of modern society and technological development largely rely on discoveries and further applications of new materials with novel functional properties. The ability to control these properties play a key role in technological developments, such as new generation of photonic and electronic devices. Quantum materials, i.e., the materials with complex interplay of charge, spin and orbital degrees of freedom, constitute a large and continuously growing group of potentially functional materials. The macroscopic state of such materials can be manipulated via external stimuli, such as hydrostatic pressure, intense magnetic or electric field, carrier doping, etc [1]. Thus, fundamental understanding of the physical mechanisms underlying the phase transitions between these states, i.e., quantum phase transitions, in quantum materials is a central task of current condensed matter physics. Low-dimensional organic conductors are good candidates for studies of quantum phase transitions, because various ground states, ranging from ordered insulators to metals or superconductors, can be continuously tuned in these materials by external pressure [2]. Owing to the recent progress in the development of pressure cells for optical measurements [3, 4], the microscopic interaction parameters, which govern the phase transitions, can be extracted via the broadband optical measurements.

In this thesis, we present the results of pressure-dependent infrared spectroscopy measurements on a series of quasi-two-dimensional organic materials, including the Dirac semimetal α -(BEDT-TTF)₂I₃, the quantum spin-liquid candidate compounds β' -EtMe₃Sb[Pd(dmit)₂]₂ and κ -(BEDT-TTF)₂Cu₂(CN)₃, and the charge-ordered insulator β'' -(BEDT-TTF)₂SF₅CHF₂CF₂SO₃. By these studies, optical spectroscopy have been proved to be an important tool to probe not only the low-energy electronic excitation but also the lattice degrees of freedom under pressure.

In α -(BEDT-TTF)₂I₃, we reveal that the charge-ordered insulating state at ambi-

ent pressure gradually gets suppressed and evolves into a metal. Above around 0.8 GPa the low-temperature electronic bands possess tilted Dirac-like cones. The high-pressure metallic state is well described by a Drude component and a frequency-independent optical conductivity, which strongly indicates the coexistence of the trivial and massless Dirac electrons in this system. In addition, our infrared investigations disclose that an energy gap opens in the vicinity of the phase transition between insulating and metallic states as a result of the correlated massive Dirac fermions. The gap can be gradually suppressed when pressure increases.

For the half-filled Mott insulator β' -EtMe₃Sb[Pd(dmit)]₂, systematic pressure- and temperature-dependent infrared studies unveil both the electronic and lattice evolution upon crossing the Mott insulator-metal transition. The insulating ground state is continuously suppressed with increasing hydrostatic pressure. For $p \geq 0.6$ GPa, a zero-frequency Drude-like component appears, strongly indicating the appearance of coherent quasi-particles at the Fermi level. In the vicinity of the Mott transition, both the electronic state and vibration modes exhibit abrupt changes, evidencing the strong coupling between the lattice and the free carriers. Additionally, we observe an unexpected inverse of the anisotropy of the in-plane optical response above 0.6 GPa. Finally, we summarize these findings in a phase diagram consisting of different experimental methods.

In the case of the Mott-insulating quantum spin-liquid candidate compound κ -(BEDT-TTF)₂Cu₂(CN)₃, we clearly identify the T - and p -driven first order transition from the analysis of the far-infrared data. Furthermore, based on the infrared vibrational spectroscopy we find out that the microscopic origin of the insulator-metal transition induced by physical and chemical pressure is intrinsically different. Regardless of the aforementioned distinct mechanism for the Mott transition, the metallic state is found to obey the universal local Fermi liquid theory. Additionally, in the STF-doped compound κ -[(BEDT-STF) _{x} (BEDT-TTF) _{$1-x$}]₂Cu₂(CN)₃ with $x = 0.28$ we observe an unconventional low-energy mode in the optical conductivity spectra, which can be well described in the formalism of disorder pinned fluctuating density wave theory [5].

Finally, we investigate the pressure effect on the quarter-filled charge-ordered insu-

lator β'' -(BEDT-TTF)₂SF₅CHF₂CF₂SO₃. At ambient pressure, the charge sensitive vibrational modes clearly reveal the development of a charge-ordered state with a structural dimerization, which is in accord with the X-ray measurements. With the application of hydrostatic pressure, the charge order transition in β'' -(BEDT-TTF)₂SF₅CHF₂CF₂SO₃ is surprisingly enhanced as obtained from dc transport and infrared measurements. These findings can not be accounted for with the extended Hubbard model, indicating the importance of lattice degrees of freedom for stabilizing the charge ordering in β'' -(BEDT-TTF)₂SF₅CHF₂CF₂SO₃.

dt. Zusammenfassung

Der Wohlstand der modernen Gesellschaft und die weitere technologische Entwicklung beruht weitgehend auf der Entdeckung und weiteren Anwendung neuer Materialien mit neuartigen funktionalen Eigenschaften. Die Fähigkeit, diese Eigenschaften zu manipulieren, spielt eine Schlüsselrolle in der technologischen Entwicklung, z. B. für neue Generationen von photonischen und elektronischen Geräten. Quantenmaterialien, d.h. Materialien mit einem komplexen Zusammenspiel von Ladungs-, Spin- und Orbitalfreiheitsgraden, bilden eine große und kontinuierliche wachsende Gruppe potenziell funktioneller Materialien. Der makroskopische Zustand solcher Materialien kann durch äußere Parameter wie hydrostatischer Druck, starke magnetische oder elektrische Felder, Ladungsträgerdotierung, et cetera manipuliert werden [1]. Daher ist die Entwicklung eines grundlegenden Verständnisses der physikalischen Mechanismen, die den Phasenübergängen zwischen verschiedenen Zuständen (Quantenphasenübergängen) in Quantenmaterialien zugrunde liegen, eine zentrale Aufgabe der gegenwärtigen Physik der kondensierten Materie. Niedrigdimensionale organische Leiter sind gute Kandidaten für Untersuchungen von Quantenphasenübergängen, da hier verschiedene Grundzustände, von geordneten Isolatoren bis hin zu Metallen oder Supraleitern, durch externen Druck kontinuierlich eingestellt werden können [2]. Aufgrund jüngster Fortschritte bei der Entwicklung von Druckzellen für optische Messungen [3, 4] können die mikroskopischen Wechselwirkungsparameter, die die Phasenübergänge bestimmen, über breitbandige optische Messungen extrahiert werden.

In dieser Arbeit präsentieren wir die Ergebnisse von druckabhängigen Infrarotspektroskopie Messungen an einer Reihe von quasi-zweidimensionalen organischen Materialien, einschließlich des Dirac-Halbleiters α -(BEDT-TTF)₂I₃, der Quanten-Spin-Liquid-Kandidaten β' -EtMe₃Sb[Pd(dmit))₂]₂ und κ -(BEDT-TTF)₂Cu₂(CN)₃ und des ladungsgeordneten Isolatoren β'' -(BEDT-TTF)₂SF₅CHF₂SO₃. Bei unse-

ren Untersuchungen hat sich die optische Spektroskopie als wichtiges Instrument erwiesen, um sowohl die niederenergetischen elektronischen Anregung als auch den Gitterfreiheitsgrad unter Druck zu untersuchen.

In α -(BEDT-TTF)₂I₃ zeigen wir, dass der ladungsgeordnete isolierende Zustand bei Normaldruck allmählich unterdrückt wird und sich zu einem Metall entwickelt. Oberhalb von 0.8 GPa stellen sich die niedertemperatur elektronischen Bänder als geneigte Dirac artige Kegel dar. Der metallische Hochdruckzustand wird durch eine Drude Komponente und eine frequenzunabhängige optische Leitfähigkeit gut beschrieben, ein starker Hinweis auf die Koexistenz von trivialen und masselosen Dirac-Elektronen im System. Darüber hinaus legen unsere Infrarotuntersuchungen offen, dass in der Nähe des Phasenübergangs zwischen isolierenden und metallischen Zuständen sich infolge der korrelierten massiven Dirac-Fermionen eine Energielücke öffnet, die bei steigendem Druck allmählich unterdrückt wird.

Für den halbgefüllten Mott-Isolator β' -EtMe₃Sb[Pd(dmit))₂]₂ enthüllen systematische druck- und temperaturabhängige Infrarotstudien sowohl die elektronische als auch die interne Gitterentwicklung beim Überqueren des Mott-Isolator-Metall-Übergangs. Mit zunehmendem hydrostatischen Druck wird der isolierende Grundzustand kontinuierlich unterdrückt. Für $p \geq 0.6$ GPa erscheint eine Drude artige Komponente, welche sehr deutlich auf kohärente Quasi-Partikel auf der Fermi-Ebene hinweist. In der Nähe des Mott-Übergangs zeigt sowohl die elektronische Anregung als auch die Vibrationsanregung abrupte Änderungen, was die starke Kopplung zwischen Gitter und freien Ladungsträgern belegt. Darüber hinaus beobachten wir eine unerwartete Inversion der Anisotropie der optischen Antwort in der Region oberhalb von 0.6 GPa. Abschließend fassen wir diese Ergebnisse in einem Phasendiagramm zusammen, das weitere experimentelle Methoden enthält.

Im Fall der Quanten-Spin-Liquid-Kandidatenverbindung κ -(BEDT-TTF)₂Cu₂(CN)₃ identifizieren wir eindeutig einen T - und p - gesteuerten Übergang erster Ordnung aus der Analyse der Daten im fernen Infrarot. Auf der Grundlage der Infrarot-Schwingungs-Spektroskopie finden wir außerdem heraus, dass der mikroskopische Ursprung des Isolator-Metall-Übergangs, welcher durch physikalischen Druck induziert wird grundsätzlich von jenem durch chemischen Druck hervorgerufenen, ver-

schieden ist. Unabhängig von dem zuvor genannten unterschiedlichen Mechanismus für den Mott-Übergang kann der metallische Zustand hier durch die universelle lokale Fermi-Flüssigkeitstheorie beschrieben werden. In der STF-dotierten Verbindung κ -[(BEDT-STF) $_x$ (BEDT-TTF) $_{1-x}$] $_2$ Cu $_2$ - (CN) $_3$ mit $x = 0.28$ beobachten wir eine unkonventionelle niederenergetische Mode in den optischen Leitfähigkeitsspektren, welche gut durch eine fluktuierende Dichtewelle, verankert an Störstellen, beschrieben werden kann. [5].

Schließlich untersuchen wir den Druckeffekt im Falle des viertel gefüllten ladungsgeordneten Isolators β'' -(BEDT-TTF) $_2$ SF $_5$ CHF $_2$ CF $_2$ SO $_3$. Bei Normaldruck zeigen die ladungsempfindlichen Schwingungsmoden deutlich die Entwicklung eines Ladungsordnungszustands mit einer strukturellen Dimerisierung, in Übereinstimmung mit Röntgenmessungen. Durch die Anwendung von hydrostatischem Druck wird der Ladungsordnungsübergang in β'' -(BEDT-TTF) $_2$ SF $_5$ CHF $_2$ CF $_2$ SO $_3$ überraschenderweise verstärkt, wie durch DC und IR Messungen gezeigt werden kann. Diese Ergebnisse können im erweiterten Hubbard-Modell nicht berücksichtigt werden, was die Bedeutung der Gitterfreiheitsgrade für die Stabilisierung der Ladungsordnung in β'' -(BEDT-TTF) $_2$ SF $_5$ CHF $_2$ CF $_2$ SO $_3$ aufzeigt.

Publications

Some results from this thesis are published:

Ece Uykur[†], **Weiwu Li**[†], Christine A Kuntscher, Martin Dressel,

”Optical signatures of energy gap in correlated Dirac fermions”

In: *npj Quantum Materials* **4**, 19 (2019)

([†] These authors contributed equally to this work)

Weiwu Li, Andrej Pustogow, Reizo Kato, Martin Dressel,

”Transition of a pristine Mott insulator to a correlated Fermi liquid: Pressure-dependent optical investigations of a quantum spin liquid”

In: *Phys. Rev. B* **99**, 115137 (2019)

Other scientific publications:

Weiwu Li, Eva Rose, Minh Vu Tran, Ralph Hübner, Andrzej Łapiński, Roman Świetlik, Svetlana A. Torunova, Elena I. Zhilyaeva, Rimma N. Lyubovskaya, and Martin Dressel,

”The metal-insulator transition in the organic conductor β'' -(BEDT-TTF)₂Hg(SCN)₂Cl.”

In: *J. Chem. Phys.* **147**, 064503 (2017)

Tobias Biesner, Sananda Biswas, **Weiwu Li**, Yohei Saito, Andrej Pustogow, Michaela Altmeyer, Anja U. B. Wolter, Bernd Büchner, Maria Roslova, Thomas Doert, Stephen M. Winter, Roser Valentí, and Martin Dressel,

”Detuning the honeycomb of α -RuCl₃: Pressure-dependent optical studies reveal broken symmetry”

In: *Phys. Rev. B* **97**, 220401 (2018)

S. Reschke, F. Mayr, Zhe Wang, P. Lunkenheimer, **Weiwu Li**, D. Szaller, S. Bordács, I. Kézsmárki, V. Tsurkan, and A. Loidl,

”Optical conductivity in multiferroic GaV₄S₈ and GeV₄S₈: Phonons and electronic transitions”

In: *Phys. Rev. B* **96**, 144302 (2017)

Ksenia Weber, Maxim L. Nesterov, Thomas Weiss, Michael Scherer, Mario Hentschel, Jochen Vogt, Christian Huck, **Weiwu Li**, Martin Dressel, Harald Giessen, and Frank Neubrech,

”Wavelength Scaling in Antenna-Enhanced Infrared Spectroscopy: Toward the Far-IR and THz Region.”

In: *ACS Photonics* **4**, 45 (2017)

T. Zou, W. Xie, Z. Zhong, **Weiwu Li**, M. Widenmeyer, Y. Liu, S. Kilper, X. Xiao, P. Hansmann, M. Dressel, J. He, T. M. Tritt, A. Weidenkaff, ”Engaging light valence band and phonon scattering via Sm doping in Tetrahedrite Cu₃SbSe₄”

In: *NPG Asia Mater.* (2017), submitted.

D. Neubauer, A. Yaresko, **Weiwu Li**, A. Löhle, R. Hübner, M. B. Schilling, C. Shekhar, C. Felser, M. Dressel, A. V. Pronin,

”Optical conductivity of the Weyl semimetal NbP”

In: *Phys. Rev. B* **98**, 195203 (2018)

Marko Pinterić, David Rivas Góngora, Željko Rapljenović, Tomislav Ivek, Matija Čulo, Bojana Korin-Hamzić, Ognjen Milat, Branko Gumhalter, Predrag Lazić, Miriam Sanz Alonso, **Weiwu Li**, Andrej Pustogow, Guilherme Gorgen Lesseux, Martin Dressel, and Silvia Tomić,

”Electrodynamics in Organic Dimer Insulators Close to Mott Critical Point.”

In: *Crystals* **8**, 190 (2018)

Arkadiusz Frackowiak, R. Świetlik, O. Jeannin, M. Fourmigué, **Weiwu Li**, M. Dressel,

”Charge localization in 1D tetramerized organic conductors: the special case of (tTTF)₂ClO₄”

In: *J. Phys.: Condens. Matter* **31**, 155601 (2019)

Motivation

Quasi-two-dimensional charge-transfer salts based on the organic molecule BEDT-TTF (BEDT-TTF=bisethylenedithio-tetrathiafulvalene) and Pd(dmit)₂ molecule provide a unique platform for investigating the interplay between spin, charge and lattice degrees of freedom, because they display a intriguing phase diagram ranging from metals and superconductors to charge-ordered and Mott insulators, often combined with magnetic order but also spin-liquid properties. Since the low-temperature ground state of these salts can be strongly adjusted either by chemical or physical pressures, they have attracted a great deal of attention in the field of condensed matter physics. In particular, the Mott metal-insulator transition in these organic salts is of prime interest, because the underlying physics plays an important role in understanding the strongly correlated electron system.

According to the Mott-Hubbard model, the key parameter to govern the metal-insulator transition in half-filled system is the ratio of the Coulomb repulsion U to bandwidth W . In the case of quarter-filled system, the controlling parameter is V/W , because the intersite Coulomb repulsion V plays the superior role. For the rather soft organic compounds, hydrostatic pressure is the ideal way to purely control the bandwidth and tune across the insulator-metal phase boundary. Despite a lot of progress in understanding the metal-insulator transition in terms of dc-transport and magnetic properties, not much is known about how the dynamics of charge carriers develops as correlations advance across the metal-insulator transition.

Optical spectroscopy is the most suitable method for studying the electrodynamic properties of organic conductors, because it allows us to analyse the dynamics of the charge carriers and directly extract the Coulomb repulsion U and the bandwidth W as well as the coherent quasiparticle contribution to the dynamical conductiv-

ity. Here we want to explore in detail the transition from the Mott insulating to the metallic state by performing pressure- and temperature-dependent optical investigations on half-filled Mott insulator β' -EtMe₃Sb[Pd(dmit)₂]₂ and κ -(BEDT-TTF)₂Cu₂(CN)₃ as well as quarter-filled charge-ordered insulator α -(BEDT-TTF)₂I₃ and β'' -(BEDT-TTF)₂SF₅CHF₂SO₃. We observe how the Mott gap is suppressed on the insulating side and how the effective mass evolves on the metallic side. A thorough analysis of the vibrational features provides interesting insight into the charge distribution, the electron-phonon coupling and changes upon crossing the insulator-metal transition.

Contents

List of Abbreviations	v
Abstract	vii
dt. Zusammenfassung	xi
Publications	xv
Motivation	xvii
1. Introduction	1
1.1. Charge transfer organic salts	1
1.2. Quasi-two-dimensional structure	6
1.2.1. κ -phase	10
1.2.2. α - and β'' -phase	14
1.2.2.1. α -phase	15
1.2.2.2. β'' -phase	19
1.2.3. β' -Pd(dmit) conducting metal complexes	21
2. Theoretical Background	29
2.1. Electrodynamics	29
2.1.1. The interaction of radiation with matter	31
2.1.2. K-K relation and sum rules	34
2.2. Theoretical models	36
2.2.1. Drude model	36
2.2.2. Lorentz and Fano model	38
2.2.3. Extended Drude analysis	41

2.3. Optical properties of quantum materials	42
2.3.1. Charge order	42
2.3.2. Dirac electrons	45
2.3.3. Bad metal	47
2.3.4. Fermi liquid	49
2.3.5. Mott metal-insulator transitions	54
3. Setup	59
3.1. Principle of FTIR	59
3.1.1. Michelson interferometer	60
3.2. Pressure setup	61
3.2.1. Piston-cylinder cell	62
3.2.2. DAC pressure cell	67
3.3. Data analysis under pressure	72
4. High-pressure infrared spectroscopy of α-(ET)₂I₃	77
4.1. Background	77
4.2. Room temperature reflectivity and optical conductivity	80
4.3. T - and p -dependent reflectivity and optical conductivity	86
4.4. Optical response of massless and massive Dirac electron	91
4.5. Conclusion	98
5. Optical investigations of β'-EtMe₃Sb[Pd(dmit)₂]₂ under high pressure	101
5.1. Background	101
5.2. T - and p -evolution of the optical spectra	104
5.3. Optical spectra at 10 K	112
5.4. Electron-Lattice interactions	117
5.5. Anisotropy of the in-plane optical response	120
5.6. Conclusions	122
6. Pressure-dependent optical investigations on the spin liquid compound κ-(ET)₂Cu₂(CN)₃	125
6.1. Background	125
6.2. Vibrational properties	130
6.3. Electronic excitations	134

6.4. Fermi liquid behaviour	141
6.5. Bad-metallic behaviour	148
6.6. Conclusion	153
7. High-pressure vibrational spectroscopy of β''-(ET)₂SF₅CHFCF₂SO₃	155
7.1. Background	155
7.2. Vibrational modes at ambient condition	158
7.3. Vibrational modes under high pressures	161
7.4. Conclusions	168
8. Conclusions and Outlook	171
A. Acknowledgements	175
Bibliography	179
Declaration of originality	193

1. Introduction

In this chapter we will review some basic physical and chemical aspects of organic conductors. A more general description of organic conductors can be found in a series of books [6–11].

1.1. Charge transfer organic salts

As a typical example of low-dimensional organic conductors, special attentions will be given on the one-dimensional Bechgaard salts in this section.

The low-dimensional organic conductors represent a special class of materials, because many rich and exotic phenomena have been discovered in those salts over the last three decades. Organic molecular solids are compounds that consist of relatively light element such as C, H, S, N. These crystals are constituted by periodic arrangements of small molecules formed by the chemical bonding of above mentioned atoms (C, H, S, N). Despite the complex structures of the building molecules, the unit cell of the most studied organic crystals is quite simple. Thanks to the distinct energy scales between the intra- and inter-molecular degrees of freedom, the electronic state of these materials can be well understood using molecular orbital model [6].

When the electrons are closely bound to atoms, tight-binding theory can be applied to calculate the band structure. However, even for the simplest one-dimensional organic materials, one molecule consists of more than ten atoms. Thus, a simplified model need to be considered to deal with the complicated structure in such system. The most powerful and frequently used theory is called molecular orbital (MO) method [9], where the valence electrons can be delocalized over the whole molecule.

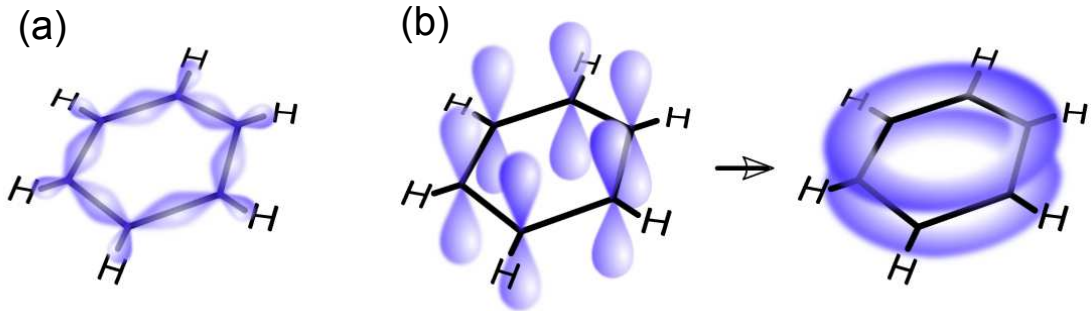
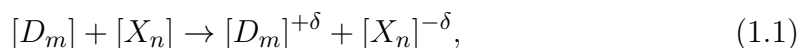


Figure 1.1.: Configurations of molecular orbitals of a benzene molecule C_6H_6 . (a) The σ bond consists of three pairs of double bonds ($C=C$), resulting from the sp^2 hybridization lying in the molecular plane. The electrons are localized between the double bonds $C=C$. (b) The π bond are formed by the overlapping of $6p_z$ unhybrid orbitals of carbon atoms. Therefore, we have a delocalized density of electrons above and below the plane. After [12]

The molecular orbitals are determined with a linear combination of the atomic s - and p -orbitals of the building atoms and can be classified into two type of orbitals, namely σ and π -orbitals. The σ orbitals are formed to be parallel to the molecular planes and correspond to the localization of the electrons along the bonding axis of the nearest atoms. In contrast to the localized behaviour of the σ -orbitals, the π -orbitals are delocalized and extended perpendicular to the molecular plane. Since the binding energy of the π -orbitals are lower than that of σ -electrons, they can be easily excited, and tend to be delocalized along the stacks of the molecules. As a simple example of the applicability of this method, the σ and π -orbitals of benzene are schematically represented in Figure 1.1.

The organic conductors discussed here belong to the donor-acceptor class, where the creation of unpaired electrons is realized by a partial transfer of charge from a positively-charged ion to a negatively-charged one. The charge transfer salts D_mX_n can be obtained through the chemical reaction



where m and n are integers, and δ stands for charge transfer ratio (in the most case $m = 2, n = 1, \delta = 1$) [9]. Here D refers to an organic electron-donor molecule, such as TMTSF, BEDT-TTF (hereafter ET) or their derivatives. X corresponds to an

electron-acceptor complex, in most cases inorganic molecule. Therefore, they are also called charge-transfer (CT) materials for the above reason. In the formation of charge transfer salts, the negatively charged anions $[X_n]^{-\delta}$ usually has a closed-shell orbital configuration, thus they do not contribute to the conducting band across the Fermi surface. On the contrary, the π -orbitals of the partially filled $[D_m]^{+\delta}$ molecules can extend perpendicularly to the molecular planes and tend to overlap between adjacent molecules due to the dense packing of the donor molecules. The delocalization of the charge carriers in these charge transfer organic systems are principally different from other classes of molecular conductors such as conjugated polymers, where high conductivity is obtained with doping of impurity. As a result, we can treat the organic conductors in a convenient way, where the highest occupied molecular orbital (HOMO) or the lowest unoccupied molecular orbital (LUMO) of the π -electrons move in a potential created by the σ electrons in the anionic layers.

As an example for the charge transfer salts, Figure 1.2 schematically describes the HOMO molecular orbitals of the TMTSF molecules. In general, the amplitude of HOMO of TTF-type and derivative donor molecules are rather large and the sign on every chalcogen atom are the same as shown in Figure 1.2. The distance between the molecules along the stacking direction is shorter than the sum of the van der Waals radii of the Se atoms. Therefore the π -orbitals of the partially-filled outer molecular shells overlap and a conducting electronic band structure is formed. Since these bands are composed by the overlap of molecular orbitals of adjacent molecules, the anisotropy and dimensionality of the electronic properties in these materials strongly depends on the relative angle and overall spatial arrangement of the donor molecules. For the TMTSF (tetramethyltetraselenafulvalene) molecule, an infinite stacking of these units structure results in a significant inter-molecular overlap of the orbitals along the stacking axis and much weaker between them. This gives rise to a quasi-one-dimensional conduction band. In contrast, packing of BEDT-TTF (bisethylenedithio-tetrathiafulvalene) molecules leads to a quasi-two-dimensional electronic structure.

Based on the molecular orbitals, a simple extended Hückel tight binding band calculation has been developed, which provided a very useful tool to quantitatively predict the physical properties of the new designed organic conductors. The trans-

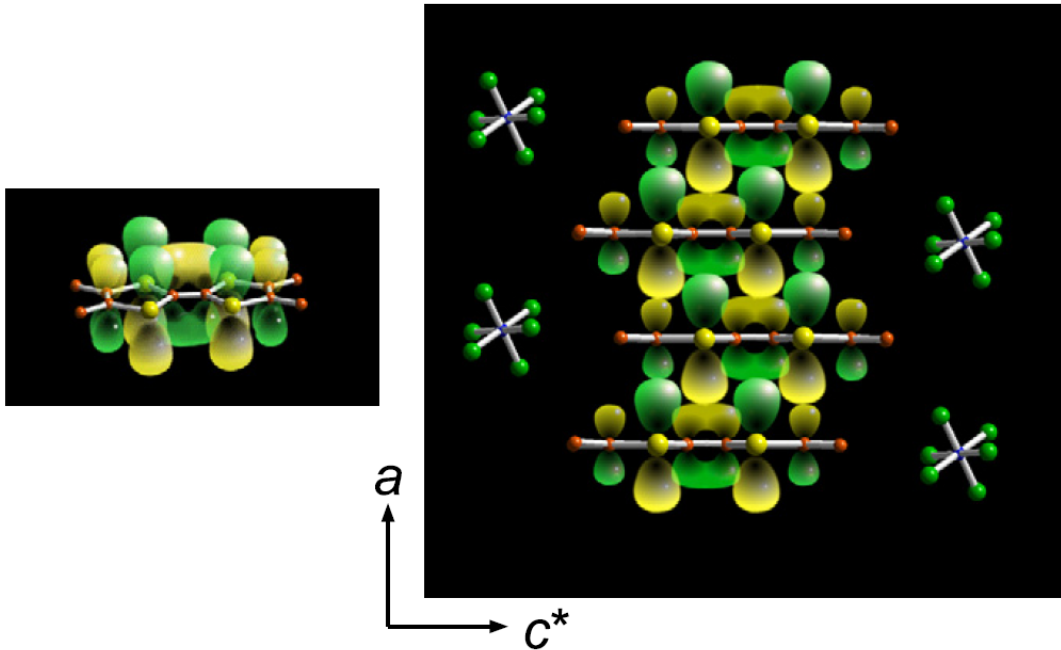


Figure 1.2.: (left) Side view of the the TMTSF molecule with HOMO π molecular orbitals seen along the b -axis. The selenium and carbon atoms are denoted by yellow and red dots, respectively. The yellow and green clouds around the atoms indicate the p_z atomic orbitals; (right) Overlapping pattern of the HOMOs along the donor stacking direction in the Bechgaard salt $(\text{TMTSF})_2\text{PF}_6$. The a -direction has the highest conductivity with the largest molecular orbital overlap, whereas the c -axis is less metallic due to the weaker transfer integral. After [13]

fer integral t_{ij} can be directly obtained according to the the following relations

$$t_{ij} = \frac{1}{2}K(E_i + E_j)S_{ij} \quad (1.2)$$

where E_i is the ionization energy at the i -th site, K is a constant usually taken to be 1.75, S_{ij} and t_{ij} are the transfer integral and the inter-molecular overlap integral of molecular orbitals, respectively [6, 9].

At ambient-pressure conditions, $(\text{TMTSF})_2\text{PF}_6$ was found to undergo a metal-insulator transition at very low temperatures with a ground state of spin density wave ordering (SDW) [15]. Upon applying hydrostatic pressure up to 12 kbar, the SDW insulating state can be suppressed with the appearance of superconductivity below $T_c = 0.9$ K [16]. It was for the first time that superconductivity was observed

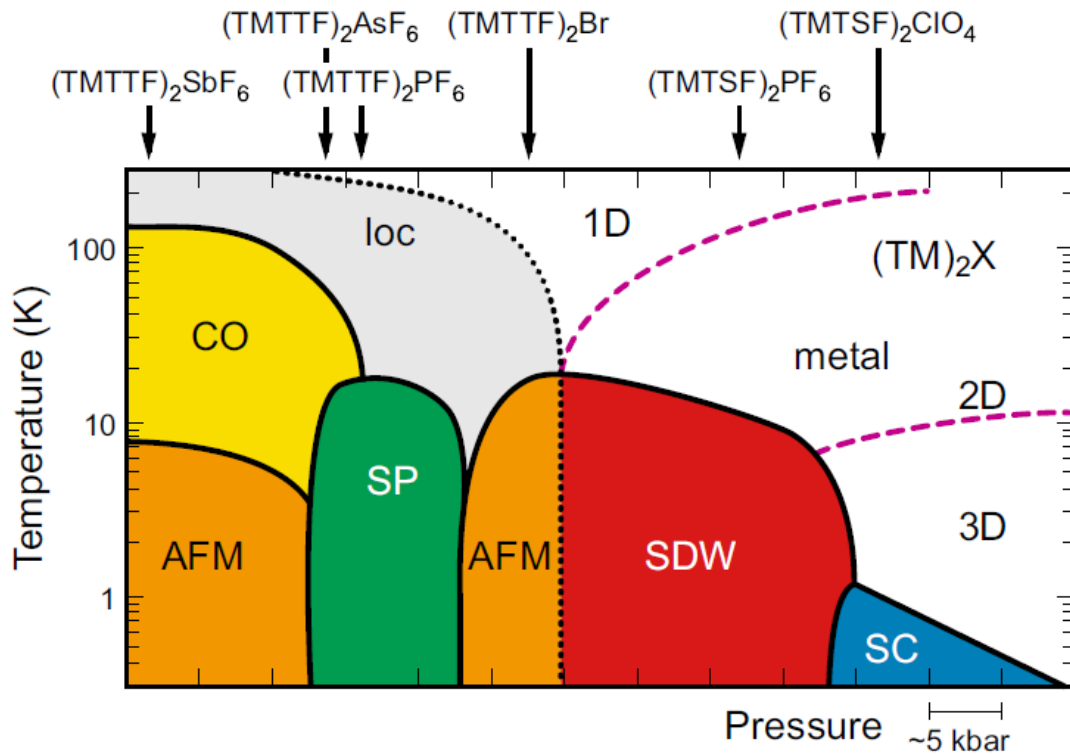


Figure 1.3.: (a) Sketch of the generic phase diagram for the quasi-one-dimensional family $(TM)_2X$ proposed by Jérôme. TM stands for TMTTF or TMTSF. The ground state in the phase diagram can be tuned by external or chemical pressure. After [14]

in an organic crystal. Since then, extensive studies have been performed on molecular conductors to search for new high T_c superconductors or new exotic physical phenomena by physicists and chemists. Later on, it was found out that many of these quasi-1D electron systems undergo a metal-insulator transition with a variety of insulating ground state, ranging from charge order to spin-Peierls and antiferromagnetic state etc. Apparently, the strong tendency of these salts to experience a metal-insulator transition cannot be explained by extended Hückel theory without consideration of the electron-electron interactions.

The bandwidth in organic materials are quite narrow due to the relatively large inter-molecular distances as compared to the shorter atomic lattice constant in inorganic systems. The small hopping integral and low dimensionality make electronic correlations very important and often give rise to the localization of the free

carriers with a splitting of the conducting bands. For this reason, the organics family was considered to be an ideal platform for the experimental investigation of Mott-Hubbard physics because of their fruitful tunability. The tunability can be reached from both dimensionality and interaction strength. The dimensionality D of the electrostatics is defined by the relative ratios between transfer integrals along different structural directions, and the relative interaction strength U/W is defined as the ratio of the onsite (intersite) Coulomb repulsion U (V) and the intermolecular bandwidth W (W is proportional to t). These parameters can be adjusted either by chemical substitution or by applying external pressure. The generic phase diagram of $(\text{TM})_2\text{X}$ family (here TM stands for TMTSF and TMTTF) can be summarized in Figure 1.3.

1.2. Quasi-two-dimensional structure

As we described in the previous section, most of the 1D organic conductors show either charge or spin instability at low temperatures due to the strong electron-phonon and electron-electron interactions. Only few of them have superconducting properties at ambient pressure condition. In order to obtain ambient pressure superconductivity in these organic materials with higher transition temperatures, it is necessary to increase their dimensionality and delocalize the electrons in other directions. This will principally suppress the low-temperature instability state. On the other side, if we can also increase the overlap integral between the adjacent molecules by using larger size molecules with enhanced π -orbitals, we can additionally enhance the mobility of the electrons. Based on above ideas, new electron donor molecule BEDT-TTF (bis(ethylenedithio)-tetrathiafulvalene) or its analogous BEDT-TSF, which has additional rings of carbon and sulfur atoms compared to TMTTF, have been used to synthesize new family of organic conductors [9]. After the first discovery of organic metallic state in β'' -(ET) $_2$ ClO $_4$ [17], in 1988 an ambient-pressure superconductor was realized in κ -(ET) $_2$ Cu(NCS) $_2$ with a transition temperature around 10 K [18], which is several times higher than that of 1D compound. Since then, many efforts have been put on this family to synthesize new 2D organic salts based on BEDT-TTF molecules. Up to now, around 100 compounds have been discovered. Most of the 2D organic salts are prepared by electrochemical crystallization [9], similar to 1D organic Bechgaard salts. The typ-

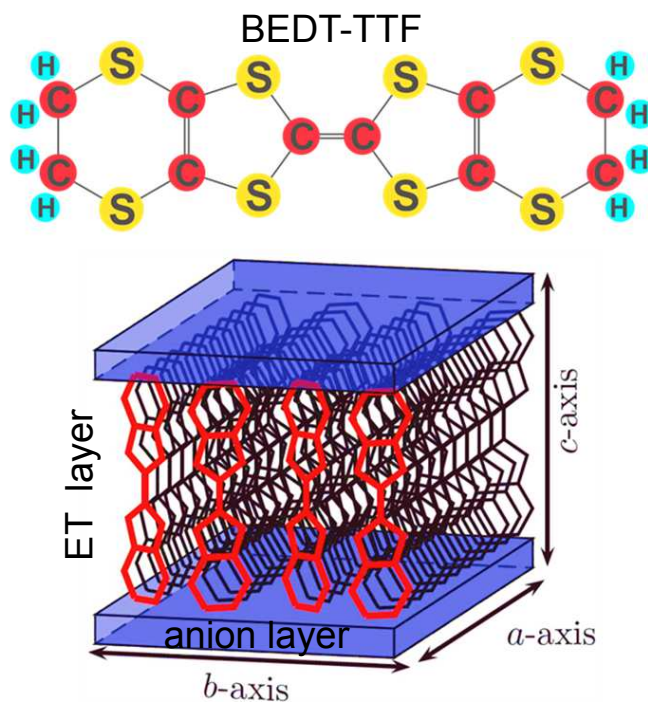


Figure 1.4.: The building block of the charge transfer salts. The quasi-two-dimensional conducting layers of ET molecules are separated by the insulating anion layers. After R. Beyer.

ical crystal structure of these organic materials is depicted in Figure 1.4.

As can be seen in Figure 1.4, the BEDT-TTF is the building block and acting as electron donor. The two-dimensional conducting layer is formed as a result of the transfer integral overlap between the neighbouring molecule in the adjacent stacks. This is in contrast to the Bechgaard family, where the donor molecules form 1D infinite stacks. Since the anion layer acts as electron acceptor and usually has closed shell, in general, it was believed that there is no direct orbital overlap between anion layer and BEDT-TTF layer. For this reason, the whole systems can be treated as a quasi-2D electronic system, which shows highly conducting behaviour within BEDT-TTF layers and much less electron hopping perpendicular to the plane. However, more recently it was found that the anion layer can also have strong influence on the electronic state of the conducting BEDT-TTF layer [19, 20].

In the course of growing organic crystals, it was found that more than one type of

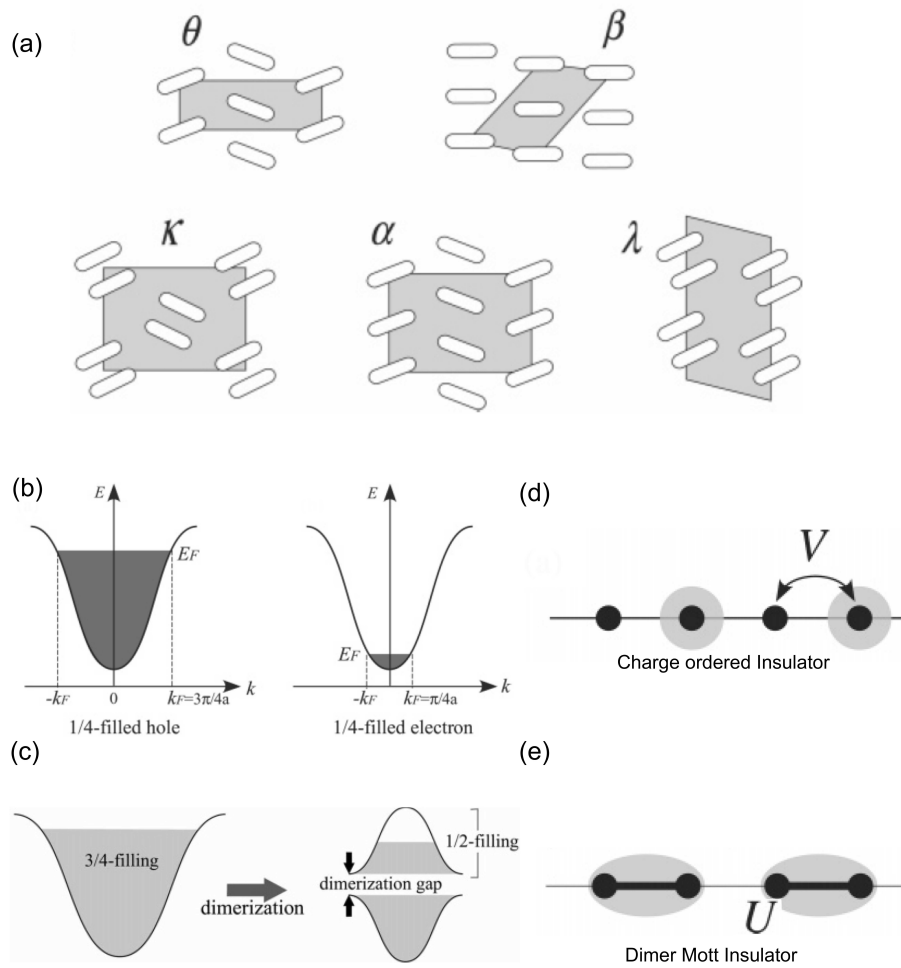


Figure 1.5.: (a) Schematic representations of spatial arrangements of these molecules in the 2D plane for different polytypes, where the ellipses and the gray area represent the molecules and the unit cells, respectively. Electronic band structures of the 1D system with (b) and without (c) the dimerization. Schematic representations of two limiting cases in one-dimensional quarter-filled system: (d) the charge ordered state and (e) the dimer-Mott insulating state. Black dots and gray circles represent the lattice sites and the localized carriers, respectively. After [22]

structure have been achieved even with the same composition. The various spatial arrangement of the BEDT-TTF in the 2D plane are in distinct contrast to the case in 1D, where $(\text{TM})_2\text{X}$ family almost has the same crystal structure. Figure 1.5 displays 6 types of the most important BEDT-TTF structure. For some historical reason, Greek characters such as α , β and κ etc. [21], have been used to distinguish between different packing motifs. From the experience of chemist, the packing patterns are strongly controlled by donor-anion interactions. Therefore, with the modification of the anionic molecules X in $(\text{ET})_2\text{X}$ we can obtain various packing motifs of the donor layers. This subsequently tunes the electronic and magnetic properties of the these salts.

Due to the $(\text{ET})_2\text{X}$ stoichiometry, the conduction bands consist of a three-quarter filled band of electrons or a quarter-filled band of holes. Therefore the BEDT-TTF molecules have one half valence in average. In some cases, the very large intermolecular transfer integral leads to a strong dimerization between adjacent ET molecules. Instead of a single ET molecule, the dimers are considered as one lattice site. This results in the opening of a dimerization gap, and thus, an effectively half-filled band. Figure 1.5 illustrates the distinct electronic band structures with and without dimerization. Thus, the polytypes of ET family can be generally classified into two groups: α , β and θ belong to the 3/4-filled model with weakly dimerized ET pairs; while λ and κ have strongly dimerized ET pairs and are described by the half-filled dimer model.

At ambient conditions, most of the organic materials exhibit insulating behaviour with various types of symmetry breaking ordering due to the strong electron-electron correlations. In the quarter-filled case, the system tends to be a long-range charge-ordered (CO) insulator with one electron on every other site, if the intersite Coulomb interaction V can not be neglected. The CO state has been realized in many of α -, θ -, β -phase and its analogous, such as β' -, β'' -phase [23]. Typically in many of the above compounds, the CO transition is accompanied by lattice distortion, resulting in a gapped spin singlet state at low temperatures. On the other hand, at half-filled case such as κ and λ , the strong on-site Coulomb repulsion U gives rise to a dimer-Mott-insulating state with uniform charge distribution on lattice site. Additionally, various magnetic ground states, ranging from antiferromagnetic state

to spin liquid state, have been observed in κ -family, depending on the degree of spin frustration [24–26].

In the following section, we will make a brief and general introduction of κ , α and β phase with several examples, showing how the electronic state can be modified under external stimulus. For the material, which we have measured, will be further described in detail in the Chapters of experimental results.

1.2.1. κ -phase

The κ -(BEDT-TTF)₂X salts with X=Cu(NCS)₂, Cu[N(CN)₂]Br and Cu[N(CN)₂]Cl are the most intensively studied and best understood family of 2D organic conductors. These 2D κ -type organic compounds give rise to great interest among physicist and chemist, since the superconducting transition temperatures was found to be much higher than that of 1D organic conductors. The highest T_C was found up to 12.8 K in the compound κ -(BEDT-TTF)₂Cu[N(CN)₂]Cl under pressure of 0.3 kbar [27]. In addition, their phase diagrams are very similar with those of high- T_C cuprate superconductors. As depicted in Figure 1.6, subtle changes in anion layers can significantly alter the band overlap between adjacent molecules within BEDT-TTF layers. Correspondingly, the ground state ranges from antiferromagnetic (AFM) to superconducting state (SC). Similar to the discussion in cuprates, the presence of AFM near to the SC phase has led to the scenario that AFM fluctuation may play a key role in creating the superconducting state [28, 29].

The electronic properties of the κ -(ET)₂X are not only sensitive to the anion X, but also can be strongly modified with application of hydrostatic pressures. Extensive studies under pressure have been performed by many groups to construct the pressure-temperature phase diagram [30–32]. The continuous control of external pressure by using helium gas technique allows them to finely tune the system across the first-order metal-insulator boundary and reveal the nature of the Mott transition in terms of charge, spin and lattice degrees of freedom. Figure 1.6 shows the three similar phase diagram investigated by applying a variety of experimental techniques such as NMR, ac-susceptibility, dc resistivity and ultrasound velocity from both isothermal and isobar sweeps.

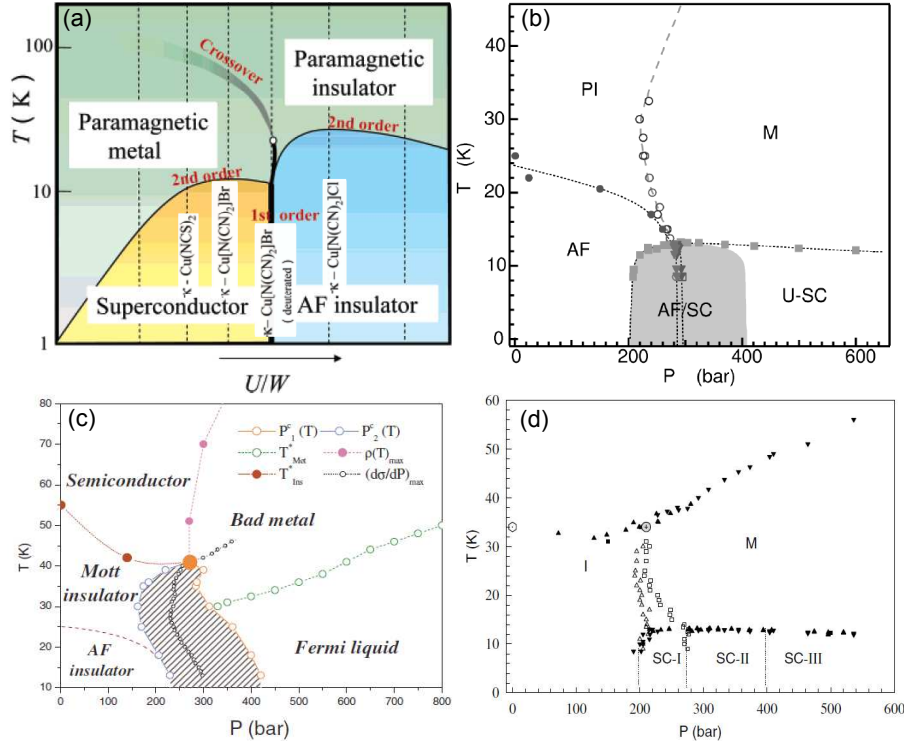


Figure 1.6.: (a) Generic phase diagram for strongly dimerized κ -(ET)₂X proposed by Kanoda from the dc -resistance and NMR measurements at ambient pressure. $Cu(NCS)_2$ and $Cu[N(CN)_2]Br$ salts are located on the metallic site with low value of U/W , while $Cu[N(CN)_2]Cl$ is AF insulator due to strong electron-electron correlation, i.e., large value of U/W . The deuterated D_8 - $Cu[N(CN)_2]Br$ lies on the phase boundary between AFI and SC. From these experiments no quantitative value of U/W was obtained. (b) Pressure-temperature phase diagram for κ -Cl (κ -Cl denotes κ -(ET)₂ $Cu[N(CN)_2]Cl$) based on pressure-dependent NMR and ac susceptibility measurements. An inhomogeneous domain, exhibiting coexistence of AF and SC order, was determined near the first-order transition line (shade area). (c) Phase diagram of κ -Cl determined from in-plane transport measurements with gas pressure technique. The phase coexistence region was confirmed. (d) Phase diagram measured of κ -Cl by ultrasonic velocity measurements under pressure. At high pressure range, additional pseudogap features and various phases of SC were discovered. Reproduced from Refs. [25, 30–32]

As depicted in Figure 1.6 (b), at low pressure ranges, the AF ordering of κ -Cl gets gradually suppressed with decreasing Neel temperature. Upon increasing pressure further, the system undergoes first-order transition from insulator to superconductivity. At the vicinity of the first-order boundary, there exists spatial inhomogeneous region with overlap between AF and SC orders, as demonstrated by the detectable hysteretic susceptibility signals. The sharp first-order Mott transition was also unveiled by other techniques: the resistance shows huge discontinuous jump with hysteresis; the sound velocity displays a sharp dip, which corresponds to the huge decrease of compression modulus and thus a divergence of electronic compressibility. Furthermore, the first-order line terminate at the critical point ($p_0 \sim 0.3$ kbar $T_0 \sim 35$ K), above which the transition is more crossover like due to the thermal fluctuation.

To further explore the nature around the critical end point, detailed and extensive studies were conducted by Kanoda's group, employing dc-transport and NMR measurements [33, 34]. The critical exponents of both the conductance and spin susceptibility, extracted from the power-law fitting, are not consistent with those known universality classes (mean-field, Ising model, XY model and Heisenberg model)[33, 34]. Therefore, it was suggested that the Mott criticality of the present case may be a new class of universality due to its low dimensionality, i.e., quasi-2D. On the other hand, another group has suggested that the Mott transition can be fully described by mean-field theory. It was shown that at least the critical exponent of the relative length changes for κ -Cl obeys exactly the theoretically predicted value [35]. Interestingly, the criticality like behaviour can also emerge at the crossover region well above the critical end point (p_0, T_0) as shown by recent transport measurements three different compounds, i.e., κ -Cl κ -Cu₂(CN)₃ and β' -EtMe₃P[Pd(dmit)₂]₂ (κ -Cu₂(CN)₃ denotes κ -(ET)₂Cu₂(CN)₃). It was observed that the crossover region exhibits fan-shaped quantum-critical behaviour with mirror symmetry regardless of the distinct ground states of these samples [36].

The magnetic and electronic properties of the Mott transition for κ -Cl has been well collected in the literatures. However, pressure-dependent dynamic properties of κ -Cl were seldom explored due to the technical difficulties in designing pressure cell for

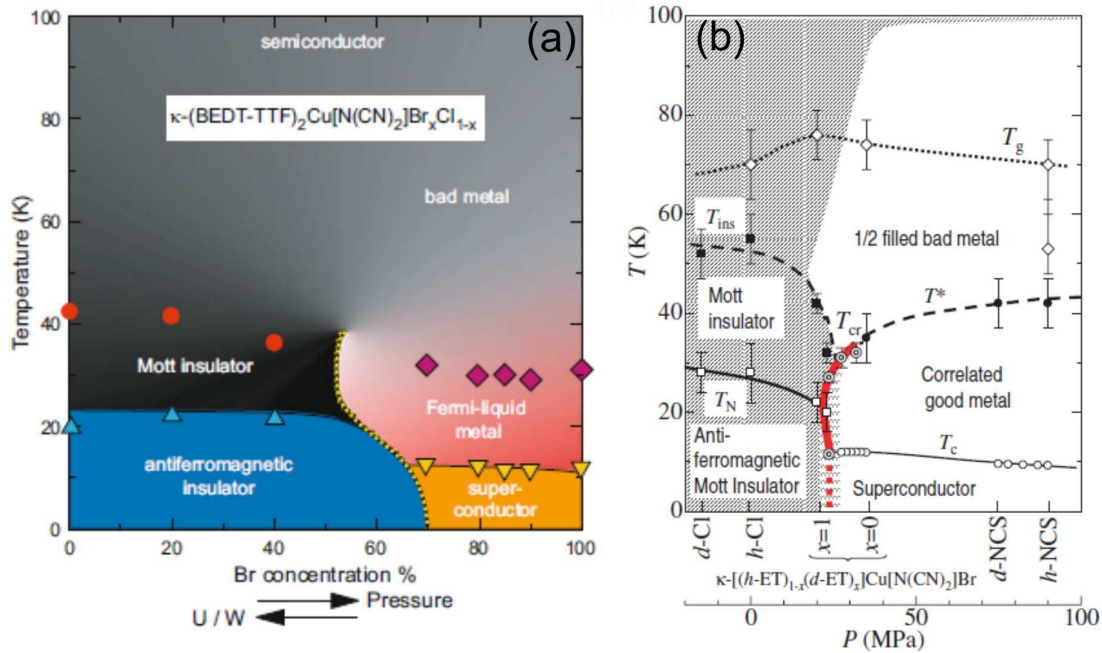


Figure 1.7.: (a) Generic phase diagram for $\kappa-(\text{ET})_2\text{X}$ explored by successively replacing Cl by Br in $\kappa-(\text{ET})_2\text{Cu}[\text{N}(\text{CN})_2]\text{Br}_x\text{Cl}_{1-x}$. Optical measurements were performed on 5 samples with various Br concentrations: 0, 0.4, 0.73, 0.85, 0.9, respectively (b) Schematic phase diagram of $\kappa-(\text{ET})_2\text{X}$. The Mott transition is investigated by using mixed crystals with the ET molecules (h-ET) partially substituted with the deuterated molecules (d-ET), i.e., $\kappa-[(h\text{-ET})_{1-x}(d\text{-ET})_x]\text{Cu}[\text{N}(\text{CN})_2]\text{Br}$. The horizontal axis displays the physical pressures and substitution ratio x . T_{g} corresponds to the temperature of ethene group ordering. The thick red curve denotes the first-order boundary and the phase separation appears nearby the dashed red curve confirmed by scanning micro-region infrared reflectance spectroscopy. After [2, 37]

optical measurements at very low pressure range, e.g., $p < 1$ kbar. An alternative approach to finely modify the bandwidth is the continuously controllable chemical substitution. This method has been widely employed in a variety of inorganic systems and allows us easily to perform optical investigation [2]. Comprehensive optical [38–40], transport [41] and magnetic studies [41] on series of chemical substituted alloys, $\kappa(\text{ET})_2\text{Cu}[\text{N}(\text{CN})_2]\text{Br}_x\text{Cl}_{1-x}$, were performed at the 1. physikalisches institut in order to map out the phase transition from the antiferromagnetic insulator to the superconductor as shown in Figure 1.7 (a). It was found that for all Br

concentrations, the crossover region at high temperature is characterized by overdamped Drude response in the optical conductivity, typically termed as bad metal behaviour. Their spectra have shown that at the lowest temperature there is clear spectral weight transfer from mid-infrared region to a zero-energy Drude part as the substitutional ratio x increases. Similar optical behaviour was observed in a series of x-ray irradiated κ -Cl compounds by T. Sasaki's *et al.* as well. In combination with systematic transport measurements they have proposed that the irradiation induced Mott gap collapse results from Anderson-type insulator-metal transition due to the molecular disorders in the anion layer [42, 43]. It is interesting to point out that the low-energy optical conductivity of their metallic sample is dominated by a non-zero frequency peak instead of a standard Drude-type response, which is a strong signature of Anderson localization [42].

As shown by many pressure-dependent measurements, the inhomogeneous phase, originating from phase separation between insulator and metal, emerges nearby the first-order boundary. With the help of scanning micro-region infrared spectroscopy using the synchrotron radiation, detailed studies of the phase separation has been performed by T.Sasaki *et al.* in the both X-ray irradiated κ -Cl compounds [44] and the deuterated system κ -[(h8-ET) $_{1-x}$ (d8-ET) $_x$] $_2$ Cu[N(CN) $_2$]Br [37], where h8 and d8 denote fully hydrogenated and deuterated molecules, respectively. Since the peak shift of the ν_3 vibrational mode is strongly coupled to electronic background, it was used to distinguish the metallic and insulating region of the sample. As a result, they have successfully observed the coexistence of metallic and insulating domains with size of ~ 100 μm in real-space imaging. It was then argued that the macroscopic size of the domains observed in organic system is intrinsically different from nano-scale inhomogeneities reported for inorganic Mott systems such as high- T_c cuprates [45].

1.2.2. α - and β'' -phase

Among those weakly dimerized phases, the nonmagnetic organic conductors with α - β'' - and θ packing motifs are of particular interest, as several species display superconductivity at ambient conditions or under high pressures. Based on extended

Hubbard model with inclusion of strong intersite Coulomb repulsion, Merino and McKenzie theoretically predicted that a superconducting state with d_{xy} pairing could be achieved via charge fluctuations when the long-range charge order is suppressed [46]. The underlying principle differs from the superconducting mechanism suggested in the half-filled κ -phase (d_{xy} symmetry), where spin fluctuations are of superior importance. Their suggestion was confirmed by different experimental methods, such as infrared spectroscopy [47, 48] and NMR [49]. In this section we will review the generic phase diagram of α - and β'' -salts with respect to their charge, spin and lattice degrees of freedom.

Before discussing the electronic properties of these salts, we will give a short introduction of the structural properties. As depicted in Figure 1.8 (c) and (d), the packing patterns of donors in quarter-filled system can be classified into several groups according to the arrangements of the intra- and inter-stacks of ET molecules. In each stacks, two ET molecules are arranged in two different structures, i.e., RB and RA modes [6, 21]. In RB structure, the molecule is slipped along the long axis and a five-membered ring of TTF is on the top of a C=C bond of another molecule. When the molecule is slipped along the short axis and a five-membered ring sits on top of a sulfur atom, this configuration is called ring-over-atom (RA) structure. Since the molecules are tilted from the columnar direction in RA configuration, the transfer integral of the interstacks are larger than those of the intra-stacks in the α - β'' - and θ -structure.

1.2.2.1. α -phase

The quasi-two-dimensional organic conductors α -(BEDTTTF)₂I₃ (hereafter denoted as α -I₃) is one of the most extensively studied compounds because of its charge-order transition at ambient pressure, superconductivity under uniaxial strains and unusual transport properties at hydrostatic pressure [50, 51]. α -I₃ undergoes a first-order metal-insulator transition around 135 K and simultaneously exhibits a sharp decrease in susceptibility, displaying a nonmagnetic ground state. This transition was later identified as a stripe-type charge-ordered state by a variety of experimental methods including X-rays [52], optics [53, 54], Raman [55, 56] and NMR [57]. The amplitude of the charge disproportion was estimated to be around $0.6e$. The

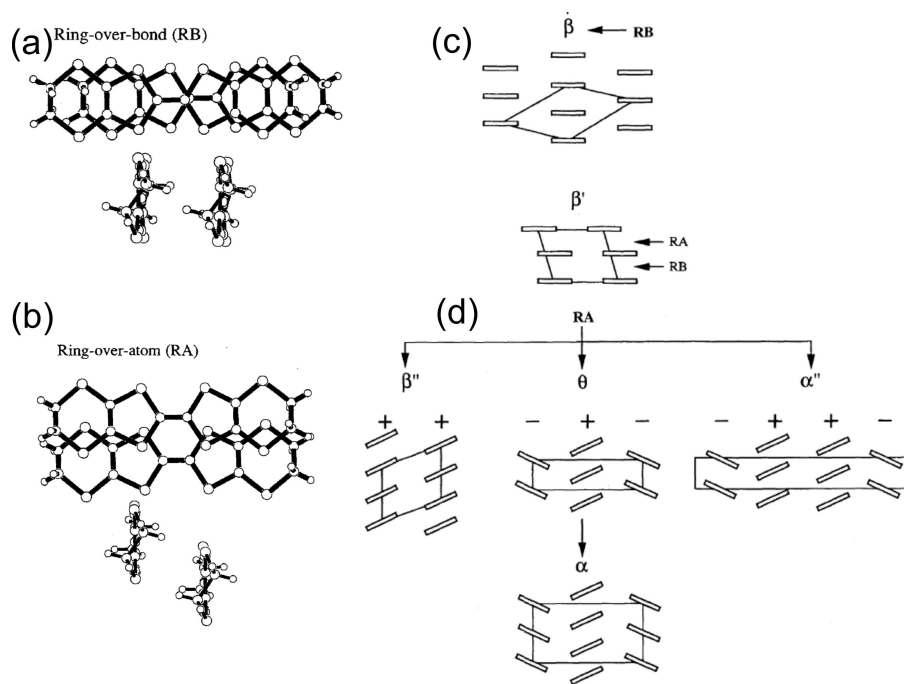


Figure 1.8.: (a) Ring-over-bond(RB) and (b) Ring-over-atom (RA) structures viewed perpendicular to the molecular plane and along the long axis of the molecular, respectively. (c) β -structure consists of repeating RB mode, while β' -structure is composed of alternate arrangement of the RB and RA modes. The molecules for both phases are all parallel to each other.(d) β'' -, α -, α'' - and θ -phase are all constructed from the RA structures. In contrast to the parallel arrangement of molecules in β'' -phase, the molecules between interstacks are inclined for α -, α'' - and θ -phase. After [21]

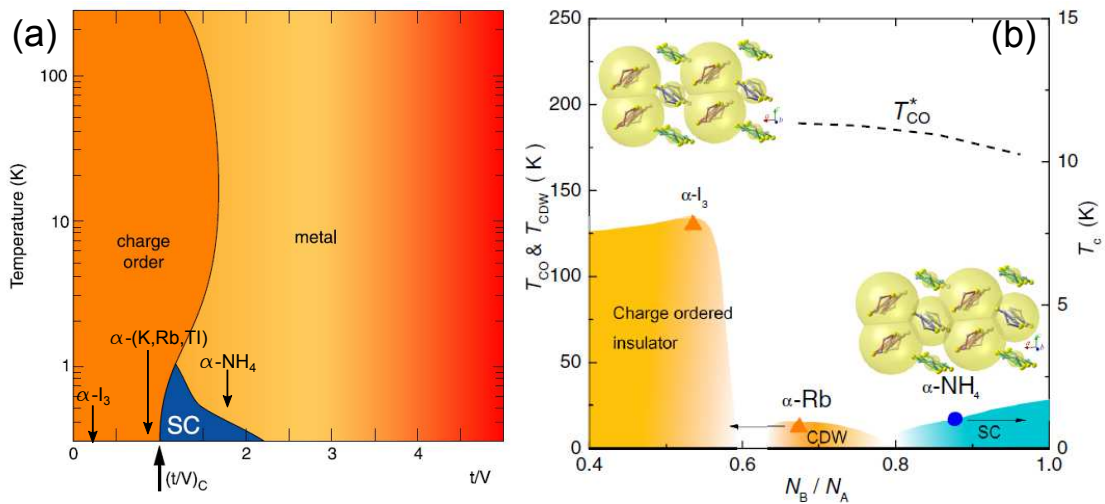


Figure 1.9.: (a) Tentative phase diagram for the quarter-filled two-dimensional organic conductors α -(BEDT-TTF) $_2$ MHg(SCN) $_4$ and α -(BEDTTF) $_2$ I $_3$ determined from optical measurements. The system undergoes phase transitions from a charge ordered state to an intermediate phase with charge fluctuations, subsequently to a metallic state under pressure. (b) Generic phase diagram for α -type BEDT-TTF salts constructed from site-selective NMR spectroscopy. The order parameter is defined as the ratio of local DOS (density of state) between at B and A sites, namely N_B/N_A . (Molecule A and B are two crystallographically independent BEDT-TTF molecules). The size of the yellow circle schematically denotes the value of the DOC on each molecular site. CDW denotes charge density wave, SC is superconductivity. After [2, 60]

driving force for the CO state has been attributed to the strong intersite Coulomb repulsion as discussed in a series of theoretical work [22, 46, 58]. However, more recently a new mechanism of the CO transition was proposed by Pouget *at el.* with consideration of anion-donor interactions. In his scenario, the zigzag I $_3^-$ anionic chains strongly couples the donor layers via the hydrogen bond, and thus give rise to the charge redistribution of holes and the opening of a gap on the Fermi surface [59].

Another characteristic member of α -salts is α -(BEDT-TTF) $_2$ MHg(SCN) $_4$ family, with M = K, Rb, Tl, and NH $_4$ (hereafter denoted as α -K, α -Rb, α -Tl and α -NH $_4$, respectively) [62, 63]. These four salts has the same crystal structure. Thus, they exhibits almost identical band structures with an quasi-one-dimensional open Fermi

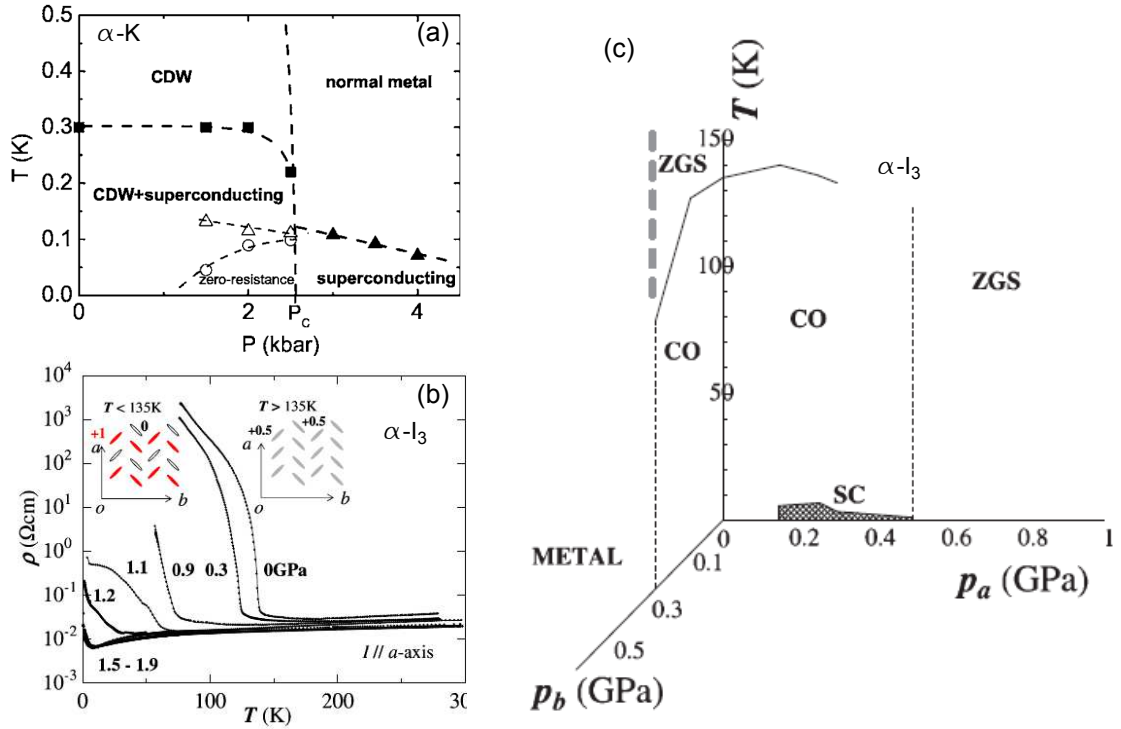


Figure 1.10.: (a) Pressure-temperature phase diagram for α -(BEDT-TTF)₂KHg(SCN)₄ measured from transport measurements. The CDW state becomes completely suppressed at critical pressure around 2.5 kbar. Below 2.5 kbar, superconductivity coexists within CDW domain walls at very low temperatures. (b) Temperature dependence of the resistivity of α -(BEDT-TTF)₂I₃ as a function of various pressures. The inset schematically displays the charge distributions on ET molecules below and above charge ordering transition temperature at ambient pressure. Under hydrostatic pressures neither good metal nor superconductivity is realized. (c) Tentative phase diagram of α -(BEDT-TTF)₂I₃ under uniaxial strains along a- and b-axis. CO and ZGS denote the charge-ordered state and zero-gap state, respectively. SC state only appears under strains along the a-direction. After [50, 61]

surface and a hole pocket according to the theoretical calculations [22, 64]. Despite the similarity in band structures, the four salts show different low-temperature behaviour. The α -K, α -Rb and α -Tl compounds are metals with an anomaly in resistivity around 10 K due to the possible Fermi surface nesting induced density waves, while the α -NH₄ salt undergoes metal-superconductor transition at 1 K [23]. Irrespective of the distinct ground state for the above four salts, optical measurements revealed that they are correlated metals influenced strongly by charge-ordered fluctuations [65]. In the optical conductivities, a pseudogap like feature was observed in the far-infrared range for α -K, but not for α -NH₄ [47]. This additional low-energy band was explained as a result of charge-ordered fluctuations. This findings are consistent with theoretical expectation based on the extended Hubbard model [46, 58, 66]. Further, extended Drude analysis has shown that the effective mass and frequency-dependent scattering rate of α -Rb and α -Tl are larger than those of α -NH₄ [65]. As a consequence, stronger electron-electron correlation are expected in α -K, α -Rb and α -Tl compounds than in α -NH₄. This conclusion was also supported by the infrared vibrational spectroscopy [67]. Figure 1.9 (a) summarizes the generic phase diagram from optical measurements. A similar phase diagram was proposed from NMR measurements [60]. They have argued that the homogeneity of the charge distribution between adjacent stacks play a crucial role in stabilizing the superconductivity. As shown in Figure 1.9 (b), when going from α -I₃ to α -Rb and further to α -NH₄, the electronic state at the A and B molecules become more uniform, and finally the superconductivity appears. The above tentative phase diagram at ambient pressure was partially confirmed by pressure-dependent transport measurements [61] as depicted in Figure 1.10 (a). With increasing pressure, the density wave gets suppressed with decreasing transition temperature and vanishes completely at 2.5 kbar, followed by the appearance of superconductivity with $T_c \approx 0.1$ K. On the other hand, as depicted in Figure 1.10 (b) and (c), hydrostatic pressure can not completely suppress the insulating state in α -I₃. However, the metallic state or superconductivity can be stabilized under uniaxial strain [50].

1.2.2.2. β'' -phase

The series of isostructural salts β'' -(ET)₂SF₅RSO₃ with R=CH₂,CH₂CF₂,CHF and CHF₂ are of particular interest [68–71], because of its completely organic com-

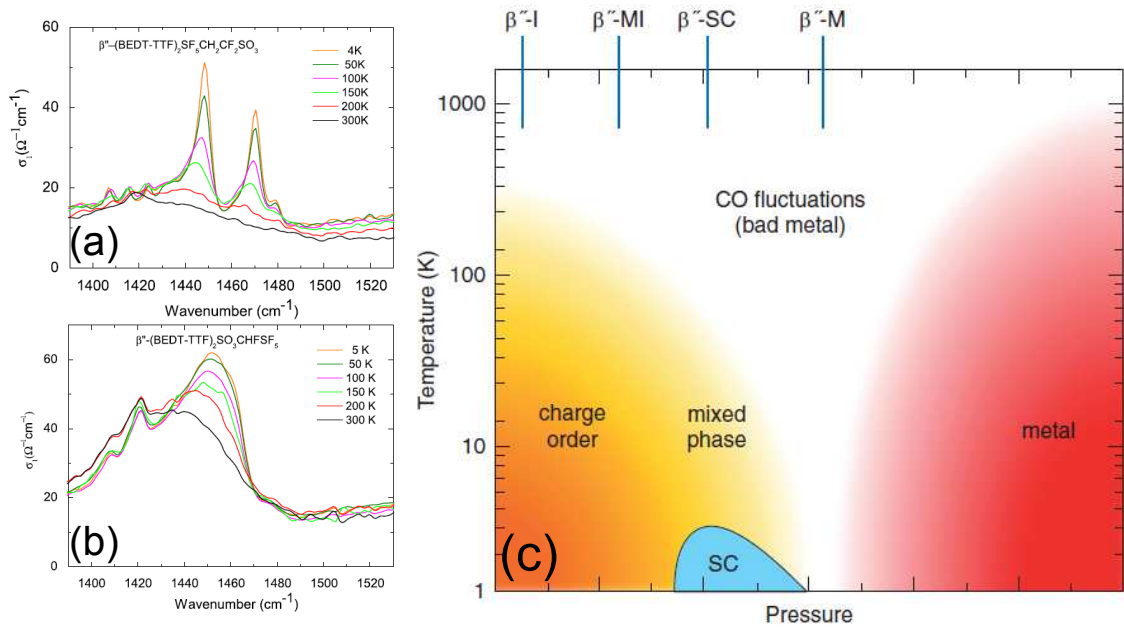


Figure 1.11.: Optical conductivity of $\beta''\text{-SC}$ (a) and $\beta''\text{-M}$ (b) measured with the electric field polarized perpendicular to the conducting layer at different temperatures. The splitting of the charge sensitive ν_{27} vibrational mode clearly indicates a charge-ordered state in $\beta''\text{-SC}$, while only one broad mode was observed in $\beta''\text{-M}$ in the whole temperature range, showing the absence of charge order. (c) Tentative phase diagram for the family $\beta''\text{-(ET)}_2\text{SF}_5\text{RSO}_3$ ($\text{R}=\text{CH}_2, \text{CH}_2\text{CF}_2, \text{CHF}$ and CHF_2) proposed by Girlando *et al.*. Charge fluctuations are presented in all four compounds. When going from $\beta''\text{-M}$ to $\beta''\text{-SC}$ and further to $\beta''\text{-MI}$ and $\beta''\text{-I}$, an additional static charge ordered state evolves in $\beta''\text{-SC}$, $\beta''\text{-MI}$ and $\beta''\text{-I}$, while $\beta''\text{-M}$ remains metallic down to the lowest temperature without any further development of charge disproportionation. After [72, 73]

position in both anion and donor layers and the presence of distinct ground state as shown in Figure 1.11 (b). $\beta''\text{-(ET)}_2\text{SF}_5\text{CH}_2\text{SO}_3$ (hereafter $\beta''\text{-I}$) is a charge-ordered insulator already at room temperature. $\beta''\text{-(ET)}_2\text{SF}_5\text{CHF}_2\text{SO}_3$ ($\beta''\text{-MI}$) undergoes a first-order like metal-insulator phase transition at 180 K with nonmagnetic charge ordering accompanied by lattice dimerization. The $\beta''\text{-(ET)}_2\text{SF}_5\text{CH}_2\text{CF}_2\text{SO}_3$ ($\beta''\text{-SC}$) is a metal and turns into superconductor at $T_c = 5$ K at ambient pressure, while $\beta''\text{-(ET)}_2\text{SF}_5\text{CH}_2\text{SO}_3$ ($\beta''\text{-M}$) remains metallic in the whole temperature.

Extensive infrared and Raman investigations have been performed on both $\beta''\text{-SC}$

and β'' -M salts [2, 48, 72, 73]. As can be seen in Figure 1.11 (a) and (b), in β'' -SC the charge sensitive ν_{27} mode splits into two bands below 200 K with the degree of static CO estimated as $0.2e$, while no signs of splitting was observed in β'' -M. In both samples, a very broad background was present. It has been assigned to the contribution of the charge fluctuation between two adjacent ET stacks and can be well described by two-states-jump model [73]. Similar conclusions were given by Raman experiments. In addition, two strong infrared bands around 300 cm^{-1} and 40 cm^{-1} developed in the in-plane optical conductivity of β'' -SC, which were absent in β'' -M. These two additional bands have been interpreted as a result of charge-ordered fluctuations and strong electron-lattice coupling in β'' -SC, respectively. This gives strong evidence of the scenario of charge-order induced superconductivity in quarter-filled organic systems [48]. From the recent infrared vibrational spectroscopy, the amplitude of the CO was around $0.5e$ in β'' -I, and $0.3e$ in β'' -MI [74]. Therefore, it can be concluded that β'' -I and β'' -MI are strongly correlated insulator at ambient pressure, while β'' -M is metal with less correlation and β'' -SC is a superconductor probably induced by charge-ordered fluctuation.

1.2.3. β' -Pd(dmit) conducting metal complexes

Apart from (BEDT-TTF)-based organic materials, another very interesting family of organic charge transfer conductors is metal dithiolene complex based on the $M(\text{dmit})_2$ ($M=\text{Ni}$ and Pd) molecule with transition metal elements in the molecular center [75–77]. In the $(\text{BEDT-TTF})_2\text{X}$ and $(\text{TMTTF})_2\text{X}$ cases, the electronic properties can be well described by the single band Hubbard model. This is because the molecular orbital HOMOs are well separated from the LUMOs with a relatively large energy difference ($\Delta E \sim$ several eV) [19, 78, 79]. Only the HOMOs participate in the formation of conduction bands around the Fermi level. However, the d-orbital of metal ion in the dithiolene complex leads to a much smaller gap between HOMO and LUMO, $\Delta E < 1\text{ eV}$ [77], which is comparable to the bandwidth as shown in Figure 1.12. Therefore, it is possible that both orbitals can contribute to the conduction band.

The reduced energy gap between HOMO and LUMO play a very important role in the electronic structure of $M(\text{dmit})_2$ family. In a dithiolene crystal with formula $X[M(\text{dmit})_2]_2$ (X denotes a closed-shell cation), $M(\text{dmit})_2$ molecules usu-

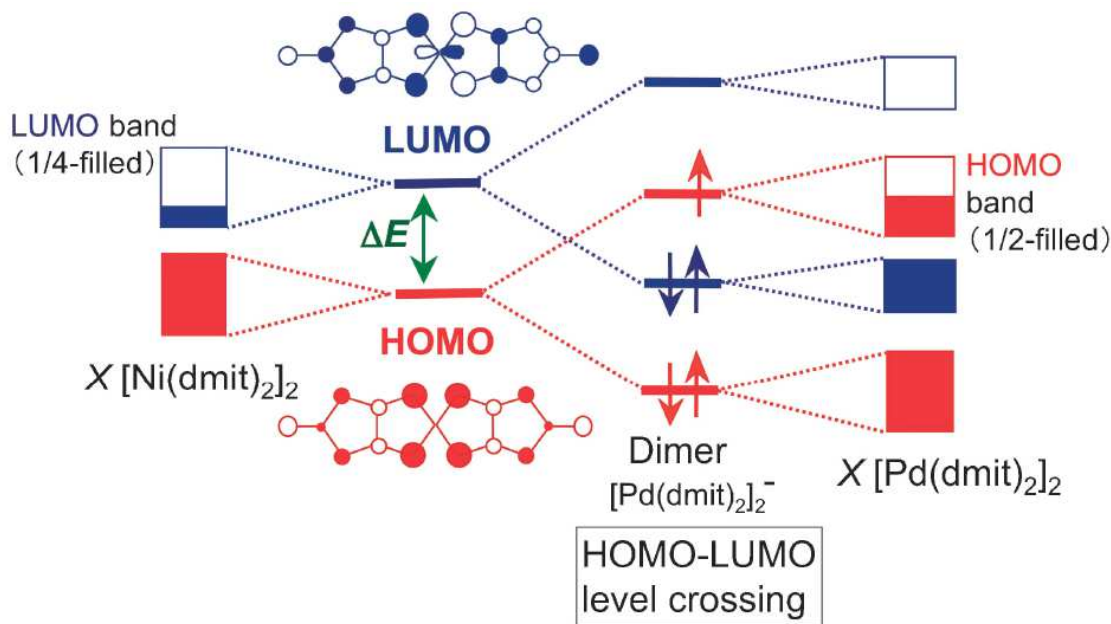


Figure 1.12.: Energy scheme of the $M(\text{dmit})_2$ ($M = \text{Ni}$ and Pd) systems. The strong dimerization of a dimer unit $[\text{Pd}(\text{dmit})_2]_2^-$ cause a HOMO–LUMO interchange. After [77]

ally form dimeric radical anion as $[\text{Pd}(\text{dmit})_2]_2^-$, which is in contrast to the cation $(\text{BEDT-TTF})_2^+$ in $(\text{BEDT-TTF})_2\text{X}$. Depending on the degree of dimerization, distinct electronic structures are found for different compounds. In Figure 1.12, we plot the band structures for $M(\text{dmit})_2$ with both strongly dimerization and weakly dimerization. If the dimerization gap is small enough, all the bonding and antibonding of the LUMOs are located above those of HOMOs. Therefore, those HOMO bands are fully occupied and LUMO bands form the conduction bands with quarter-filled. Due to the antisymmetric configuration of the LUMO with respect to the molecular center, the transfer integrals along the interstack are much smaller than those along the intrastack. As a result, many $X[M(\text{dmit})_2]_2$ tend to be quasi 1-dimensional conductor. On the other hand, the large dimerization gap lift the antibonding of the HOMO band above the bonding of the LUMO band in the strong dimerization case. This is also called HOMO-LUMO band inversion. Such band inversion gives rise to a half-filled conduction band. Since the free electrons in the HOMO band have symmetry orbital configuration, the band structure of $X[\text{Pd}(\text{dmit})_2]_2$ is quasi 2-dimensional. This is quite similar to the case of κ -

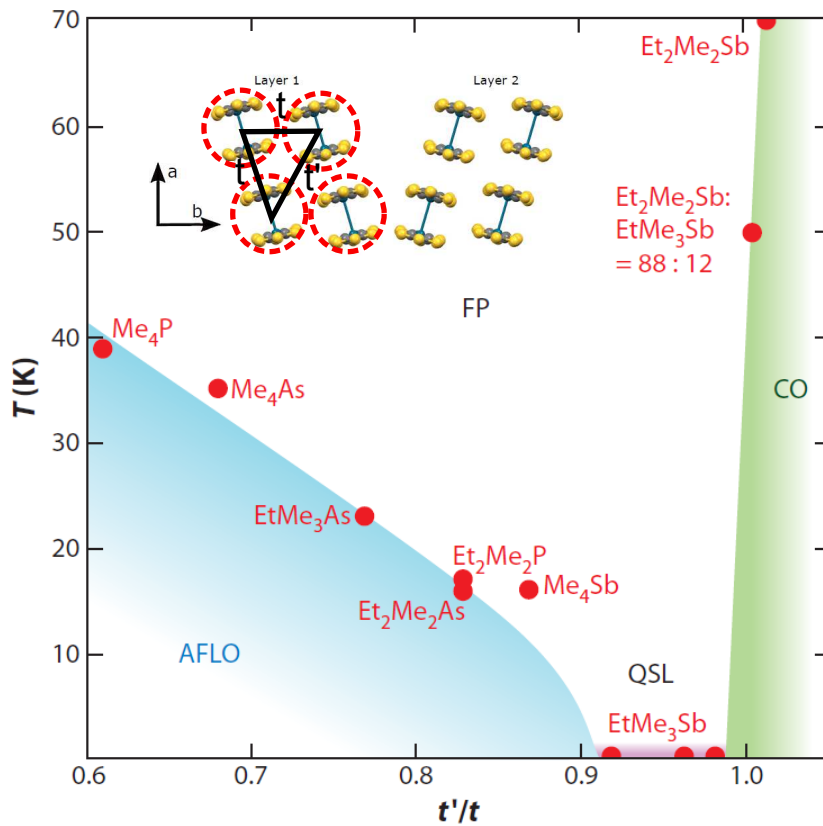


Figure 1.13.: Phase diagram for the β' -Pd(dmit)₂ salts. Abbreviations: FP, frustrated paramagnetic (state); AFLO, antiferromagnetic long-range ordered (state); CO, charge-ordered (state); QSL, quantum spin liquid (state). [Pd(dmit)₂]₂ dimer acts as a building unit. After [26]

(BEDT-TTF)₂X. In addition, the degree of dimerization is supposed to be stronger than that in the κ -phase, because the A_g vibrational modes of $X[\text{Pd}(\text{dmit})_2]_2$ is much shaper.

In the following review, we will mainly focus on the fascinating electronic behaviour of the strongly demirized compounds $X[\text{Pd}(\text{dmit})_2]_2$. Similar to the κ -phase, we can describe the electronic structure of this system utilizing Hubbard model on an anisotropic triangular lattice as depicted in the inset of Figure 1.13. Figure 1.13 shows the schematic phase diagram for β' - $X[\text{Pd}(\text{dmit})_2]_2$ as a function of frustration t'/t [26]. As the frustration parameter t'/t is increased from 0.6 to 1.0, the ground state undergoes two phase transitions from antiferromagnetic order to

quantum spin liquid state with decreasing Néel temperature, and subsequently to charge-ordered state. Such transition can be realized by chemical substitution of the cation. In the narrow regime, where gapless spin liquid is located, we can finely tune the magnetic ground state of β' -EtMe₃Sb[Pd(dmit)₂]₂ by mixing the EtMe₃Sb cation with Et₂Me₂Sb molecules. Extensive theoretical and experimental studies have been performed on mixed crystals β' -(EtMe₃Sb)_x(Et₂Me₂Sb)_{1-x}[Pd(dmit)₂]₂ by Kato's group [77]. The distinct magnetic properties of the above mentioned different insulating state can be well demonstrated by SQUID measurements as illustrated in Figure 1.14 (a). At high temperatures, all three compounds behaves like paramagnetic insulators and can be well described by spin-1/2 Heisenberg model on a triangular lattice with antiferromagnetic interaction $J \sim 250$ K [26]. Upon cooling, the less frustrated Me₄Sb ($t'/t = 0.86$) salt exhibits antiferromagnetic long-range order with increase of susceptibility below 18 K. The susceptibility of the strong frustrated Et₂Me₂Sb ($t'/t = 1$) salt almost vanishes below 80 K due to the charge-order induced intradimer spin singlet state. Despite the large J , the EtMe₃Sb ($t'/t = 0.91$) salt display no signature of spin ordering down to 1.37 K [80] as shown in Figure 1.14 (b). To summarise, when the t'/t value is close to 1, the β' -X[Pd(dmit)₂]₂ tends to reduce the spin frustration either by forming quantum spin liquid state or undergoing structure transition towards nonmagnetic spin singlet state.

Another very interesting compounds is β' -EtMe₃P[Pd(dmit)₂]₂ with monoclinic structure ($P2_1/m$) [81]. The t'/t value for β' -EtMe₃P is also close to unity, which leads to a VBS (valence bond state) with nonmagnetic properties. The mechanism for the transition is quite similar to that occurred in β' -Et₂Me₂Sb. But the results differ in two aspects: Here the charge disproportion happens within intradimer and the spin singlet state appears due to tetramerization between interdimer as depicted in Figure 1.15 (b).

As shown in Figure 1.15, the VBS phase can be fully suppressed with the application of hydrostatic pressure around 4 kbar. As the pressure is increased further, it turns into superconducting followed by the metallic state. The first order transition is clearly demonstrated by the sharp insulator-metal and re-entrant metal-insulator transition found in the temperature dependence of resistivity. The

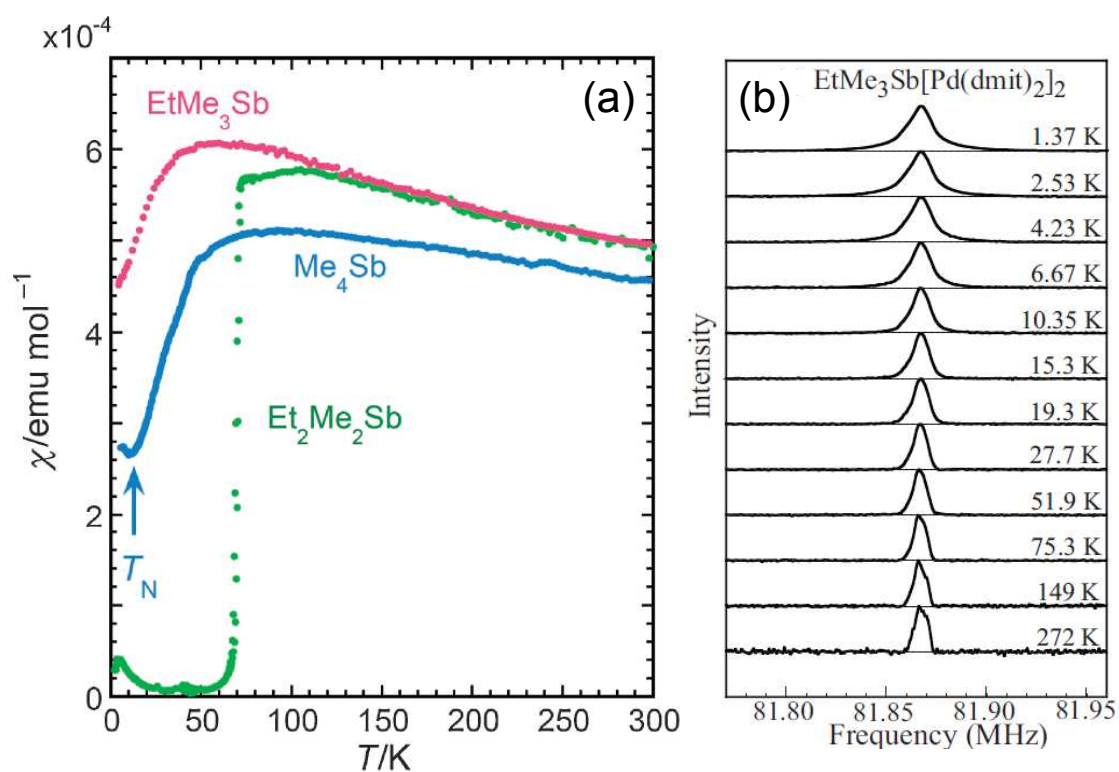


Figure 1.14.: (a) Temperature dependence of the spin susceptibility of β' - $X[\text{Pd}(\text{dmit})_2]_2$ ($X=\text{EtMe}_3\text{Sb}$, Me_4Sb , $\text{Et}_2\text{Me}_2\text{Sb}$). (b) ^{13}C -NMR spectra for randomly oriented samples of β' - $\text{EtMe}_3\text{Sb}[\text{Pd}(\text{dmit})_2]_2$. With decreasing temperature, no critical broadening of the spectrum was observed. After [26, 80]

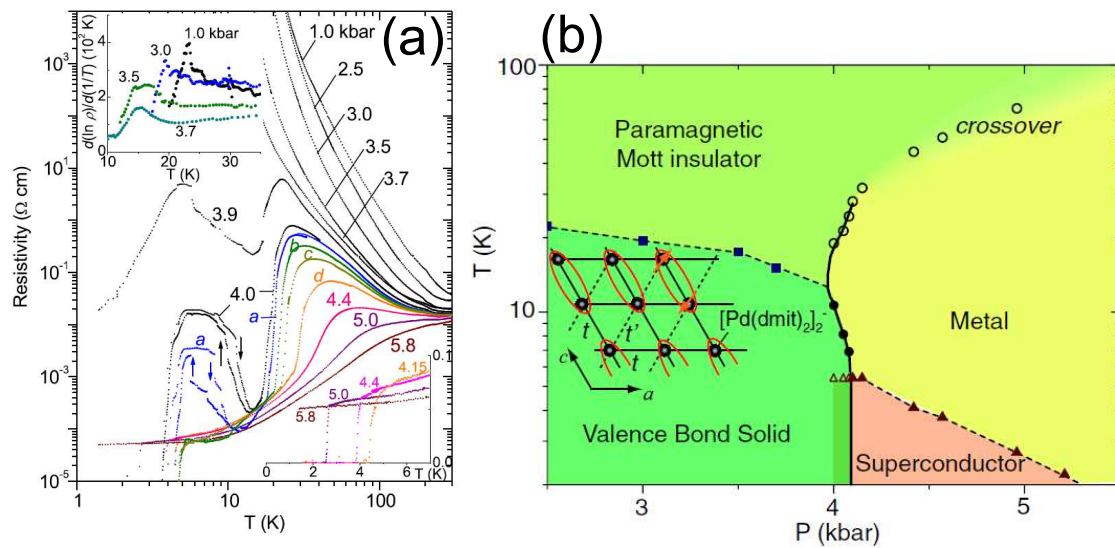


Figure 1.15.: (a) Temperature-dependent resistivity of $\text{EtMe}_3\text{P}[\text{Pd}(\text{dmit})_2]_2$ under various hydrostatic pressures. Inset shows the temperature dependence of the activation gap. (b) Phase diagram of $\text{EtMe}_3\text{P}[\text{Pd}(\text{dmit})_2]_2$ based on resistivity measurements. The solid and dotted lines stand for the first-order and second-order transitions, respectively. Inset schematically displays the valence bond state (VBS) of $[\text{Pd}(\text{dmit})_2]_2^-$. After [81]

pressure-temperature phase diagram of β' -EtMe₃P salt is quite similar to that of κ -phase, regardless of the different magnetic ground state. This hints that the electron-electron correlation may play an important role in the formation of superconductivity in both organic materials.

2. Theoretical Background

The first section introduces the fundamental Maxwell equations, the deduced optical constants and the relations between different quantities, which are frequently used in the experimental analysis. In addition, the Kramers-Kronig relations and sum rules are introduced and the importance of the physical meaning are also discussed. The second section describes the standard phenomenological models such as the Drude-Lorentz model and Fano model, which are used to analyze the electronic and vibrational contributions of the underlying physics. Furthermore, the extended Drude model is presented to understand the properties of Mott transitions in strongly correlated systems. The last section discusses the optical properties of correlated electrons with various ground states such as the charge-ordered state, the Mott-insulating state in the strong correlation limit and the Fermi-liquid state in the weak limit.

2.1. Electrodynamics

The mathematical equations and physical interpretations presented in this section are mainly based on Ref [82].

Various interesting phenomena in strongly correlated many-body systems are not entirely understood yet. The multiple and complex interactions among spin, charge and lattice degrees of freedom give rise to exotic ground states such as unconventional superconductivity, charge and spin density waves, Fermi (spin) liquids or other collective modes. The characteristic energy of such collective excitations ranges from a few meV to several eV. For example, the energy gap or pseudogap

in high- T_c cuprates is typically dozens to hundreds of meV and the charge transfer band in organic and molecular conductors is around several eV. Hence, infrared spectroscopy, performed in the energy range from 1 meV to several eV, turns out to be a very powerful tool not only for the confirmation of the existing picture of semiconductors and Fermi-liquid metals but also for uncovering exotic ground states of correlated materials as depicted in Figure 2.1. In principle, all information about the interactions among electrons manifest itself as macroscopic experimental observables emerging in the Maxwell's equations. These observables are the optical constants of materials, which describe the stiffness of electrons under influence of electro-magnetic field. For example, the optical conductivity is simply the linear response function defined as the ratio of applied electric field to the induced current [82]. Therefore, we can attribute different contributions of spectra to different excitations and mechanisms by disentangling the obtained experimental optical data and comparing them with theoretical model as shown in Figure 2.1.

In general, compared to other spectroscopic techniques, such as STM (Scanning Tunnelling Microscopy) [83], ARPES (Angle-resolved Photo-Emission Spectroscopy) [84] and Raman spectroscopy [85], infrared spectroscopy mainly has the following characteristics: (1) The electromagnetic waves of the infrared probe can penetrate into the metal up to a depth of around few hundred nano-meters, or in other terms around 10 to 100 unit cells [82]. Unlike STM and ARPES probes, it can thus be considered as a bulk sensitive macroscopic technique. Specifically for most organic materials the process of cleaving proves very difficult, therefore there is rarely data provided by STM and ARPES; (2) It is a momentum-averaged tool which can not provide further information of the shape of the Fermi surface in k -space. (3) Usually it is not sensitive to magnetic excitation. This is opposite to Raman spectroscopy, which is widely used to detect magnetic excitations such as magnons. However, it was theoretically proposed that infrared spectroscopy is also sensitive to spinon excitations and has indeed been verified in spin liquid systems in recent optical experiments [86].

Specifically in the case of organic conductors, a direct extraction of the electronic structure (U and W) via ARPES or STM methods under pressure is impossible limited by the technique. And Raman spectroscopy can only investigate the vibrational

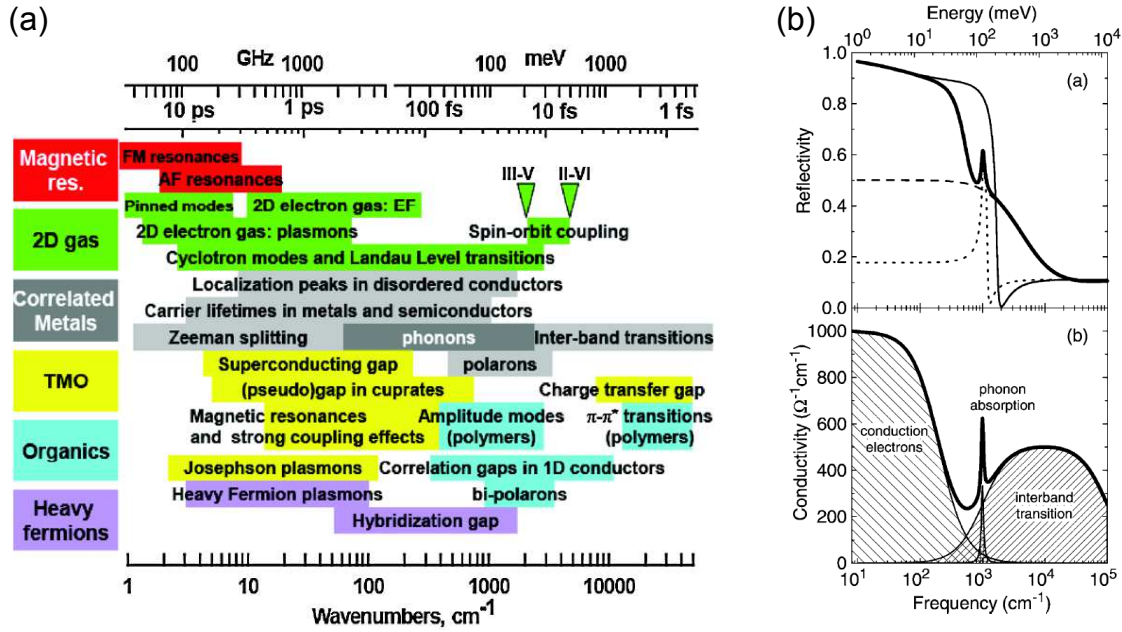


Figure 2.1.: (a) Schematic view of typical energy scales found in strongly correlated electron systems. Energies are usually displayed in wavenumbers (unit cm^{-1}) in infrared spectroscopy. The cm^{-1} has the following relations with other units: $1 \text{ meV} = 8 \text{ cm}^{-1}$, $1 \text{ THz} = 33 \text{ cm}^{-1}$ (b) Electronic and vibrational contributions of the reflectivity (upper panel) and optical conductivity spectra (lower panel) in a typical organic metal. The itinerant free electrons are described by the Drude model. The interband transitions and sharp vibrational modes are modeled by a very broad and narrow Lorentz model respectively. Adapted from Refs. [87, 88]

degrees of freedom. Therefore infrared spectroscopy is considered to be a uniquely powerful technique able to shed light on both the evolution of the electron-electron correlation and the electron-phonon coupling under high pressures.

2.1.1. The interaction of radiation with matter

When an electromagnetic wave propagates through a medium, it will cause in electric dipoles, magnetic moments, polarization charges and induces microscopic currents. In turn, these terms interact with the wave and modify its propagation.

Therefore, Maxwell's equations in the presence of the medium are expressed as:

$$\nabla \cdot \mathbf{D} = 4\pi\rho \quad (2.1)$$

$$\nabla \times \mathbf{E} = -\frac{1}{c} \frac{\partial \mathbf{B}}{\partial t} \quad (2.2)$$

$$\nabla \times \mathbf{B} = 0 \quad (2.3)$$

$$\nabla \cdot \mathbf{H} = \frac{1}{c} \frac{\partial \mathbf{D}}{\partial t} + \frac{4\pi}{c} \mathbf{j}. \quad (2.4)$$

Here \mathbf{D} is electric displacement vector, \mathbf{H} is the magnetic field vector and \mathbf{E} is the electric field, \mathbf{B} is magnetic induction vector, ρ is the charge density, \mathbf{j} is the current density, which obeys the Ohm's law, i.e., $\mathbf{j} = \sigma_1 \mathbf{E}$ (σ_1 is the conductivity of the material) and c is the speed of light in vacuum. In the absence of external charge and current, the electric field \mathbf{E} and the electric displacement vector \mathbf{D} are connected by

$$\mathbf{D} = \epsilon_1 \mathbf{E} \quad (2.5)$$

where ϵ_1 is the dielectric function of the bound electrons. The magnetic field \mathbf{H} and the the magnetic induction \mathbf{B} are connected via

$$\mathbf{B} = \mu_1 \mathbf{H}, \quad (2.6)$$

where μ_1 is the magnetic permeability. With the definitions above we can rewrite Maxwell's equations :

$$\nabla^2 \mathbf{E} = \frac{4\pi\mu_1\sigma_1}{c^2} \frac{\partial \mathbf{E}}{\partial t} + \frac{\mu_1\epsilon_1}{c^2} \frac{\partial^2 \mathbf{E}}{\partial t^2} \quad (2.7)$$

$$\nabla^2 \mathbf{H} = \frac{4\pi\mu_1\sigma_1}{c^2} \frac{\partial \mathbf{H}}{\partial t} + \frac{\mu_1\epsilon_1}{c^2} \frac{\partial^2 \mathbf{H}}{\partial t^2}. \quad (2.8)$$

For an infinite medium without any boundary condition the solution can be written as general form of a wave equation:

$$\mathbf{E}(\mathbf{x}, t) = \mathbf{E}_0 e^{i(\mathbf{k}\mathbf{x} - \omega t)} \quad (2.9)$$

And \mathbf{k} follows

$$k = \frac{\omega}{c} \left(\mu_1 \left[\epsilon_1 + i \frac{4\pi\sigma_1}{\omega} \right] \right)^{\frac{1}{2}}. \quad (2.10)$$

If we define the complex dielectric function as

$$\hat{\epsilon} = \epsilon_1 + i \frac{4\pi\sigma_1}{\omega}. \quad (2.11)$$

then we can define the complex conductivity as

$$\hat{\sigma} = i \frac{\omega}{4\pi} (1 - \hat{\epsilon}). \quad (2.12)$$

The complex refractive index is defined as

$$\hat{N} = \sqrt{\hat{\mu}\hat{\epsilon}} = n_1 + in_2. \quad (2.13)$$

If we consider the case of nearly normal incidence at the interface between the sample and vacuum, the complex reflection coefficient (r) reads:

$$\hat{r} = |\hat{r}| e^{i\phi_r} = \frac{\hat{N} - 1}{\hat{N} + 1}. \quad (2.14)$$

Here ϕ_r denotes the phase difference between the reflected and the incident wave. $R = |\hat{r}|^2$ is defined as reflectivity and reads

$$R = |\hat{r}|^2 = \left| \frac{\hat{N} - 1}{\hat{N} + 1} \right|^2. \quad (2.15)$$

In experiments R is simply the ratio of power intensity reflected from the sample to that from a perfect reference mirror. If both R and ϕ_r are given, the real part and imaginary part of the complex refractive index are expressed as:

$$n_1 = \frac{1 - R}{1 + R - 2\sqrt{R} \cos \phi_r} \quad (2.16)$$

$$n_2 = \frac{2R \sin \phi_r}{1 + R - 2\sqrt{R} \cos \phi_r}. \quad (2.17)$$

Here n_1 and n_2 are the index of the refraction and extinction coefficient of the measured materials respectively. If we assume the material is not magnetic, i.e., $\hat{\mu} = 1$, the real part and the imaginary part of the dielectric constant are given by the expressions

$$\epsilon_1 = n_1^2 - n_2^2 \quad (2.18)$$

$$\epsilon_2 = 2n_1n_2. \quad (2.19)$$

The complex dielectric constant, the complex conductivity and complex refractive index are referred to as optical constants, characterizing electrodynamic properties of the material in response to the external field. In general cases, those quantities are frequency dependent. All of those complex quantities are related to each other and therefore each contains identical information.

2.1.2. K-K relation and sum rules

The response of the solid to electromagnetic radiation is described by the various material parameters and optical constants such as the dielectric function or the optical conductivity. In principal, we can calculate the responses function using the Kubo formula within the framework of linear response theory, however experimentally we extract them through the Maxwell equations by measuring the reflections. They are all complex quantities consisting of a real and an imaginary part. The real and imaginary parts are not independent and are related to each other via the Kramers-Kronig relations. More fundamentally speaking, it is the causality of the physical principle that preserves this relation. The K-K relations play an important role in experimental physics that allow for the evaluation of the components of the complex dielectric constant or conductivity when only one parameter is measured. For instance, the phase shift of electromagnetic wave, which cannot be measured experimentally, is calculated by the measured reflectivity from K-K analysis [82].

In the following part we will omit the general and detail procedures for verifying the K-K relation and just list some useful formulas that are used in this thesis.

Any complex response function $G(\omega)$ can be written in terms of the real part and imaginary part as $G(\omega) = G_1(\omega) + iG_2(\omega)$, so the K-K relations tell us that

$$G_1(\omega) = \mathbf{P} \frac{2}{\pi} \int_0^{\infty} \frac{\omega' G_2(\omega')}{\omega'^2 - \omega^2} d\omega', \quad (2.20)$$

$$G_2(\omega) = -\mathbf{P} \frac{2\omega}{\pi} \int_0^{\infty} \frac{\omega' G_1(\omega')}{\omega'^2 - \omega^2} d\omega', \quad (2.21)$$

Using these general relations we can derive various expressions for optical constants. For instance, the complex dielectric function can be expressed as

$$\hat{\epsilon}(\omega) = \epsilon_1(\omega) + i\epsilon_2(\omega), \quad (2.22)$$

$$\epsilon_1(\omega) - 1 = \mathbf{P} \frac{2}{\pi} \int_0^\infty \frac{\omega' \epsilon_2(\omega')}{\omega'^2 - \omega^2} d\omega', \quad (2.23)$$

$$\epsilon_2(\omega) = -\mathbf{P} \frac{2\omega}{\pi} \int_0^\infty \frac{\omega' \epsilon_1(\omega')}{\omega'^2 - \omega^2} d\omega', \quad (2.24)$$

For the complex optical conductivity it yields

$$\hat{\sigma}(\omega) = \sigma_1(\omega) + i\sigma_2(\omega), \quad (2.25)$$

$$\sigma_1(\omega) = \mathbf{P} \frac{2}{\pi} \int_0^\infty \frac{\omega' \sigma_2(\omega')}{\omega'^2 - \omega^2} d\omega', \quad (2.26)$$

$$\sigma_2(\omega) = -\mathbf{P} \frac{2\omega}{\pi} \int_0^\infty \frac{\omega' \sigma_1(\omega')}{\omega'^2 - \omega^2} d\omega', \quad (2.27)$$

The most important K-K relation for optical investigations is the one between the reflectivity $R(\omega)$ and the phase shift $\phi_r(\omega)$.

$$\phi_r(\omega) = -\mathbf{P} \frac{\omega}{\pi} \int_0^\infty \frac{\ln R(\omega')}{\omega'^2 - \omega^2} d\omega', \quad (2.28)$$

As we can see, in order to use this method we have to extrapolate the measured reflectance to zero frequency on the low frequency regime of the measured range and to infinite frequency on the high frequency regime. We use the following extrapolations. For $\omega \rightarrow 0$ the reflectance was extrapolated by assuming a Hagen-Rubens frequency dependence: $1 - R(\omega) \propto \sqrt{\omega}$ for metallic states and $(1 - R(\omega)) \propto C$ (constant) for the insulating state. For $\omega \rightarrow \infty$ the reflectance has been extended by free electron behaviour ($R \propto \omega^{-4}$). By combining the measured data over a broad frequency range ($80 \text{ cm}^{-1} - 300000 \text{ cm}^{-1}$) and by properly extrapolating low and high frequency limits we can use the K-K analysis to calculate the phase shift and further other optical constants.

The optical constants of solids obey the sum rule, which plays an important role in the analysis of the spectral weight. For instance the integration of the conductivity from zero to infinite frequency yields

$$\int_0^\infty \sigma_1(\omega) d\omega = \frac{\pi n e^2}{2m}, \quad (2.29)$$

where n refers to the total number of electrons and m to the bare electron mass. The above equation indicates that the total spectral weight integral of σ_1 is finite,

conserved, and proportional to n/m . In reality, since the optical conductivity is a linear response to the external electric field, it can be disentangled into different excitations. Typically, for organic conductors, the intra- and interband contributions are well separated. One can define a partial sum rule by replacing the upper limit (∞) in the integration in Equation (2.29) with a cut-off frequency (ω_c), which corresponds to the band width of the electronic system. The partial sum rule is given as

$$\int_0^{\omega_c} \sigma_1(\omega) d\omega = \frac{\pi n e^2}{2m}. \quad (2.30)$$

Now, n and m refer to the conduction electron density and their effective mass.

2.2. Theoretical models

2.2.1. Drude model

The Drude model is widely used to describe the response of free charge carriers in conducting metallic state [89]. This model is further developed by Sommerfeld taking into account the quantum effect of electrons [90]. Since the conclusion derived from classical Drude model and Sommerfeld model are quite identical, in this section we discuss the the characteristic properties of metal using classical Drude model.

In the framework of Drude theory, the independent free electron approximation is assumed. Namely, we neglect the underlying interaction of electron-electron and electron-phonon. Further, we assume that there exists an average relaxation time restoring the system back to equilibrium. In the presence of an external electric field E , the equation of motion becomes

$$m \frac{d^2 \mathbf{x}(t)}{dt^2} + m\Gamma \frac{d\mathbf{x}(t)}{dt} = -e\mathbf{E}(t) \quad (2.31)$$

Where m is the mass of the electron; e is the charge of the electron; $\Gamma = 1/\tau$ corresponds to the scattering rate, and E is the external electric field as the driving force. The time-dependent electric field has the form

$$\mathbf{E}(t) = \mathbf{E}_0 e^{-i\omega t} \quad (2.32)$$

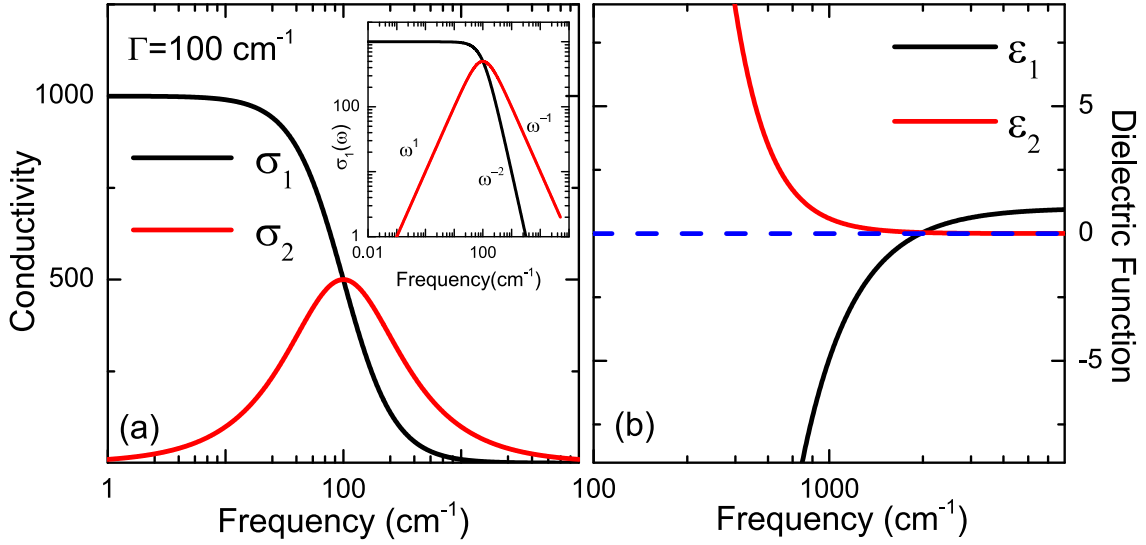


Figure 2.2.: (a) The frequency dependent optical conductivity of the Drude model in logarithmic scale. The real part σ_1 is almost frequency independent well below the scattering rate and corresponds to the dc-conductivity. Well above Γ it decreases as ω^{-2} . While the σ_2 reaches a maximum at Γ and then falls as ω^{-1} in both low and high energy limit. The inset shows the same plot with double-logarithmic scale. (b) The frequency dependent dielectric constant of the Drude model on a logarithmic scale. The real part of the dielectric constant ϵ_1 changes its sign from negative to positive at the plasma frequency. The ϵ_2 is always positive, but changes slope at the Γ .

After obtaining the solution of the equation of motion, we can derive the complex, frequency dependent dielectric constant

$$\hat{\epsilon}(\omega) = 1 - \frac{\omega_p^2}{\omega^2 + \Gamma^2} + i \frac{\Gamma \omega_p^2}{\omega(\omega^2 + \Gamma^2)}. \quad (2.33)$$

with the real and imaginary parts. Where $\omega_p^2 \equiv 4\pi n e^2 / m$ is defined as plasma frequency and describes the oscillator strength. The real and imaginary parts of optical conductivity are

$$\hat{\sigma}(\omega) = \sigma_{\text{dc}} \frac{1}{1 + (\omega/\Gamma)^2} + i \sigma_{\text{dc}} \frac{\omega/\Gamma}{1 + (\omega/\Gamma)^2} \quad (2.34)$$

where σ_{dc} represents the dc conductivity.

Here, we can see that at sufficiently high frequencies the real part of the dielectric constant can be written as $1 - \frac{\omega_p^2}{\omega^2}$. This equation was used to derive the sum rules

in the previous section. In the Drude model, all the various optical parameters are fully characterized by two frequencies: the plasma frequency (ω_p) and the scattering rate (Γ). A calculation of the frequency-dependent optical constants within the framework of the Drude model is shown in Figure 2.2.

2.2.2. Lorentz and Fano model

In this section, we introduce the Lorentz model to account for localization of electron state such as phonons, magnons and the optical transition between different interbands in a solid. In principal, in order to describe the electronic transitions between a ground state and excited states of many body systems, we have to solve the time dependent Schrödinger equation under an electric field utilizing perturbation theory [82]. For the sake of simplicity, here we derive all useful results by assuming an equivalent model with classical harmonic oscillators [91].

The similarity of the zero energy mode in the Drude model and the finite energy mode in the Lorentz model indicates that the Lorentz formalism can be generalized from Drude's formulas. This can be realized by adding an additional restoring force term to the Equation 2.31 and keeping the inertial and relaxational term. Therefore the Lorentz model is:

$$m \frac{d^2 \mathbf{x}(t)}{dt^2} + m\Gamma \frac{d\mathbf{x}(t)}{dt} + m\omega_o^2 \mathbf{x}(t) = -e\mathbf{E}(t). \quad (2.35)$$

Here ω_o^2 describes the strength of the harmonic oscillator. After obtaining the solution of the equation of motion, we can derive the frequency dependent complex dielectric constant

$$\hat{\epsilon}(\omega) = 1 + \frac{4\pi n e^2}{m} \frac{1}{\omega_o^2 - \omega^2 - i\Gamma\omega}. \quad (2.36)$$

Then we can obtain ϵ_1 and ϵ_2

$$\epsilon_1(\omega) = 1 + \omega_p^2 \frac{\omega_o^2 - \omega^2}{(\omega_o^2 - \omega^2)^2 + (\Gamma\omega)^2} \quad (2.37)$$

$$\epsilon_2(\omega) = \omega_p^2 \frac{\Gamma\omega}{(\omega_o^2 - \omega^2)^2 + (\Gamma\omega)^2}. \quad (2.38)$$

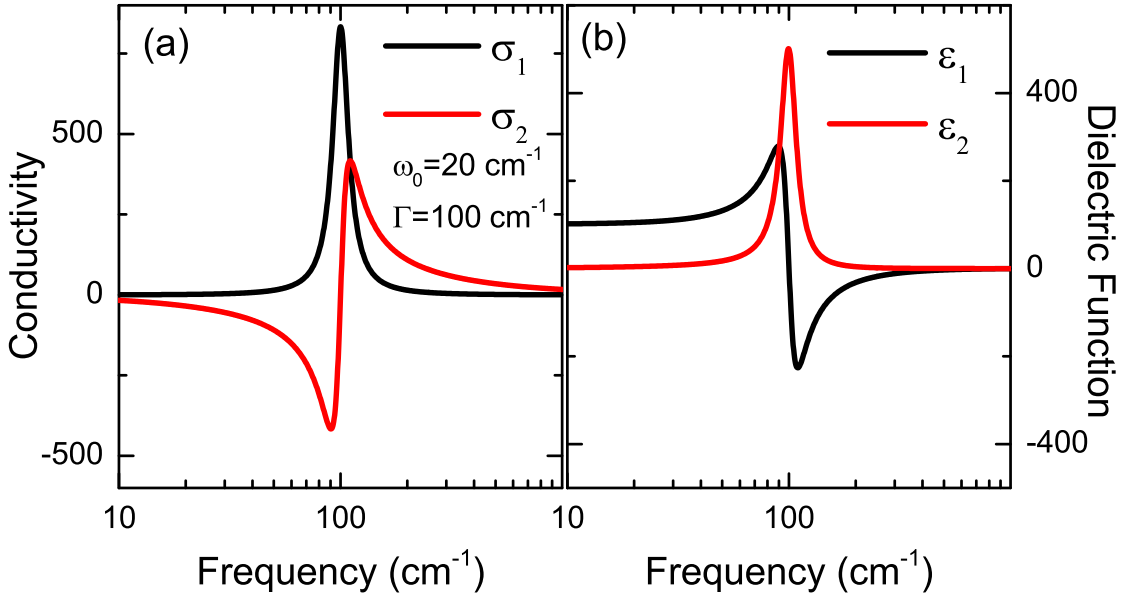


Figure 2.3.: Calculated frequency dependent optical conductivity (a) and dielectric constant (b) of Lorentz model with the following parameters: $\omega_0 = 20 \text{ cm}^{-1}$, $\Gamma = 100 \text{ cm}^{-1}$

For the real and imaginary parts of the optical conductivity we have

$$\sigma_1(\omega) = \frac{\omega_p^2}{4\pi} \frac{\Gamma\omega^2}{(\omega_0^2 - \omega^2)^2 + (\Gamma\omega)^2} \quad (2.39)$$

$$\sigma_2(\omega) = -\frac{\omega_p^2}{4\pi} \frac{\omega(\omega_0^2 - \omega^2)}{(\omega_0^2 - \omega^2)^2 + (\Gamma\omega)^2}. \quad (2.40)$$

The Drude model can be restored from the Lorentz model by setting $\omega_0 = 0$.

Figure 2.3 displays the real and imaginary parts of the optical conductivity and dielectric constants on a logarithmic frequency scale. As a result, σ_1 and σ_2 behave very similar to ϵ_2 and ϵ_1 . The σ_1 and ϵ_2 have extrema at ω_0 with a width Γ representing the scattering rate, while the σ_2 and ϵ_1 cross zero at approximately the resonance frequency ω_0 .

In the context of our experimental analysis, we utilize the Lorentz model to fit the localized Hubbard band and other interband excitations. However, the features of the vibrational A_g modes in organic systems are rather asymmetric and strongly deviate from simple Lorentzian shape. Therefore fitting with Lorentz modes results

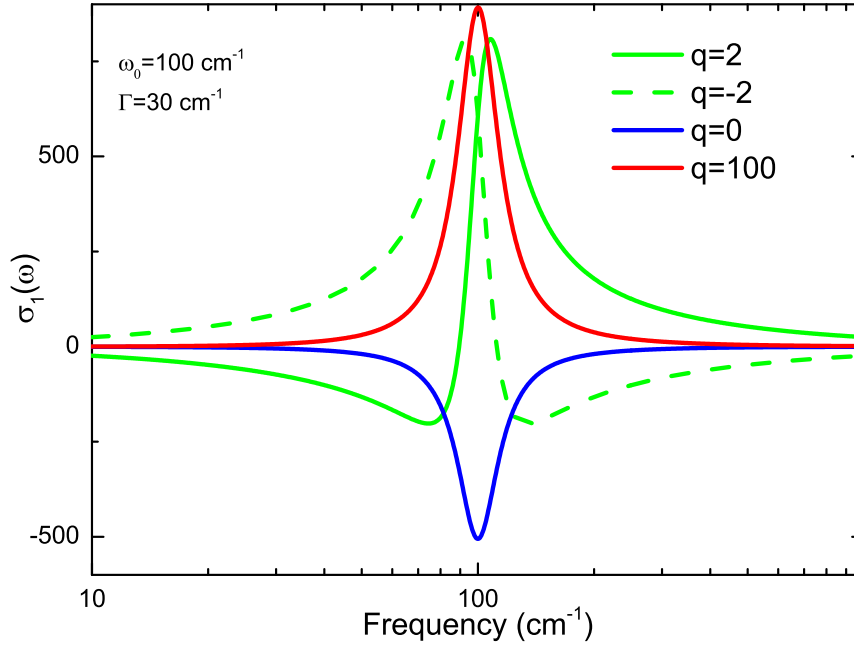


Figure 2.4.: Illustrations of asymmetric Fano line-shapes for various values of the parameter q and $\omega_0 = 100 \text{ cm}^{-1}$, $\Gamma = 30 \text{ cm}^{-1}$

in imprecise description.

In order to more quantitatively and better describe the A_g modes, we have to apply the phenomenological Fano model [92]. Here the mathematical expression of the real and imaginary part of optical conductivity reads:

$$\sigma_1(\omega) = \sigma_0 \frac{\Gamma\omega[\Gamma\omega(q^2 - 1) + 2q(\omega^2)^2 - \omega_0^2]}{(\omega_0^2 - \omega^2)^2 + (\Gamma\omega)^2} \quad (2.41)$$

$$\sigma_2(\omega) = \sigma_0 \frac{\Gamma\omega[(q^2 - 1)(\omega^2)^2 - \omega_0^2] + 2\Gamma\omega}{(\omega_0^2 - \omega^2)^2 + (\Gamma\omega)^2}. \quad (2.42)$$

where σ_0 is the amplitude of the Fano contribution and q is the dimensionless phenomenological coupling parameter. This model was first introduced and extensively discussed by Fano to describe the interaction of a discrete atom ionized state with a electronic continuum in atomic and nuclear systems. In Figure 2.4, we plot the frequency dependent optical conductivity as a function of coupling constant q . Here extremely strong coupling ($q = 0$) results in an antiresonance with Lorentzian shape and no coupling ($q = \pm\infty$) yields a standard Lorentzian shape; when q is positive (negative) $\sigma_1(\omega)$ has a minimum (maximum) with negative value at low frequency

and a maximum (minimum) at high frequency.

2.2.3. Extended Drude analysis

For a simple metal, the low energy electrodynamic properties can be well captured using Drude model with only frequency independent parameters. However, it is commonly observed that in many metallic systems such as heavy-fermion materials and high-Tc cuprates, the complicated optical conductivity strongly deviates from this model [87]. Therefore the extended Drude model has been developed to describe these strange metals in the presence of strong electron-electron or electron-boson correlations.

In correlated metals the optical conductivity usually consists of one coherent peak centered at zero frequency and another broad incoherent contribution at mid-infrared range, which the Drude formalism fails to describe. To account for the intraband (coherent+incoherent) response, we can either add new Lorentz terms to the Drude component or we keep the single component model and generalize the Drude theory by making the scattering rate term complex and frequency-dependent. The later one is referred to as extended Drude analysis [93].

The extended Drude model offers a detailed description of the charge carrier scattering spectrum and mass. The standard form of optical conductivity for the Drude model

$$\sigma(\omega) = \frac{i}{4\pi} \frac{\omega_p^2}{i1/\tau + \omega} \quad (2.43)$$

can be extended to include a frequency-dependent scattering rate

$$\sigma(\omega) = \frac{i}{4\pi} \frac{\omega_p^2}{[i1/\tau(\omega, T) + \omega\lambda(\omega, T)] + \omega} \quad (2.44)$$

In addition, an extra real quantity $\omega\lambda(\omega, T)$ is added to the scattering rate, which is related with the mass enhancement of the electronic excitation due to strong many-body interactions. This is necessary to preserve the K-K relation between σ_1 and σ_2 . In this formalism, the complex conductivity also can be expressed in terms

of the memory functions ($M(\omega, T)$) as:

$$\sigma(\omega) = \frac{i}{4\pi} \frac{\omega_p^2}{M(\omega, T) + \omega} \quad (2.45)$$

Here $M(\omega, T) = M_1(\omega, T) + iM_2(\omega, T)$ describes all the information about the effect of electron-electron interactions and the coupling to collective modes [94]. The complex memory function $M(\omega, T)$ holds the causality principle, which means M_1 and M_2 make a K-K pair. Very often it is also called as optical self-energy, i.e., $M = -2\Sigma^{op}$, which is quite similar to the single-particle self-energy averaged over the Fermi surface [95]. Here we should keep in mind that this model can not describe the interband transition, therefore the frequency range of the calculation is restricted to the intraband.

From Equation (2.2.3) and (2.44), we can get the following relations:

$$M_1(\omega, T) = \omega\lambda(\omega, T) = \frac{\omega_p^2}{4\pi} \frac{\sigma_2(\omega)}{(\sigma_1^2(\omega) + \sigma_2^2(\omega))} - \omega \quad (2.46)$$

$$M_2(\omega, T) = \frac{1}{\tau(\omega, T)} = \frac{\omega_p^2}{4\pi} \frac{\sigma_1(\omega)}{(\sigma_1^2(\omega) + \sigma_2^2(\omega))} \quad (2.47)$$

$$\frac{m_{opt}^*}{m} = 1 + \lambda \quad (2.48)$$

From $M_1(\omega, T)$ we can extract the mass enhancement as a function of frequency and temperature.

2.3. Optical properties of quantum materials

2.3.1. Charge order

One of the important features in the infrared spectra of organic conductors are these asymmetric, Fano-type vibrational modes, which are superimposed on the electronic background. These infrared inactive BEDT-TTF intramolecular vibrations are activated via the so called electron-molecular vibration (EMV) coupling [88]. As shown in Figure 2.5 (a), due to the dimerization of these molecules in the crystal, out-of-phase vibration induces the differences between the transfer integrals

on the opposite sides of the molecule, consequently a charge flow and a dipole moment. Therefore the dipole moment can couple to the infrared radiation, and finally can be observed in the optical spectra.

The eigen-frequencies of these symmetric A_g vibrations of the BEDT-TTF molecule are plotted in Figure 2.5 (b). It was demonstrated by many groups that these modes are sensitive to the charge population on the molecules. As depicted in Figure 2.5 (d), the four most studied modes, which involve C=C vibrations show a significant shift towards lower frequencies as the neutral BEDT-TTF get oxidized. Hence, we can analyze the value of charge location on the molecule utilizing infrared and Raman spectroscopy.

The infrared-active (*ungerade*) molecular vibrational mode $\nu_{27}(B_{1u})$ mode is regarded as the best probe of the local charge on the molecules, since it is free from disturbing electronic background [88, 96]. The $\nu_{27}(B_{1u})$ band mainly involves the out-of-phase C=C vibrations in the BEDT-TTF rings as shown in Figure 2.5 (c). This mode leads to a dipole-moment change parallel to the long axis of BEDT-TTF molecule, therefore it can be measured with the electric field $E||c$, i.e. polarized perpendicular to the conducting layer. To quantitatively characterize the observed charge imbalance, the charge per molecule can be evaluated from the vibrational frequency by using the relationship [96, 97]:

$$\nu_{27}(\rho) = 1398 \text{ cm}^{-1} + 140(1 - \rho) \text{ cm}^{-1}/e \quad , \quad (2.49)$$

where ρ is the site charge in units of the elementary charge e .

Apart from the infrared-active $\nu_{27}(B_{1u})$ mode, there are two fully symmetric C=C stretching vibrations, namely ν_3 and ν_2 modes, that allow to determine the charge on the BEDT-TTF molecules with the help of Raman spectroscopy. The ν_2 mode is weakly coupled to electronic background and suitable for estimating the ratio of charge disproportionation. From the splitting of the $\nu_2(A_g)$ feature we calculate $2\delta_\rho = 0.2e$ in the charge-ordered state according to

$$\nu_2(\rho) = 1447 \text{ cm}^{-1} + 120(1 - \rho) \text{ cm}^{-1}/e \quad . \quad (2.50)$$

The temperature dependent investigation of the center frequency and linewidth of the above two modes can give us the detailed information on the charge disproportionation and fluctuation in organic systems. The fully symmetric ν_3 molecular

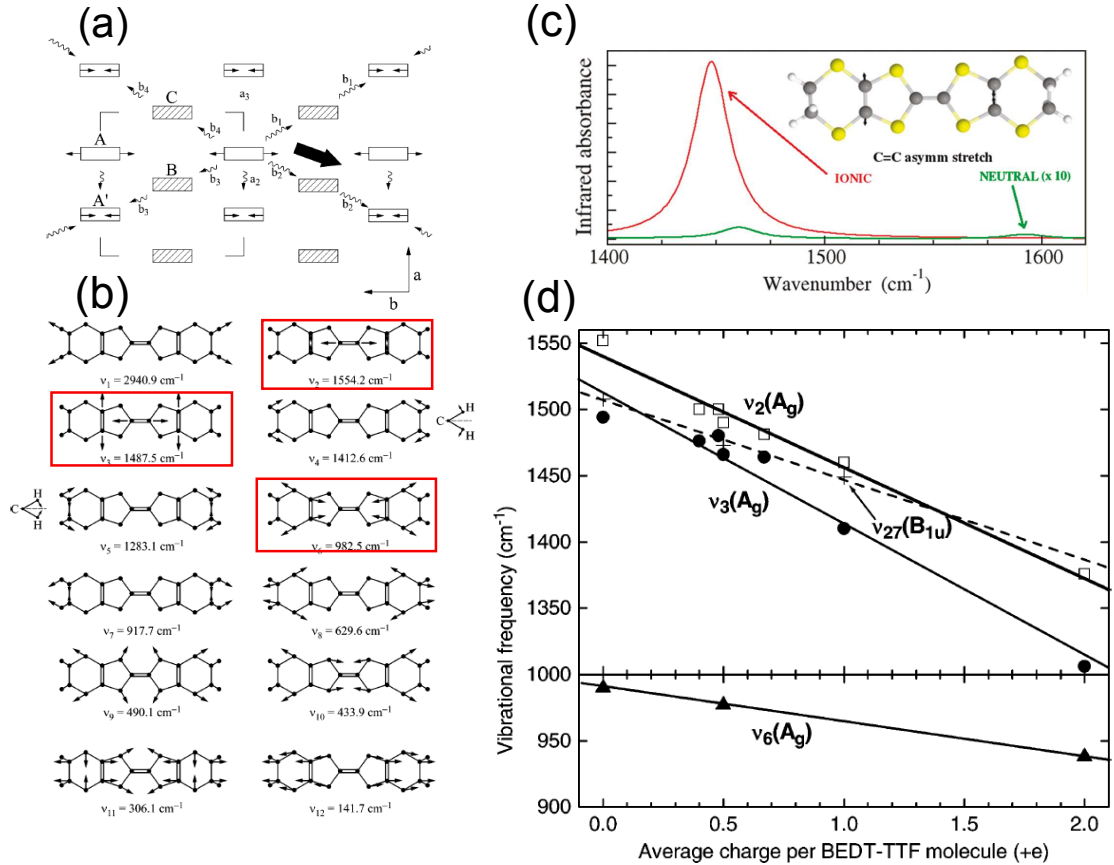


Figure 2.5.: (a) Sketch of the so called electron-molecular vibration coupling (b) Schematic configuration of the 12 A_g modes of BEDT-TTF. The three optically most active modes are highlighted by red square (c) The charge sensitive mode ν_{27} splits upon passing through a charge order transition. Theoretical calculations of ν_{27} in the charge order state (red) and normal state (green). (d) Plot of the frequencies of the four most studied charge sensitive infrared-active vibrational modes of BEDT-TTF as a function of the ionicity. After [88, 96]

vibration is insensitive to the charge and strongly couples to the electronic background as shown by the strong infrared intensity [98–101]. It has the strongest EMV-coupling constant among all the A_g modes EMV coupled vibrations show up as Fano-like features and are even more shifted. The intensity of this mode has often been used to describe the degree of dimerization based on a one-dimensional dimerized tight-binding model [102]. Furthermore the $\nu_{10}(A_g)$ and $\nu_9(A_g)$ modes involving C-S stretching vibrations, and the $\nu_{60}(B_{3u})$ mode that involves a ring-breathing vibration are known to be very sensitive to charge disproportionation and

dimerization [103].

Consequently, from the analysis of the temperature behaviour evolution of the pure vibrational modes and the EMV-coupled vibronic features, we can clarify the low-temperature ground state in organic conductors, where the structural distortion and charge disproportionation are often closely related.

2.3.2. Dirac electrons

Monolayer graphene is a very interesting 2-dimensional electronic system for investigating the relativistic nature of the quasi-particles, which is described by the Dirac equation. Its unique linear band dispersion is expected to give rise to unusual optical, transport and thermodynamic properties, which are quite different from those of quadratic massive bands [104, 105]. The interband optical conductivity is predicted to be energy independent and proportional to a universal conductance $\frac{4e^2}{h}$, which is mainly determined by the low-energy electronic structure at the Dirac point, where conical electron and hole bands meet each other.

The universal value can be derived by a simple scaling analysis as described by Kuzmenko *et al.* [106]. Let's first assume that the monolayer graphene is charge neutral, which means the chemical potential is zero and the Fermi energy is exactly located at the Dirac point. Then the interband conductivity characterizing the transition between the initial state with energy $-\frac{\hbar\omega}{2}$ and the final state with energy $\frac{\hbar\omega}{2}$ is determined by the following formula:

$$\sigma_1(\omega) \propto \frac{e^2}{\omega} |v(\omega)|^2 D(\omega) \left[f\left(-\frac{\hbar\omega}{2}\right) - f\left(\frac{\hbar\omega}{2}\right) \right] \quad (2.51)$$

where $f(\epsilon) = [\exp(\epsilon/k_B T) + 1]^{-1}$ is the Fermi-Dirac distribution, v corresponds to the velocity matrix element and $D(\omega)$ indicates the joint density of states. Given that graphene has an isotropic 2D linear energy dispersion near the Fermi level and the dispersion is given by $E = \hbar\omega = \hbar\nu_F$ as shown in inset of Figure 2.6, then v is simply the Fermi velocity ν_F and the density of states per unit energy and unit area is given by $D(\omega) \propto \frac{\hbar\omega}{(\hbar\nu_F)^2}$. Therefore at zero temperature the two frequency dependent terms $|v(\omega)|^2 D(\omega)$ cancel each other and σ_1 is only determined by $\frac{4e^2}{h}$

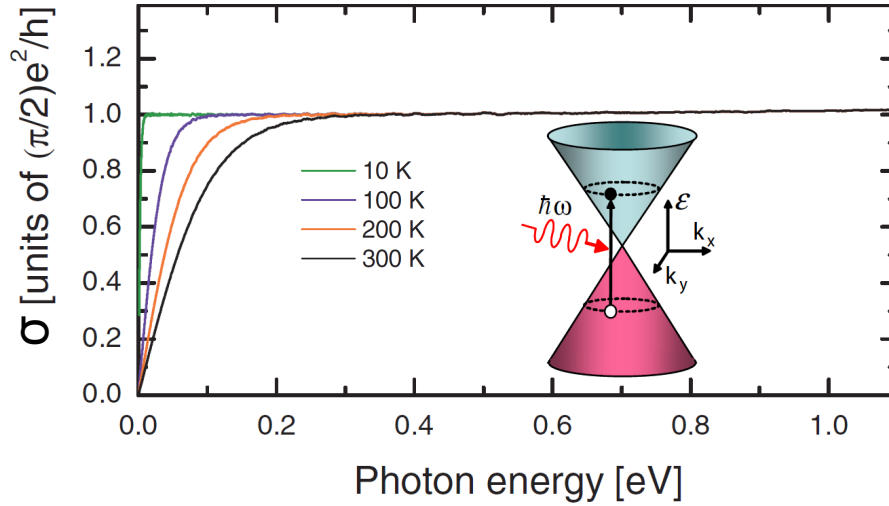


Figure 2.6.: Calculated real part of the optical conductivity of undoped graphene for various temperatures. The thermo-excited Drude contributions are ignored here. The inset describes the interband optical transitions between occupied and unoccupied bands in monolayer graphene. Redrawn from Ref. [106]

regardless of the microscopic details of materials.

The more complicated case, where temperature, chemical potential and impurity induced scattering rate have been taken into account, was extensively studied and discussed by Gusynin *et al.* [107], and the generalized analytical expressions at finite temperature T follow

$$\sigma_1(\omega) = \frac{4e^2}{h} \frac{2T\Gamma}{\omega^2 + 4\Gamma^2} \ln(2\cosh \frac{\mu}{2T}) + \frac{\pi e^2}{2h} \frac{\sinh(\omega/2T)}{\cosh(\mu/2T) + \cosh(\omega/2T)} \quad (2.52)$$

Here μ is the chemical potential and Γ is the impurity scattering rate. The first term corresponds to the intraband Drude contribution due to the thermally excited electrons and holes at finite temperature T . In Figure 2.6, the temperature dependence of the second term for the undoped graphene ($\mu = 0$) is plotted. Upon heating, the interband term decreases in the low energy region and the missing spectral weight is transferred to the intraband contribution, since $SW = \int_0^\infty \sigma_{intra}(\omega) d\omega \propto T$. For the case $\omega \gg T$, the universal conductance is recovered and temperature-independent.

It is also interesting to note that the interband optical response of 3-dimensional Dirac electrons is supposed to follow a linear frequency dependence [108, 109]

$$\sigma_1(\omega) \propto \omega \quad (2.53)$$

which has been experimentally observed in a series of Weyl semimetal [110]. However, in a special case, where a nodal line exists in the 3D band structure, $\sigma_{inter}(\omega)$ is frequency independent as well, but not universal anymore [111].

2.3.3. Bad metal

As we have shown in the previous section, in the framework of Drude formalism, the electron dynamics are dominated by momentum-relaxing (such as lattice or disorder scattering) mechanisms, obeying the Boltzmann equation. In weakly interacting metallic systems exist well defined and long-lived quasiparticles, which account for low energy properties of the dc-transport. As the system is heated up, the resistivity increases due to the increase of the mean-free path of the quasi-particles. Therefore, when the mean free path l satisfies $k_F l \sim 1$ (k_F is the Fermi wavevector), namely is comparable to the interatomic length, the quasi-particle picture breaks down and the resistance saturate at the so called Mott-Ioffe-Regel (MIR) resistivity bound [112, 113]

$$\rho_{MIR} \sim \frac{\hbar}{e^2}. \quad (2.54)$$

However, in many strongly correlated bad metals, such as cuprates, pnictides, heavy fermions, vanadium dioxide, and organics, this MIR limit is often violated. In their phase diagram exists a region near the quantum critical phase with a T -linear resistivity, crossing the MIR bound and extending towards high temperatures [114]. Thus, a new universal bound, the diffusivity bound, was proposed by Hartnoll based on the holographic theory, to describe the diffusive processes in an incoherent metal [114]. In this formalism, the low energy effective description of the strongly correlated system has Planckian dynamics. If we apply energy-time uncertainty principle to the quasiparticle lifetime $\frac{1}{\tau} \sim \frac{k_B T}{\hbar}$ ($k_B T$ is the quasiparticle energy) the diffusivity bound reads

$$\rho_D \sim \frac{k_B T}{E_F} \frac{\hbar}{e^2} \quad (2.55)$$

where E_F is the Fermi energy and k_B is the Boltzmann constant. As shown in Figure 2.7 (a) the destruction of quasiparticles may occur well below MIR bound.

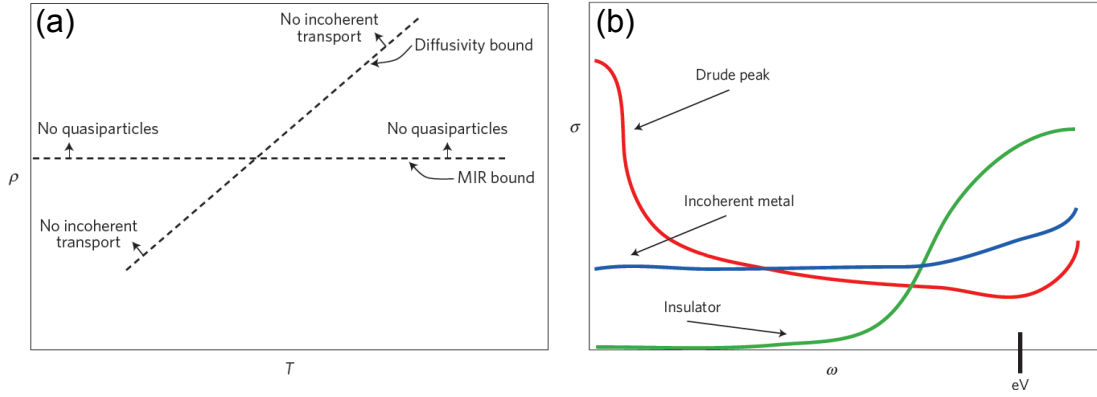


Figure 2.7.: (a) Cartoon of the Mott-Ioffe-Regel (MIR) resistivity bound on quasiparticle transport and Diffusivity bound on incoherent transport in the resistivity versus temperature plane. (b) Schematic plot of the optical conductivity in conventional metals, bad metals and insulators. After [114, 115]

The ratio of diffusivity bound to MIR bound follows

$$\frac{\rho_D}{\rho_{MIR}} \sim \frac{k_B T}{E_F}. \quad (2.56)$$

Thus, when $k_B T \sim E_F$, the incoherent bound cross the MIR limit. That can explain the reason why in organic system (low E_F) the T -linear resistivity happens at relatively low temperatures compared to those of high- T_c cuprate (high E_F). From optical point of view, the bad metals are characterized by a broad infrared peak instead of a coherent Drude peak as shown in Figure 2.7 (b).

Moreover, in a large number of bad metals, the infrared peak has a strong temperature dependence [5]. The half-width of the peak gets narrow and the peak shifts to low frequencies as the temperature is decreased, which is distinct from the behaviour of metals and weakly pinned charge density waves, as depicted in Figure 2.8 (c-e). In a charge density wave (CDW) insulating state, it is well known that weak disorder can pin the charge density wave and induce an intragap absorption [82, 116] as shown in Figure 2.8 (a) and (b). However, disorder-induced momentum relaxation will only broaden the Drude peak but does not move the Drude peak away from zero frequency. To quantitatively account for the non-quasiparticle properties in the bad metallic state, a new approach based on hydrodynamics of CDW has been recently developed [5, 117]. The main result for the optical conductivity

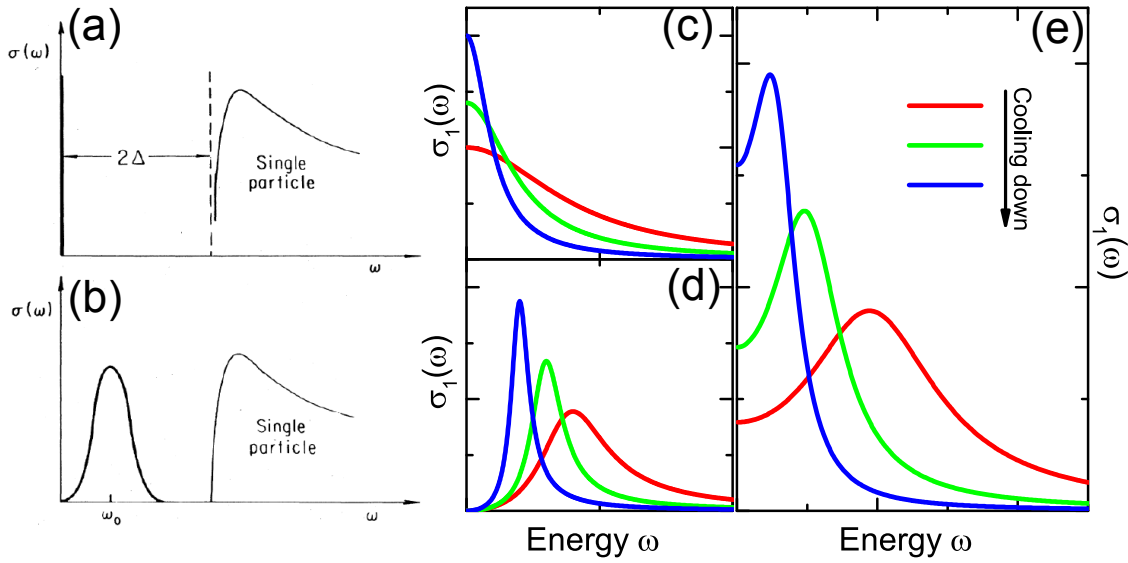


Figure 2.8.: Frequency-dependent optical conductivity of the charge density state (a) without pinning (gap opening), and (b) with pinning (finite frequency intragap absorption). Illustrative plots of the temperature dependence of the optical conductivity of good metals (c), weakly pinned charge density waves (d) and bad metals (e). The peak shown in the bad metals broaden and then moves away from zero frequency. Panel (a) and (b) are adapted from Ref. [116]

reads:

$$\sigma(\omega) = \sigma_0 + \frac{e^2 n}{m} \frac{\Omega - i\omega}{(\Omega - i\omega)(\Gamma - i\omega) + \omega_0^2} \quad (2.57)$$

Here Ω is the phase relaxation rate describing the phase fluctuation of the CDW, ω_0 is the pinning frequency due to the effects of broken translation invariance, and σ_0 corresponds to the background. The other parameters are the same as defined in the Drude model. When Ω and ω_0 are set to 0, the equation 2.57 has Lorentz form, which is used to describe the pinned charge density wave. For the case $\Omega \rightarrow \infty$, the standard Drude expression is recovered. For a moderate value of Ω , it can capture the non-zero frequency peak structure in the bad metals.

2.3.4. Fermi liquid

Despite the success of the Drude model in describing metals [118], a more accurate and generic formalism of Fermi liquid was proposed by Landau that takes into

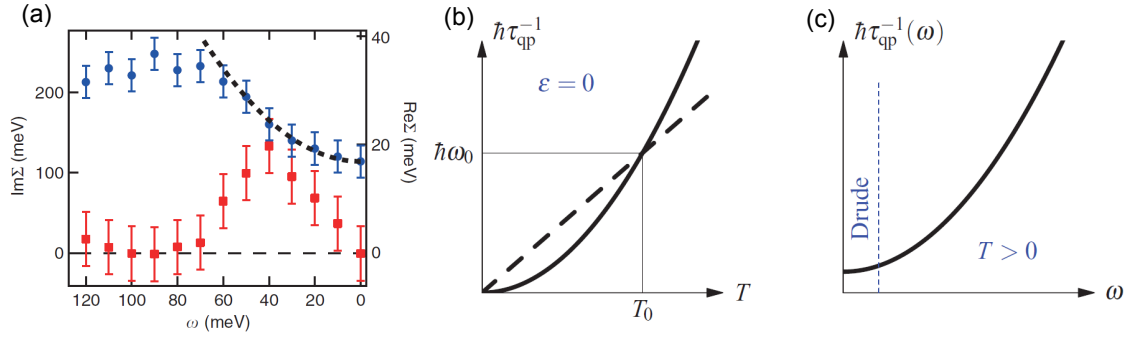


Figure 2.9.: (a) Self-energy Σ of the organic metal $(\text{BEDT-TTF})_3\text{Br}$ obtained by ARPES. The real part of the self-energy $\text{Re}\Sigma$ (blue circles) clearly indicates linear dependence in $\hbar\omega$ (dashed line) and $\text{Im}\Sigma$ (red squares) shows a ω^2 dependence. The Fermi liquid scattering rate increases quadratically with temperature (b) and with frequency (c). The dashed line in panel (b) denotes $\hbar\omega = 2\pi k_B T$ and it intersects with \hbar/τ_{qp} at temperature T_0 and frequency $\hbar\omega_0 = 2\pi k_B T_0$. Panel (c) shows that only at very low frequencies the system can be described using Drude model with frequency-independent scattering rate. After [123]

account of the interactions between electrons using quantum theory [119]. The key idea behind this theory is the existence of a one-to-one correspondence of the ground state between the non-interacting Fermi gas and interacting Fermi liquid. As we turn on the interaction slowly, the elementary excitations are replaced by quasiparticle with renormalized mass, velocity and other dynamical properties, but with the unchanged mass, charge and momentum of the free electrons. In the following section, we will show the universal characteristics of a Fermi liquid, which qualitatively deviates from the Drude model [120–122].

Specifically, we focus on the optical response of the local Fermi liquid with the assumption that the single-particle self-energy $\Sigma(\omega)$ obeys the behaviour of Landau Fermi-liquid theory and is independent of momentum. The temperature- and frequency-dependent self-energy of a Landau quasiparticle in a Fermi liquid is mathematically expressed as

$$\Sigma(\omega, T) = \left(1 - \frac{1}{Z}\right)\hbar\omega - \frac{i}{Z\pi k_B T_0} [(\hbar\omega)^2 + (\pi k_B T)^2] \quad (2.58)$$

Here, $\Sigma_1(\omega) = \text{Re}\Sigma$ and $\Sigma_2(\omega) = \text{Im}\Sigma$ contain the information of the energy dispersion and life time of the quasi-particle peak in the spectral function. $Z =$

$m/m^* = \nu_F^*/\nu_F$ is defined as the quasiparticle spectral weight, which corresponds to the renormalization of the mass and Fermi velocity due to the electron-electron interactions. And the prefactor T_0 has the energy scale of the Fermi energy and is proportional to the bandwidth of the bare band, which is related to the correlation strength in the system. Namely, the smaller T_0 is, the stronger the electron-electron interactions are and thus the larger is Σ_2 .

Experimentally, the self energy can be directly obtained by angle-resolved photoelectron spectroscopy (ARPES) using the spectral function with the following relation [84]

$$A(k, \omega) = \frac{-\Sigma_2(\omega)\pi}{[\omega - \varepsilon_k - \Sigma_1(\omega)]^2 + [\Sigma_2(\omega)]^2} \quad (2.59)$$

In this expression, $\varepsilon_k = E_k - \mu$ and μ is the chemical potential. Here E_k is the non-interacting bare band dispersion with typical parabolic shape. Figure 2.9 (a) shows the results of Σ derived from the ARPES band map of the two-dimensional organic conductor (BEDT-TTF)₃Br(pBIB) [123]. The $\text{Im}\Sigma$ and $\text{Re}\Sigma$ exhibit a clear ω^2 and ω dependence, respectively, which is a strong demonstration of the Fermi-liquid behaviour.

The quasiparticle scattering rate is defined as twice the value of Σ_2

$$\frac{\hbar}{\tau_{qp}} \equiv 2Z|\Sigma_2(\omega = 0, T)| \quad (2.60)$$

It has the physical meaning of the twice the width of the quasi-particle peak in the spectral function, which is slightly different from the optical scattering rate as shown later. The dependence of the scattering rate on temperature and frequency are illustrated in Figure 2.9 (b) and (c). As shown in Figure 2.9 (c), the Drude picture can only be valid when $\hbar\omega \ll 2\pi k_B T$, while non-Drude response appears when $\hbar\omega \sim 2\pi k_B T$.

In general, the complex optical conductivity is related to the self energy by the following formula [122]

$$\sigma(\omega) = \frac{i\Phi(0)}{\omega} \int_{-\infty}^{\infty} d\epsilon \frac{f(\epsilon) - f(\epsilon + \hbar\omega)}{\hbar\omega + \Sigma^*(\epsilon) - \Sigma(\epsilon + \hbar\omega)} \quad (2.61)$$

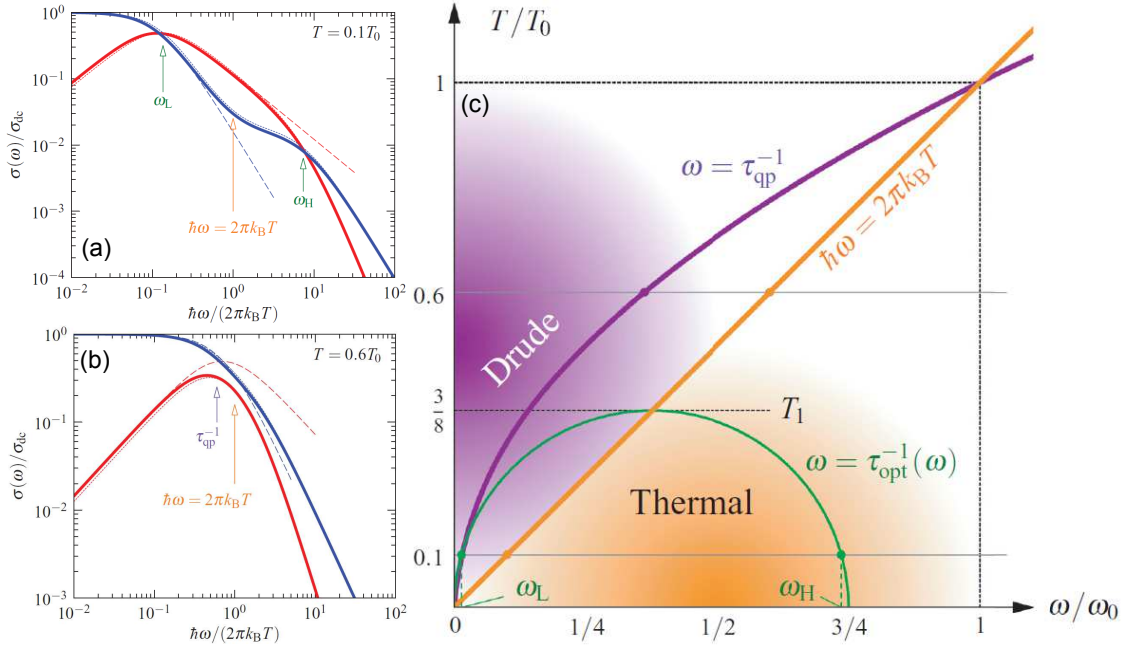


Figure 2.10.: Characteristic optical conductivity of Fermi-liquid at low temperatures (a) and high temperatures (b). The blue (red) lines correspond to the real (imaginary) part of the conductivity. At relatively low temperatures the real part and imaginary part cross each other, whereas at high temperature no crossing is predicted and the optical conductivity are dominated by the simple Drude model. (c) Schematic phase diagram of Drude regime and thermal regime predicted by local Fermi-liquid theory. After [122]

where $\Phi(0)$ is an constant characterizing the spectral weight in the Drude peak, and f is Dirac-Fermi distribution function. In the simplest case, when $Z = 1$ and Σ is set to be constant, the above equation reduces to a simple Drude term. If we insert Equation 2.58 into Equation 2.61, we obtain

$$\sigma(\omega) = \sigma_{dc} \Psi\left(\frac{\hbar\omega}{2\pi k_B} T, \omega\tau_{qp}\right) \quad (2.62)$$

Here $\Psi(x, y)$ is a complex function $\Psi(x, y) \approx 1/(x^2 - 3iy/4)$. Let's first look at the behaviour of the real and imaginary parts of the calculated optical conductivity at very low temperatures $T = 0.1T_0$. As depicted in Figure 2.10 (a), we can clearly identify three distinct energy regimes based on the two crossing points between σ_1 and σ_2 . (1) At low frequency $\hbar\omega \ll 2\pi k_B T$, this regime is called "Drude regime" since the conductivity follows the Drude model with frequency-independent scattering rate $1/\tau_D$. The σ_1 saturates well below $1/\tau_D$ and decreases as ω^{-2} above it.

(2) When $\hbar\omega$ is comparable to $2\pi k_B T$, we have the relation $\sigma_2 > \sigma_1$ in this "thermal regime". σ_1 (σ_2) exhibits an additional shoulder structure with much weaker (stronger) frequency dependence. (3) At very high energies $\hbar\omega \gg 2\pi k_B T$, σ_1 recover the Drude like ω^{-2} decay, and σ_2 falls faster than σ_1 . Such dissipation-like behaviour ($\sigma_1 > \sigma_2$) is not physical, which is due to the artefact of the unbounded ω^{-2} increasing behaviour in the self energy at high frequencies.

In the thermal regime, the non-Drude behaviour is described utilizing extended Drude model and the optical scattering rate reads

$$\frac{\hbar}{\tau_{op}} = \frac{2}{3\pi k_B T_0} [(\hbar\omega)^2 + (2\pi k_B T)^2] + 2Z\Gamma \quad (2.63)$$

Here, $2Z\Gamma$ denotes the impurity scattering rate. We should notice that \hbar/τ_{op} has a factor of 2π indicating the two-particle process (both electron and hole) [122, 124], while the single quasi-particle lifetime displays only π in Equation 2.58. However, experimentally it was very often found that the factor is not simple 2π , but with a generalized form [121]

$$\frac{\hbar}{\tau_{op}} = \frac{2}{3\pi k_B T_0} [(\hbar\omega)^2 + (p\pi k_B T)^2] + 2Z\Gamma \quad (2.64)$$

where p can be any real number. It has also been pointed out that not only the optical scattering rate but also the quantity $1-R(\omega)$ follows the same scaling law [125]

$$1 - R(\omega) \propto \frac{[\omega^2 + (2\pi k_B T)^2]}{3\pi k_B T_0} + Z\Gamma \quad (2.65)$$

The two crossing point in the "thermal regime" can be analytically solved with the the condition $\sigma_1 = \sigma_2$ and yields

$$\hbar\omega_{L,H} = \frac{3}{4}\pi k_B T_0 [1 \pm \sqrt{(1 - (\frac{8T}{3T_0})^2)}] \quad (2.66)$$

As plotted in Figure 2.10 (b), when the temperature is increased above $T_1 = 3T_0/8$, the relation $\sigma_1 > \sigma_1$ applies at all frequencies and thus the local Fermi-liquid scaling law breaks down. The ω - and T -dependence of the "Drude regime" differs clearly from that of the "thermal regime" in the colour plot as shown in Figure 2.10 (c).

2.3.5. Mott metal-insulator transitions

In many strongly correlated materials, the electronic properties can not be described in the framework of the free electron model. In order to understand those insulating states better, Mott proposed another approach based on real space picture instead of standard band theory [126]. The main mechanism for the metal-insulator transition is due to the strong Coulomb interactions between electrons sitting on neighbour lattice site as shown in Figure 2.11. Mott's picture is quantitatively described by so called Mott-Hubbard model [127–131], which is defined explicitly as

$$H = \sum_{ij,\sigma} (-t_{ij} c_{i\sigma}^\dagger c_{j\sigma} + H.c.) + \sum_{ij} V_{ij} n_i n_j + \sum_i U_{eff} n_{i\uparrow} n_{i\downarrow} \quad (2.67)$$

Here, t_{ij} is the nearest neighbour transfer integral between sites i and j , characterising the kinetic energy. $c_{i\sigma}^\dagger/c_{j\sigma}$ denote the creation/annihilation operator of electron or hole on i -th lattice site with spin σ , $n_{i\sigma} = c_{i\sigma}^\dagger c_{j\sigma}$ describes the number of electrons on site i with spin σ . For the half-filled strongly dimerized organic system, the inter-site Coulomb repulsion can be ignored, while V plays an important role for the quarter-filled system. In the following discussion, we describe the simplest Hubbard model without V . One of the most important features of the Hubbard model is that the electronic properties of the correlated system are simply controlled by the competition between the first term, favouring the delocalization of electrons, and the local Coulomb repulsion U , freezing the electrons.

As depicted in Figure 2.12 (a), the phase diagram predicted by Hubbard model is determined mainly by two parameters, U/W and T/W . Here W is the bandwidth and proportional to the hopping term t_{ij} . At very low temperature, the system undergoes the first-order metal-insulator transition as the U/W increases and crosses the critical region ($U/W \sim 1$). At higher temperatures, the system exhibits crossover from bad metal to bad insulator as the electron interactions increase.

To quantitatively characterize the dynamic properties of electron occupancy at a particular lattice site in the strongly correlated systems, a time-dependent quantity, namely the Green function, has been introduced [130, 131]. A single-particle Green function is defined as the probability, describing the correlation between the creation and annihilation of one electron with spin σ on i -th site, at time τ and τ' respectively

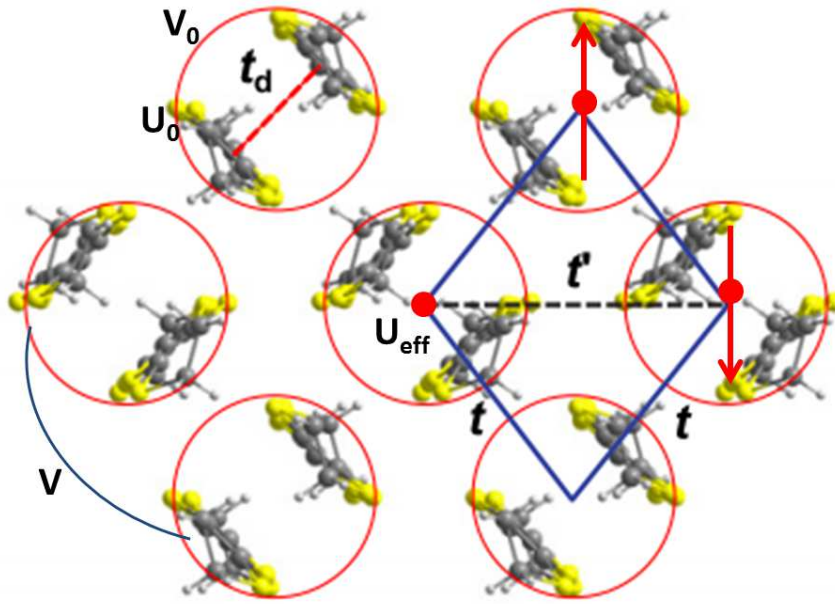


Figure 2.11.: Plot of lattice structure for a typical strongly dimerized organic system. One site consists of two dimerized molecules, indicated by a red circle. U_0 and V_0 are the on-molecule nearest neighbour Coulomb interactions, while U_{eff} , V are the on-site and inter-site Coulomb interactions respectively. t and t' are the transfer integrals between inter-dimers. Spins are indicated by red up and down arrows.

and has the following mathematical expression:

$$G_{i\sigma}(\tau - \tau') \equiv -\langle c_{i\sigma}^\dagger(\tau) c_{i\sigma}(\tau') \rangle \quad (2.68)$$

The spectral function is defined as the imaginary part of the Green function. Therefore, as long as the Green function of the Hubbard model is solved, the full information about the temporal and spatial evolution of a single electron is known. Despite the simplicity of the Hubbard formalism, in most cases the Green function is difficult to calculate exactly. A new approach named dynamical mean field theory (DMFT) was developed to simplify the calculations. In DMFT the Hubbard model is mapped to the Anderson impurity model where a single impurity atom interacts with an external electronic bath. The general Hamiltonian of this quantum

impurity model reads

$$H_{AIM} = H_{bath} + H_{atom} + H_{mix} \quad (2.69)$$

$$= \sum_{\nu,\sigma} \varepsilon_{\nu}^{bath} n_{\nu,\sigma}^{bath} + (U_{eff} n_{0\uparrow} n_{0,\downarrow} - \mu \sum_{i,\sigma} c_{i\sigma}^{\dagger} c_{i\sigma}) + \sum_{\nu,\sigma} (V_{\nu} c_{0\sigma}^{\dagger} a_{\nu,\sigma}^{bath} + H.c.) \quad (2.70)$$

where the first term H_{bath} describes the electronic bath with energy levels ν^{bath} , the second term in brackets stands for the single atomic degree of freedom, the third term denotes the hybridization energy between the single atom ($c_{0\sigma}$) and the environmental bath ($a_{\nu,\sigma}^{bath}$) with coupling constant V_{ν} . The dynamic properties of this model are characterized by the hybridization function $\Delta(\omega)$, which describes the ability of absorbing or emitting electrons into the surrounding reservoir of non-interacting electrons for the single atom on a time scale $1/\omega$. The mathematical expression of $\Delta(\omega)$ follows:

$$\Delta(\omega) = \sum \frac{|V_{\nu}|^2}{\omega - \varepsilon_{\nu}^{bath}} \quad (2.71)$$

The solutions of the H_{AIM} can be solved iteratively using the self-consistency condition, requiring the identity of the impurity Green function and the self energy of the Anderson model with those of Hubbard model, that is $G_H = G_{imp}$, $\Sigma_H = \Sigma_{imp}$.

Figure 2.12 (b) and (c) show a cartoon of density of states (DOS) with corresponding optical conductivity for various values of correlations based on DMFT calculations at $T = 0$ for a half-filled system. In the non-interacting limit ($U/W = 0$), the electron is delocalized with plane-wave properties and behaves like a free electron. The DOS possesses a peak at the Fermi energy with band width W and the real part of the optical conductivity exhibits a simple Drude peak at zero energy. In the atomic limit ($U/W = 2$), the quasiparticle peak at Fermi level vanishes and two Hubbard bands develop with separation energy of U . The ground state is described as Mott insulator with a gap opening in optical conductivity. At intermediate correlation region $U/W \sim 1$, we can observe both quasiparticle feature and two Hubbard bands in the density of states. As a result, apart from the Drude peak, the optical spectra contains additional two peak structures corresponding to optical excitations from both the quasi-particle peak to the upper Hubbard band and lower

to upper Hubbard band. In conclusion, Mott-type metal-insulator transition leads to a continuous transfer of spectral weight from the Drude peak to the Hubbard bands as U/W is increased.

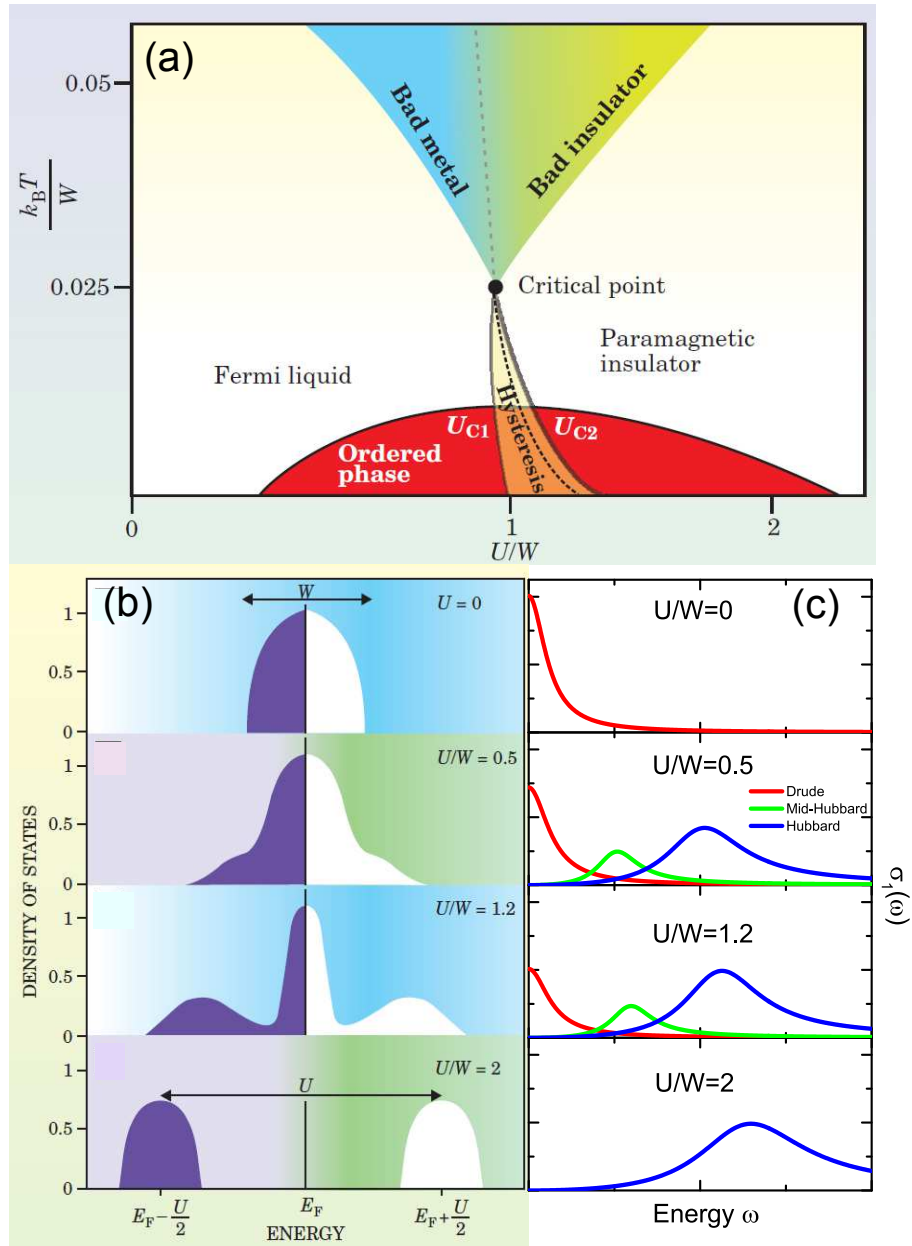


Figure 2.12.: (a) Schematic phase diagram of the Mott-type metal–insulator transition for a strongly correlated electron system. (b) The density of states (DOS) of electrons as a function of U/W predicted by DMFT for half-filling at zero temperature. The electronic DOS evolves from a Fermi-liquid like density at the Fermi level ($U/W = 0$) to an insulating one with well separated lower and upper Hubbard bands. (c) Plots of optical conductivity for various values of correlation strength. Modified from Rev. [130]

3. Setup

At the beginning of this chapter, we present the main experimental techniques used in classical infrared spectroscopy at ambient pressure followed by a description of the techniques that were used to perform infrared spectroscopy under high pressure and low temperature. Then we will describe how to extract the optical conductivity under pressure.

3.1. Principle of FTIR

Frequency-dependent optical properties of solids can be obtained by several measurement techniques with different principles. We can measure the optical response as a function of frequency in a straightforward way by irradiating monochromatic radiation and detecting the amplitude and phase of the response at one frequency. The same procedure need to be performed for several times as to cover the energy range of interest. Another powerful technique for measuring the charge dynamics in the lower energy range is time domain terahertz transmission measurement [132]. Instead of measuring the response of a solid by applying monochromatic radiation varied over a wide frequency range, the electrodynamical information of the solids are obtained by carrying out experiments in the time domain using a voltage pulse with all the energy of interest. The third one is the Fourier-transform spectroscopy which plays a dominant role for the measurement of infrared spectra. This method is based on the Michelson interferometer where a beam of radiation is split into two paths by beamsplitter and recombined at the beamsplitter after following different paths. The detected light intensity exhibits an interference pattern as a function of the relative difference of the two paths. The frequency dependence of the power spectra can be extracted from the intensity of the recombined beam as a function of

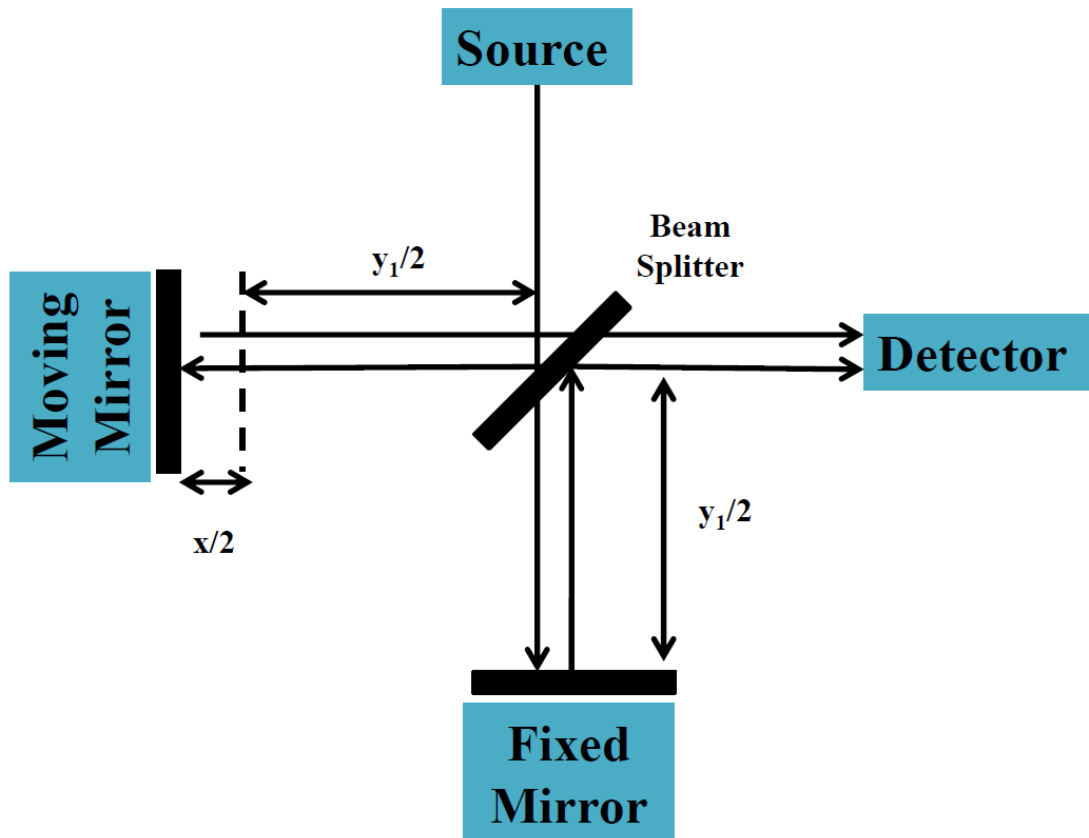


Figure 3.1.: Schematic view of Michelson interferometer. The beam of the source is divided into two parts by the beamsplitter. One of the beam is reflected by the fixed mirror and the other part by moving mirror, at distances $y_1/2$ and $y_1/2 + x/2$, respectively. The intensity of the recombined beam is a function of x . Modified from Ref.[82]

optical path difference via the Fourier transformation. A more detailed description of different technique can be found in book [82].

3.1.1. Michelson interferometer

Figure 3.1 displays the schematic view of a simple Michelson interferometer. The light from the source is divided into two separate beams at the beamsplitter. One beam is reflected by the moving mirror while the other by the fixed mirror, and finally are brought together again at the beamsplitter. Then the superimposed beam

Table 3.1.: Light sources, detectors and beamsplitters for the macroscopic system

Measurement range	Light source	Beamsplitter	Detector
Far infrared 80~600 cm^{-1}	Mercury Lamp	Mylar 6 μm	4.2 K Bolometer
Middle infrared 550~8000 cm^{-1}	Globar Lamp	KBr	MCT/DTGS
Near infrared 3500~10000 cm^{-1}	Tungstem Lamp	Si/CaF ₂	InSb Diode
Visible 9000~20000 cm^{-1}	Tungsten Lamp	UV/CaF ₂	Silicon Diode

propagates to the sample and to the detector finally.

With a simple mathematical calculation, the intensity detected by the detector is written as a function of x

$$I(x) = \int_0^{\infty} I(\omega)(1 + \cos(2\pi\omega x))d\omega \quad (3.1)$$

Where ω is the wave number with a unit of cm^{-1} , I is the frequency dependent intensity profile of the polychromatic source and x is the path difference. The frequency dependent intensity I can be derived from the intensity as a function of path difference x utilizing a Fourier transform.

$$I(\omega) = \int_0^{\infty} (I(x) - 1/2I(0))(1 + \cos(2\pi\omega x))d \quad (3.2)$$

By comparing the power spectrum of the sample with that of background, we can obtain the spectrum of the sample in the wanted energy range.

The Fourier-transform infrared spectrometers covers a very broad frequency range from approximately 80 cm^{-1} to 20000 cm^{-1} . In order to achieve the spectra over such wide range, a series of combinations of light sources, beamsplitters and detectors are needed for data collection. Table 3.1 lists the spectral range for several optical elements including sources, beamsplitters and detectors.

3.2. Pressure setup

In the following section, we are going to discuss the most important technical aspects of infrared optical measurements under pressure on the organic crystals. The

pressure-dependent optical investigation have been conducted in two different setups. One is located in 1. Physikalisches Institut of the University of Augsburg, and the other is located in the 1. Physikalisches Institut of the University of Stuttgart. The two setups are based on two different pressure generating methods using two kinds of pressure cell, namely DAC and piston-cylinder pressure cell. For both pressure cells a type IIA diamond has been used, which is suitable for infrared measurements due to its transparent properties over a broad energy range. These discussions and descriptions follow mostly Refs. [3, 4, 133]

3.2.1. Piston-cylinder cell

Temperature-dependent reflectivity measurements below 1 GPa were performed from 100 cm^{-1} to 8000 cm^{-1} between 6 K and 300 K using a home-built cryostat setup that is coupled to a Bruker Vertex 66v/S Fourier-transform infrared spectrometer as depicted in Figure 3.2. In this case the collection optics works only in reflection geometry and does not involve a microscope.

In general, the piston-cylinder cell is slightly different from a DAC. In this case, the optical access is constituted by a cylindrical wedged diamond window with a diameter of 3 mm, a height of 2 mm, and a wedge of 2° . The relatively large diamond size can avoid the diffraction limit and allows us to measure the very low energy physics of solid state systems. On the other hand, the increase of the sample surface will limit the maximum achievable pressure. For this reason, the maximum applied pressure is restricted to about 2.5 GPa [3].

The referencing of the absolute sample-diamond reflectivity R is in this case realized using diamond with wedged plane surfaces. As sketched in Figure 3.3 (a), we describe the simple procedure for the measurement of R . The wedge angle not only allows a clear spatial separation of the beams reflected from the sample-diamond I_{sd} and from the diamond-vacuum I_{vd} interfaces, but also can avoid the interference fringes coming from multiple reflections. The absolute sample reflectivity can be calculated by using the diamond-vacuum reflection as a reference, since the diamond optical constants are well known. A more detailed and generalized description of the calculating procedure will be discussed in the last section. Since it is sufficient

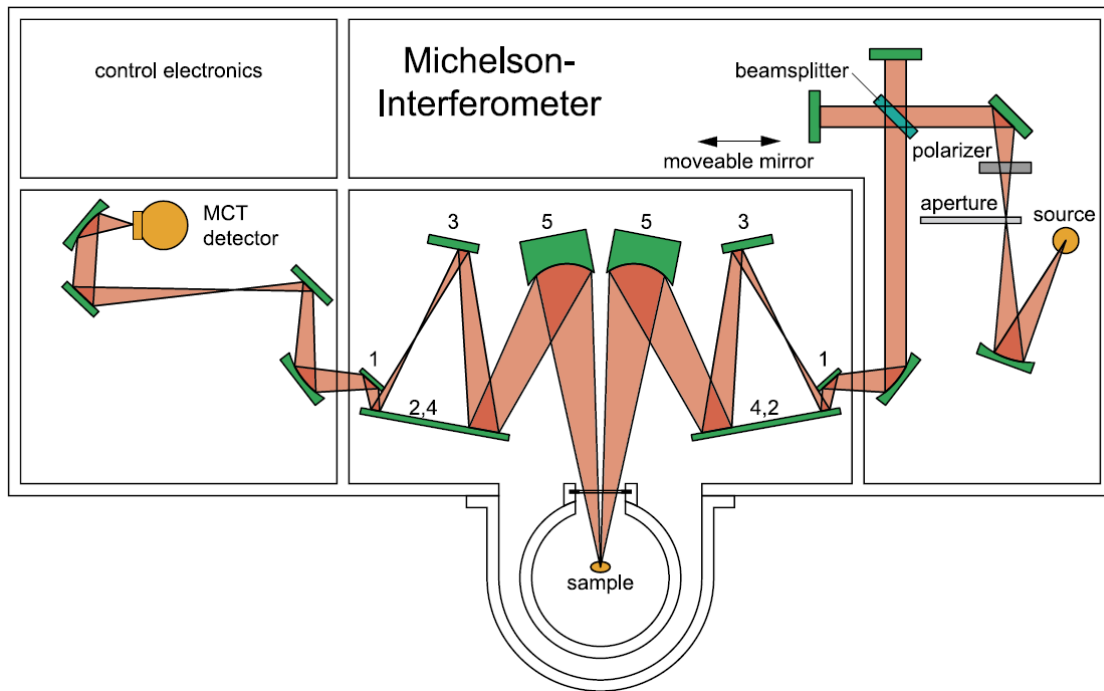


Figure 3.2.: Sketch of optical arrangement of the Fourier-transform infrared spectrometer Bruker IFS 66v/S. The sample chamber is modified with a large home-made extension chamber, where the new beam focus and pressure cell are located. The optical path is adjusted using several planar and parabolic mirrors to focus it into the cryostat located outside the spectrometer. Finally, the beam is reflected back to the detector by an identical arrangement of mirrors in opposite way. Adapted from Ref. [3]

to cause angular deviation between the two reflected beams by a few degree rotation, we can still consider the two optical configurations as nearly normal incidence.

As depicted in Figure 3.3 (a), in our setup, the piston cell of type CC33 designed and manufactured by the Institute for High Pressure Physics of the Russian Academy of Sciences in Troitsk, Russia is applied. The body of the cell is fabricated from beryllium copper (CuBe), nuts and insets from NiCrAl alloys, and tungsten carbide (WC). To completely separate the two reflected beams, a conical opening angle of 36° bored into the diamond holder is required in our optical arrangement. On the other side, the maximum pressure we can apply is reduced because of the conical opening, which weakens the mechanical structure of the pressure cell. Together

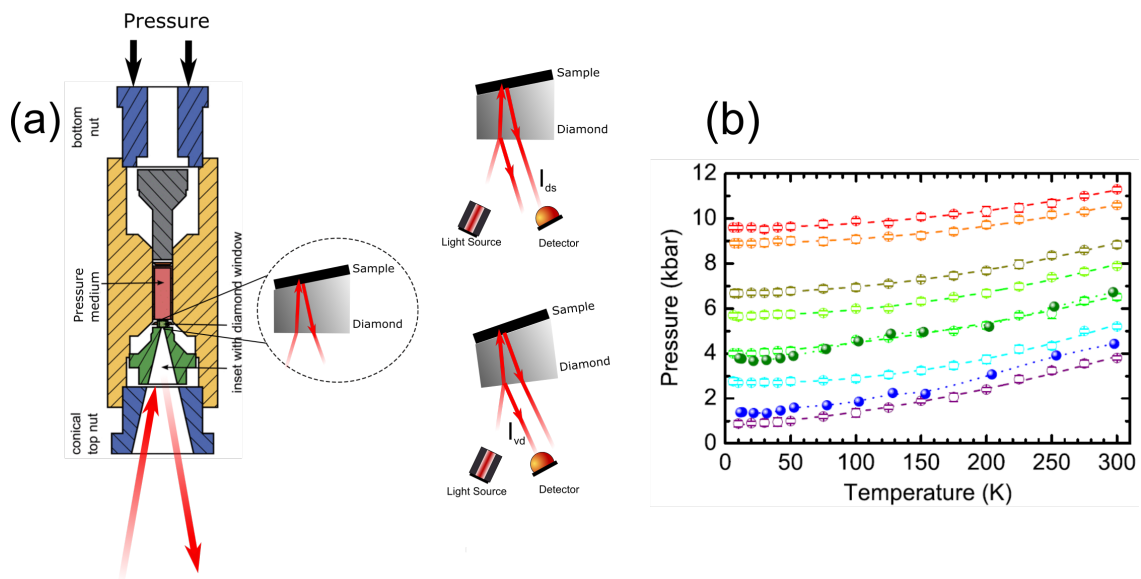


Figure 3.3.: (a) Sketch of the pressure cell for optical investigations. The sample is mounted on the inner surface of the diamond window which has $d = 3$ mm aperture, the angle of wedging between the two surfaces of the window allows for a complete separation of the reflected beam from the vacuum-diamond and diamond-sample interfaces (I_{vd} and I_{sd} , respectively). (b) Temperature-dependent pressure loss for different pressures applied at room temperature. Here open symbols indicate the actual pressure inside the cell measured in situ by ruby fluorescence, and solid symbols correspond to the data monitored by a Manganin wire. Panel (a) and (b) are modified and redraw from Ref. [3].

with diamond it provides the optical access.

In this case, the hydrostatic pressure medium of choice is Daphne 7373 oil owing to its good low-temperature properties and the sample is fixed directly onto the diamond window before introducing the oil. It is well known that the actual pressure inside the piston pressure cells is slightly reduced upon cooling due to the solidification of the liquid oil and thermal contraction of the pressure cell at low temperatures. Therefore, we have to calibrate the temperature dependence of the pressure inside the cell at each applied pressure. Principally, the pressure loss depends on both the materials used to fabricate the pressure cell but also on the employed pressure medium. To determine the real pressure, two pressure gauges are utilized, namely: the pressure- and temperature dependent resistivities of a

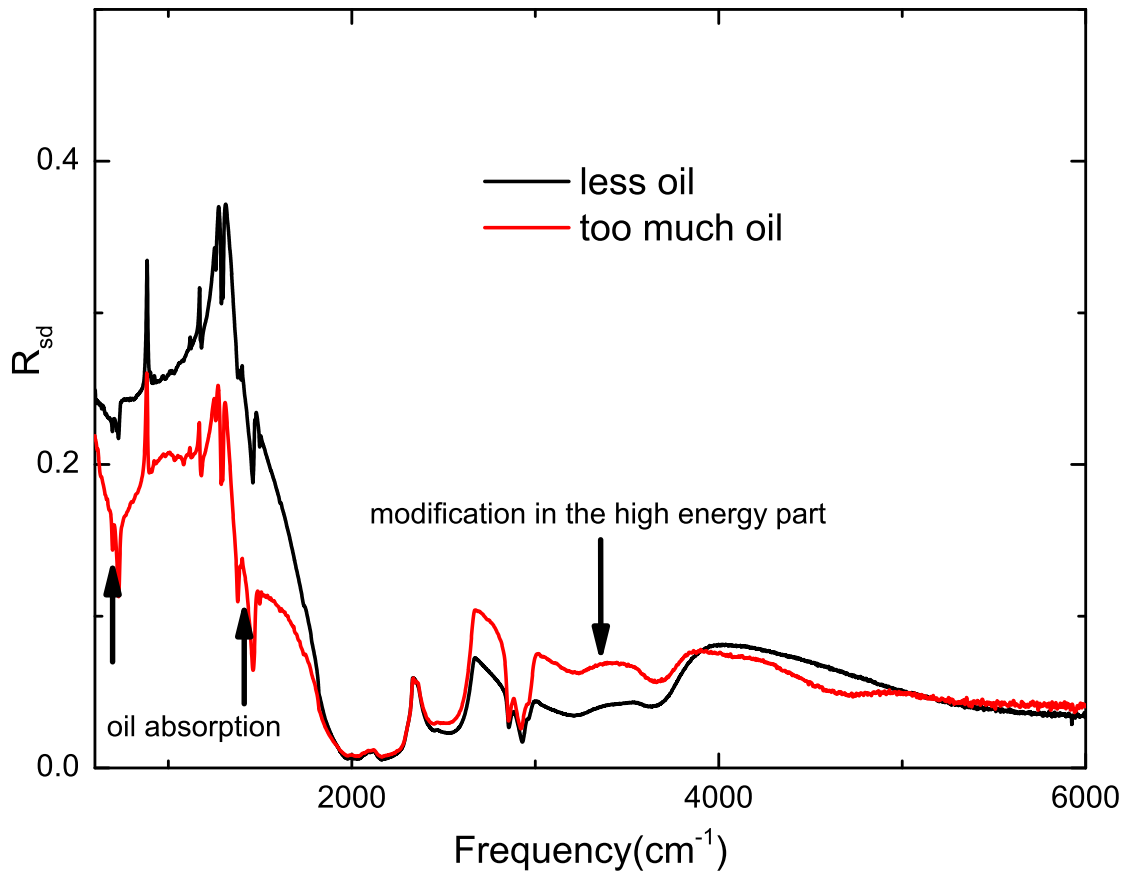


Figure 3.4.: Oil effect on the spectra of κ -(BEDT-TTF) $_2$ Cu $_2$ (CN) $_3$ measured at $T = 300$ K and $p = 0.7$ GPa. The black line indicates a good spectrum with less oil effect, while the red line corresponds to a spectrum strongly distorted by absorptions of Daphne oil as indicated by the black arrows.

Manganin wire and ruby fluorescence. As displayed in Figure 3.3 (b), the pressure in the cell decreases upon cooling. As a result, the pressure loss is more pronounced at low pressure range, which makes it difficult to obtain good spectra as the oil enters into the interface between sample and diamond, and weaker at high pressure values. Unlike the case of DAC, we cannot perform in situ monitoring of pressure by a resistive sensor or ruby fluorescence, while simultaneously measuring the optical reflectance due to the different sample mounting. Thus, in this case the measurements of pressure are performed at room temperature, and then are modified based on the previous calibrated values as shown in Figure 3.3 (b).

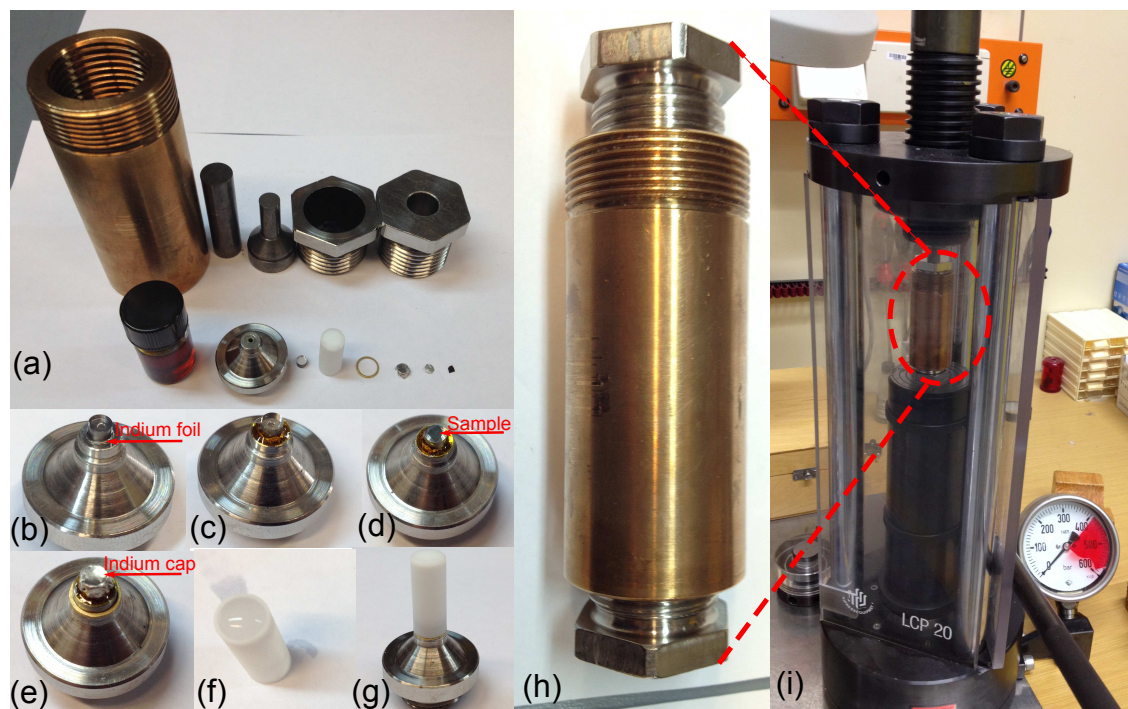


Figure 3.5.: Various phases of the preparation of the optical access: First of all, (a) all parts for the preparation of the pressure cell such as safety cover, nuts, T-shaped piston, circular rings, Teflon cap, indium foil and cap, sample, GE-varnish are collected and put nearby; (b) a small disk of indium foil and the diamond window need to be cleaned, then the window is positioned on the indium foil and centered with respect to the hole; (c) glue the diamond and diamond holder together with GE-varnish; (d)-(e) the sample is put on top of diamond and is covered by indium cap; (f)-(g) the whole inset is immersed in the teflon cap fully filled with oil; (h)-(i) finally, the inset is closed and assembled in the pressure cell and pressurized in the big press by mechanical force.

Due to the fact that piston pressure cell works with a liquid pressure transmitting medium, Daphe oil, it is important to isolate the sample from the oil medium. When a tiny layer of Daphe oil enters into the interface between sample and diamond, it will cause strong distortions in the spectrum especially in the middle infrared range due to the multilayer structure of diamond/oil/sample as displayed in Figure 3.4. Furthermore, the pressure medium adds additional vibrational absorption lines. In order to keep the liquid from entering the space between sample and diamond window, it is possible to use a small indium foil wrapped around the sample and the diamond as a protection.

In Figure 3.5, we show the detailed mounting phases of the piston pressure cell. First of all we have to clean all parts of the pressure cell using acetone and propanol carefully to avoid dust during the whole measurement. Before mounting the window with glue it is necessary to insert, between the diamond and its metal holder, a small indium foil with thickness around $100\ \mu\text{m}$. The presence of the indium foil allows to distribute the applied pressure homogeneously over the whole diamond surface, thus avoiding any damage of the diamond. Then we apply a small amount of Ge-varnish to cover around the base of the diamond before pressurization. The glue should be put surrounding the indium and diamond edge less than half of the height of diamond. It should be avoided to have extra glue on the top surface of diamond or on the side of inset. The glue is applied 2-3 times and then left overnight to get dried. After that the sample is put on top of diamond and is covered by indium cap. The $100\ \mu\text{m}$ thick cap should cover the sample completely and fit tightly on the diamond. Next, we glue the cap edges on the diamond using GE-varnish and leave it to dry for 24 hours, therefore making sure that the glue does not get into contact with the sample. After placing the thick extrusion ring in the inset holding, we fill the teflon cap with daphne oil and fix the whole inset in the teflon cap. Finally, the inset is closed and assembled in the pressure cell and pressurized in the big press.

3.2.2. DAC pressure cell

The pressure and temperature dependent reflectivity of $\alpha\text{-(BEDT-TTF)}_2\text{I}_3$ was measured using a home-built infrared microscope coupled to a Bruker Vertex 80/v FTIR spectrometer. The scheme of the infrared microscope is depicted in Figure 3.6. By simply switching the position of the movable mirror 1, we can operate the setup either in reflection or in transmission mode. The beam from the lamp is guided using several mirrors to focus it on the focal plane of the Schwarzschild objective and then is focused on the sample by all reflecting home-made Schwarzschild objective with a large working distance of about 55 mm and 14 magnification. Finally the beam is reflected back to the detector. The above described setup allows for polarization-dependent measurements over a broad energy range (from far-infrared $100\ \text{cm}^{-1}$ to visible $8000\ \text{cm}^{-1}$) for temperatures between 10 and 300 K, and pres-

sures up to 20 GPa in both reflection and transmission mode [133].

In order to reach high pressures, a diamond anvil cell (DAC) equipped with type IIA diamonds was used. The working mechanism of the DAC is pretty simple. Two diamonds with a flat tip squeeze a metallic gasket which has a hole in the center that confines the sample, as depicted in Figure 3.7. The pressure in the DAC is determined in situ by the standard ruby-fluorescence technique. Ruby nanoparticles have been widely used as a universal standard for pressure calibration up to 100 GPa [134, 135]. A 532 nm laser (green arrow) first excites the electrons of Ruby into an excited state, which relax back to ground state through photon emission, finally recorded with a grating spectrometer (CCD detector). The radiative levels responsible for the fluorescence are known as the R1 and the R2 lines, which at ambient conditions are centred at 694.25 nm and 692.85 nm respectively and are relatively sharp. As these two excitation lines scale in a linear fashion over a wide temperature and pressure range, the ruby manometer allows for in situ and accurate determination of pressures. The shift of the fluorescence spectra as a function of pressure and temperature are shown in Figure 3.7. In contrast to the behaviour for piston cylinder cell, the pressure inside DAC increases with decreasing temperature due to shrinkage of the metallic gasket. The lowest pressure that can be realized at 10 K was around 0.8 GPa, therefore in general the DAC is fittable for measurements in system with critical pressure above 1 GPa.

The detailed process of preparation for DAC are described in Figure 3.8. The investigated sample is placed between two diamond anvil tips, closed in a metallic sample chamber and a strong external force is applied on the diamonds that will compress the sample. The size of the cutlet of the anvils is set based on the maximum desired pressure, defined as force over surface ($P = F/S$), and the wider the cutlet, the smaller the reachable pressure. In this measurement 400 μm have been used to reach highest pressure around 4 GPa. Finely ground CsI powder (transparent under high pressure) is chosen as quasi-hydrostatic pressure transmitting medium to reach quasi-hydrostatic pressurization conditions.

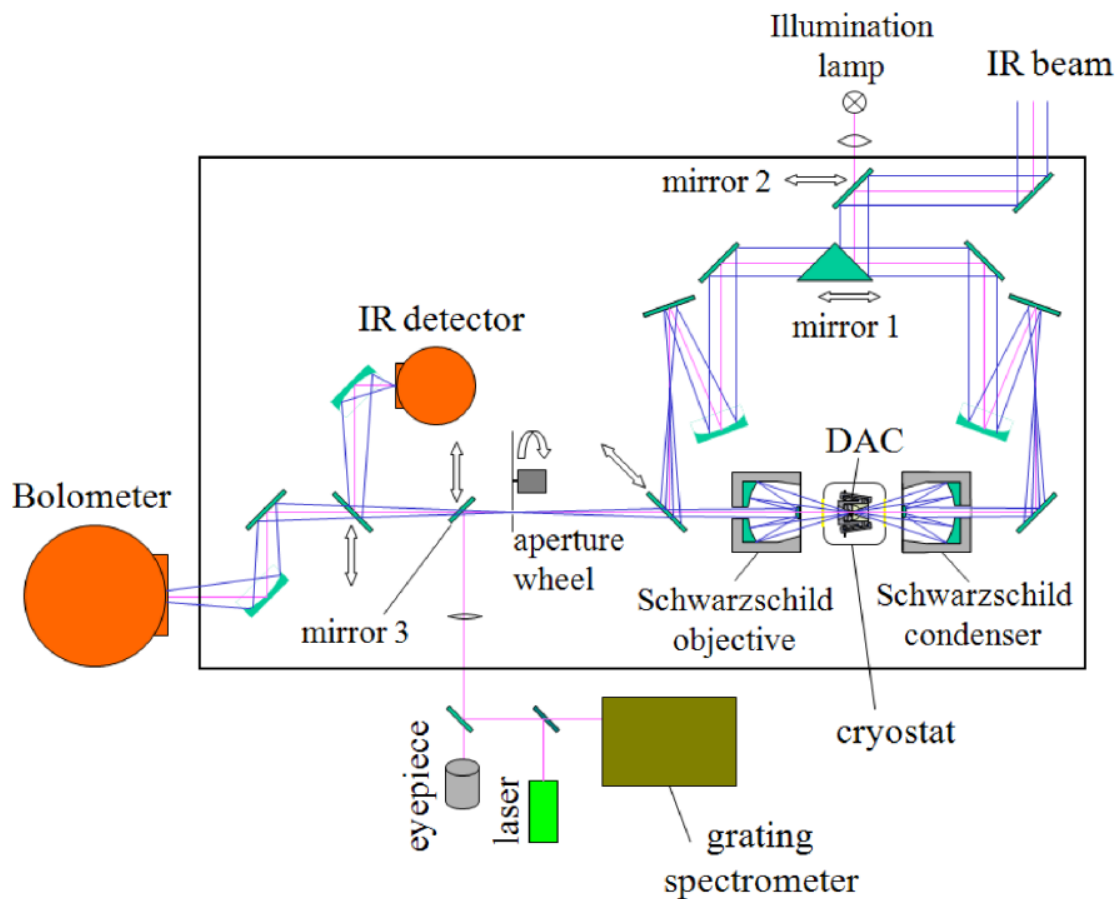


Figure 3.6.: Schematic view of the home-built Bruker Vertex 80/v FTIR spectrometer coupled to infrared microscope for both optical reflectivity and transmission measurements. By adjusting the position of mirror 1 the setup can be operated in either reflection or transmission mode. The direct observation of the sample is possible via the eye piece or with a video camera by moving mirror 2 and 3. Additionally two Schwarzschild objectives are used to focus the light on the sample. The DAC was mounted on the cold finger of a continuous flow helium cryostat. In order to determine in situ pressure, the ruby balls are prepared in the DAC and the ruby fluorescence spectra are recorded with a grating spectrometer. Redrawn from Ref.[133]

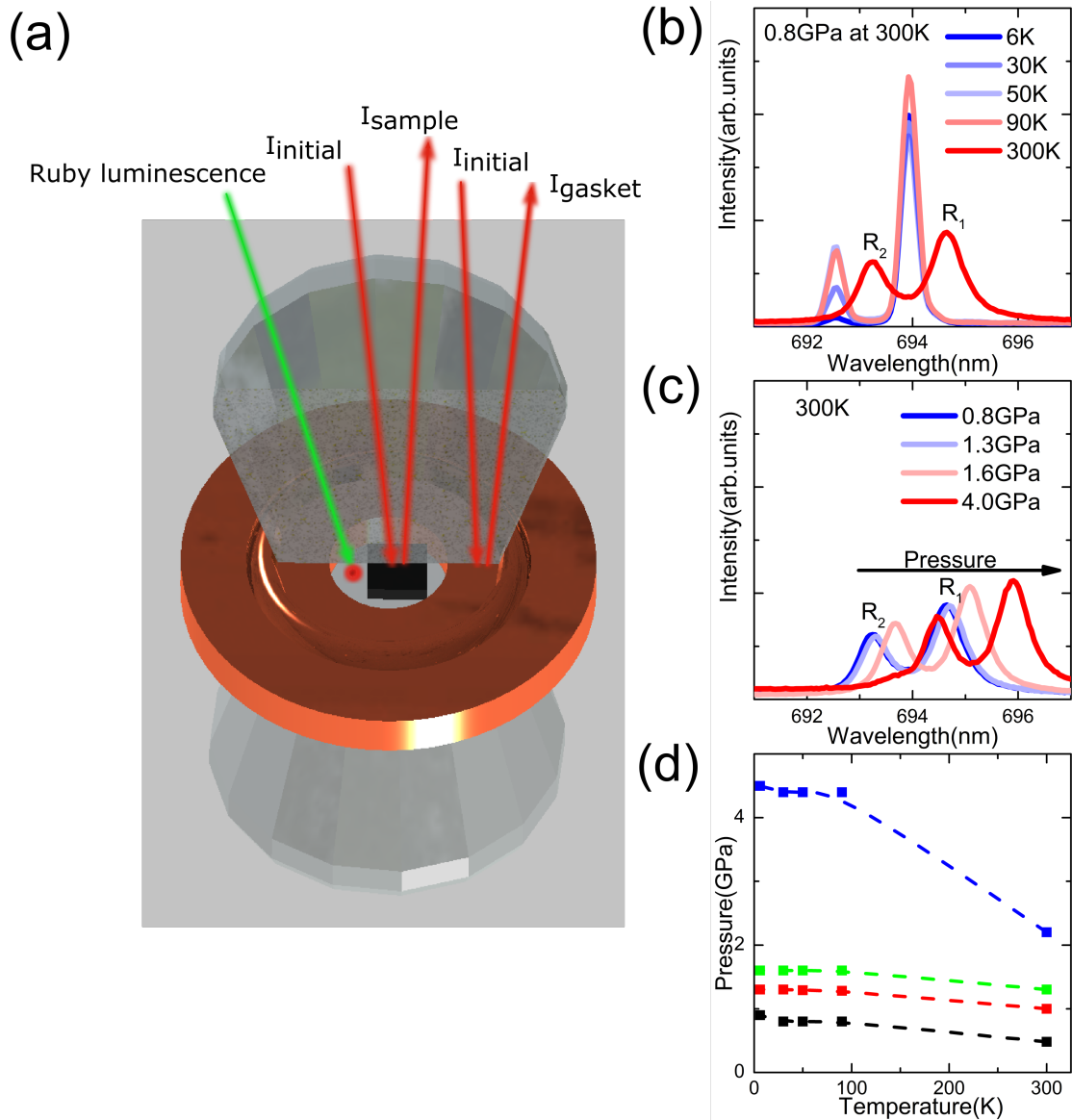


Figure 3.7.: (a) Schematic representation of the diamond anvil cell. Two diamonds with a flat tip squeeze a metallic gasket which has a hole in the centre that confines the sample (dark disc). A few rubies (red dot) are added on the sample surface for an accurate in-situ pressure measurement. The green and red light beam represent the laser used to excite the ruby and the typical light access through the diamond anvils, respectively. (b) position of the R_1 and R_2 lines as a function of temperature at 0.8 GPa (300K) (c) Fluorescence spectra of ruby under pressure with shift of the R_1 and R_2 lines. (d) In situ determination of pressures at measured temperature.

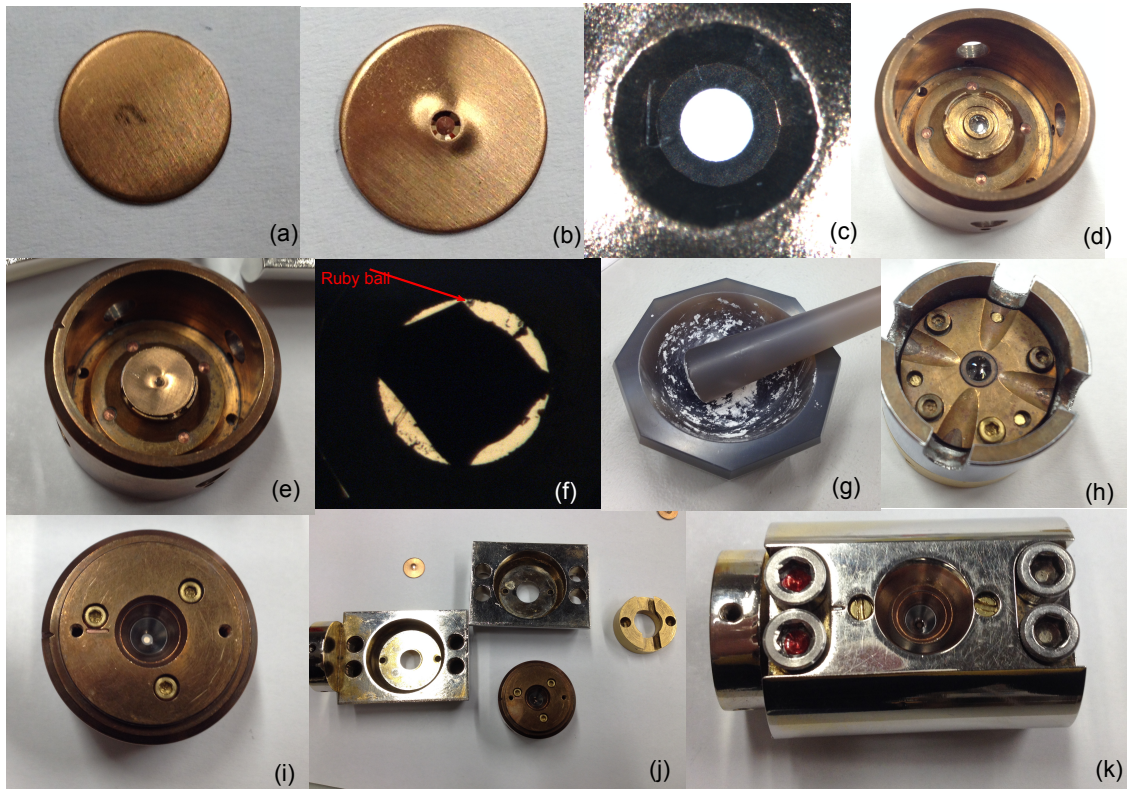


Figure 3.8.: Detailed preparations of the DAC: (a)-(c) metallic gasket with a hole in the center is prepared (d) bottom part of the diamond cell (e) metallic gasket is put on top of the bottom of diamond (f) sample and ruby ball are put inside gasket hole with carefully treatment (e) solid pressure medium CsI powder is heated up and then ground homogeneously (h)-(i) diamond anvil cell is closed by slowly pushing the up part inside the bottom part (j)-(k) DAC is closed by the metallic shell and high pressure is realized by gradually closing the four screws

3.3. Data analysis under pressure

In standard ambient pressure measurements, the absolute value of reflectivity is calculated by measuring the reflected signal at the air-sample interface and air-mirror interface, and finally by taking the ratio of these two quantities. From the optical point of view the presence of diamond optical access in pressure cell, drastically changes the referencing technique which is frequently used for the extraction of R at ambient condition. In the presence of a pressure cell, a simple setting of gold mirror or gold evaporation technique is no longer possible anymore. Therefore, a complete redefinition of the measuring procedure is needed in order to reconstruct the reflectivity curves. For the experiments shown in this thesis, two procedures have been applied according to different pressure cells. With a DAC, the reflectance signal is measured between the sample/diamond interface, and then normalized by the signal reflected between the gasket/diamond interface. For the piston pressure cell, instead of gasket the diamond itself is taken as reference. Afterwards the absolute reflectivity R_{sd} is obtained with a correction of prefactor taken from literature, which is the absolute value of the reflectivity of diamond and gasket [3, 133]. Quantitatively R_{sd} is calculated according to

$$R_{sd} = R_{dia} \cdot \frac{I_{sd}}{I_{vd}} \quad (3.3)$$

where I_{sd} is the intensity reflected from the sample-diamond interface I_{vd} is the intensity reflected from the vacuum-diamond or gasket-diamond interface and R_{dia} is the absolute reflectivity of the vacuum-diamond or gasket-diamond interface

As we already shown in the theory part according to Fresnel's formula the normal-incidence reflectance of a sample relative to a transparent medium of (real part) refractive index n_0 is given by the:

$$R = |\hat{r}|^2 = \left| \frac{\hat{N} - \hat{n}_0}{\hat{N} + \hat{n}_0} \right|^2. \quad (3.4)$$

Here, $\hat{N} = n_1 + in_2$ is the complex refractive index of the sample, and $n_0 = 2.4$ for diamond and 1.0 for vacuum. Here, we denote reflectivity at sample/diamond interface as R_{sd} , and that at sample/vacuum interface as R_0 . From Equation 3.4, we can easily notice that R_{sd} of a sample measured in pressure cell can be substantially

different from R_0 . In contrast, the optical conductivity of sample is independent of the transparent medium and can describe the intrinsic property of the material.

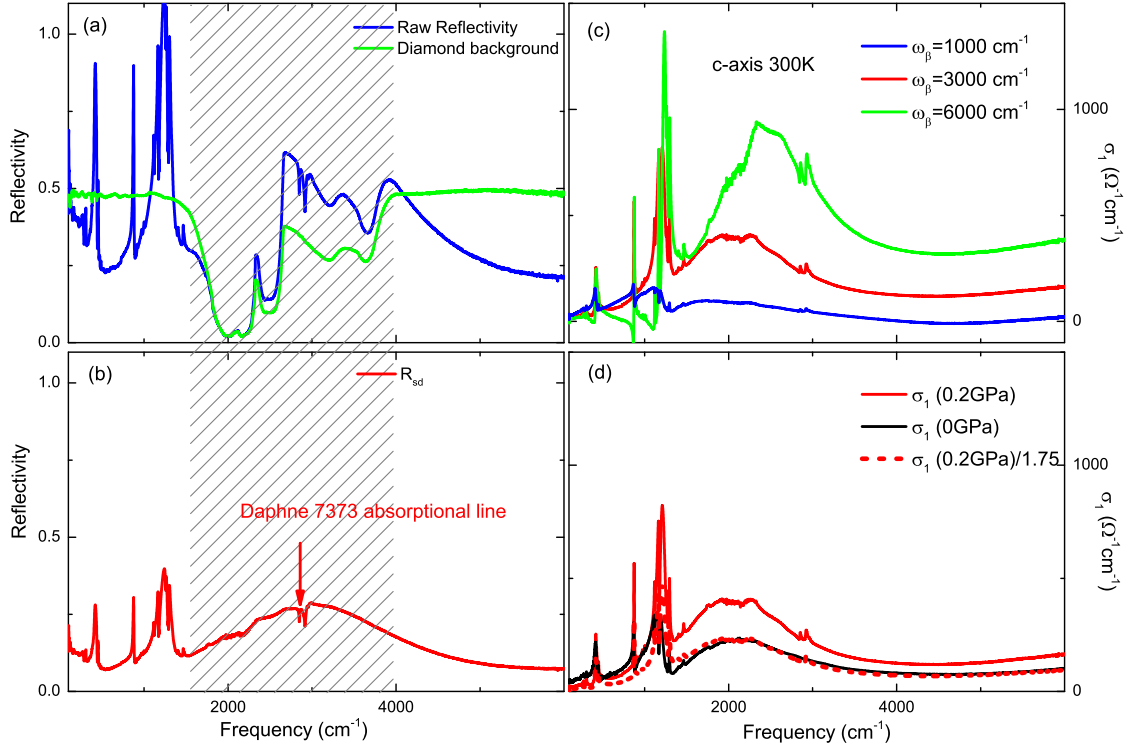


Figure 3.9.: Process of extracting optical conductivity at 300 K and 0.2 GPa for κ -(BEDT-TTF) $_2$ Cu $_2$ (CN) $_3$: (a) Blue line indicates the raw reflectivity defined as $\frac{I_{sd}}{I_d}$. Green line corresponds to the background spectra without sample. Multiphonon absorption bands of the diamond are shown by grey dash lines. (b) Reflectivity spectra after normalizing to diamond background. Red arrow indicates the absorption lines of Daphne 7373. (c) Calculated optical conductivity with chosen different value of ω_β . (d) Comparison of the normalized optical conductivity at 0.2 GPa with that at ambient pressure.

In the rest part we will consider the Kramers-Kronig (K-K) analysis of R_{sd} data measured in pressure cell. K-K analysis has been widely used to derive optical constants such as the refractive index, dielectric function and optical conductivity from a measured R_0 spectrum. However, due to the difference between R_0 and

R_{sd} discussed above, the usual K-K analysis method cannot be straightforwardly applied to R_{sd} . To derive optical constants from R_{sd} , therefore, a modified K-K transform will be introduced. Equations and interpretations are mainly based on the following Refs. [136, 137]

As we discussed in the theoretical part, in the case of sample/vacuum reflection ($n_0 = 1$), the K-K relation is expressed as

$$\phi(\omega) = \frac{\omega}{\pi} \cdot P \int_0^{\infty} \frac{\ln(R(\omega_1))}{\omega_1^2 - \omega^2} d\omega_1 \quad (3.5)$$

Here, P corresponds to the principal value. The above relation is only valid, when $\ln(R(\omega_1))$ has no poles on the imaginary axis in the whole upper complex frequency plane. This condition is satisfied in case of measurements on the sample/air interface ($n_0 = 1$) since $R(\omega_1) \rightarrow 0$ only when $\omega \rightarrow \infty$. However, as for sample/diamond interface when $n_0 = 1$, at some point on the upper imaginary axis the relation $\hat{N} = n_0$ can be satisfied. Therefore, at these points $R(\omega_1) = 0$ and $\ln(R(\omega_1))$ has poles at $\omega = i\omega_\beta$, where ω_β is a real, positive and finite number.

As a result, the standard K-K relation in sample/diamond case must be modified to

$$\phi(\omega) = \frac{\omega}{\pi} \cdot P \int_0^{\infty} \frac{\ln(R(\omega_1))}{\omega_1^2 - \omega^2} d\omega_1 + \pi - 2 \arctan \frac{\omega_\beta}{\omega}. \quad (3.6)$$

Namely, the additional phase term $\pi - 2 \arctan \frac{\omega_\beta}{\omega}$ must be taken into account due to the presence of a transparent medium with $n_0 > 1$. We can also notice that the extra phase shift is a decreasing function of $\frac{\omega_\beta}{\omega}$. Thus when $\omega_\beta \rightarrow \infty$, namely $\arctan \frac{\omega_\beta}{\omega} \rightarrow \frac{\pi}{2}$, the extra phase term vanishes and the original K-K relation is recovered. In the case of actual experimental studies, however, the precise value of ω_β may not be known in advance. Accordingly, the value of ω_β has been estimated from experimentally measured data. The basic idea is to measure the complete spectra without pressure cell and get its optical conductivity via the usual K-K analysis. Then we measure the same sample in the cell at very low pressure so that the conductivity should be basically the same as for the free-standing sample. Then

we apply the modified K-K analysis and vary ω_β in order to get the best agreement with the optical conductivity spectra at ambient pressure. Once we find the proper ω_β we will use it for all higher pressures.

The detailed procedure of calculating the optical conductivity in diamond cell are shown in Fig.3.9. As an example, first of all the measured raw reflectivity spectra of κ -(BEDT-TTF)₂Cu₂(CN)₃ are modified by dividing the diamond background. As we can see in Fig.3.9 (a), there exist very strong multiphonon absorption bands of the diamond in the range 1700–2700 cm⁻¹, which make it very difficult to obtain reliable data in these energy region. In the perfect case, when the optical path are aligned very well, we still can get good data by dividing the diamond reference. Most of the time, we get random data even after correction of background. Therefore, usually the reflectivity in the diamond absorption range 1700–2700 cm⁻¹ was linearly interpolated. In Figure 3.9 (c) we shown the results of calculated optical conductivity by using modified K-K relation. The experimentally determined $\omega_\beta = 3000$ cm⁻¹ which is in best agreement with ambient data. We can see clearly that an alternative choose of ω_β , either smaller or larger than 3000 cm⁻¹, leads to a strong deviation from the spectra at ambient condition.

In general it is very difficult to obtain the absolute value of optical conductivity in the diamond cell. Therefore, we consider a scaling factor C that is determined with the experimentally measured optical conductivity [138]. The normalized optical conductivity should best satisfy our assumption $\sigma_1(\omega, p = 0.2 \text{ GPa}) = C \cdot \sigma_1(\omega, p = 0 \text{ GPa})$. Namely, we assume that the optical conductivity of the sample in the DAC at 0.2 GPa (our lowest pressure curve is very close to the optical conductivity of the sample at ambient pressure condition ($p = 0$ GPa)). The introduction of C serves to compensate the absence of absolute normalisation. Here C is assumed to be independent of pressure and temperature. Therefore, we kept constant C for all pressure and temperature curves. For the demonstration of the applied data analysis, a comparison of these two spectra is given in Figure 3.9 (d) for two different pressures ($p = 0$ GPa and $p = 0.2$ GPa); obviously, the agreement between the spectra is very good.

4. High-pressure infrared spectroscopy of α -(ET)₂I₃

In the following chapter, we will present the pressure-dependent optical spectroscopy results for α -(BEDT-TTF)₂I₃. In the background part we will briefly introduce the material and its literature. After that, the optical response of the massless Dirac electrons and their correlation effects will be presented. All the experimental results are summarized in the conclusion part with a schematic drawing of the density of state and corresponding optical conductivity. Most of the data and analysis shown in this chapter has been published in Ref. [139].

4.1. Background

The organic conductor α -(BEDT-TTF)₂I₃ is composed of alternatively conducting layers of BEDT-TTF (bis-(ethylenedithio)tetrathiafulvalene) molecules and insulating layers of tri-iodine anions (I₃⁻), as shown in Figure 4.1. Since the interlayer conductivity (*c*-axis) is 1000 times smaller than the one along the in-plane (*a*, *b*-axis), this compound can be well considered as quasi-two-dimensional system with quarter-filling, where the bulk electronic state can be described mostly by the contribution of the electron hopping in the *ab*-plane due to the BEDT-TTF molecular orbital overlap [140].

As we already described in the introduction part of this thesis, at ambient pressure, α -(BEDT-TTF)₂I₃ undergoes a transition from a metallic state to a CO state at 135 K. Under external pressure above 1.5 GPa the insulating state is suppressed and can be tuned to a zero-gap electronic state, and even superconductivity is reached

under uniaxial strain condition at low temperatures [50]. It was found that the high-pressure resistance is almost constant in the temperature range from 300 K to 2 K. Based on the results of magnetoresistance and Hall resistance measurements, the carrier density (n) and the mobility (μ) was estimated. It was shown that with decreasing temperature, the carrier density increases as $n \propto T^2$, while the mobility decreases as $\mu \propto T^{-2}$. Apparently the above mentioned behaviours cannot be explained as a simple metal or gapped insulator. Thus, Tajima *et al* has proposed that the band structure of α -(BEDT-TTF)₂I₃ under hydrostatic pressure can be well described using Dirac equation with linear dispersion $E_k = \hbar\nu_F k$ (ν_F is Fermi velocity) [141]. With this assumption, the calculated carrier density is exactly proportional to T^2 and conductance is estimated to be constant ($\sigma \propto e^2/\hbar$). Since the relation $\sigma = ne\mu$ holds, which leads to $\mu \propto T^{-2}$. Hence, all the experimental results are consistent with the theory of Dirac electrons.

The above findings were further supported by energy band calculations from Suzumura *et al.* [142–145]. Figure 4.1 (b) shows the band structure based on tight-binding model under uniaxial pressure. In the first Brillouin zone, the conduction band and valence band are accidentally degenerate at two general points. At the vicinity of the contact point, there exists Dirac cone-type linear band dispersion. Interestingly, the Dirac cone are strongly tilted with a large anisotropy in Fermi velocity. Thus, the energy of the electron- and hole-band at a given momentum k is not equal anymore, leading to the electron-hole asymmetry. It has been also pointed out that the existence of Dirac state is verified in a wide pressure range and the positions of contact points can be tuned upon pressure. These results are in contrast to the case of graphene, where isotropic Dirac cone emerges only at high symmetry points in k -space [104].

Despite the successful agreement between theory and experimental data, an assumption of non-interacting Dirac electronic state can not explain all the physical phenomena. For example, it has been pointed out by Tajima *et al.*, there was an anomalous upturn in resistance at very low temperatures [141]. The mechanism of this anomaly in resistance is still unclear. With the above experimental facts in mind, recently new transport measurements have been performed by Kanoda *et al.* in a wide pressure range [146]. They have found out strong evidences of the close relationship between the resistance anomaly and electron-electron interactions. In

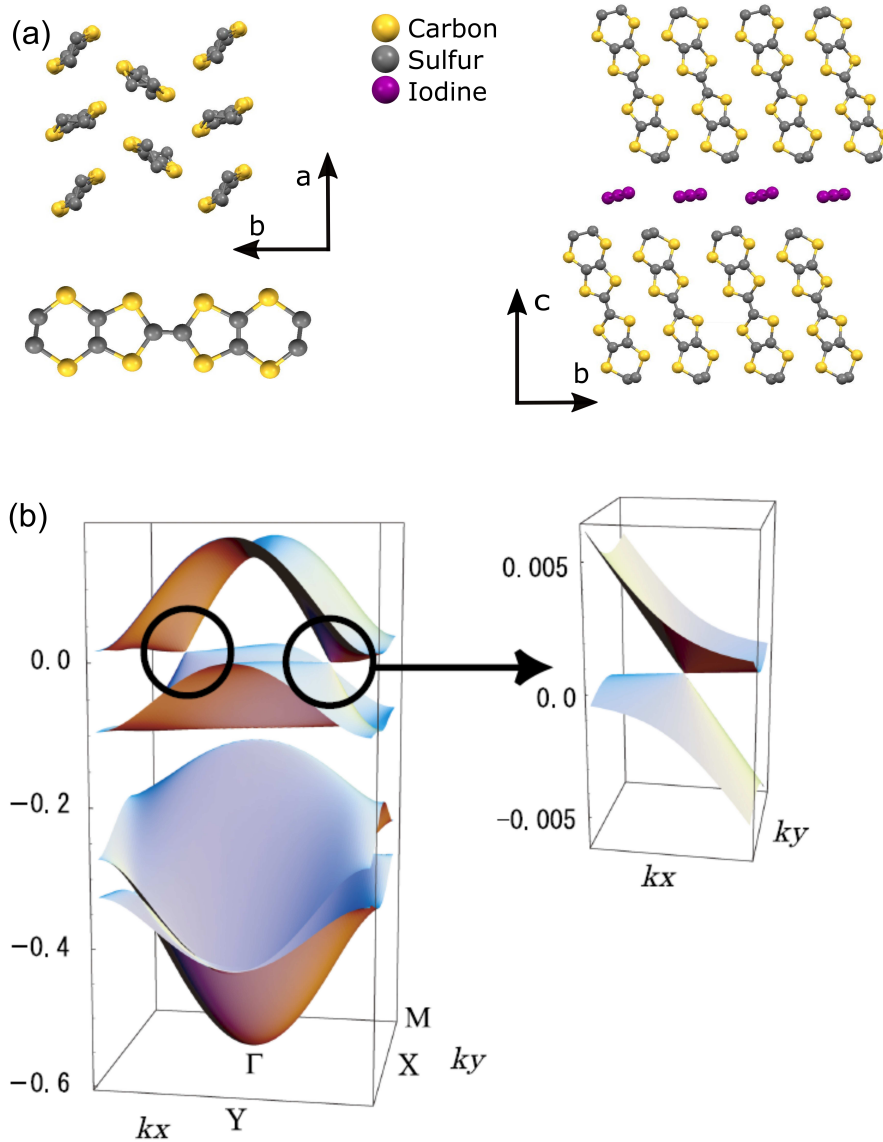


Figure 4.1.: (a) (left panel) BEDT-TTF (ET) molecule and ET conducting plane viewed from c -axis. (right panel) Crystal structure of out-of-plane viewed from a -axis. Tri-iodine anions (I_3^-) are sandwiched by ET molecules (b) Band dispersion of α -(BEDT-TTF)₂I₃ under uniaxial pressure along the a -axis, i.e., the stacking axis of the ET molecule, determined by tight-binding model. (left panel) In first Brillouin zone the hole and electron bands touch at two contact points (denoted by black circle). (right panel) Enlarged Dirac cone with a linear dispersion around one contact point. Due to the quarter-filling in α -phase, the Fermi energy is exactly located at the contact point. Panel (b) is adapted from Rev. [145]

their experiments it was shown that the charge ordering get completely suppressed above 1.1 GPa, and a new phase was uncovered as the pressure is increased further. As shown in Figure 4.2 this new phase was characterized as massive Dirac fermion (MDF), which is enhanced at the boundary of the critical CO-MDF transition region and persisted up to 4 GPa. Thus, the low-temperature anomaly of resistance was claimed to be resulted from those massless Dirac electron correlations.

Apart from the transport properties of the interacting Dirac electrons, detailed information of the low-energy dynamic properties around the Dirac cone have been explored by NMR measurements [148]. Combined with theoretical efforts their experimental results has revealed that the Fermi velocity is strongly renormalized and thus the shape of the titled Dirac cone is modified, which is a result of both long-range and short-range parts of the Coulomb repulsions. These unscreened Coulomb correlations not only give rise to a strong bandwidth reduction, but also lead to a gap opening near the Dirac point, driving the massless Dirac electrons to be massive-like. The correlation induced mass generation results in an unexpected increase of both NMR relaxation rate and Korringa ratio, which was recently verified by NMR measurement and renormalization group simulations [149].

Pressure-dependent optical measurements has been performed by Beyer *et al.*, to clarify the pressure evolution of the electronic structure across the CO-MDF transition [147]. It was found that the optical gap of the CO decreases in a linear manner under pressure, while no metallic state appears up to the highest accessible pressure, i.e., ~ 1 GPa. Hence, an extension of the optical studies under much higher pressure is necessary to learn more about the Dirac physics in α -(BEDT-TTF)₂I₃.

4.2. Room temperature reflectivity and optical conductivity

High quality single crystals of α -(BEDT-TTF)₂I₃ were prepared by conventional electrochemical oxidization method as described elsewhere [140]. In our high pressure infrared spectroscopy experiments, we have utilized α -(BEDT-TTF)₂I₃ single crystals with the typical size of $300 \mu\text{m} \times 300 \mu\text{m} \times 60 \mu\text{m}$. To ensure the reliability of our measured data and self-consistency of the data analysis, two pieces of flat,

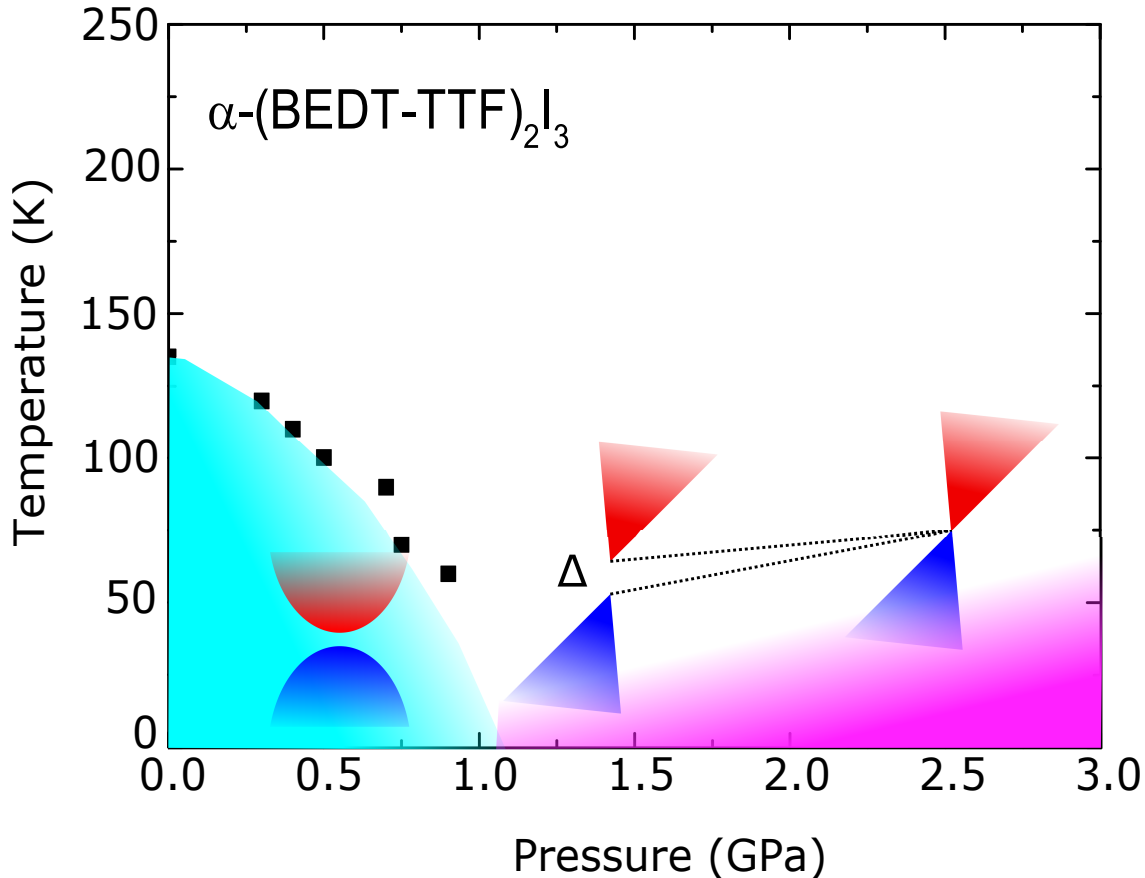


Figure 4.2.: Tentative phase diagram of α -(BEDT-TTF) $_2$ I $_3$. At ambient pressure charge-ordered state has been observed with a large gap opening below 135 K. Charge ordering is gradually suppressed with increasing pressure. Black squares denote the charge ordering transition temperatures, taken from [147]. Massless Dirac state with linear band dispersion is observed at high pressure regime, while the correlated massive Dirac electrons can be identified at the boundary between charge ordered state and Dirac state based on transport, NMR measurements [146, 148, 149]. Red areas correspond to the unoccupied hole-bands, while blue areas denote occupied electron-bands.

high-quality crystals, cut from the same big piece, were used for the far-infrared and the middle-infrared measurements. $E \parallel ab$ -plane measurement configuration has been chosen and measurements have been performed with unpolarized light. Samples were placed inside a type-IIa diamond anvil cell (DAC) [150] with a cutlet diameter of 900 μm with ruby spheres as the high pressure manometers. Detailed description of the preparation of DAC cell have been shown in the setup section.

The measured pressure range extends up to ~ 4.0 GPa. Despite the bad metallicity in this system, the reflectivity shows a clear upturn in the low frequency regime. Therefore, in the low energy range, Hagen-Rubens extrapolation has been chosen. For the high energy range, a flat conductivity followed by ω^{-4} free carrier approximation have been utilized. Detailed procedures about the extraction of optical conductivity can be seen in the setup section.

Figure 4.3 shows the room-temperature reflectivity and optical conductivity spectra of α -(BEDT-TTF)₂I₃ for various pressures. As can be seen in Figure 4.3 (b), the overall shape and the absolute value of $\sigma_1(\omega)$ measured at lowest pressure is very similar to previous results recorded under ambient conditions [147, 151], indicating the high quality and reproducibility of our experiments. Already at ambient temperature, the optical properties strongly depend on the applied external pressure as shown in Figure 4.3 (a). In general, upon pressurizing the absolute value of the reflectivity get enhanced in the whole energy range. More significant changes of reflectivity are observed in the far-infrared range, while less changes can be seen above 3000 cm^{-1} . Correspondingly, below 1000 cm^{-1} , $\sigma_1(\omega)$ becomes enhanced by pressure with a progressive change from a broad to a narrower Drude behaviour above 0.8 GPa, suggesting a bad metal- to good-metal transition, i.e. from incoherent to more coherent transport. The mid-infrared band persists up to pressure as high as 4.0 GPa with a gradual suppression in intensity. The enhancement of the low-frequency $\sigma_1(\omega)$ is in line with our p -dependent dc-resistivity measurements [147] and recent results from Kanoda's group[146], where resistivity decreases with increasing pressure at high temperatures. Thus our optical results clearly suggests that even at room temperature the electronic state significantly changes with applied pressure.

The spectrum at $p = 0.3$ GPa consists of a strong mid-infrared absorption band around 3000 cm^{-1} and an overdamped Drude contribution. Due to the complex structure of this material in addition to the electronic excitations, many small vibration modes are expected [53, 54] between 400 and 1300 cm^{-1} , originating from the electron-molecular vibrational-coupled totally symmetric A_g modes [88]. We can consistently resolve the ones with strong enough contributions. Especially three of these vibration modes are quite large and contribute to the spectra significantly,

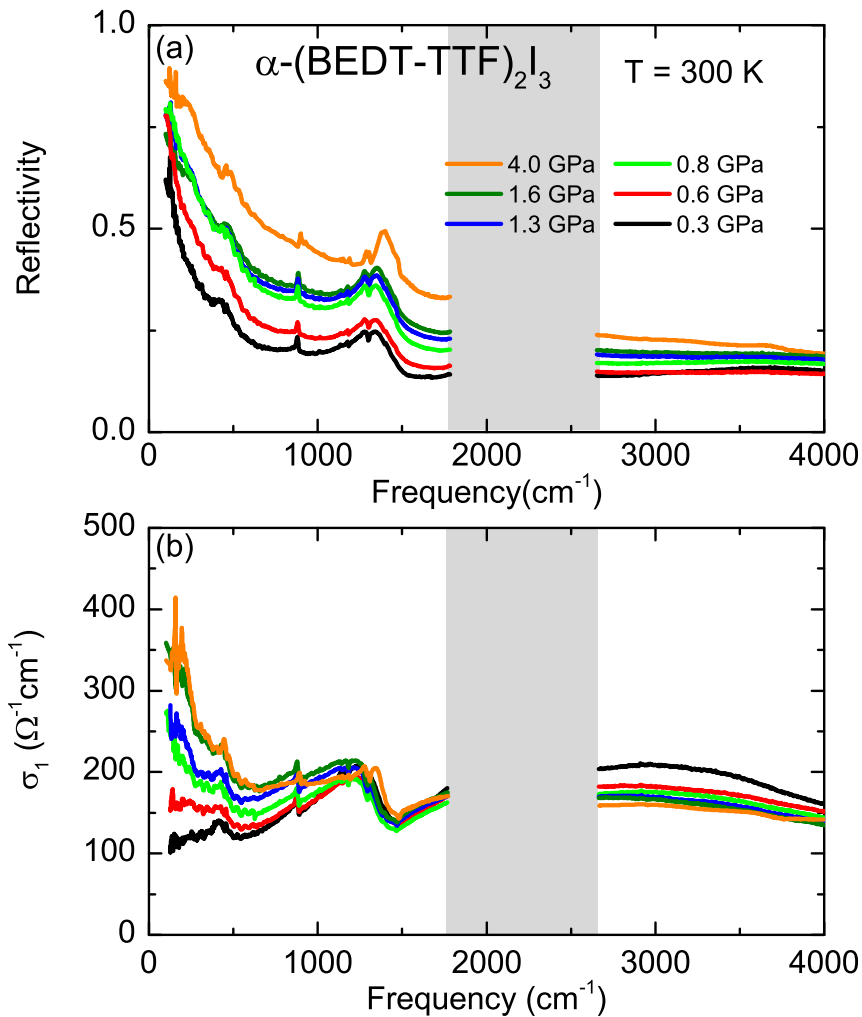


Figure 4.3.: (a) Pressure-dependent reflectivity spectra of α -(BEDT-TTF) $_2$ I $_3$ at room temperature. (b) Pressure evolution of the corresponding optical conductivity obtained by a Kramers-Kronig analysis from the data of (a). A narrow Drude-like component gradually develops in the low energy range during the compression in DAC, indicating the incoherent-coherent metal transition. No apparent structural transition is observed from our vibrational spectroscopy. Grey shaded area indicates the spectral region, where the diamond multi-phonon absorptions due to the pressure cell are dominated.

namely, ν_3 , ν_7 , and ν_9 modes. The energy range of the determined vibration modes are fit well with the literature [53, 54]. Furthermore, we didn't observe any splitting of the above modes with a frequency resolution of 2 cm^{-1} over the whole pressure range, indicating no structure transition under high pressures. This conclusion is consistent with the X-ray measurement at high-pressure as well, showing no symmetry breaking up to 1.8 GPa [152].

In Figure 4.4 (a), we demonstrated the overall fit of our 0.3 GPa spectrum and the measured one at room temperature. Since these vibrational modes obscure the electronic background, we fitted our conductivity spectra by a Drude component for the low energy free carrier contribution, a Lorentz component for the high energy mid-infrared absorption, and Fano terms for the vibration modes; an example is given in Figure 4.4 (b). The Fano-shaped vibration modes have been well established in this molecular compound as well as other counterparts [53]. It is reasonable to observe a very broad ν_3 mode with linewidth around 500 cm^{-1} , because the ET molecules in α -phase are weakly dimerized. Therefore, such fitting procedure is justified. For the further analysis vibration modes have been subtracted as plotted in Figure 4.4 (b), where the spectrum without the vibration modes is given with the individual contributions: Drude (blue), high energy Lorentz (green).

To quantitatively characterize the charge dynamics under pressure, the spectral weight of the zero-frequency and mid-infrared bands is plotted in Figure 4.4(c). With increasing pressure the spectral weight systematically transfers from high energies to the Drude component; this trend seems to saturate above $p \approx 2 \text{ GPa}$. The energy range that the spectral weight transfer is observed is comparable to the on-site Coulomb repulsion $U \approx 0.4 \text{ eV}$ [142]; this is reminiscent of the behaviour observed in the bandwidth-controlled metal-insulator transition in Mott insulators [87] and also occurs in other charge-ordered organic compounds [65, 88]. The mid-infrared excitation arising from transitions between the bands split by electronic correlations; the enhancement of the Drude-like response corresponds to the overlap of the two bands that increases with pressure [153]. Hence our room-temperature optical studies provide strong evidence that electronic correlations play an important role in α -(BEDT-TTF) $_2$ I $_3$. This conclusion is supported by recent dc transport [146] and NMR measurements [148, 149]. The band structure of Dirac

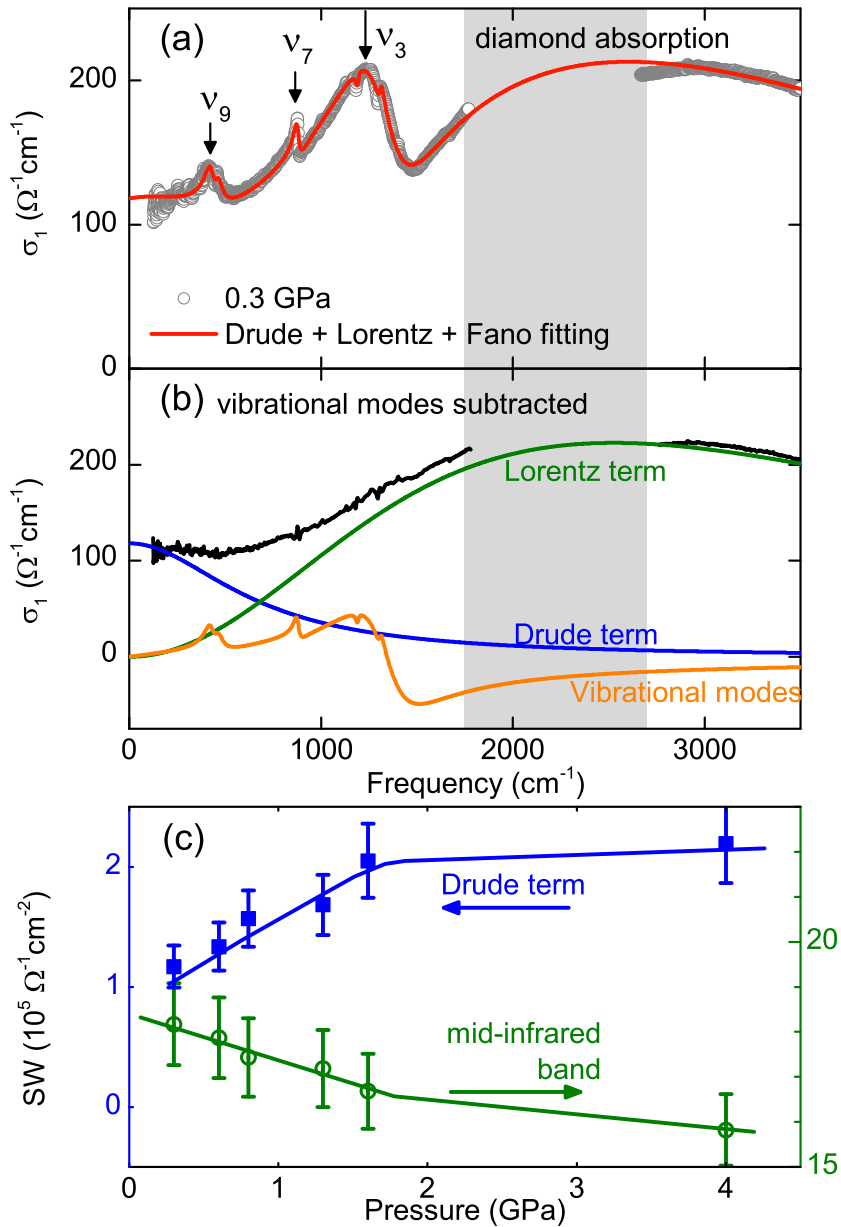


Figure 4.4.: Optical conductivity fitting. (a) Experimental optical conductivity and the Drude (low energy incoherent carrier contribution) + Lorentz (high energy excitations) + Fano modes (vibrational features) fitting at 0.3 GPa as example. Three main vibration modes (ν_3 , ν_7 , and ν_9) are labelled consistently with the literature. (b) Optical conductivity spectra after the vibrational features (ochre) are subtracted is given with the different contributions. (c) Pressure dependence of the spectral weight (SW) for Drude and Lorentz components at $T = 300\text{ K}$; the blue squares (Drude) stands for the left axis, the open green dots (Lorentz) correspond to the right axis.

electrons in α -(BEDT-TTF)₂I₃ has been described by many distinct theoretical approaches: in the early time Dirac cone has been predicted by tight-binding and first principle calculations under uniaxial pressure; later on it was argued that conventional tight-binding band calculation failed to realize Dirac cone at hydrostatic pressure conditions without introduction of site potentials; more recently, based on first-principle DFT, it was shown that anion-donor interaction can stabilize a zero gap state with a tilted Dirac-cone-type linear dispersion. However, our findings are clearly consistent with conclusions based on the extended Hubbard model, which considers on-site and inter-site Coulomb repulsion [142–144].

4.3. *T*- and *p*-dependent reflectivity and optical conductivity

The temperature-dependent conductivity spectra without the vibration modes are displayed in Figure 4.5 at various pressures. Previously we showed [147] that the low-pressure regime (0-0.8 GPa at 8 K) is characterized as a charge-ordered ground state at low temperatures. As depicted in Figure 4.6 (a), at ambient pressure, at 150 K just above the CO transition temperature, the absolute value of the reflectivity increases steeply with decreasing frequency in the low energy range, a typical semi-metallic behaviour. Below the CO temperature (T_{CO}) the behaviour changes to the insulating one with a sudden drop of the reflectivity at the low energy range and the vibration modes become sharper. The calculated $\sigma_1(\omega)$ can describe this first order transition very well: The non-zero but relatively small SW below 400 cm⁻¹ at 150 K is suppressed when the first order transition is reached at T_{CO} with a clear gap opening (marked with green arrow in Figure 4.6 (a)).

As can be seen from Figure 4.5 (a-d), on the other hand, the temperature evolutions of $\sigma_1(\omega)$ at pressures above 0.8 GPa are qualitatively different. Taking the conductivity at 0.8 GPa (Figure 4.5 (a)), for instance, α -(BEDT-TTF)₂I₃ exhibits metallic behaviour with a characteristic spectral weight transfer towards low energies as *T* decreases, and a Drude-like response below 500 cm⁻¹. The energy range of this transfer (~ 0.5 eV) suggests strong modifications of the trivial bands (non-

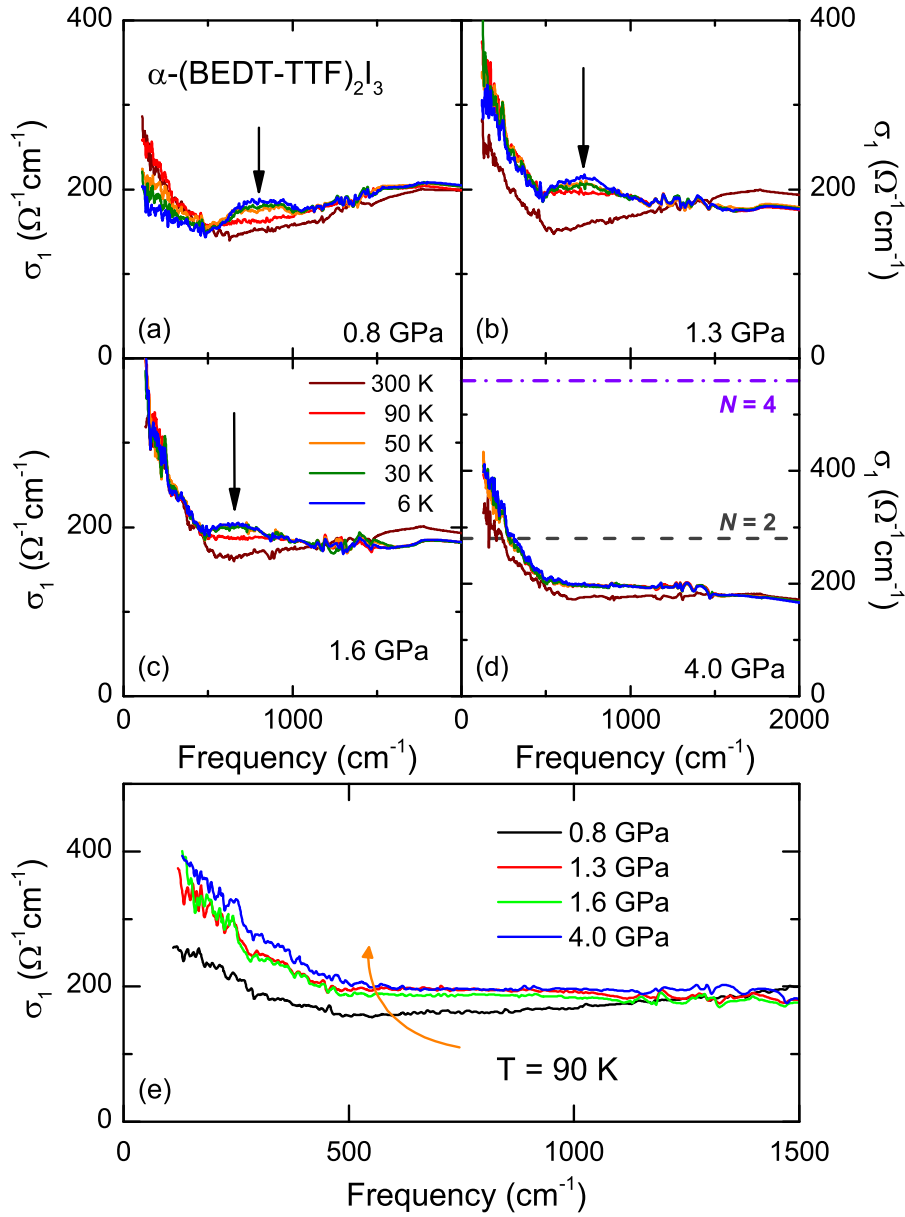


Figure 4.5.: Temperature and pressure dependent optical conductivity. (a-d) Temperature-dependent optical conductivity at $p=0.8, 1.3, 1.6,$ and 4.0 GPa. The black arrows mark the absorption feature due to excitations across an energy gap. In panel (d) the bulk conductance corresponding to $G(\omega)/c$ for $N = 2$ and 4 is indicated by dashed gray and dash-dotted purple lines, respectively, where $c \approx 1.7$ nm is the c -axis lattice constant [140, 152]. (e) $\sigma_1(\omega, T = 90$ K) for various pressures; between $p = 0.8$ and 1.3 GPa $\sigma_1(\omega)$ becomes frequency independent above 500 cm^{-1} .

Dirac bands, possibly possess parabolic dispersion) upon pressure. This metallic behaviour persists up to the maximum pressure measured (4.0 GPa), indicating that the ground state above $p \approx 0.8$ GPa is distinct from the charge-ordered state; obviously we have entered a phase where Dirac electrons exist; in accord with previous dc transport measurements [146].

A close inspection of $\sigma_1(\omega, T)$ at $p = 0.8$ GPa reveals a gradual transition at low temperatures. In Figure 4.6 we make a direct comparison of the optical spectra between at ambient pressure and at 0.8 GPa. As for the 0.8 GPa spectra, disappearance of the sharp drop of the optical conductivity suggest that the charge ordering is not the case for this pressure, while the lack of ω -independent optical conductivity indicate that the system is not in the Dirac regime, either. The existence of the significantly large vibration mode at around 1300 cm^{-1} compared to the higher pressure range further support that this pressure is somewhat very close to the crossover regime between the insulator and Dirac metallic state.

As shown in Figure 4.5 (a), the low-frequency conductivity is suppressed for $T < 90$ K, and a pronounced peak emerges at around 800 cm^{-1} that we assign to excitations across an energy gap and defined as a "pseudogap" opening. With increasing pressure, this peak-like structure shifts to lower energies and gets gradually suppressed. We can unambiguously trace the gap feature up to $p = 1.6$ GPa; but at 4.0 GPa we cannot resolve the band anymore within the accessible temperature and energy range. Thus, we conclude that the gap-like feature is completely suppressed and/or shift to the very far-infrared range below 100 cm^{-1} .

We would like to emphasize that the low-energy suppression of the optical conductivity and a concomitant high energy peak-like structure is already visible in the as measured spectra, as well, which is different and well separated from the vibration modes. In Figure 4.7, we plot the as-measured frequency-dependent reflectivity (a-d) and the calculated optical conductivity spectra (e-h) as a function of temperature for various pressure. With lowering temperature, one can see a clear suppression of the low energy reflectivity below a certain temperature, while a clear bending of the spectra is also marked with arrows. This behaviour is reflected in the corresponding optical conductivity spectra, as well (Figure 4.7 (b)) as described above. The arrow

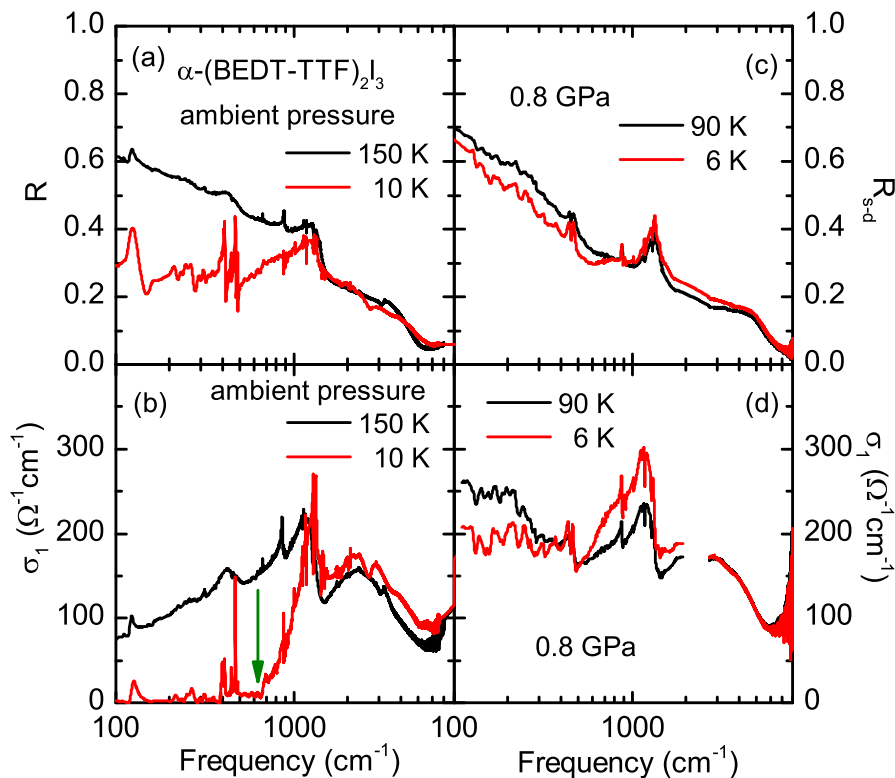


Figure 4.6.: Reflectivity (a,c) and optical conductivity (b,d) of α -(BEDT-TTF) $_2$ I $_3$ at ambient pressure (left) and 0.8 GPa (right). The ambient-pressure $\sigma_1(\omega)$ above and below the metal-insulator transition T_{CO} clearly shows the opening of the charge-order gap (green arrow). Redraw from Ref. [53].

marks the peak-like structure in the presence of the vibration modes, a clear slope change below 90 K is well defined. This absorption feature will be discussed later in terms of excitonic gap due to electron-electron correlations in Dirac metal.

In Figure 4.8 (a) and (b), we further demonstrate that this additional absorption band due to pseudogap is not an artefact of our fitting procedure and is not caused by the vibration modes. At 90 K, we can reproduce the optical conductivity very well with the above mentioned contributions, namely, a Drude, mid-infrared Lorentz, and Fano-shaped vibration modes. With cooling down, as expected, vibration modes are getting sharper. On the other hand, the small absorption feature (marked with *) cannot be reproduced with taking into account only the vibration modes. We plotted the best fits in Figure 4.8 (b) w/ (red curve) and w/o (blue

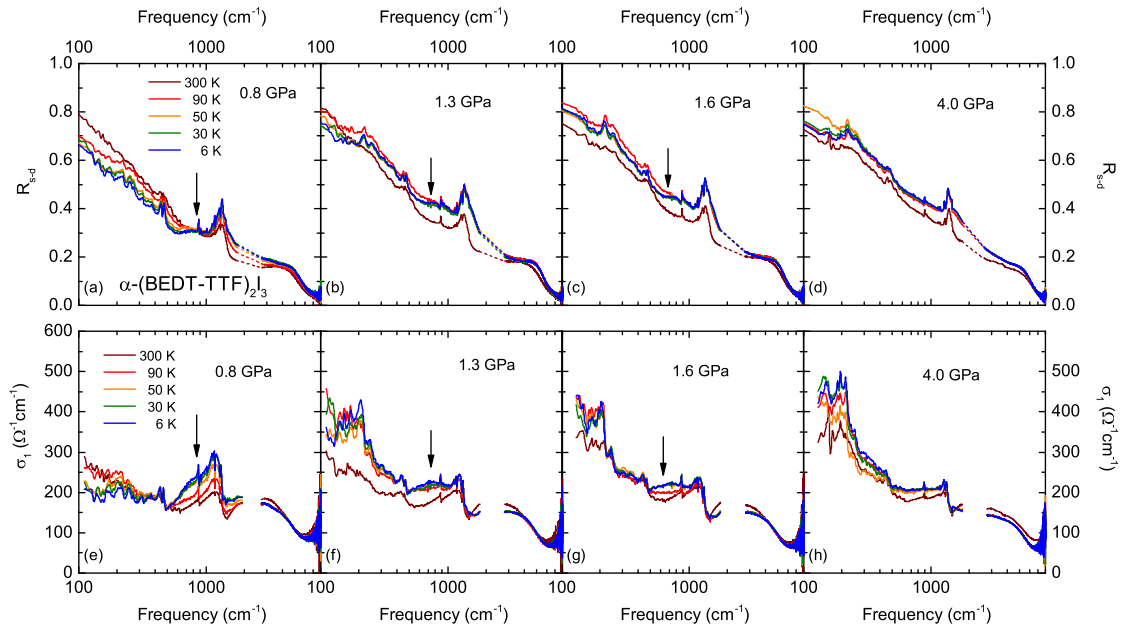


Figure 4.7.: (a-d) Temperature- and pressure-dependent reflectivity. A systematic decrease of the reflectivity with lowering temperature is visible below the energy range marked with the arrow. A linear extrapolation have been used in the multiphonon diamond absorption region shown with dashed curves. (a-d) Optical conductivity spectra of α -(BEDT-TTF) $_2$ I $_3$ calculated with Kramers-kronig analysis from the reflectivity spectra in (a). The suppression of the low energy optical conductivity and appearance of a peak-like structure (shown with an arrow) indicates the low energy to high energy spectral weight transfer due to pseudogap opening. When cooling down from 300 K to 90 K, there is spectral weight transfer from mid-infrared to far-infrared region, indicating a typical metallic behaviour.

curve) this feature for a comparison. This mode is very broad to be an additional vibration mode, also have not been reported before.

Our discovery of a metallic ground state with a gap feature is in line with the anomalous upturn observed by pressure-dependent transport behaviour [146]. Here we can further discuss about the energy range of the observed pseudogap feature. A similar behaviour is observed in density-wave systems with an only partially-gapped Fermi surface due to the nesting[154], or Mott insulators with metallic carriers remaining [39, 86], or a peak structure, resulted from the transitions between the Van Hove singularities at the saddle points of the conduction and valence bands, which

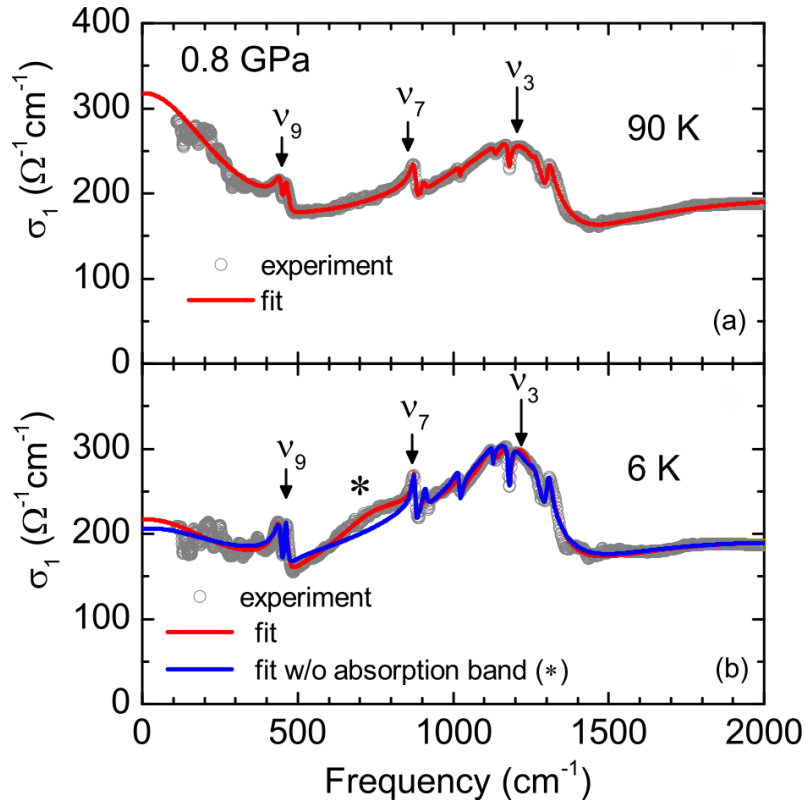


Figure 4.8.: Fitting procedure of the low temperature spectra at the high pressure regime (0.8 GPa as an example). (a) 90 K spectra can be reproduced very well with a Drude + Lorentz + Fano fitting as described in Figure 4.4. (b) Upon cooling a peak-like structure starts to evolve at the frequency range 500 - 1000 cm^{-1} . The best fitting attempt with only Drude+Lorentz+Fano components described previously is given as the blue curve. As one can see, the absorption feature needs to be taken into account for a good fitting (given with a red curve).

was discussed by Ohki *et al.* [155]; hence we have to discuss the origin of the peak structure and in-gap absorption in more detail.

4.4. Optical response of massless and massive Dirac electron

Two-dimensional massless Dirac electrons manifest themselves in a frequency-independent conductivity; the interband conductivity per layer should be a universal constant

$G(\omega) = N\pi G_0/4$, with N the number of non-degenerate Dirac cones and $G_0 = 2e^2/\hbar$ is the quantum conductance. Such peculiar $\sigma_1(\omega)$ behaviour has been discussed theoretically and experimentally, for instance, in monolayer graphene [156] and quasi-two-dimensional graphite [106].

As displayed in Figure 4.5 (f) $\sigma_1(\omega)$ becomes constant between 400 and 1200 cm^{-1} as pressure increases from 0.8 to 1.3 GPa and then remains unchanged. The flat conductivity observed in this large spectral range is taken as strong evidence for massless Dirac fermions; the observed value is quite close to the predicted conductance for $N = 2$ (Figure 4.5 (d)). We also notice that the value of the conductivity does not exactly agree with the expected universal constant for Dirac electrons. According to the pressure dependent transport measurements performed by Tajima's and Kanoda's group, the value of the sheet resistance is either higher or lower than theoretical predicted value with a factor of 2-5 [141, 146]. From these measurements they can not really determine the number of Dirac cones in this material. That is because of the disadvantage of the dc measurement, as it depends highly on the geometry of the sample and detects both the massless Dirac and massive electrons at the zero energy limit. The slight difference of the absolute values between theory and experiment, which has also been discovered and discussed in graphite and other 2D Dirac materials, may be due to the effect of strong interlayer coupling [106]. This point was supported by recent interlayer transport measurements. It was shown that the interlayer resistance also exhibits metallic behaviour under hydrostatic pressures above 1.2 GPa [157]. Additionally, in a theoretical study of uniaxial pressure [158], it was recently predicted that the three quarter of the bands possess linear dispersion; further experiments have to show whether this is of relevance for the optical conductivity. Nevertheless, the pressure-independence of the flat conductivity gives strong evidence that it is a universal quantum resistance arising from the interband transition of the Dirac electrons. Besides that our optical measurements give strong evidence that the Dirac cone is formed at low temperature range rather at room temperature. This point has never been discussed by other measurements.

In comparison to the case of graphite (1000 cm^{-1} to 5000 cm^{-1} and graphene, the energy region of the ω -independent conductivity is observed in a relatively narrow

range (400 cm^{-1} to 1200 cm^{-1}). It is quite reasonable to have a comparatively limited region, because the transfer integral is ten times lower than that in graphite [106]. In addition, as we discussed at the beginning, since there are existing strong correlation in this system, Hubbard band is expected at higher energy range. As a result, our observation is in agreement with theory [143] and NMR experiments [148, 149].

With the modifications of the trivial bands and the existence of the Dirac state it is rather challenging to analyze the low-energy behaviour of $\sigma_1(\omega)$. Since the Drude component below 300 cm^{-1} does not show a significant T -dependence above 1.3 GPa , we suggest two contributions: (i) the correlated massive electrons and (ii) the thermally excited massless Dirac electrons. The former contribution should become stronger as the temperature decreases. For a pure Dirac system with the chemical potential located exactly at the contact point, the spectral weight of the intraband response should decrease upon cooling [106]. Magnetotransport and optical measurements [147, 159, 160] indicate the coexistence of massive and Dirac carriers. This coexistence can also explain the deviations from the universal quantum resistance observed in $\rho(T)$ between 300 and 10 K [141, 146, 147]. The tilting of the Dirac cones present in α -(BEDT-TTF) $_2$ I $_3$ [148, 149] leads to a strong anisotropy of the Fermi velocity and modifies the interband transitions of the Dirac electrons. A systematic studies of optical response of massless Dirac electrons in organic conductors as a function of tilting and doping has been conducted by Suzumura *et al.* [161] as shown in Figure 4.9. It was found that the asymptotic value of $\sigma_1(\omega)$ for $\omega \rightarrow \infty$ is independent of tilting (η) and polarization (α). Slightly different conclusion was drawn by another group [162]. It was predicted that the limiting value of $\sigma_1(\omega)$ depends actually on polarization (α), but the product of these two conductivities is universal, i.e., $\sigma_N^{\pi/2} \cdot \sigma_N^0 = [\pi^2/8]^2$. On the other hand, the tilting has strong influence on the intraband excitation, which displays a local maximum at low frequencies depending on the degrees of tilting. In accord with the theoretical prediction for α -(BEDT-TTF) $_2$ I $_3$ [161], we expect a visible effect of tilting only in the THz optical response (around 20 cm^{-1} as shown in Figure 4.9, and not at higher energies where we observe $\sigma_1(\omega) = \text{const.}$

Our optical results not only provide strong evidence of interacting Dirac fermions,

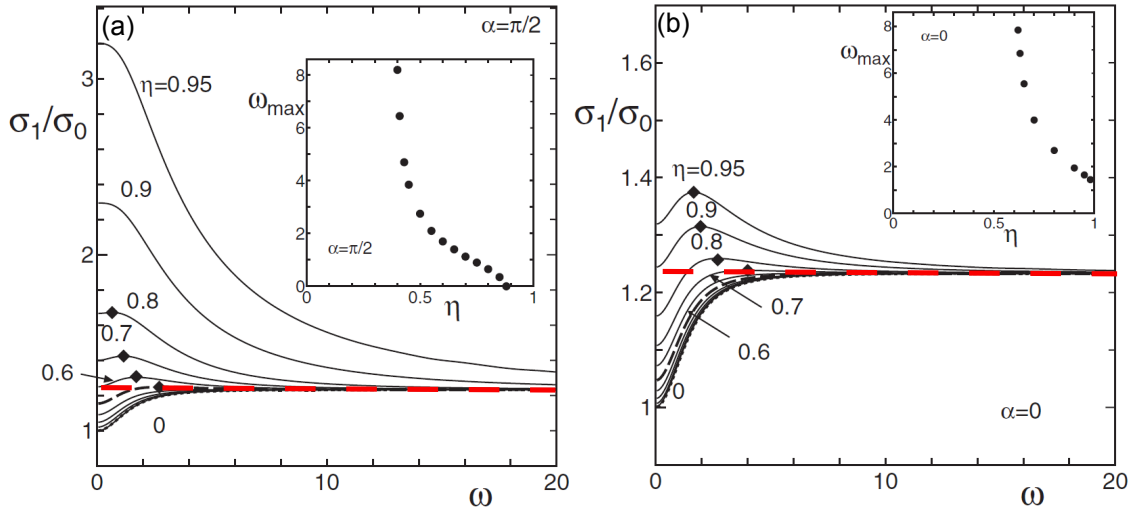


Figure 4.9.: Normalized optical conductivity $\sigma_N = \sigma_1/\sigma_0$ as a function of tilting for two polarizations, i.e., $\alpha = \pi/2$ (a) and $\alpha = 0$ (b). The red dashed line denotes the limiting value of $\sigma_N = \pi^2/8$ at very high energy. η denotes the parameter for the degree of tilting, ranging from 0 (isotropic) to 1 (90 tilted). The α corresponds to the angle between the external electric field and the tilting direction. Here $\sigma_0 = e^2/(8\pi\hbar)$. The tilting induced local maximum in σ_N is denoted by diamond. The frequency ω_{\max} , where σ_N reaches maximum is plotted as a function of tilting in the inset. After [161].

but give insight into the actual density of electronic states. For a better illustration, in Figure 4.10 (a) we plot the difference of the conductivity between $T = 6$ and 90 K. The opening of a pseudogap is well identified as peaks in $\Delta\sigma_1(\omega)$ and indicated by arrows. From a proposed density of states as displayed in the inset for the different pressure values, a fit to the difference of the optical conductivity (solid lines) can be obtained. In our model we simply assume the one-dimensional optical joint density of states to be proportional to $\epsilon_2 = 4\pi\sigma_1(\omega)/\omega$ and neglect the effect of the matrix elements [82]. At low temperatures ($T = 6$ K) a pronounced pseudogap is present with a significant reduction of the density of states. The spectral weight missing below the gap is recovered at higher energies, which manifest itself with a spectral weight transfer from low to high energies resulting an absorption peak in the optical spectra. We defined the energy of this peak structure as 2Δ (shown with arrows in Figure 4.5 and 4.10 (a)), and for the pseudogap we obtain $\Delta = 410, 350,$ and 310 cm^{-1} at $p = 0.8, 1.3,$ and 1.6 GPa respectively; and it seemed to

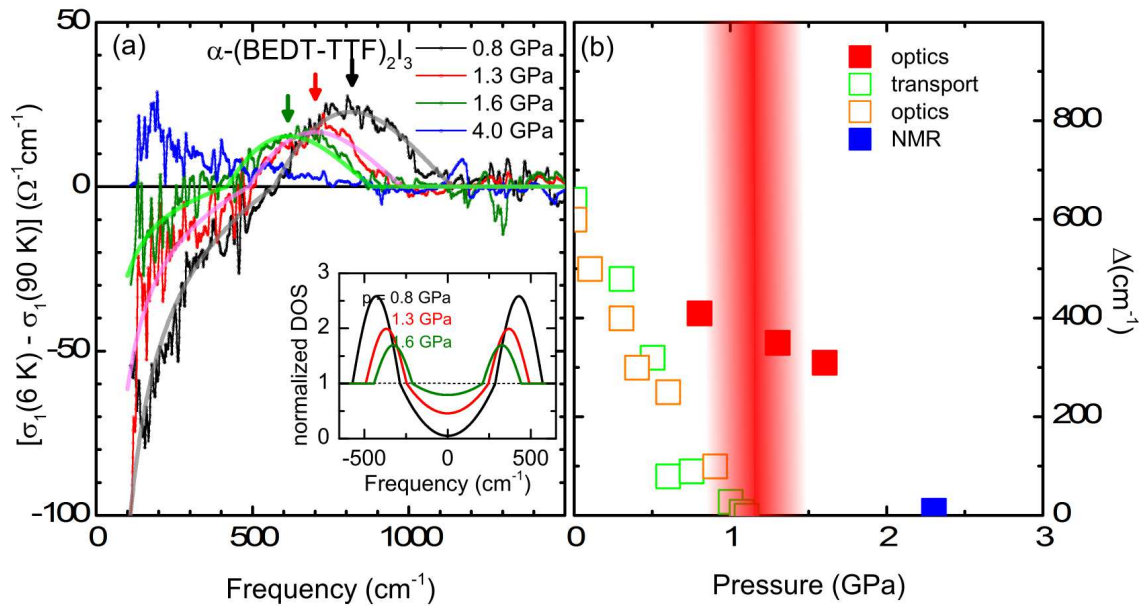


Figure 4.10.: (a) Pressure-dependent difference spectra demonstrating the pseudogap behaviour. Pressure dependence of the changes in the optical conductivity between $T = 90$ and 6 K. The peak structure indicated by the arrows shifts toward lower energies and diminishes as pressure increases. The solid lines correspond to $\Delta\sigma_1(\omega)$ calculated from the electronic density of states shown in the inset. The pseudogap closes by pressure and is completely absent at $p = 4$ GPa. (b) Pressure-dependence of CO gap and pseudogap. Ochre open square stands for optical gap determined from the optical studies. Lime open square corresponds to activation gap obtained from transport measurements. CO gap decreases with increasing pressure and completely vanishes around 1 GPa. Red and blue filled square corresponds to the pseudogap measured from our optical experiments and NMR spectroscopy, respectively. Red area denotes the critical region, where CO state is completely suppressed and a gapped state with massive Dirac electrons appears.

be completely suppressed at 4.0 GPa. As can be seen from the fits in Figure 4.10, with rising pressure, an assumption of the decrease of Δ and suppression of the pseudogap by gradual filling in states from above can reproduce the experimental finding satisfactorily.

To further clarify the physical origin of the pseudogap, we plot the pressure-dependence of the charge-ordered (CO) gap and pseudogap. With rising pressure, the CO gap seemed to be completely suppressed above 1 GPa as confirmed by two groups.

However, the pseudogap is enhanced in the vicinity of the charge order transition and decreases gradually as the pressure is increased. Since the symmetry of the lattice is preserved over the whole pressure ranges as confirmed by X-ray [152] and our vibrational spectroscopy, a sudden change in the Fermi surface can be ruled out. As shown by theoretical calculations, the Fermi surface of α -(BEDT-TTF)₂I₃ is composed of electron and hole pockets, in distinct contrast to the open planar sheets found in CDW candidate α -(BEDT-TTF)₂ K₂Hg(SCN)₄ [163]. Thus, our results not favour the nesting-driven density wave scenario. Although the peak structure due to the Van Hove singularity displays similar sharp changes around the critical phase region [155], the pressure-dependence of the peak is in opposite to our findings. Since the number of Dirac cone was proved to be one from our measurements, the Van Hove singularity would not exist in the density of state. In addition, in many Weyl semimetals it was found that the optical response of Van Hove singularity typically has no temperature dependence [164]. Hence, we will describe the above critical behaviour in the framework of correlation effect, which was indeed predicted and well described by theory.

We compare these findings quantitatively to the excitonic gap values estimated by Khveshchenko [165] using:

$$\Delta = v_F \hbar \Lambda \exp[(-2\pi + 4 \arctan \sqrt{2\tilde{\alpha} - 1})/(\sqrt{2\tilde{\alpha} - 1})]/k_B \quad , \quad (4.1)$$

where $\tilde{\alpha} = \alpha/(1 + N\pi\alpha/8\sqrt{2})$, and $\Lambda = 0.667 \text{ \AA}^{-1}$ is a momentum cutoff at the inverse lattice constant [152]. ϵ_∞ can be defined as the contribution of the higher energy optical transitions to ϵ_1 (real part of the permittivity), which one can directly obtain from our optical conductivity as $\epsilon_1(\omega) = 1 - 4\pi\sigma_2(\omega)/\omega$. The real $\sigma_1(\omega)$ and imaginary $\sigma_2(\omega)$ part of the optical conductivity can be calculated from the measured reflectivity via Kramers-Kronig analysis. The obtained temperature- and pressure-dependent $\epsilon_1(\omega)$ are given in Figure 4.11. The value of $\epsilon_1(\omega)$ at the high energy limit is ≈ 4 , which can be taken as ϵ_∞ . The temperature-independent optical conductivity at high energy range suggests this value does not change with temperature as well as shown in Figure.4.11 (a-d). As depicted in Figure 4.11 (e), the signature of pseudogap can be clearly identified already in the raw spectra of $\epsilon_1(\omega)$. The pseudogap give rise to a peak structure in $\epsilon_1(\omega)$ and are well separated from the strong vibration modes ν_3 .

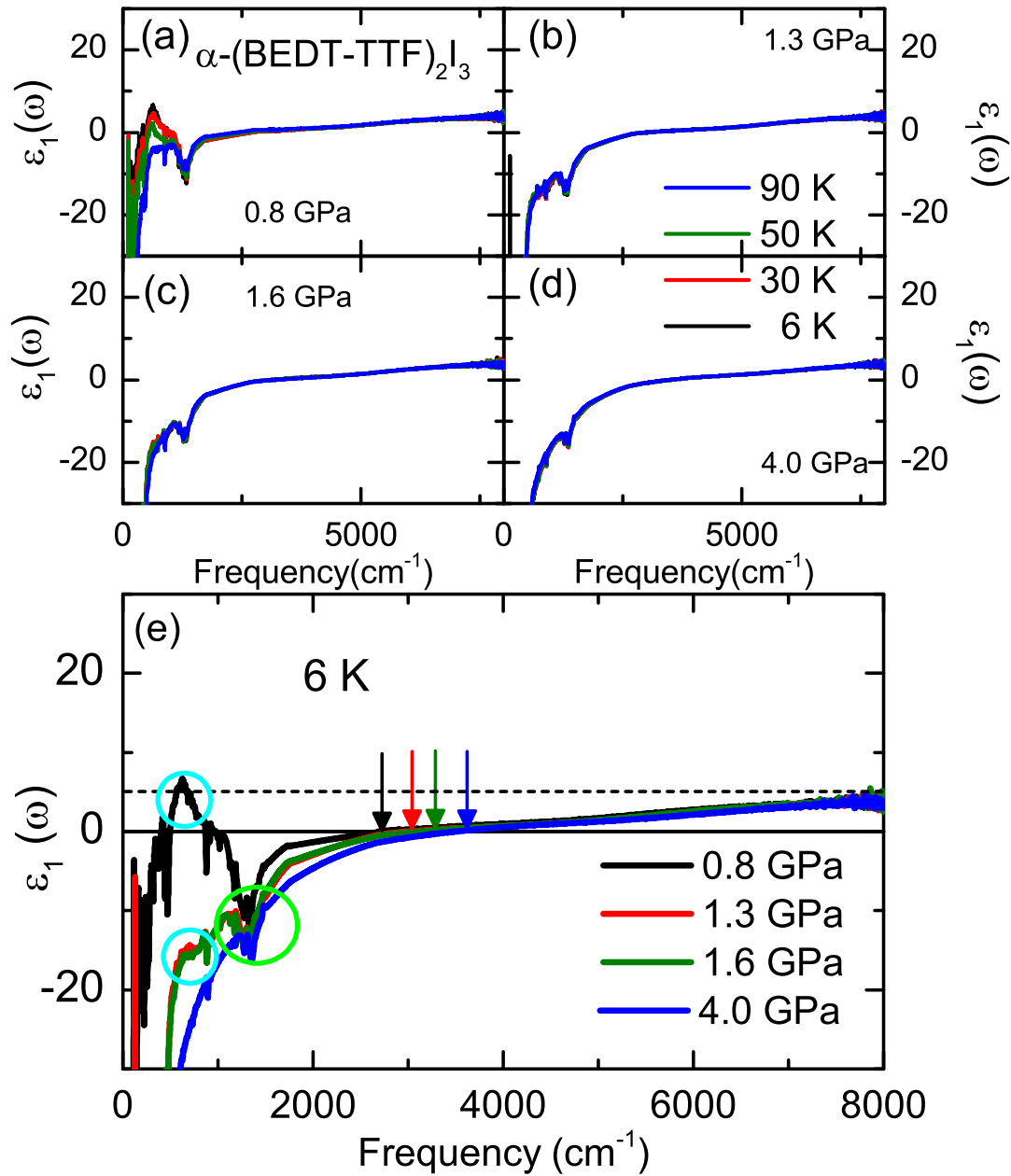


Figure 4.11.: (a-d) Temperature-dependent and (e) pressure-dependent real part of the dielectric constant (ϵ_1) of $\alpha\text{-(BEDT-TTF)}_2\text{I}_3$. Cyan circle denotes the pseudogap behaviour seen in ϵ_1 . The vibration modes are located at higher energy than those of pseudogap shown by lime circle. With increasing pressure, the screened plasma frequency, i.e., the zero-crossing of $\epsilon_1(\omega)$, increases as indicated by arrows. The value of $\epsilon_1(\omega)$ at the high energy limit is $\epsilon_\infty \approx 4$ shown by dashed line.

Our value of ϵ_∞ is much smaller than that used in NMR analysis ($\epsilon_\infty = 30$) [149]. In their calculation, the ϵ_∞ was obtained from fitting the susceptibility. The underestimate of the ϵ_∞ leads to underestimate of Coulomb coupling constant α and exotic gap. Since we directly measured the high energy contribution via optical method, the value used here is more reliable. The Fermi velocity $v_F \approx 2.4 - 10 \times 10^4 \text{ ms}^{-1}$ was taken from Refs. [59, 141, 148]. With the assumption of $N = 2$, we obtain $\Delta \approx 300 \text{ cm}^{-1}$, in good agreement with our optical data. The estimated ratio $2\Delta/k_B T_{PG} \approx 10$ (T_{PG} is assumed to be 90 K) is much larger than the mean-field BCS value, but is in good agreement with theory [166]. There are two non-degenerate Dirac cones ($N = 4$) predicted [59, 167], which merge into one at high pressure ($N = 2$) [142]. According to the theory [166], the critical value of fermion species N_c , below which the mass gap is formed is expected to be around 7 (or 2). Thus the large gap observed in our experiments favours a small value of N , i.e., $N = 2$. In combination of the observed universal constant conductance and the pseudogap, our present optical study yields strong evidence of a single Dirac cone. Suggestions that the massless Dirac electrons are strongly correlated due to the unscreened long-range Coulomb repulsion giving rise to an anomalous increase in $\rho(T)$ [146], strong modification of the Fermi velocity [148] and excitonic mass generation at low T [149] further support our findings in optical spectra.

4.5. Conclusion

The conclusions drawn from our pressure-dependent optical investigations are summarized in the schematic density of states and $\sigma_1(\omega)$ sketched in Figure 4.12. At room temperature and for low pressure, α -(BEDT-TTF)₂I₃ is a bad metal with a overdamped Drude contribution to $\sigma_1(\omega)$ originating from the thermally excited electrons at the Fermi energy. With decreasing temperature, these excitations freeze out and a clear charge-order gap emerges in the optical conductivity. With rising pressure these bands get closer to each other and finally overlap, giving rise to a more-or-less coherent Drude contribution (dark green curve). As we cool down, the edges of the two bands develop linear dispersions. In the high-pressure range $\sigma_1(\omega)$ is composed of three components: (i) a low-energy Drude response (red area), (ii) frequency-independent conductivity due to the massless Dirac electrons (blue area)

and (iii) mid-infrared band arising from the incoherent transitions due to on-site and inter-site Coulomb repulsion (green area). Upon further cooling, electronic correlations cave in a pseudogap with states piling up at the edges. As a result, the Drude spectral weight is transferred to finite energies, resulting in local peaks in $\sigma_1(\omega)$ around 800 cm^{-1} (blue curve). Note, the behaviour is distinct from superconductivity, where the missing spectral weight condenses in a $\delta(\omega = 0)$ -peak [82]. The phase diagram as a function of external pressure depicted in the lower part of Figure 4.12 can be divided into three parts: (i) the charge order insulating state at low pressure; (ii) metallic states in the intermediate pressure regime consisting of massless Dirac electrons, next to carriers in correlation-split and trivial bands; (iii) above 4.0 GPa only the Dirac electronic state and carriers in trivial bands remain (dashed red curve). Our optical results demonstrate clear fingerprints of the electronic correlations between the Dirac electrons; the correlation strength can be tuned by temperature and pressure. We call for complementary spectroscopic experiments to directly confirm our findings and further efforts for a theoretical description of our observations.

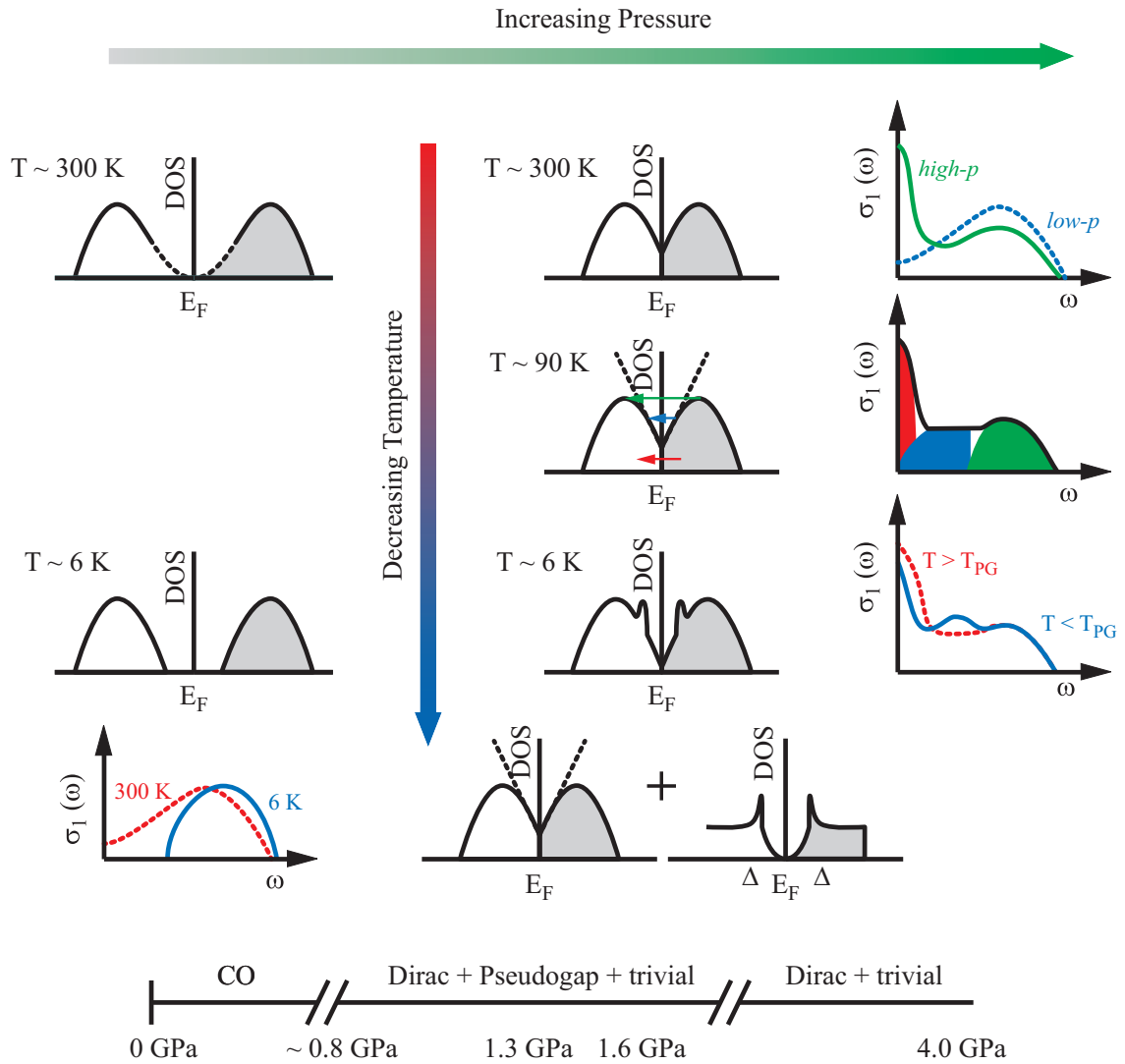


Figure 4.12.: Schematic diagrams for the electronic structure and corresponding optical conductivity of α -(*BEDT-TTF*)₂I₃. Diagrams are given for the low-pressure insulator state and the high-pressure Dirac state at various temperatures. Here T_{PG} stands for the temperature, where the pseudogap starts to open. At the bottom the pressure evolution of the various electronic phases of α -(*BEDT-TTF*)₂I₃ at low temperatures is summarized. For a detailed description see Conclusions.

5. Optical investigations of β' -EtMe₃Sb[Pd(dmit)₂]₂ under high pressure

This chapter will provide the comprehensive results for β' -EtMe₃Sb[Pd(dmit)₂]₂ based on the published data [168].

5.1. Background

As shown in Figure 5.1, the organic conductor β' -EtMe₃Sb[Pd(dmit)₂]₂ consists of alternatively conducting layers of [Pd(dmit)₂]₂ (bis-(ethylenedithio)tetrathiafulvalene) molecules and insulating layers of EtMe₃Sb. This compound can be well described as a half-filled quasi-two-dimensional system with one electron and a spin-1/2 on a [Pd(dmit)₂]₂ dimer. The dimerized units form a triangular lattice with strong geometrical frustration, giving rise to a quantum-spin-liquid ground state as confirmed by NMR [80] and optical [170] methods. Since the unit cell is composed of two crystallographically identical anion layers with different stacking directions, the Fermi surface has two equivalent cylinders in the k -space. According to the tight-binding and first-principle DFT calculations [169], the bulk electronic state stems from the conduction band formed by the dominant p -orbital of the sulphur atom in [Pd(dmit)₂]₂. The bands of cation EtMe₃Sb are well below the Fermi level, leading to negligible contribution in conduction bands. Using the X-ray data, it was shown that the anisotropy of the triangular lattice t'/t increases with lowering temperature, despite the enhancement of both transfer integrals. On

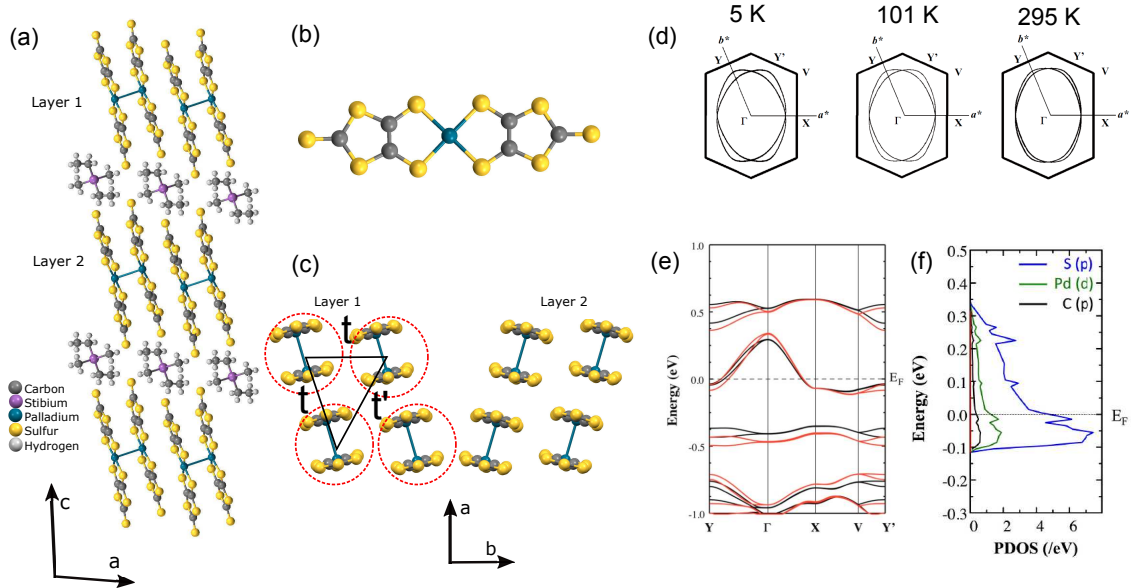


Figure 5.1.: (a) Side view of the layered structure of β' - $\text{EtMe}_3\text{Sb}[\text{Pd}(\text{dmit})_2]_2$ along the b -axis. It is composed of two different $\text{Pd}(\text{dmit})_2$ conducting layers (layer 1 and layer 2) separated by the closed-shell insulating counterions EtMe_3Sb layers. (b) Illustrations of molecular structure of $\text{Pd}(\text{dmit})_2$ and (c) in-plane conducting layers of $[\text{Pd}(\text{dmit})_2]_2$ dimers (red dashed circles) with notations of interdimer transfer integrals. (d) Fermi surfaces of the β' - $\text{EtMe}_3\text{Sb}[\text{Pd}(\text{dmit})_2]_2$ obtained by first-principles DFT calculations at 5 K, 101 K and 295 K. (e) Band dispersion at 5 K (red) and 295 K (black) in the first Brillouin zone. Only one conduction band crosses the Fermi energy and is well separated from other bands. (f) Partial density of states (PDOS) for various atomic orbitals in the conduction bands at 5 K. The PDOS of C atoms in the EtMe_3Sb cation is comparatively small as indicated by the red line. Adapted from Ref. [169].

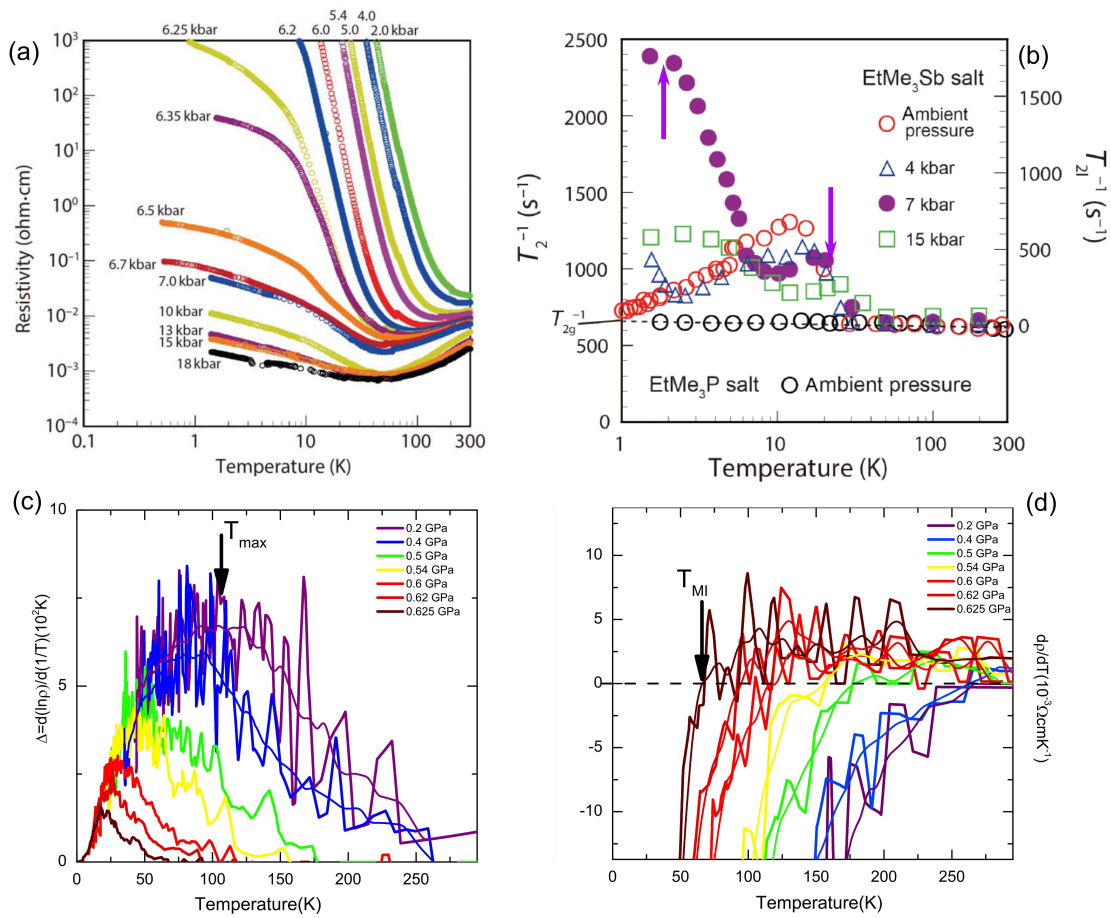


Figure 5.2.: (a) Temperature-dependent in-plane resistivity of β' - EtMe_3Sb in the pressure range from 2 kbar to 18 kbar. The system undergoes a first-order Mott transition at 6.5 kbar. (b) Temperature dependence of the spin-spin relaxation rate T_2^{-1} (left axis) for β' - $\text{EtMe}_3\text{Sb}[\text{Pd}(\text{dmit})_2]_2$ under various pressures determined from NMR measurements. The open black circles stand for those data of β' - $\text{EtMe}_3\text{P}[\text{Pd}(\text{dmit})_2]_2$ at ambient pressure. The right axis indicates the value of T_{2l}^{-1} , which is obtained by subtracting the temperature-independent background T_{2g}^{-1} from T_2^{-1} . The two additional components of T_{2l}^{-1} of EtMe_3Sb -salts are indicated by arrows. (c) The transport data are digitized from panel (a). Activation energy defined as $\Delta = d \ln \rho / d(1/T)$ at various pressures below 0.65 GPa. T_{max} corresponds to the temperature, where Δ reaches its maximum. (d) The derivative of resistance with respect to temperature, namely $d\rho/dT$. The T_{MI} denotes the zero crossing point of $d\rho/dT$, defining the metal-insulator transition temperature. The black dashed line corresponds to $d\rho/dT = 0$. After [172].

the other hand, recent dielectric measurements [171] revealed that both, the cation-anion coupling via Me and Et groups and van der Waals interaction, play important roles in the electronic properties of β' -EtMe₃Sb[Pd(dmit)₂]₂.

At ambient conditions, β' -EtMe₃Sb[Pd(dmit)₂]₂ is an insulator with relatively large optical and activation gaps [86, 172]. As pressure increases, the insulating state is gradually suppressed with decreasing activation energy and transition temperature, see Figure 5.2. In contrast to the case of β' -EtMe₃P[Pd(dmit)₂]₂, even in the high-pressure metallic state, the resistivity exhibits an upturn without any signs of superconductivity at low temperatures, indicating no temperature-driven first-order transition. To clarify this anomalous behaviour, NMR measurements have been performed on β' -EtMe₃Sb[Pd(dmit)₂]₂ with focus on the electronic dynamics around the Mott boundary. It was pointed out that the temperature-dependent spin-lattice relaxation rate T_1^{-1} behaves like Fermi liquid in the high pressure region, while the spin-spin relaxation rate T_2^{-1} exhibits a strong deviation from the expected constant value, accompanied by the enhancement in intensity between kilohertz and megahertz regions as depicted in Figure 5.2 (b). This anomaly was then explained as a result of both charge and spin fluctuations of the randomness in β' -EtMe₃P[Pd(dmit)₂]₂, which is responsible for the upturn observed in resistance. In order to gain a deeper insight into the low-energy dynamics of the charge carriers and the electron-phonon coupling upon crossing the Mott insulator-metal transition, pressure-dependent optical measurements are strongly desired.

5.2. T - and p -evolution of the optical spectra

High quality single crystals of β' -EtMe₃Sb[Pd(dmit)₂]₂ were prepared by an aerial oxidation method as described elsewhere [173]. Samples with shiny and flat surfaces were picked up for optical measurements. The large sample size, up to 0.5 mm, allowed measuring the low-energy response down to far-infrared. High-pressure experiments from 0.23 GPa to 1.2 GPa were conducted in a clamp-type BeCu cell. Temperature-dependent reflectivity measurements spanning from 150 to 8000 cm⁻¹ were performed down to $T = 10$ K. The use of proper polarizers allowed us to probe the response along different crystal directions. Detailed information about the ex-

traction of optical conductivity can be found in the Setup section.

The frequency dependence of as-measured signal reflected off the interface between the diamond window and the β' -EtMe₃Sb[Pd(dmit)₂]₂ sample is plotted in Figure 5.3 and Figure 5.4 for light polarized along the two principal axes of the conducting plane, $E||a$ and $E||b$, respectively. The outer diamond surface was used as a reference.

While at low pressures the low-frequency reflectivity decreases with decreasing temperature (indicating an insulating state with gap opening), for $p > 0.6$ GPa the metallic state emerges and $R(T)$ increases upon cooling. The overall behaviour looks rather similar for both polarizations, e.g., a clear plasma edge is observed around 3000 cm^{-1} in both cases; however, there are subtle changes in the anisotropy as discussed below.

Figure 5.5 displays various temperature-dependent optical conductivity spectra obtained with light polarized parallel to the a-axis for all pressures. As depicted in Figure 5.6, the temperature dependence of optical response along the b-axis is qualitatively similar. Below 0.6 GPa, the overall behaviour and temperature evolution of σ_1 is quite similar to the spectrum measured at ambient pressure [86]. Taking the spectrum at 0.23 GPa as an example, one can conclude that at room temperature the conductivity is composed of a pronounced mid-infrared absorption around 2000 cm^{-1} and a non-zero incoherent low-frequency Drude contribution, which is a general behaviour observed in the majority of families of organic metals. Apart from the electronic contributions, there are two sharp and strong vibrational modes around 1200 cm^{-1} , resulting from electron-molecular vibrational (EMV) modes, which have been extensively investigated by Yamamoto *et al.* [174–176]. A detailed pressure- and temperature-dependent investigations of these vibrational modes will be given later. As the temperature is lowered, the low-energy optical conductivity increases slightly, but below 200 K it starts to frozen out with a complete opening of a Mott gap at the lowest temperature of 10 K.

The false-color contour plots for 0.23 GPa and 1.2 GPa can clearly allow us to see the qualitatively different behaviour in the insulating and metallic regimes. To

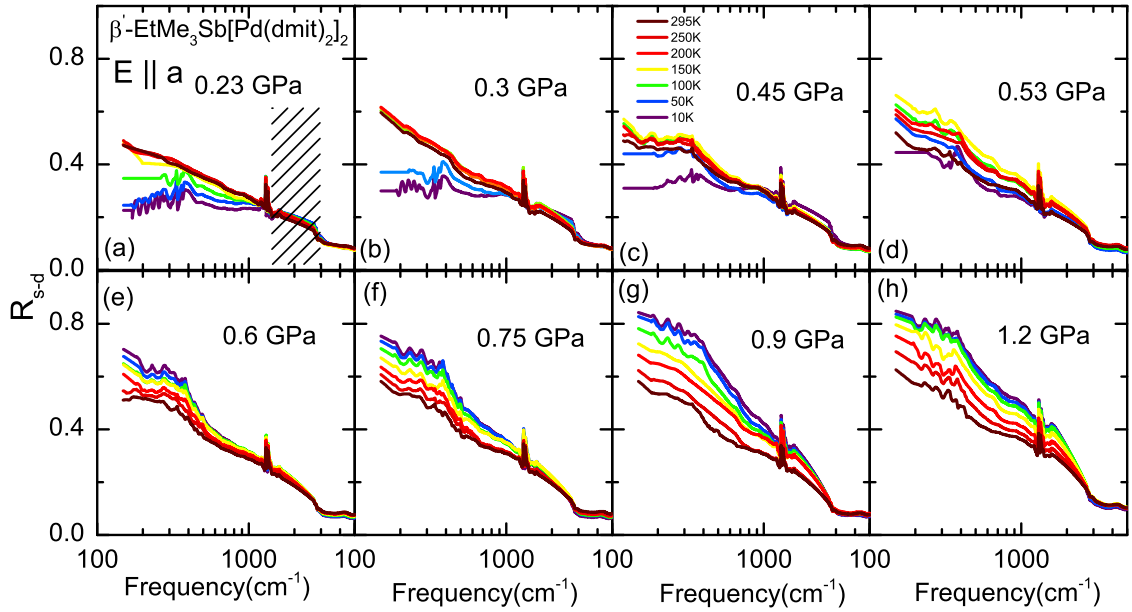


Figure 5.3.: (a-h) Reflectivity spectra of β' -EtMe₃Sb[Pd(dmit)₂]₂ obtained from room temperature down to 10 K for various pressures along the *a*-axis. The black dashed area denotes frequency range, where the data is unavailable due to the strong light absorption by the diamond. Therefore a linear extrapolation has been used in this energy region.

quantitatively characterize the temperature dependence at low energies, we have calculated the spectral weight defined as $SW = \int_0^{700} \sigma_{\text{Drude}}(\omega) d\omega$. In the insulating state, the spectral weight first increases with lowering temperature and then it starts to decrease, indicating the continuous opening of the Mott charge gap. With increasing pressure, the transition temperature, at which the *SW* starts to decrease, shifts to low temperatures. The above observed behaviour is in line with the pressure-dependent transport measurements [172], where the crossover temperatures, distinguishing the regions between metallic-like ($d\rho/dT > 0$) and insulating states ($d\rho/dT < 0$), are reduced with increasing pressure. In a complete contrast to the insulating behaviour, for all pressure points above 0.6 GPa, the *SW* increases continuously upon cooling down to 10 K. It was reported that there is an anomalous low-temperature upturn in the high-pressure resistivity [172]. However, we do not observe any indication of a complete energy gap or pseudogap based on our current results. The reason maybe due to the limitation of the lowest accessible frequencies

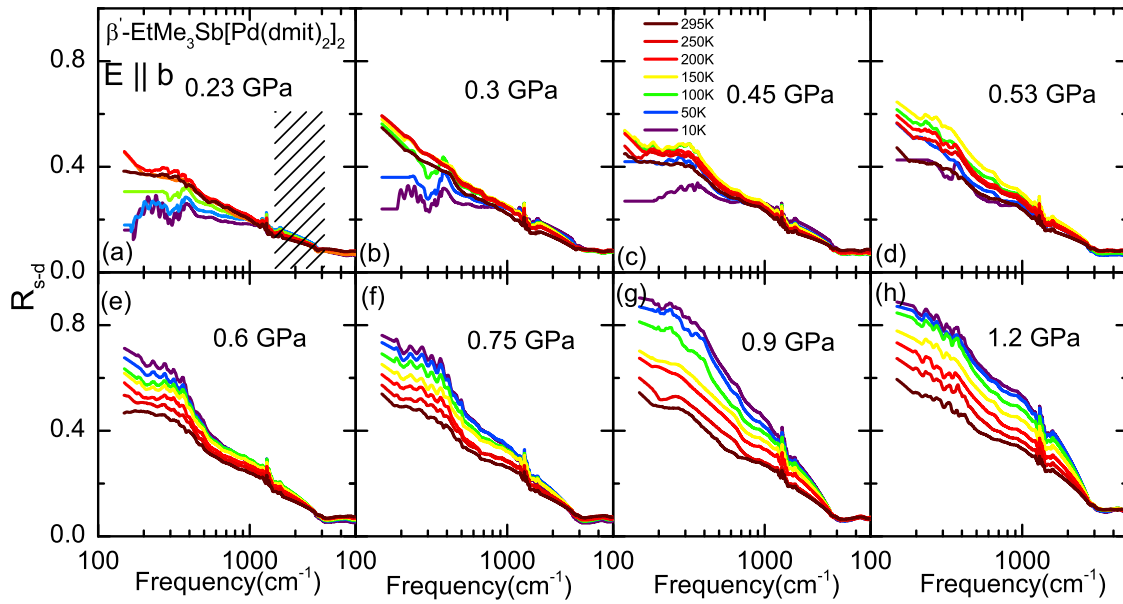


Figure 5.4.: (a)-(h) Temperature-dependent *b*-axis reflectivity data of β' - $\text{EtMe}_3\text{Sb}[\text{Pd}(\text{dmit})_2]_2$ as a function of frequency for various pressures. The dashed area refers to the frequency range, where linear extrapolations have been used.

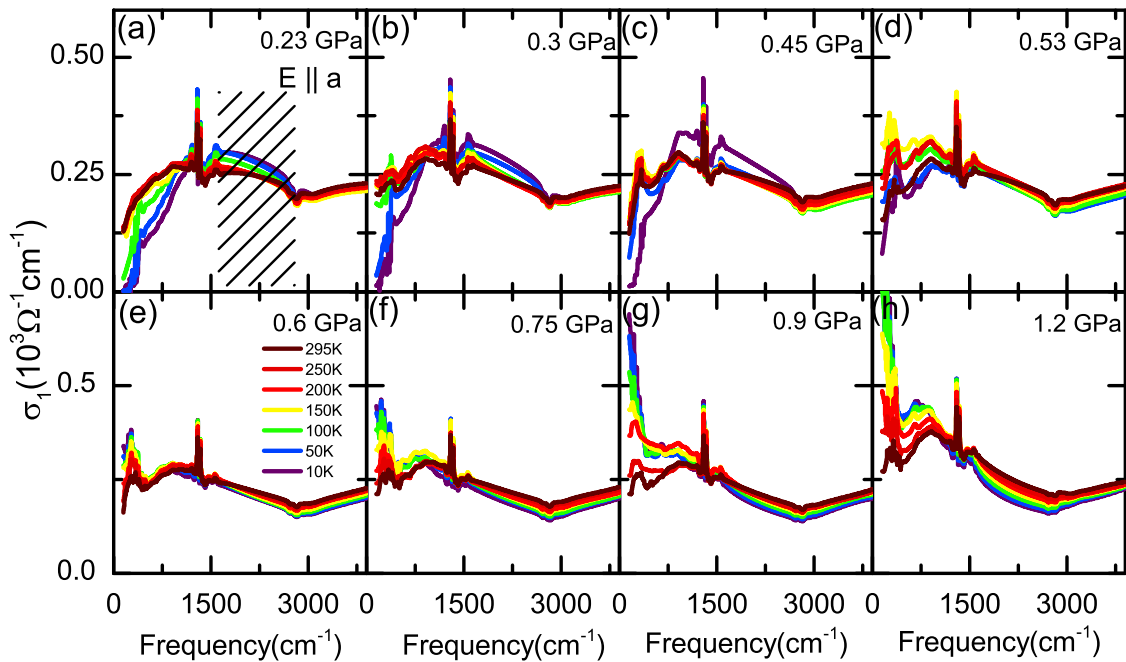


Figure 5.5.: (a-h) Temperature-dependent optical conductivity spectra of β' - $\text{EtMe}_3\text{Sb}[\text{Pd}(\text{dmit})_2]_2$ determined from the reflectivity spectra measured along the *a*-axis in the pressure range from 0.23 to 1.2 GPa.

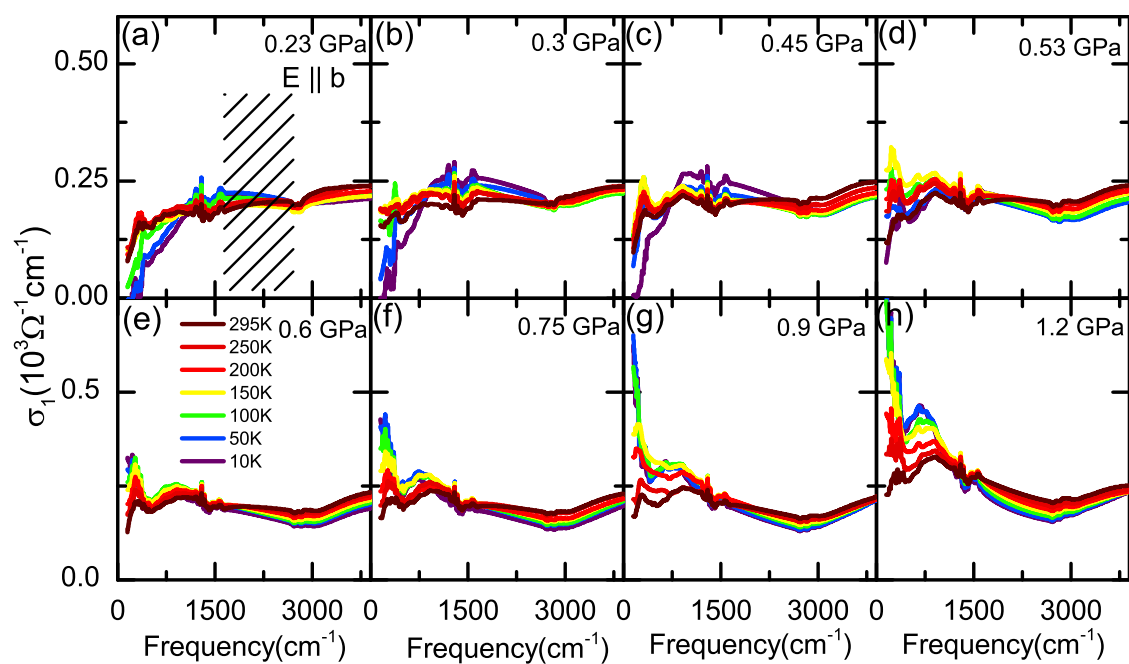


Figure 5.6.: (a-h) *b*-axis optical conductivity spectra of β' -EtMe₃Sb[Pd(dmit)₂]₂ from room temperature to 10 K for various pressures.

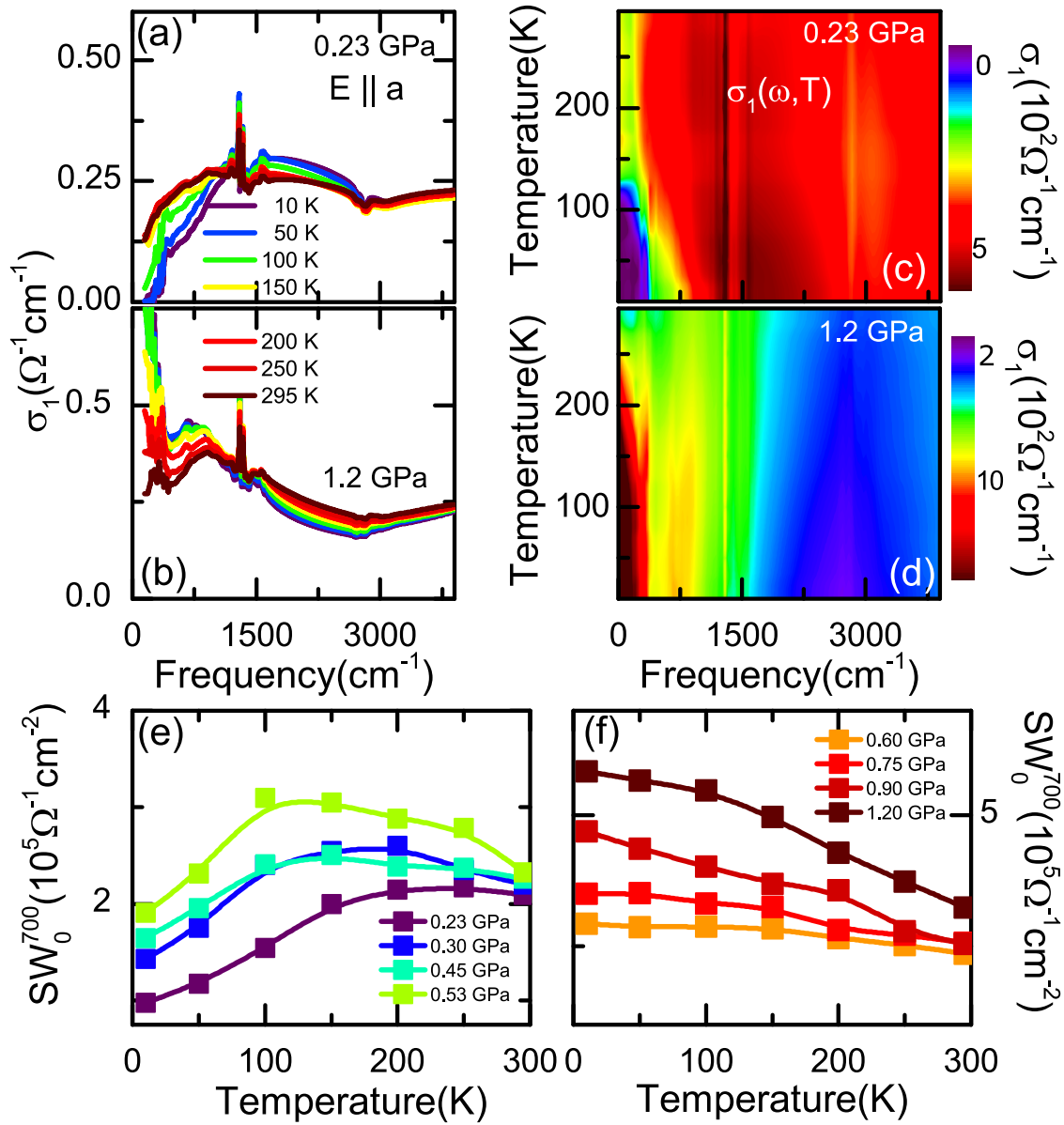


Figure 5.7.: (a,b) Temperature evolution of the a -axis optical conductivity of β' - $\text{EtMe}_3\text{Sb}[\text{Pd}(\text{dmit})_2]_2$ for selected hydrostatic pressures both below and above the Mott transition at $p_c = 0.6\text{GPa}$, as indicated. (c,d) The distinct temperature dependent behaviour of the insulator and metal can be clearly seen in the false-color contour plot for 0.23GPa and 1.2GPa . In panel (e) and (f), the low-energy spectral weight (SW) below 700cm^{-1} , defined as $\int_0^{700} \sigma_{\text{Drude}}(\omega)d\omega$, is displayed as a function of temperature for all measured pressures as indicated.

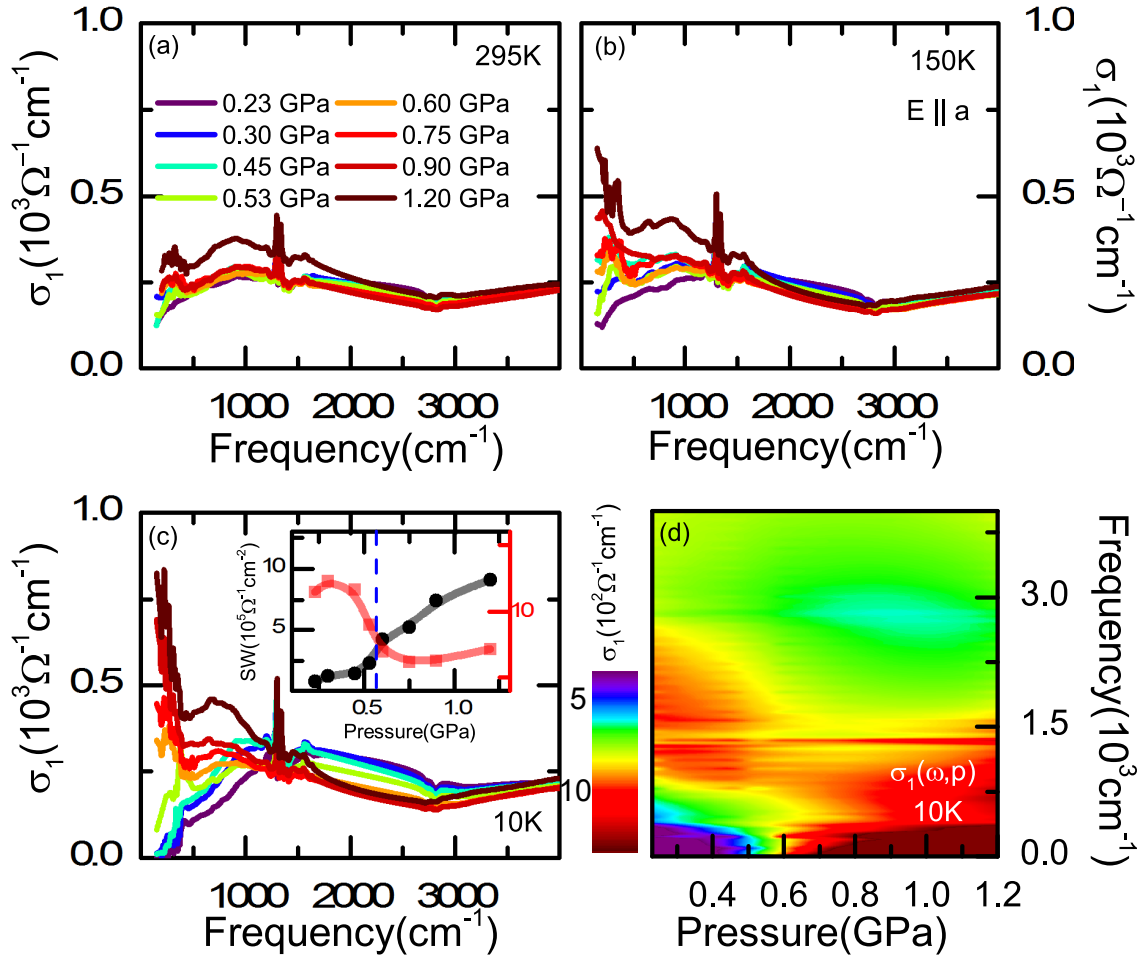


Figure 5.8.: (a)-(c) Pressure dependence of the optical conductivity of β' - $\text{EtMe}_3\text{Sb}[\text{Pd}(\text{dmit})_2]_2$ at selected temperatures, i.e., 295 K, 150 K and 10 K. The inset of panel (c) shows the pressure evolution of the spectral weight at 10 K for the low-energy and mid-infrared regions as explained in the main text. The black circles (low-energy SW) correspond to the left axis; the red squares (mi-infrared SW) refer to the right axis. The blue dashed line indicates the critical pressure p_c of the Mott transition. The pressure effects on the optical conductivity spectra at 10 K can be traced from the false-color contour plot of $\sigma_1(\omega, p)$, shown in panel (d).

and temperatures in our setup. Further experiments need to be done to confirm such a low-energy gap, which has been observed in the strongly correlated Dirac system α -(ET)₂I₃ [139].

The pressure-dependent optical conductivity spectra for various temperatures are plotted in Figure 5.8(a). With increasing pressure the mid-infrared absorption at 295 K doesn't change so much, whereas the spectra in the low-energy range increase slightly and gradually, but without developing a pronounced Drude peak, i.e., β' -EtMe₃Sb[Pd(dmit)₂]₂ remains a bad metal over the whole pressure range. The overall pressure evolution of optical spectra at room temperature is in good agreement with reported transport measurements indicating a decrease of resistivity within a factor of 10 as pressure increases to 1.8 GPa [172].

The difference between low- and high-pressure spectra becomes more prominent as temperature goes down to 150 K. As we can clearly see in Figure 5.8 (b), a sharp Drude peak develops below 500 cm⁻¹ for 0.9 GPa and 1.2 GPa, in strong contrast to the case of 0.23 GPa, where the conductivity in the far-infrared region gets further suppressed as a result of gradual opening of the Mott gap upon cooling. With further cooling down to the lowest temperature (10 K), the thermally excited charge carriers completely freeze out and a full gap can be clearly resolved in the insulating Mott state ($p < 0.6$ GPa). Above 0.6 GPa, a Drude peak appears and becomes enhanced, accompanied with a suppression of mid-infrared component with increasing pressure. To quantitatively analyze the evolution of charge dynamics under pressure, the spectral weight of the Drude peak ($\int_0^\infty \sigma_{\text{Drude}}(\omega)d\omega$) and mid-infrared region ($\int_{\omega_l}^{\omega_u} \sigma(\omega)d\omega$, with the lower and upper bound $\omega_l=1000$ cm⁻¹ and $\omega_u=3000$ cm⁻¹, respectively) are calculated and shown in the inset of Figure 5.8 (c) as a function of pressure. Below 0.6 GPa, the low-energy *SW* remains very low and increases only slightly due to the gradually closing of the Mott gap with applied pressure, while it grows significantly when pressure exceeds $p_c=0.6$ GPa and continuously increases up to 1.2 GPa. At the same time, the mid-infrared *SW* drops suddenly as the system is tuned across the Mott boundary at around 0.6 GPa. Hence, the pressure-driven *SW* transfer over such a large energy scale can be considered as an evidence of strong correlations in this system [87]. It can be easily seen from the energy-pressure-conductivity map in Figure 5.8 (d) that a clear

changeover from low optical conductivity (in insulating state) to high optical conductivity (in metallic state) occurs between 0.53 GPa and 0.6 GPa. These results undoubtedly demonstrate the pressure-induced band-gap narrowing and metallization.

5.3. Optical spectra at 10 K

In order to further clarify the origin of different contributions in the complete energy region, we performed a Drude-Lorentz analysis of our spectra, which allows us to directly compare the results with theoretical prediction made by DMFT calculations [86, 129, 131, 177].

As examples, we plot in Figure 5.11 the low-temperature optical conductivity spectra with corresponding fits for 0.23 GPa and 1.2 GPa. For the insulating state (0.23 GPa), the spectra can be well fitted by a single broad mid-infrared contribution (dark blue) centered around 1500 cm^{-1} and an additional high-energy tail (cyan) accounting for the interband transitions. In contrast, the simplest fit of σ_1 at 1.2 GPa requires two additional contributions: one Drude peak at zero frequency and an additional mid-infrared peak centered around 750 cm^{-1} . The above-mentioned difference between insulating and metallic states can be well captured by single-band DMFT calculations. The theory predicts that in the strongly correlated case, the broad feature with width $2W$ is assigned to transitions between the lower and upper Hubbard bands separated by U . When U/W drops below a critical value $(U/W)_c$, a Drude peak appears in the optical spectra, corresponding to the coherent quasi-particle peak at the Fermi level. Besides that, a mid-infrared peak shows up around $U/2$ with width W as a result of the excitation between the upper Hubbard band and the quasi-particle peak[153].

Fits for the entire pressure range are depicted in Figure 5.10. The extracted values of U , W and U/W are shown in Figure 5.11 (b,c) as a function of pressure. The analysis reveals that the onsite Coulomb repulsion U varies only slightly with applied pressure, while the bandwidth increases continuously as pressure increases. As a result, the effective correlation U/W decreases with increasing pressure. The critical value of U/W is estimated to be around 1.1 at 0.6 GPa, which is in a very

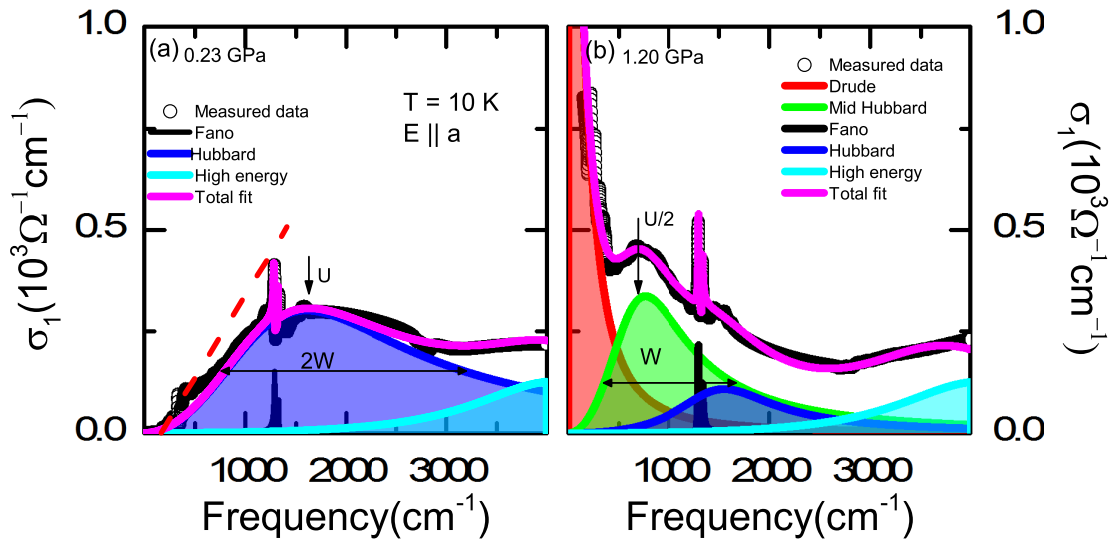


Figure 5.9.: (a) and (b) display the Drude-Lorentz-Fano fits to the spectra of β' - $\text{EtMe}_3\text{Sb}[\text{Pd}(\text{dmit})_2]_2$ measured at $T = 10 \text{ K}$ and $p = 0.23$ and 1.2 GPa . The red dashed line in panel (a) corresponds to the linear extrapolation of the absorption edge. The crossing point with the frequency-axis is defined as the gap energy. The definitions of U and W are from Ref. [153].

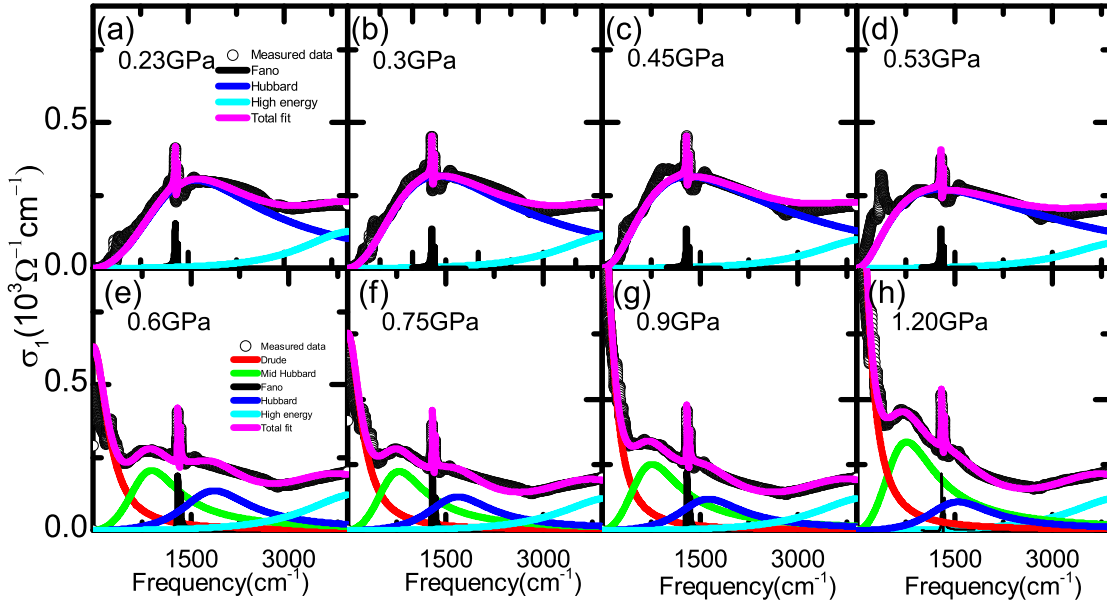


Figure 5.10.: (a-h) The a-axis optical conductivity of β' - $\text{EtMe}_3\text{Sb}[\text{Pd}(\text{dmit})_2]_2$ and the corresponding Drude-Lorentz-Fano fits for all pressures at 10 K. The extracted values of U , W and the spectral weight (SW) are shown in Figure 5.11.

good agreement with the recent DMFT predictions, giving $(U/W)_c \approx 1.3$ [86].

In the next step, we analyse the pressure evolution of the optical gap. In the insulating state, we estimate the energy gap 2Δ by extrapolating the steeply increasing part of the optical absorption edge to zero (dashed lines in Figure 5.9 (a)). At ambient pressure, the gap value of β' -EtMe₃Sb[Pd(dmit)₂]₂ ($2\Delta_0=600$ cm⁻¹) is much larger than those of κ -(BEDT-TTF)₂Cu(CN)₃ ($2\Delta_0 < 50$ cm⁻¹) and κ -(BEDT-TTF)₂Ag(CN)₃ ($2\Delta_0 \sim 100$ cm⁻¹). This indicates that β' -EtMe₃Sb[Pd(dmit)₂]₂ is located far away from the Mott critical region [86]. With increasing pressure, the bandwidth gets larger, leading to the gradual closing of the charge gap. The pressure-dependent optical gap is fitted with a power law, $\Delta(p) = 2\Delta_0(p_c - p)^\delta/p_c$. As depicted in Figure 5.11 (a), the best fit yields $\delta=0.96$, indicating a quasi-continuous nature of the pure Mott transition [178]. This value of δ is quite close to the theoretical prediction [178]. It is interesting to note that recent transport measurements on related spin-liquid Mott insulator κ -(BEDT-TTF)₂Cu(CN)₃ reveal a similar behaviour [179].

The degree of electronic correlations can be described by the effective mass m_{op}^* , which can be derived from the spectral weight analysis. As already shown in the inset of Figure 5.8 (c), the loss of low-energy SW with decreasing pressure in the metallic region strongly demonstrates the enhancement of correlations. In Figure 5.11 (d), we plot the pressure-dependent SW of both the Drude component and the intraband contribution obtained by subtracting the interband contributions, i.e. $SW_{intra} = SW_{total} - SW_{inter}$. For a quantitative analysis, the effective mass enhancement m_{op}^*/m is defined as:

$$m_{op}^*/m = \frac{SW_{intra} = \int_0^\infty \sigma_{intra}(\omega)d\omega}{SW_D = \int_0^\infty \sigma_{Drude}(\omega)d\omega}, \quad (5.1)$$

The pressure evolution of m_{op}^*/m is plotted in Figure 5.11 (d)

The effective mass can also be obtained using the extended Drude analysis, in which both mass and scattering rate have frequency-dependence, as we discussed in the theory section. In Figure 5.12, we plot the calculated effective mass and scattering rate as a function of frequency at 10 K for various pressures above $p_c=0.6$ GPa. The

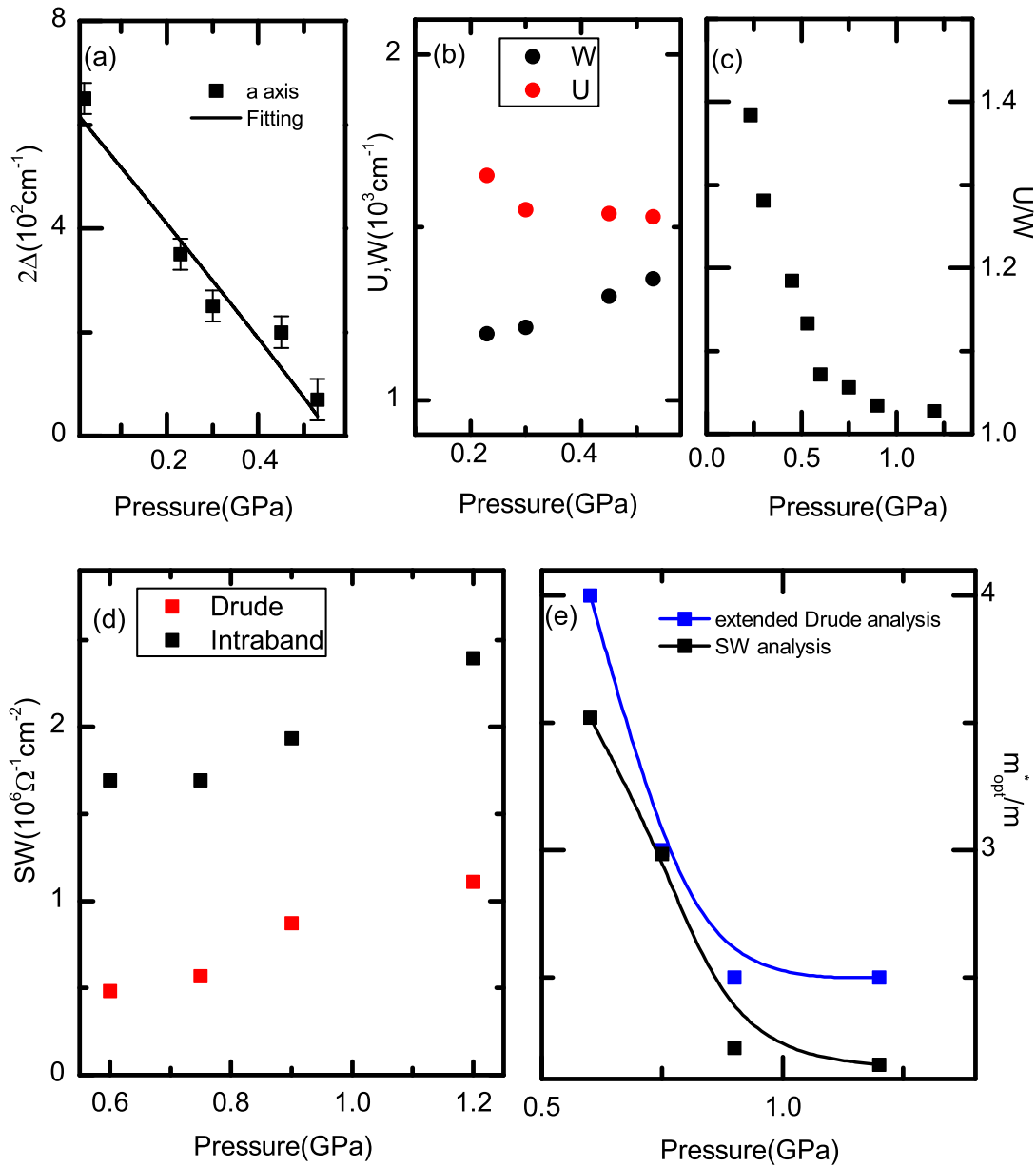


Figure 5.11.: (a) Pressure dependence of the extracted values for the Mott gap and corresponding power law fitting via $\Delta \propto (p - p_c)^\delta$. Here, $p_c=0.6$ GPa is used. (b) Extracted values of the Coulomb repulsion U and the bandwidth W below 0.6 GPa. (c) Pressure evolution of the effective correlations U/W based on the extracted values shown in panel (b). (d) Pressure-dependent spectral weight of the Drude component (red squares) and the total intraband contribution (black squares). (e) Optical effective mass plotted as a function of pressure on the metallic side. Red squares refer to the results from extended Drude analysis; black squares are obtained from spectral weight analysis.

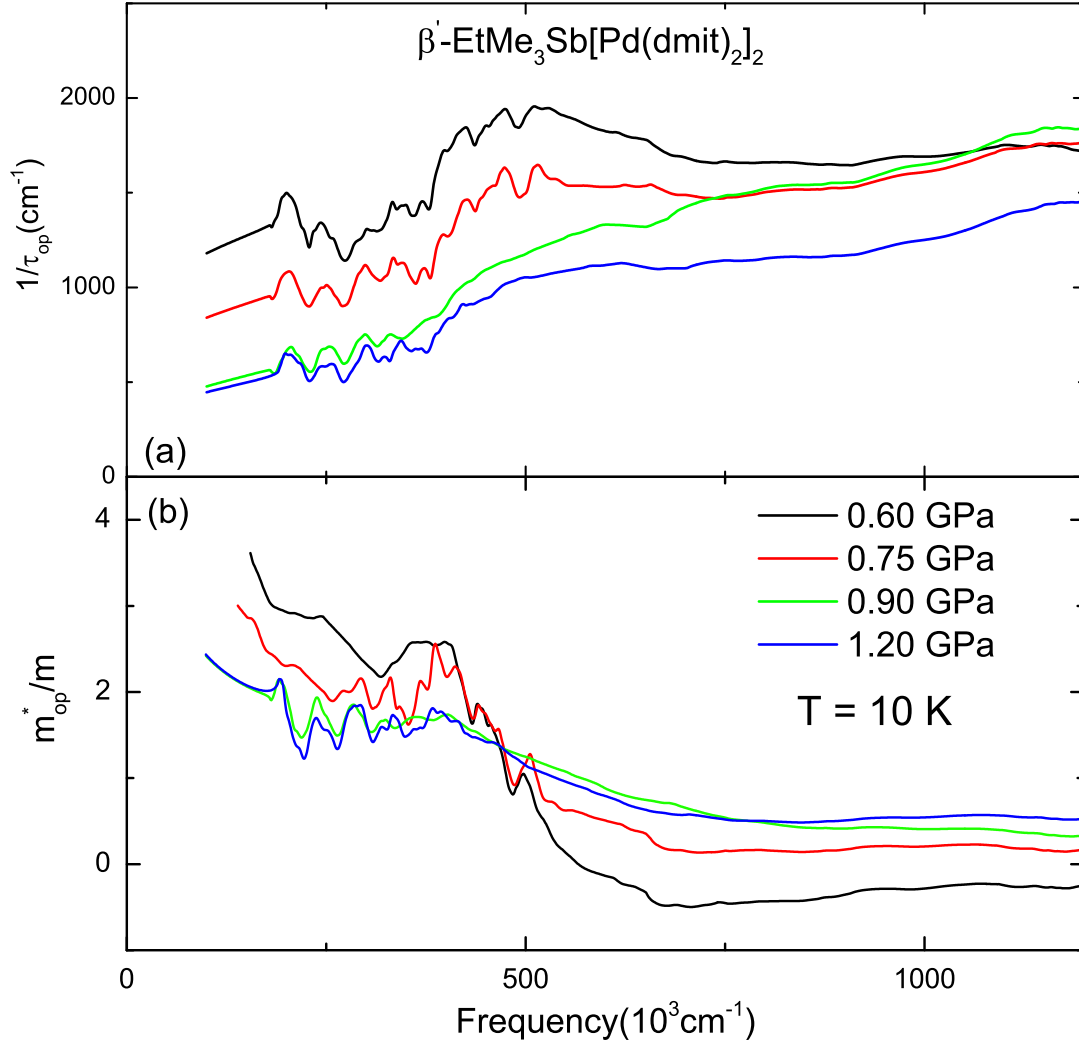


Figure 5.12.: Frequency dependence of the (a) scattering rate $1/\tau_{op}(\omega)$ and (b) effective mass $m_{op}^*(\omega)$ of β' -EtMe₃Sb[Pd(dmit)₂]₂ determined using the extended Drude analysis of the optical conductivity measured for various pressures in the metallic state at 10 K. In this estimation, the plasma frequency, $\omega_p^2 = \int_0^{\omega_c} \sigma(\omega)d\omega$, is calculated up to the cutoff frequency of $\omega_c = 3000 \text{ cm}^{-1}$, which separates the intraband transitions from interband ones.

scattering rate $1/\tau_{op}(\omega)$ increases when we go up in frequency, and then remains almost unchanged for frequencies above 600 cm^{-1} . With increasing pressure, the scattering rate gets suppressed, correspondingly resulting in a decrease of effective mass. Unfortunately, due to the insufficient data quality at low energies and fairly large systematic errors, we could not perform a meaningful Fermi-liquid-scaling analysis for this compound. Further experiments are desired to identify the optical signature of the Fermi-liquid behaviour, as evidenced by NMR measurements.

The values of m_{op}^*/m extracted from both the *SW* (black squares) and extended Drude analysis (blue squares) are plotted as a function of pressure in Figure 5.11 (e). As far as the pressure dependence and the absolute value is concerned both results well agree with each other. As the pressure increases, driving the system away from the critical region, m_{op}^*/m in the metallic phase gets suppressed, indicating a decrease of electron-electron correlations. The corresponding analysis of the $E||b$ spectra yields the same conclusion. These experimental results are in good accord with the Brinkman-Rice scenario, where both susceptibility and effective mass are found to diverge at the critical value of the interaction. Similar mass enhancement has also been observed from optical investigations in the superconducting κ -(ET)₂Cu[N(CN)₂]Cl and κ -(ET)₂Cu(NCS)₂ tuned by physical and chemical pressure [38, 39, 180, 181].

5.4. Electron-Lattice interactions

Since the metal-insulator transition is realized by pressurizing the crystal lattice, the vibrational modes of β' -EtMe₃Sb[Pd(dmit)₂]₂ are inevitably influenced by its electronic structure. Optical spectroscopy provides the unique tool to investigate the vibrational response of the molecular and crystal structure at the phase transition boundary in order to extract information on changes in structure and charge distribution. Here, we will turn to the detailed discussion of the pressure and temperature evolution of these vibrational modes. The two vibrational modes depicted in Figure 5.13 (a) are the two strongest modes among all A_g modes [175]. The four C=C bonds in the Pd(dmit)₂ molecular dimer vibrate such that they are in phase within one molecule but out of phase with respect to the sibling molecule

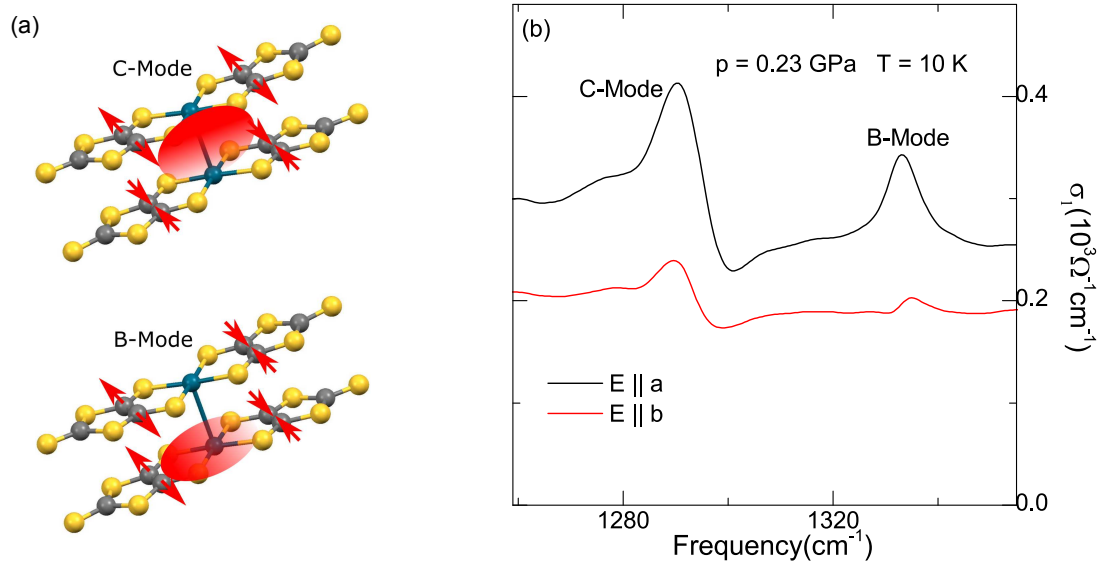


Figure 5.13.: (a) Schematic view of infrared active C=C stretching modes of [Pd(dmit)₂]₂ dimers. The motion of the carbon atoms is indicated by red arrows. The light and dark red color correspond to the local electron density, which induces a dipole moment. The electrical dipole moment of C-mode and B-mode is perpendicular to the dimer and along the long axis of Pd(dmit)₂, respectively. (b) Examples of C- and B-mode optical conductivity spectra for both polarizations obtained at $p=0.23$ GPa and $T=10$ K.

(C-mode); the B-mode denotes the out-of-phase vibration within the molecules. Since the electric dipole is perpendicular to the molecular axis, the C-mode couples stronger to the electronic background compared to the B-mode where the dipoles point along the Pd(dmit)₂ axes [174–176].

Figure 5.14 displays the behaviour of C-mode of β' -EtMe₃Sb[Pd(dmit)₂]₂ as a function of temperature and pressure. Due to thermal contraction, the vibrational features in general harden upon cooling; for low pressure range ($p < 0.6$ GPa), however, we observe a blue shift at the Mott transition and the Fano shape becomes more pronounced (Figure 5.14 (a-f)). We interpret this behaviour as indication that the electronic screening changes upon approaching the metal-insulator transition. This behaviour clearly reflects the spectral weight redistribution upon formation of the Mott gap at lower frequencies, which modifies the electronic background at the vibration frequency. While the mode is sitting on the low-energy side of optical Hubbard excitations in the insulating state, where it couples to a highly polariz-

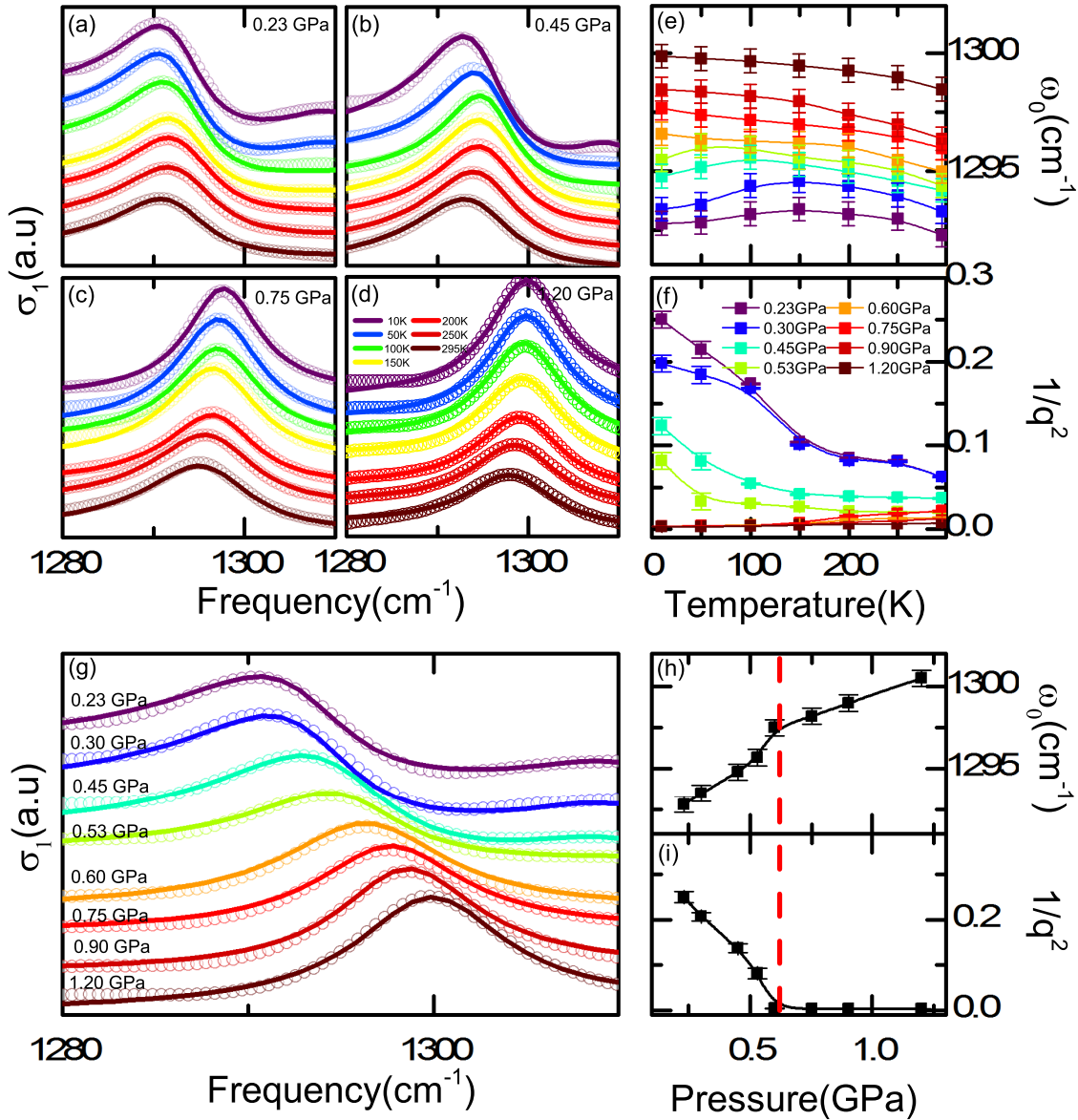


Figure 5.14.: (a-d) Temperature dependence of vibrational C-mode and corresponding Fano fitting for selected pressures, as indicated. Panels (e) and (f) display the temperature evolution of the fitting parameters: (e) central frequency ω_0 and (f) Fano coupling constant $1/q^2$ for all measured pressures from 0.23 GPa to 1.2 GPa. (g) Pressure dependence of 10 K spectra and fitting data. The obtained ω_0 and $1/q^2$ are shown in (h) and (i). The red dashed line indicates the critical pressure, $p_c = 0.6$ GPa, of the Mott transition, where both the center frequency ω_0 and coupling constant $1/q^2$ display an anomaly.

able background, the spectral weight transfer to lower frequencies at larger T and p involves the onset of screening.

The low-temperature spectra exhibit a clear change in frequency and electronic coupling when the pressure drops below p_c , as depicted in Figure 5.14(g)-(i). Here, we want to point out that over the whole pressure range, there is no splitting of any modes, suggesting no structure transition or charge-ordered state. It is also interesting to note that thermal expansion measurements on the related compound κ -(BEDT-TTF)₂Cu[N(CN)₂]Cl also reveal a jump of the expansion coefficient when tuned by pressure across the first-order insulator-metal line [35].

Our optical investigations now give conclusive evidence that the strength of itinerant (inter-dimer) charge contribution increase with pressure but on the expense of the localized (intra-dimer) spectral weight. This is also reflected in vibrational features. The mode shifts up in frequency as pressure increases above the Mott transition. On the other hand we find the Fano coupling constant $1/q^2$ vanishing at $p_c = 0.6$ GPa as the vibrational features become simple Lorentzians. This implies that above $p_c = 0.6$ GPa the modes become decoupled from the electronic background.

5.5. Anisotropy of the in-plane optical response

β' -EtMe₃Sb[Pd(dmit)₂]₂ is a quasi-two-dimensional conductor with a small anisotropy at ambient conditions: $\sigma_{1a} > \sigma_{1b}$. While the ratio $\sigma_{1b}/\sigma_{1a} = 0.8$ to 0.9 remains constant throughout the insulating state ($p < p_c$), the Drude term is found to increase more rapidly for $E \parallel b$ than for $E \parallel a$ when entering the metallic phase. In Figure 5.15 we present the temperature and pressure dependence of the anisotropy σ_{1b}/σ_{1a} as obtained from the $\omega \rightarrow 0$ data indicating the inversion for low temperature and high pressure. Similar results are obtained from the analysis of the spectral weight of the Drude term in both directions.

First of all, we can rule out the possibility that our results are due to the artefact of the anisotropy of the applied pressure. Because the anisotropy only changes abruptly when the Mott transition is crossed and gets enhanced with increasing pressure in the metallic side, indicating the intrinsic behaviour of the quasi-particle at the Fermi surface. We also realized that similar results has been observed in the doped Mott insulator κ -(ET)₂Cu[N(CN)₂]Cl from the dc-transport measure-

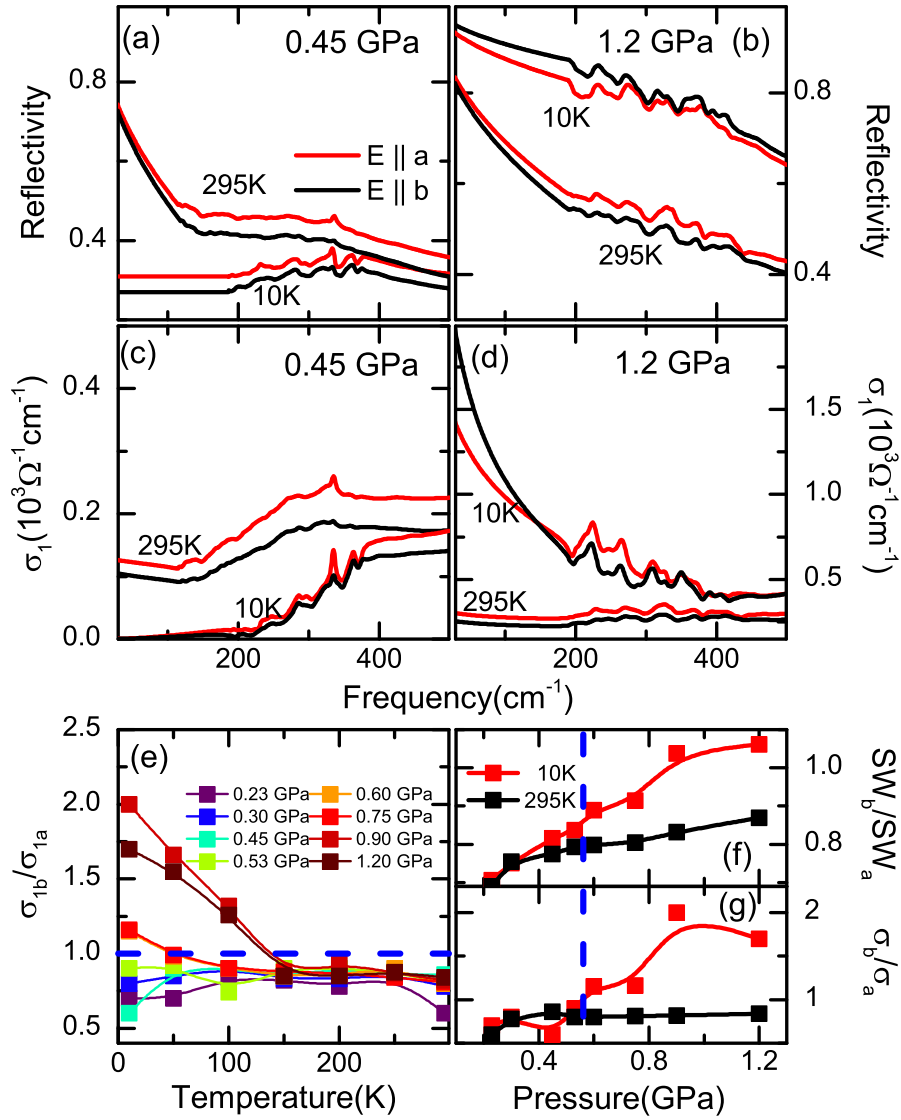


Figure 5.15.: (a) 0.45 GPa and (b) 1.2 GPa reflectivity spectra of β' - $\text{EtMe}_3\text{Sb}[\text{Pd}(\text{dmit})_2]_2$ at 295 K and 10 K for polarized light along the a-axis and b-axis. The inverse of the anisotropy within in-plane can be clearly seen from the raw reflectivity data. (c,d) Corresponding optical spectra recorded at 295 K and 10 K for $E||a$ and $E||b$. (e) Temperature dependence of anisotropy ratio of the conductivity along the b-axis to that along the a-axis, i.e., $\sigma_{1b}/\sigma_{1a}(\omega \rightarrow 0)$ at various pressures. In the metallic state, the Hagen-Rubens extrapolated values are used, while in the insulating state, the values are extracted just above the gap (since the conductivity is almost zero inside the gap). Blue dashed line displays the ratio of $\sigma_{1b}/\sigma_{1a}=1$. (e,g) show the pressure-dependent anisotropy of the spectral weight and conductivity ($\omega \rightarrow 0$) for 295 K and 10 K. Blue dashed line refers to the critical pressure $p_c = 0.6\text{GPa}$ of Mott transition

ments [182]. It was found that the anisotropy only increases upon cooling only in the hole doped side, owing to the correlation-induced pseudogap opening on the Fermi surface. Surprisingly, our optical results are in excellent agreement with the optical spectra calculated by Kato's group [182]. Despite the different approaches of metallization, the good similarities between both results demonstrate the importance of the Fermi surface topologies. Thus, our findings infer the opening of a pseudogap along the a -axis. Regarding the origin of the gap, we can not pin down only by this experiment. As shown by another experiment, the change of the anisotropy in superconducting κ -(BEDT-TTF)₂Cu(NCS)₂ was assigned to the formation of density-wave order, which is induced by the Fermi surface nesting, instead of electron-electron correlations [183]. Nevertheless, our results should arise more detailed studies of the Fermi surface of β' -EtMe₃Sb[Pd(dmit)₂]₂.

5.6. Conclusions

In conclusion, we have successfully performed a detailed spectroscopic study of the spin-liquid candidate β' -EtMe₃Sb[Pd(dmit)₂]₂ using temperature- and pressure-dependent optical measurements. Based on our observations, we constructed the $(p - T)$ phase diagram for β' -EtMe₃Sb[Pd(dmit)₂]₂ (Figure 5.16(a)) and complemented it with dc-transport measurements under pressure [172]. In general, the phase diagram can be divided into three regions. A bad-metal state exists at high temperature with small amount of thermally excited free charge carriers around the Fermi level and the vibrational modes moderately coupled to the mid-infrared excitations. Upon cooling, the system can be tuned either into the insulating state with a clear gap opening and strong electron-lattice coupling, or into the metallic state with formation of a Fermi surface and weaker electron-lattice coupling. Thus, the pressure-dependent evolution of the optical conductivity follows qualitatively the characteristic features predicted by DMFT calculations. Our results unambiguously confirm the realization of the pure bandwidth-controlled metal-insulator transition via tuning external pressure. In the insulating state, the universal values of $(T/W, U/W)$ decrease approximately from (0.1, 1.4) to (0.01, 1) as shown in Figure 5.16 (b). This is quantitatively in good agreement with the theoretical values [86].

The metallic phase is further characterized as an anomalous metal with possible pseudogap opening along the a-axis. Such intriguing feature is calling for further theoretical attention in order to clarify whether it is connected to the fact that no superconductivity was found in this compound. It is very interesting to notice that around the critical region, a new phase, characterized as a Griffiths phase with slow spin fluctuations, have been identified by NMR measurements [172]. Owing to its slow dynamic properties, low-frequency dielectric measurements under pressure are strongly suggested for the future plan [184, 185].

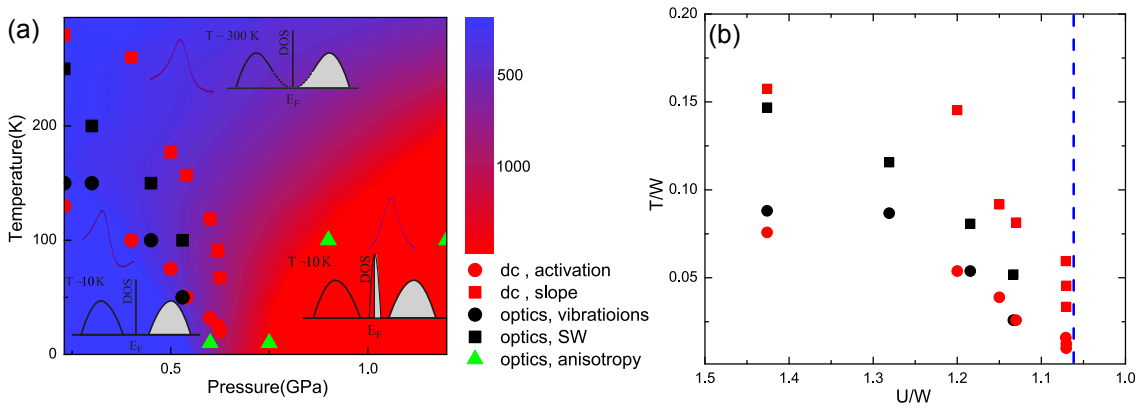


Figure 5.16.: (a) Schematic ($p - T$) diagram for β' - $\text{EtMe}_3\text{Sb}[\text{Pd}(\text{dmit})_2]_2$ based on our optical experiments. The false-coloured contour plot is constructed using the a-axis optical conductivity in the dc-limit ($\omega \rightarrow 0$). The black squares and circles are defined as the crossover temperatures, where the temperature dependence of the spectral weight (shown in Figure 5.7) and the vibrational modes (plotted in Figure 5.14), respectively, show maxima, respectively. The red squares refer to the metal-insulator transition temperature ($d\rho/dT=0$) from the transport measurements. The red circles correspond to the temperatures, at which the activation energy, defined as $d(\ln\rho)/d(1/T)$, exhibits maxima. Details can be found in Figure 5.2. Green triangles represent the temperatures, where the σ_b/σ_a ratio is above 1. (b) The same phase diagram normalized by bandwidth obtained from fits at 10 K. The vertical dashed line refers to the critical value of $(U/W)_c$.

6. Pressure-dependent optical investigations on the spin liquid compound κ -(ET)₂Cu₂(CN)₃

In this chapter, we will discuss the pressure-dependent experimental results on κ -(BEDT-TTF)₂Cu₂(CN)₃ in comparison with the optical results obtained by chemical substitution [74]. In this section, \hbar and k_B are set to 1; $\hbar\omega$ and $k_B T$ have the same unit of cm^{-1} .

6.1. Background

Like other κ -phase organic salts, conducting layers of BEDT-TTF molecules are separated by planes of insulating Cu₂(CN)₃ anions in κ -(BEDT-TTF)₂Cu₂(CN)₃ as depicted in Figure 6.1 (a). Within the conducting plane, two BEDT-TTF molecules form dimers with strong intra-dimer transfer integral, leading to a splitting of the band; this effectively causes a half-filled conduction band. These dimers are considered as lattice sites and constitute an nearly isotropic triangular lattice with strong geometrical frustrations. In the early time, it was widely believed that those BEDT-TTF dimers play a dominant role in the charge dynamics of κ -(BEDT-TTF)₂Cu₂(CN)₃ [24, 26]. However, recent numerical calculations and infrared measurements provided strong evidence that the Cu₂(CN)₃ anions are strongly coupled to the BEDT-TTF layers. This leads to an unusual low-energy excitation in the THz region [186].

The strong geometrical frustration found in κ -(BEDT-TTF)₂Cu₂(CN)₃ make this

compound very unique among κ -(BEDT-TTF)₂X family. The magnetic properties of κ -(BEDT-TTF)₂Cu₂(CN)₃ was systematically studied by Shimizu *et al.* utilizing NMR and static susceptibility measurements [187]. As illustrated in Figure 6.1 (d,e), there is no indication of long-range antiferromagnetic order down to 32 mK, despite the large antiferromagnetic interaction with the exchange constant $J \sim 250$ K. This finding is in strong contrast to the case of κ -(BEDT-TTF)₂Cu₂[N(CN)₂]Cl, which exhibits weaker frustration and antiferromagnetic order below $T = 27$ K. Thus, κ -(BEDT-TTF)₂Cu₂(CN)₃ turns out to be the first candidate in organic salts showing quantum spin liquid ground state. Later on, comprehensive infrared investigations of the charge sensitive vibrational modes showed that there is no indication of any sizeable charge disproportionation in κ -(BEDT-TTF)₂Cu₂(CN)₃ [188]. This implies that the κ -(BEDT-TTF)₂Cu₂(CN)₃ can be considered as a genuine Mott insulator without any charge or magnetic ordering.

The optical properties of κ -(BEDT-TTF)₂Cu₂(CN)₃ were first investigated by Kézsmárki *et al.* [189]. It was pointed out that there is no distinct optical gap in the energy range investigated from 8 meV to 5 eV, despite a clear charge gap found in the resistivity. On the contrary, the charge carriers become more localized with the development of a large Mott gap around 800 cm⁻¹ in the case of antiferromagnetic insulator κ -(BEDT-TTF)₂Cu₂[N(CN)₂]Cl. Thus, the relatively depressed optical gap seen in κ -(BEDT-TTF)₂Cu₂(CN)₃ was attributed to the contributions of the strong spin fluctuations due to the spin-liquid state at low temperatures. Later on, the low-energy charge dynamics of κ -(BEDT-TTF)₂Cu₂(CN)₃ was further investigated with an extension of the frequencies down to THz by Elsässer *et al.* [190]. It was shown that the weak charge gap seen in the optical conductivity follows a power-law behaviour. These findings are qualitatively consistent with the theoretical predictions that the gapless spinons can couple to the light, leading to additional contributions to the optical conductivity inside the Mott gap [191]. However, the extracted exponents are much smaller than the predicted values and has remained a puzzle. More recently, the unusual excess absorption observed in κ -(BEDT-TTF)₂Cu₂(CN)₃ was successfully and consistently explained as metallic fluctuations based on the combined optical and theoretical investigations of a series of organic quantum spin liquids [86].

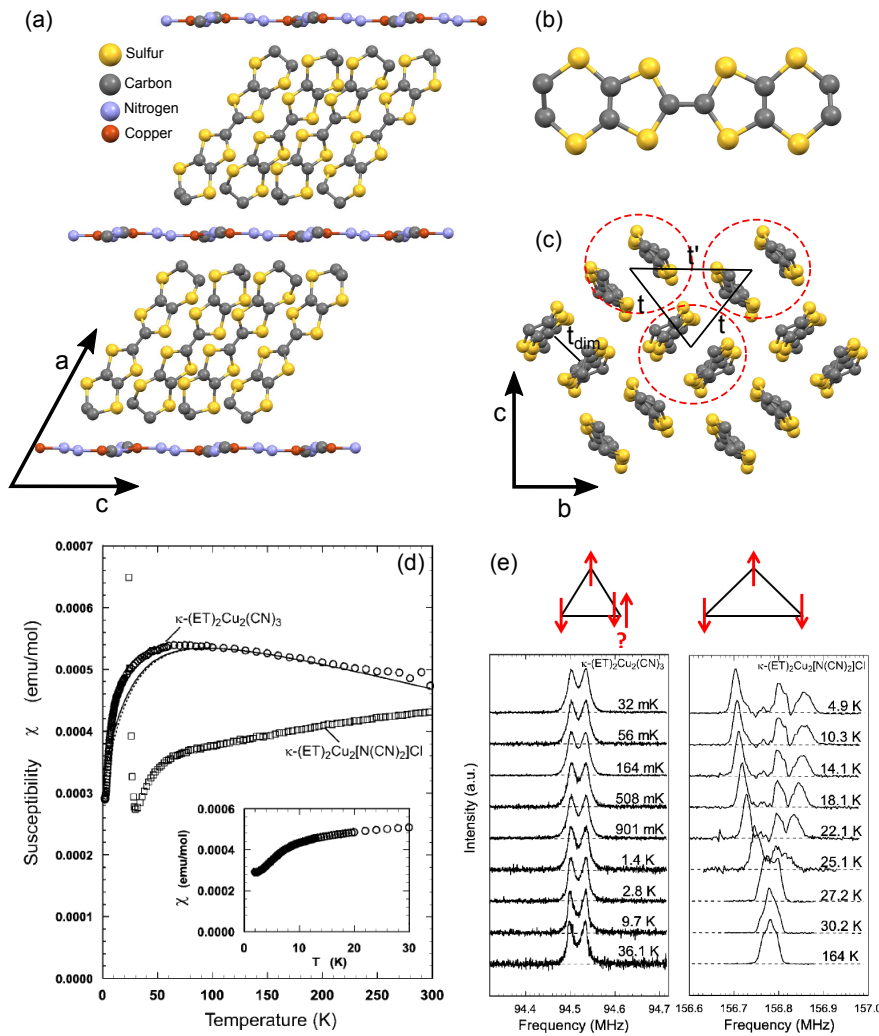


Figure 6.1.: (a) Crystal structure viewed along the b -axis. (b) BEDT-TTF molecule and (c) Packing motif of the ET conducting (bc)-plane viewed from a -axis. BEDT-TTF pairs are strongly dimerized and highlighted by red dashed circles. The intradimer transfer integral is much larger than interdimer one, i.e., $t_{dim} \gg t', t$. The BEDT-TTF dimers are forming triangular lattice with strong geometrical frustration ($t'/t \approx 1$). (d) Temperature evolution of the static susceptibility for κ -(BEDT-TTF)₂Cu₂(CN)₃ and κ -(BEDT-TTF)₂Cu₂[N(CN)₂]Cl. The susceptibility of κ -(BEDT-TTF)₂Cu₂[N(CN)₂]Cl exhibits a clear upturn below 27 K due to the AF order, while the one for κ -(BEDT-TTF)₂Cu₂(CN)₃ stays non-zero down to 1.9 K, indicating paramagnetic state. (e) Temperature-dependent NMR spectra for κ -(BEDT-TTF)₂Cu₂(CN)₃ and κ -(BEDT-TTF)₂Cu₂[N(CN)₂]Cl. In contrast to the clear splitting of the spectra in κ -(BEDT-TTF)₂Cu₂[N(CN)₂]Cl, neither broadening nor splitting is observed for κ -(BEDT-TTF)₂Cu₂(CN)₃ down to 32 mK. Panels (d) and (e) are adapted from Ref. [187]

The absence of magnetic order in κ -(BEDT-TTF)₂Cu₂(CN)₃ affects not only the electronic properties at ambient pressure but also the pressure-temperature phase diagram under external pressures. The entire phase diagram was constructed by Kurosaki *et al.* from pressure-dependent NMR and transport measurements [192]. As shown in Figure 6.2 (a), the spin liquid state persists under pressure up to the boundary of Mott transition. It implies that the system undergoes insulator-metal transition without the emergence of any magnetic order. Additionally, it was observed that the spin frustration in κ -(BEDT-TTF)₂Cu₂(CN)₃ has strong effects on the Mott transition at low temperatures. In comparison to the case of κ -(BEDT-TTF)₂Cu₂[N(CN)₂]Cl, κ -(BEDT-TTF)₂Cu₂(CN)₃ exhibits no re-entrant transition of insulator-metal-insulator and possesses a positive gradient of $dT/dp > 0$, owing to the suppression of entropy in the spin liquid state. Thus, κ -(BEDT-TTF)₂Cu₂(CN)₃ was considered to be the first organic salt, exhibiting first-order Mott transition purely driven by the enhancement of bandwidth under pressure as shown in Figure 6.2 (b).

An alternative way to trigger insulator-metal transition in κ -(BEDT-TTF)₂Cu₂(CN)₃ is applying chemical pressure with partial substitution of sulfur atoms by isovalent selenium atoms [193]. Since both selenium and sulfur atom belong to the chalcogens, the replacement of sulfur atom with selenium atom will neither change the crystal structure nor the band filling. The bandwidth is enhanced by the increase of the transfer integral due to the larger size of selenium atoms. Similar alloying-induced insulator-metal transition has been explored in the series of κ -(BEDT-TTF)₂Cu₂[N(CN)₂]Cl_{*x*}Br_{1-*x*} with different concentrations of Br atoms in anion layers [38, 39]. As shown in Figure 6.2 (c,d), the system is shifted across the Mott phase boundary upon applying physical pressure or Se-alloying. Despite the similarities between pressure- and alloying-effect seen by dc transport measurements, the difference between them are expected to occur at finite frequencies. In Figure 6.2 (b), we schematically demonstrate the distinct microscopic mechanisms of the insulator-metal transitions induced by Se-alloying and the hydrostatic pressure. The application of physical pressure homogeneously increases the bandwidth, whereas Se-substitution will inevitably introduce local impurities or disorders, which are possibly responsible for the Anderson localization in κ -(BEDT-TTF)₂Cu₂(CN)₃.

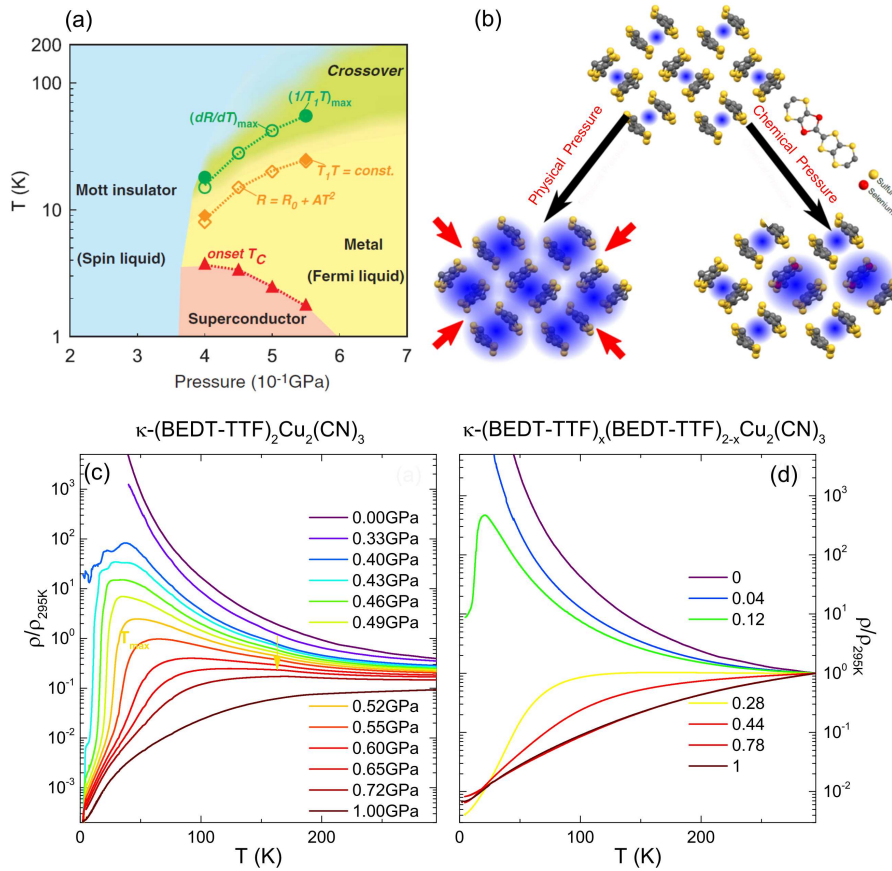


Figure 6.2.: (a) Schematic $p - T$ phase diagram of κ -(BEDT-TTF) $_2$ Cu $_2$ (CN) $_3$ obtained from transport and NMR measurements under external pressures. Due to the spin frustration the Mott boundary has a positive gradient ($dT/dp > 0$) in the whole temperature range; after [192]. (b) Two approaches to realizing Mott insulator-metal phase transition in half-filled two-dimensional organic system. The bandwidth can be tuned either by external physical pressure or chemical substitution. In the later case, local disorder will give rise to additional vibrational modes and electronic excitations. The value of the bandwidth are schematically denoted by the size of the blue circle. (c) Pressure evolution of the resistance for κ -(BEDT-TTF) $_2$ Cu $_2$ (CN) $_3$ as a function of temperatures. (d) Temperature-dependent resistance of κ -[(BEDT-STF) $_x$ (BEDT-TTF) $_{1-x}$] $_2$ Cu $_2$ (CN) $_3$ for different BEDT-STF molecule substitution ratios. The resistivity data are measured by A. Löhle.

Up to now, the magnetic and electrical properties of κ -(BEDT-TTF)₂Cu₂(CN)₃ have been extensively investigated by NMR and dc-resistivity measurements under pressure, while the frequency-dependent charge dynamics under pressure has not been explored yet. In this study, we want to elucidate the electronic and vibrational evolution of the pressure-tuned metal-insulator transition in the spin liquid candidate κ -(BEDT-TTF)₂Cu₂(CN)₃ via pressure- and temperature-dependent infrared reflectivity measurements. In addition, we will compare the results under pressure with those of Se-alloyed samples.

6.2. Vibrational properties

Single crystals of κ -(BEDT-TTF)₂Cu₂(CN)₃ were grown by standard electrochemical methods [194, 195]. The same method was employed for the growth of single crystals of κ -[(BEDT-STF)_{*x*}(BEDT-TTF)_{1-*x*}]₂Cu₂(CN)₃ for various concentrations of BEDT-STF molecules [193]. The substitution ratio *x* was calculated through the comparison of the intensity of sulfur atoms with that of selenium atoms utilizing energy-dispersive X-ray spectroscopy with κ -(BEDT-TTF)₂Cu₂(CN)₃ as a reference. Samples with nicely shining surfaces were picked up for optical measurements. Two samples have been used for the pressure-dependent infrared measurements. For sample 1, only far-infrared have been performed at various pressures from 0.1 GPa to 1.1 GPa. For sample 2, we have measured the optical spectra over a broad energy range from 80 to 8000 cm⁻¹ for a selection of pressures, i.e., *p* = 0.15, 0.85, 0.95, 1.1 GPa. In all cases, the spectra were collected with light polarized in the two main crystallographic axis from room temperature down to the lowest temperature 10 K.

The lattice parameters of κ -(BEDT-TTF)₂Cu₂(CN)₃ and κ -(BEDT-STF)₂Cu₂(CN)₃ at room-temperature are summarized in Table 6.1 [196]. Both compounds exhibit the same crystal structure of monoclinic space group, while the lattice constants and volume of the STF-substituted compounds are expanded compared with the pristine sample κ -(BEDT-TTF)₂Cu₂(CN)₃. This is simply due to the larger atomic radius of the Se ions of the BEDT-STF molecules. In contrast, hydrostatic pressure induces a decrease in the lattice parameters and the unit cell volume. Similar expansion of lattice was observed in the Ag-substituted κ -(BEDT-TTF)₂Ag₂(CN)₃ as

Table 6.1.: Crystallographic data for κ -(BEDT-TTF) $_2$ Cu $_2$ (CN) $_3$ at ambient conditions ($T = 293$ K). For comparison, we also list the data for the Ag-substituted κ -(BEDT-TTF) $_2$ Ag $_2$ (CN) $_3$ [197] and STF-substituted κ -(BEDT-STF) $_2$ Cu $_2$ (CN) $_3$ analogues. The data for κ -(BEDT-STF) $_2$ Cu $_2$ (CN) $_3$ were provided privately from Y. Saito.

Chemical formula	C $_{23}$ H $_{16}$ Cu $_2$ N $_3$ S $_{16}$ κ -(BEDT-TTF) $_2$ Cu $_2$ (CN) $_3$	C $_{23}$ H $_{16}$ Ag $_2$ N $_3$ S $_{16}$ κ -(BEDT-TTF) $_2$ Ag $_2$ (CN) $_3$	C $_{23}$ H $_{16}$ Cu $_2$ N $_3$ S $_{12}$ Se $_4$ κ -(BEDT-STF) $_2$ Cu $_2$ (CN) $_3$
Form. weight M_W	974.52	1063.09	1162.05
Crystal system	monoclinic	monoclinic	monoclinic
Space group	P2 $_1$ /c	P2 $_1$ /c	P2 $_1$ /c
a (Å)	16.117(5)	15.055(1)	16.2965(8)
b (Å)	8.5858(9)	8.7030(7)	8.6082(5)
c (Å)	13.397(3)	13.412(1)	13.3985(6)
α (deg.)	90	90	90
β (deg.)	113.42(2)	91.307(1)	113.13(6)
γ (deg.)	90	90	90
Volume V (Å 3)	1701.11	1756.8	1728.5
Z	2	2	2
Density D_c (g/cm 3)	1.902	2.010	2.233

well [197]. The Ag substitution basically works at negative pressure, which drives the system away from the Mott transition to a stronger correlated region. On the contrary, the application of negative pressure by BEDT-STF substitution actually leads to a metallic ground state in κ -(BEDT-STF)₂Cu₂(CN)₃. This is associated with the much larger spread of the selenium 4d orbitals, which locally induce an increased inter-molecular interactions through Se-Se contacts, and thus, an enhancement of the bandwidth.

Figure 6.3 shows the b- and c-polarized reflectance spectra at room temperature in the frequency range from 300 cm⁻¹ to 600 cm⁻¹ for all applied pressures and studied STF substitutions. At ambient conditions, several molecular vibrational modes can be well resolved for both directions of polarization. These modes are related with the in-plane totally symmetric A_g modes and show up due to strong coupling to the charge transfer band. In this study, we temporally assign the two strong lines around 433 cm⁻¹ to ν_{10} and these weak features around 490 cm⁻¹ to ν_9 , following the suggestions from Eldridge *et al.* [198–200]. Both modes involve the C-S stretching vibrations and are sensitive to both charge disproportionation and structural changes. The observed ν_{10} (ν_9) doublet (instead of singlet) implies that there are two slightly different ET dimers per unit cell in this salt. Upon pressurizing, the two ν_{10} modes exhibit a blue shift, arising from the contraction of the unit cell volume under pressure, while the ν_9 modes remain nearly unchanged. Besides that, the intensity of all modes become less pronounced as a result of the increasing electronic background. From our analysis of these two modes, there is no indication of any structural changes upon approaching the critical pressure of $p_c \sim 0.35$ GPa. In contrast to the observed hardening of the ν_{10} modes under pressure, the vibrational spectra behave qualitatively different upon Se alloying. The replacement of S atoms by Se atoms mainly have two effects on the spectra of ν_{10} modes: firstly, it will affect the force constants of C-S bonds and the reduced mass of whole molecule. This only causes a shift in the vibrational frequencies; secondly, its asymmetrical molecular geometry will give rise to the multiple splitting. For simplicity, we omit the change in force constants, since the lattice expands slightly in κ -(BEDT-STF)₂Cu₂(CN)₃. The expected value of the ν_{10} of BEDT-STF molecule would be $\omega_{\nu_{10}} = 434(m_S/m_{Se})^{0.5} = 368$ cm⁻¹, which is very close to the observed value shown in Figure 6.3 (d,e). Since the A_g modes in infrared

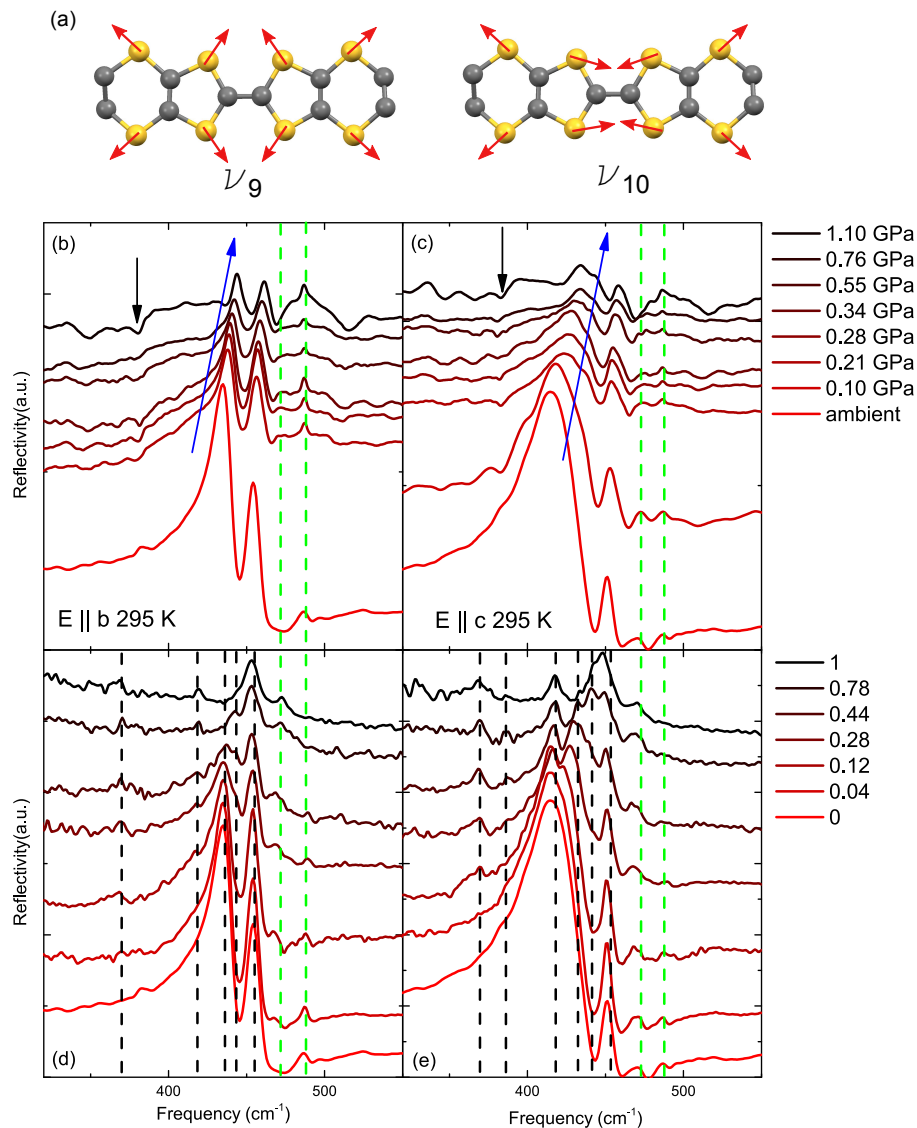


Figure 6.3.: (a) Atomic displacement vectors of the two totally symmetric EMV-activated A_g modes, i.e., ν_9 and ν_{10} . Both vibrations involve the stretch of the C-S bonds. (b,c) Pressure-dependent infrared spectra of κ -(BEDT-TTF) $_2$ Cu $_2$ (CN) $_3$ for $E \parallel b$ and $E \parallel c$ at room temperature. The black arrow denotes the artefact due to the vanishing of the spectral intensity at this frequency. Blue arrows are a guide to the eye. (d,e) Infrared spectra of κ -[(BEDT-STF) $_x$ (BEDT-TTF) $_{1-x}$] $_2$ Cu $_2$ (CN) $_3$ as a function of x . Black dashed lines stand for the multiplet of ν_{10} mode occurred at (BEDT-STF)-rich sample. ν_{10} modes remain almost unchanged (green dashed line). All spectra are offset for clarity

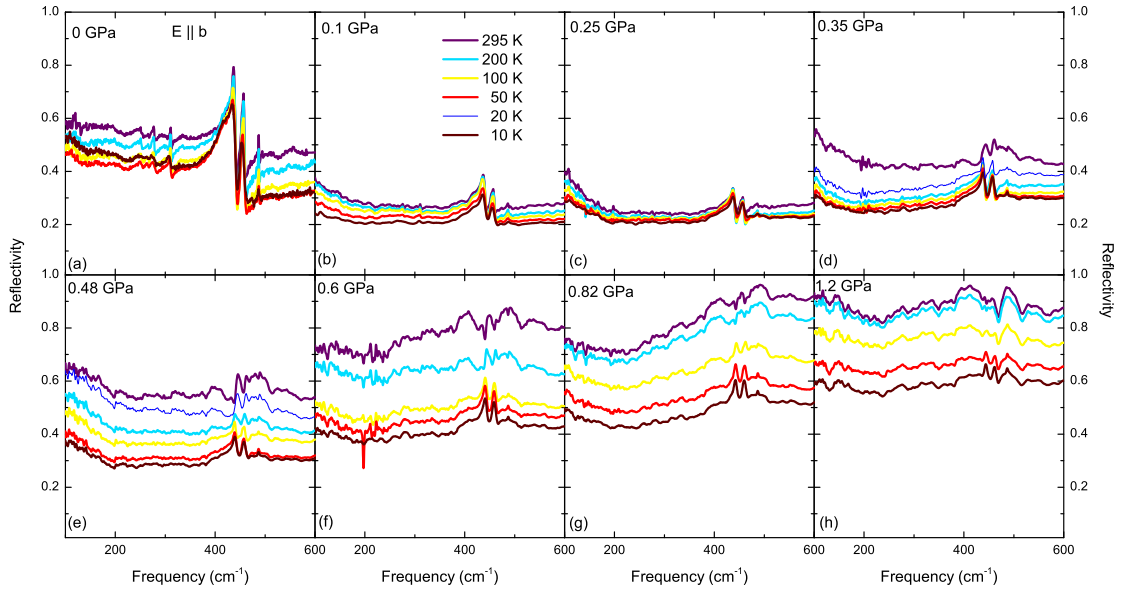


Figure 6.4.: Pressure dependence of the optical reflectivity spectra of $\kappa\text{-(BEDT-TTF)}_2\text{Cu}_2(\text{CN})_3$ as a function of temperature in the far-infrared energy range for $E||b$. Note that it is reasonable to have lower absolute value of reflectivity at the sample-diamond interface compared to that at ambient pressure condition. After first round of the far-infrared measurements, we found out that too much oil has entered into interface between sample and diamond. Thus, unfortunately we can not obtain the mid-infrared spectra.

spectra is softened with respect to that in Raman spectra, it will be very interesting to perform Raman measurements on $\kappa\text{-(BEDT-TTF)}_2\text{Cu}_2(\text{CN})_3$ under physical and chemical pressure, in order to probe the barre mode frequencies of these modes in future.

6.3. Electronic excitations

Figure 6.4 shows the b-polarized reflectivity spectra of $\kappa\text{-(BEDT-TTF)}_2\text{Cu}_2(\text{CN})_3$ (sample 1) for pressures below and above the critical pressure $p_c = 0.35$ GPa at various temperatures, ranging from room temperature down to 10 K, in the frequency range from 100 cm^{-1} to 600 cm^{-1} . At ambient pressure conditions, the spectra are composed of a relatively flat electronic background and several vibra-

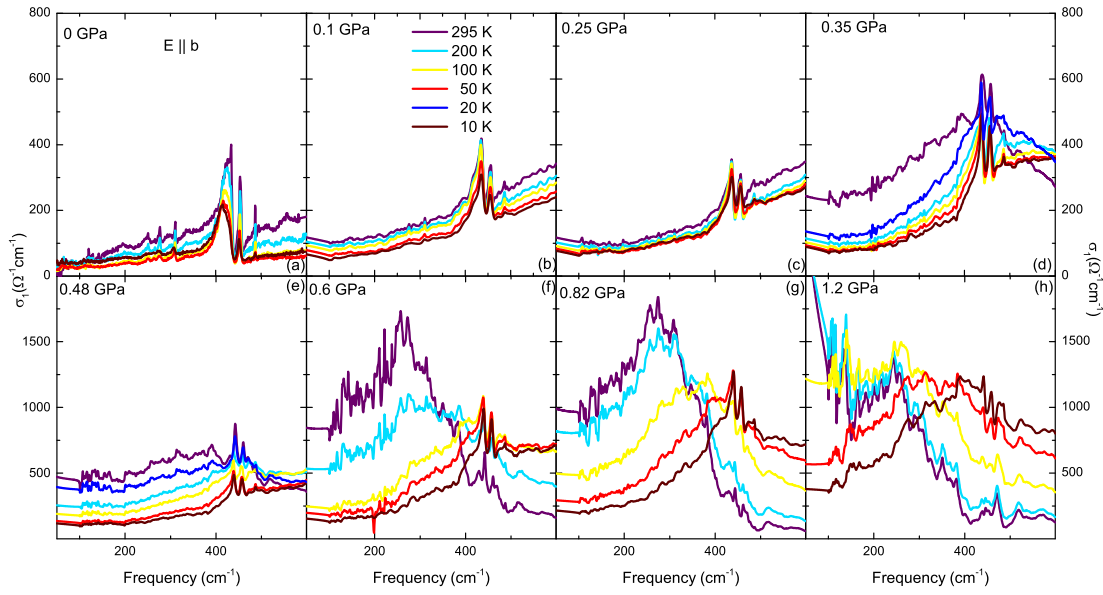


Figure 6.5.: Temperature- and pressure-dependent optical conductivity $\sigma_1(\omega)$ for $E||b$. Since we do not have obtained the mid-infrared data for high pressures, the ones at ambient condition are used for the K-K analysis.

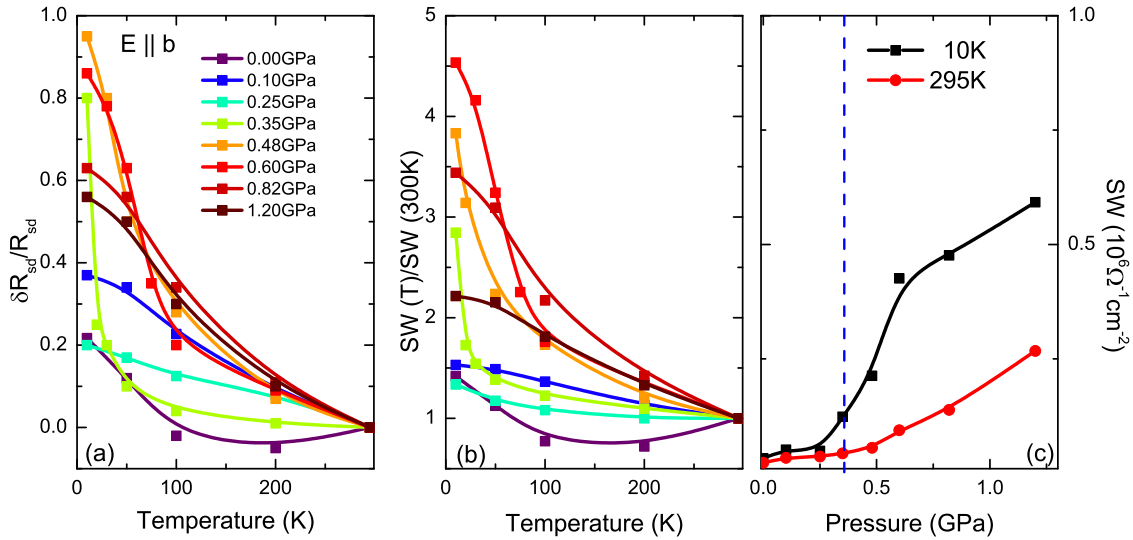


Figure 6.6.: (a) Temperature evolution of the normalized change of the reflectivity $\delta R(p, T)/R(p, 300K)$ at various pressure as indicated. The values of reflectivity are taken at 100 cm^{-1} . (b) Normalized spectral weight as a function of temperature for various pressures. $SW = \int_0^{\omega_C} \sigma_{\text{Drude}}(\omega) d\omega$ ($\omega_C = 400 \text{ cm}^{-1}$) (c) Spectral weight as a function of pressure at 295 K and 10 K. Dashed black line denotes the critical pressure $p_c = 0.35 \text{ GPa}$. Solid lines are guide for the eye.

tional A_g modes with the strongest ν_{10} modes centered around 400 cm⁻¹. With decreasing temperature, these vibrational modes get sharper and shift slightly to the high energy region. Interestingly, the low-frequency reflectivity increases gradually as the temperature is lowered. This is in strong contrast to the case of β' -EtMe₃Sb[Pd(dmit))₂]₂ and κ -(BEDT-TTF)₂Ag₂(CN)₃ [86]. Similar temperature evolution is observed below 0.35 GPa. When the pressure is raised to 0.35 GPa, a sharp increase in the reflectivity is observed below 20 K, demonstrating clearly the temperature-driven first-order insulator-metal transition occurred at the Mott boundary. These findings are well in line with the results from pressure-dependent resistance measurements shown in Figure 6.2 (c), where a drastic resistance drop appears at around 20 K under a pressure of 0.4 GPa. With further application of pressure up to 1.2 GPa, the reflectivity rises continuously with a loss of intensity of the vibrational modes upon cooling. This indicates that the metallic state is entered above 0.35 GPa. The quantitative illustration of the pressure-induced change of the reflectivity can be seen in Figure 6.6 (a).

The temperature dependence of the calculated optical conductivity spectra is presented in Figure 6.5. Below 0.35 GPa, the low-energy optical conductivity actually increases as the temperature is reduced, despite the opening of an energy gap observed in dc resistivity. The absence of a clear optical gap and anomalous temperature dependence of optical conductivity imply that the κ -(BEDT-TTF)₂Cu₂(CN)₃ salt is located much closer to the Mott boundary compared to the κ -(BEDT-TTF)₂Ag₂(CN)₃ and β' -EtMe₃Sb[Pd(dmit))₂]₂ compounds, where a well defined Mott gap was found at low temperatures [86]. On the other hand, qualitatively different features of the electrodynamic response were observed in the STF-substituted κ -[(BEDT-STF)_{*x*}(BEDT-TTF)_{*1-x*}]₂Cu₂(CN)₃ salts. In the insulating state with low STF-content, an additional strong far-infrared excitation develops for low temperatures. With lowering the temperature, the new peak softens but comes to a halt at finite energy, and gains spectral weight at the same time [74]. In the κ -[(BEDT-STF)_{*x*}(BEDT-TTF)_{*1-x*}]₂Cu₂(CN)₃ case, BEDT-STF molecules can inevitably induce local disorder, and thus lead to Anderson localization. According to the theoretical calculation of a 2D disordered Mott system [201–203], the Mott gap vanishes and new excitations emerge within the gap as disorder increases. Such features indeed have been confirmed experimentally through the detailed angle re-

solved photoemission measurements on Cu-intercalated 1T-TaS₂ [204], in which the disorder generates a finite spectral weight at zero energy, together with a spatially inhomogeneous state. These observations strongly suggest the intrinsically distinct nature of the Mott transition driven by physical and chemical pressure as illustrated in Figure 6.2 (b).

To quantitatively characterize the temperature evolution of low-energy charge dynamics, we plot the spectral weight normalized to the one at room temperature in Figure 6.6 (b). The overall temperature-dependent behaviour is quite similar to those of the change in reflectivity. In the insulating state ($p < 0.35$ GPa), we observe a gradual increase in SW below 200 K. The first-order Mott transition at $p = 0.35$ GPa gives rise to a sharp rise of the SW below 20 K. At higher pressures ($p > 0.35$ GPa), the change becomes gradually smoother, suggesting the entrance to the crossover regime. The difference of the pressure effects on the SW at 295 K and 10 K can be clearly seen in Figure 6.6 (c). While pressure induces a continuous changes up to 1.2 GPa at room temperature, the SW significantly grows as the system is tuned across the Mott boundary under $p = 0.35$ GPa at 10 K.

The room-temperature optical spectra of the κ -(BEDT-TTF)₂Cu₂(CN)₃ with improved sample quality (sample 2) are reported in Figure 6.7 in a broad energy range between far- and mid-infrared (100-8000 cm⁻¹) for selected values of pressures as indicated. As can be seen in Figure 6.7 (a,c), the general features of the spectra at 0.2 GPa are quite similar to these measured at ambient conditions. The absolute value of reflectivity at 0.2 GPa is relatively low, showing typical semiconductor behaviour. The dip seen at around 5000 cm⁻¹ clearly defines the energy boundary between intra-band and inter-band contributions. The broad absorption bands centered at about 3000 cm⁻¹ in the optical conductivity, are induced by transitions between the lower and upper Hubbard band. Additionally, strong vibrational modes show up at around 400, 900 and 1300 cm⁻¹, which are A_g modes of the BEDT-TTF molecule activated by electron-molecular vibrational coupling (EMV) [88]. With increasing pressure, an increase in the absolute value of the reflectivity is observed in the whole energy range. Especially, the slope of the reflectivity in the far-infrared range, changes significantly from negative to positive, indicating the gradual metallization occurs at room temperature. As a result, the mid-infrared

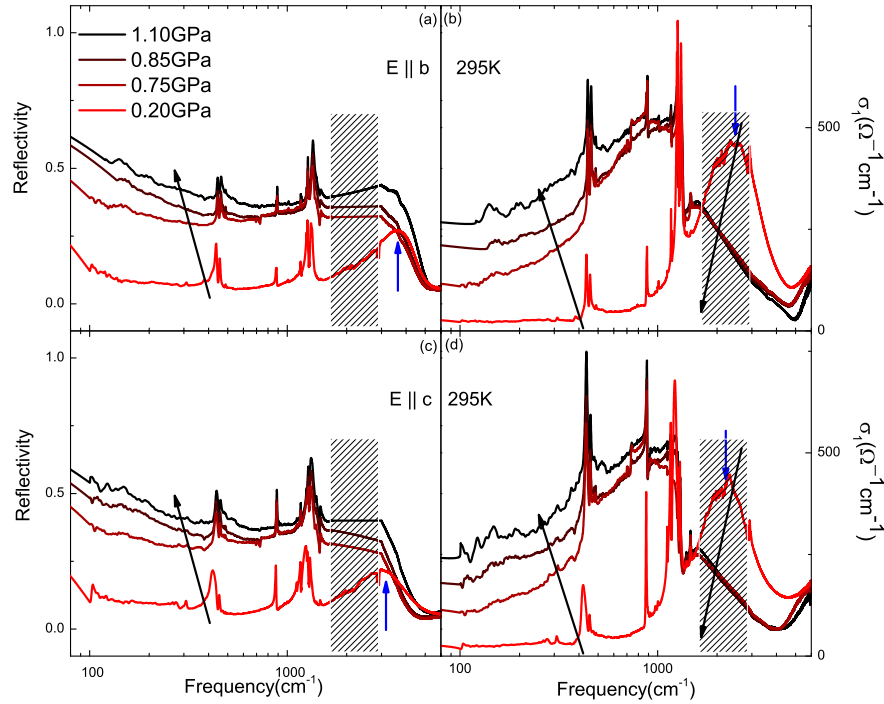


Figure 6.7.: Room-temperature reflectivity spectra of κ -(BEDT-TTF)₂Cu₂(CN)₃ measured at the sample-diamond interface as a function of pressure for $E||b$ (a) and $E||c$ (c). The dashed area corresponds to the frequency range where strong diamond absorption occurs. A linear extrapolation has been used in this energy range. (b,e) Calculated optical conductivity spectra at various pressures as indicated.

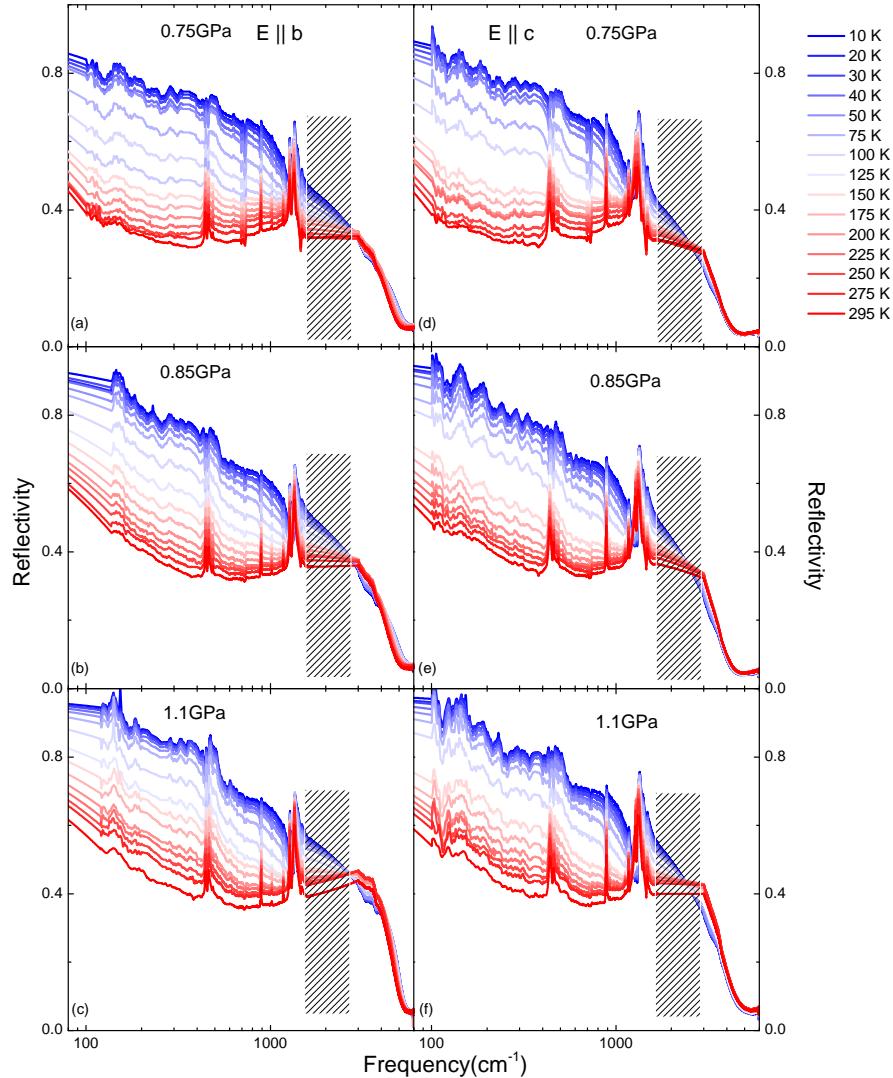


Figure 6.8.: Temperature- and pressure-dependent reflectivity spectra of κ -(BEDT-TTF) $_2$ Cu $_2$ (CN) $_3$ for the polarizations $E||b$ (a-c) and $E||c$ (d-e). The dashed area corresponds to the frequency range where strong diamond absorption occurs. Due to the influence of the polyethylene window of the cryostat, there are periodic fringes on top of the spectra in the far infrared range at low temperatures.

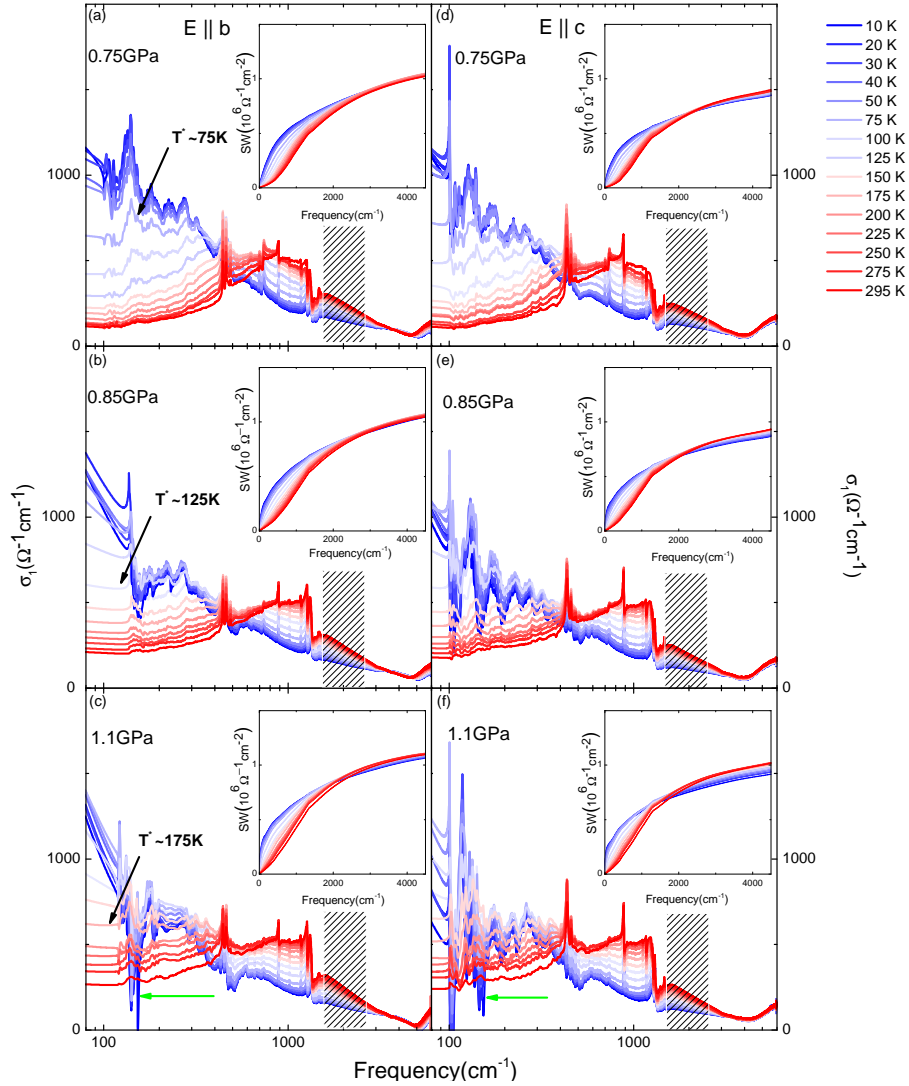


Figure 6.9.: Pressure-dependent optical conductivity spectra of $\kappa\text{-(BEDT-TTF)}_2\text{Cu}_2(\text{CN})_3$ for the polarizations $E||b$ (a-c) and $E||c$ (d-e) obtained at different temperatures. The insets show the temperature-dependent spectral weight ($SW = \int_0^{\omega_C} \sigma_{\text{Drude}}(\omega) d\omega$) as a function of cut-off frequency ω_C . The crossover temperature T^* was identified as the temperature, at which the optical conductivity $\sigma_1(\omega)$ starts to show negative slope at the low-energy range. The green arrows denote the oil absorption lines at low temperatures

absorption band gets suppressed with a spectral weight transfer to the low-energy region below 1000 cm^{-1} . Up to pressure as high as 1.2 GPa, the low-energy optical conductivity still remains very broad with no signature of narrow Drude response. This indicates that a bad metallic instead of Fermi liquid state is realized in κ -(BEDT-TTF) $_2$ Cu $_2$ (CN) $_3$. Nevertheless, our room-temperature results are consistent with pressure-dependent dc-resistivity measurements, suggesting clearly the enhancement of the density of state at Fermi level due to the increase in bandwidth upon increasing pressure.

To investigate the development of the electronic properties toward low temperatures in the highly metallic state, Figure 6.8 depicts the temperature-dependent reflectivity spectra for both b- and c-axis at selected high pressures as indicated. The absolute value of the reflectivity increases significantly below 3000 cm^{-1} and the low-energy part changes progressively to $1-\omega^2$ like with lowering the temperature, indicating the crossover from incoherent to coherent conduction state. At the same time, the vibrational modes get weaker and become Fano line shape due to the strong coupling with the enhanced itinerant electrons. As can be seen in Figure 6.9, the low-energy optical conductivity continuously gets enhanced with a gain in spectral weight and a Drude-like response develops upon cooling, which is a signature of the coherent quasi-particle response. Correspondingly, a strong suppression is observed in the mid-infrared region. Such T -driven spectral-weight transfer is in good agreement with the predictions of theoretical calculations in the bandwidth-controlled metal-insulator transition in Mott insulators [87]. Furthermore, the crossover temperature, differentiating good metal from bad metal, shifts towards higher temperatures with elevating pressure. This finding is also in line with the dc-transport and NMR measurements, where the broad peak, shown in dR/dT and $1/T_1T$, exhibits blueshift in temperature at high pressures [192].

6.4. Fermi liquid behaviour

In this section, we will mainly focus on the discussion of the universal optical signatures of Fermi-liquid behaviour in κ -(BEDT-TTF) $_2$ Cu $_2$ (CN) $_3$ under high pressures. The mass enhancement and scattering rate of κ -(BEDT-TTF) $_2$ Cu $_2$ (CN) $_3$ at selected high pressures are shown in Figures 6.10 and 6.11 for temperatures from 10 K to

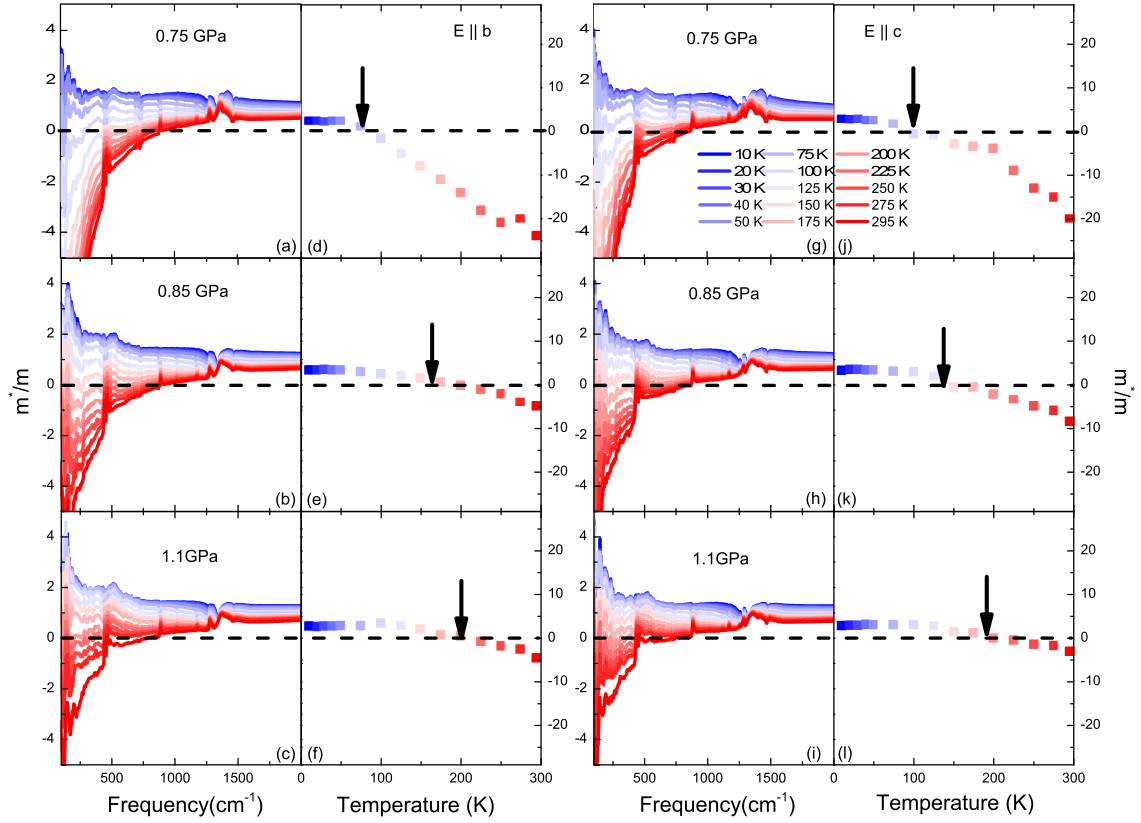


Figure 6.10.: Effective mass enhancement $m^*(\omega, T)/m$ of $\kappa\text{-(BEDT-TTF)}_2\text{Cu}_2(\text{CN})_3$ for the polarizations $E||b$ (a-e) and $E||c$ (g-i) at $p = 0.75$ GPa, 0.85 GPa and 1.1 GPa. The mass enhancement m^*/m is related to the real part of the memory function M_1 via $m^*/m = M_1/\hbar\omega + 1$ (see Equation 2.46 and 2.48). Temperature dependence of $m^*(\omega, T)/m$ taken at $\omega = 100 \text{ cm}^{-1}$ for $E||b$ and $E||c$ is plotted in panels (d-f) and (j-l), respectively. The cross over temperatures, below which the effective mass is positive, are indicated by black arrows

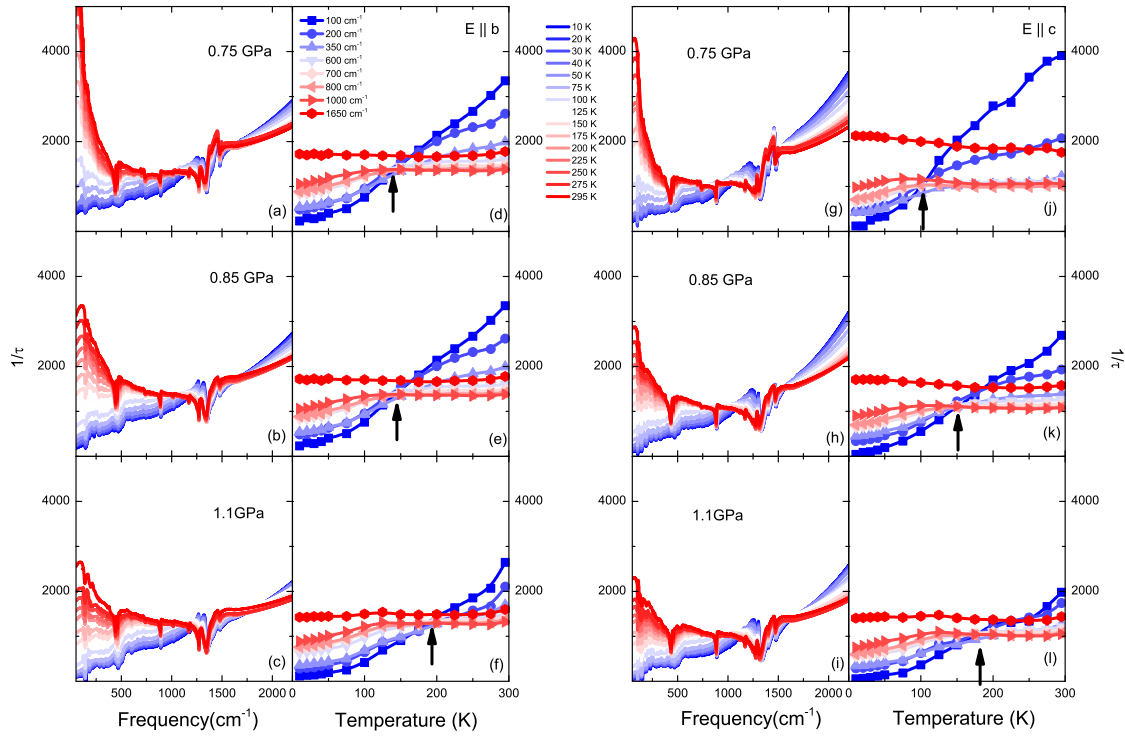


Figure 6.11.: Scattering rate $1/\tau$ of κ -(BEDT-TTF) $_2$ Cu $_2$ (CN) $_3$ for the polarizations $E||b$ (a-e) and $E||c$ (g-i) at temperatures between 10 K and 295 K. Here, scattering rate $1/\tau$ represents the imaginary part of the memory function M_2 (see Equation 2.47). Temperature-dependent scattering rate at selected values of ω from 100 cm^{-1} to 1650 cm^{-1} for $E||b$ (d-f) and $E||c$ (j-l). Black arrows stand for the isosbestic points.

295 K.

As shown in Figure 6.10 (a), the mass enhancement m^*/m at $p = 0.75 \text{ GPa}$ for $E||b$ exhibits nearly no frequency dependence and increases slightly upon cooling at high energies. However, a strong frequency-dependent behaviour is observed in the low energy region. At high temperatures, m^*/m is an increasing function of frequency, leading to a negative value of m^*/m in the far-IR region. The observed unphysical negative value of m^*/m implies that the quasi-particle is not well defined at high- T bad metallic state. With lowering the temperature, the slope of m^*/m decreases gradually, followed by a positive slope at the lowest temperature. In Figure 6.10 (d), we plot the temperature evolution of m^*/m at $\omega = 100 \text{ cm}^{-1}$. The m^*/m exhibits positive value only below certain temperature (75 K), which can be used

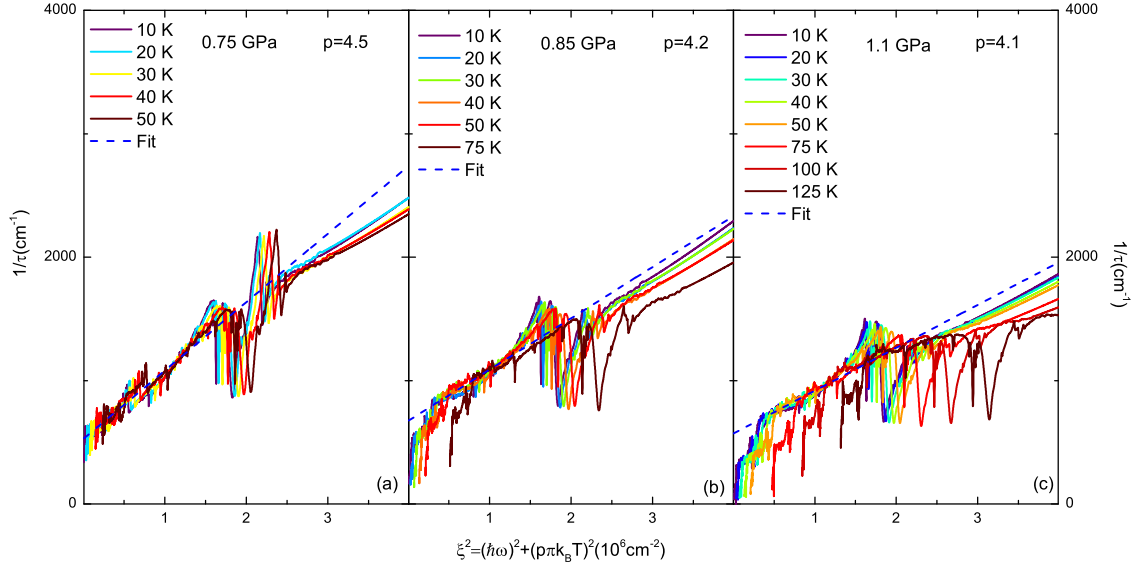


Figure 6.12.: Scattering rate of $\kappa\text{-(BEDT-TTF)}_2\text{Cu}_2(\text{CN})_3$ for $E||c$ as a function of single parameter $\xi^2 \equiv (\hbar\omega)^2 + (p\pi k_B T)^2$ with $p=4.5, 4.2, 4.1$ for $p=0.75$ GPa (a), 0.85 GPa (b) and 1.1 GPa (c), respectively. Dashed blue lines show the linear fits, displaying the universal Fermi-liquid behaviour. The deviation of $1/\tau(\xi)$ from the Fermi-liquid behaviour at low value of ξ for $p=0.85$ GPa and 1.1 GPa are most likely due to the limited quality of our far-infrared data.

as alternative way of defining the crossover temperature T^* . With the increasing pressure further, the T^* shifts to high temperatures. This is consistent with transport measurements.

Now we turn our attention to the analysis of the optical scattering rate $1/\tau$ depicted in Figure 6.11 (a). At the lowest temperature $T=10$ K, $1/\tau$ displays a ω^2 dependence upto around 1000 cm^{-1} . As T increases, we still can observe the ω^2 behaviour below 50 K. With increasing temperature further, $1/\tau(\omega)$ shows a gradual change of curvature from upward to downward. This indicates the loss of coherence of the Fermi liquid state, in other words, collapse of long-lived quasi-particles. The temperature evolution of $1/\tau$ at selected values of frequency is shown in Figure 6.11 (d). At 100 cm^{-1} , the scattering rate decreases as T^2 at the low- T range, while the temperature dependence of $1/\tau$ become less steep at higher energies. In addition, the cross over temperature shows up as isosbestic point in the temperature dependence of scattering rate. Here, the isosbestic point is defined as the temperature, at which the scattering rate obtained at different frequencies has the equal value.

The presence of ω^2 - and T^2 -component found in $1/\tau(\omega, T)$ strongly indicates that the system follows universal Fermi liquid behaviour at low temperatures and frequencies [122].

According to the local Fermi liquid theory, $1/\tau(\omega, T)$ is expected to scale with a single parameter $\xi^2 \equiv (\hbar\omega)^2 + (p\pi k_B T)^2$ [122]. Thus, we plot $1/\tau(\xi^2)$ as a function of ξ^2 in Figure 6.12, in order to check the possible universal scaling form for our data. Indeed, all data collapse onto a single curve for $\xi^2 < 2 \times 10^6 \text{ cm}^{-2}$. The slope of $1/\tau(\xi^2)$, which is inversely proportional to the scaling temperature T_0 , decreases, as pressure is raised. The enhancement of the T_0 clearly demonstrates the weakening of the correlation strength with increasing pressure. Quite interestingly, p is found to be apparently pressure-dependent. Thus, it seems to contain the information of electron-electron correlation as well. From our analysis, the obtained value of p is much larger than the theoretical predicted universal value $p = 2$, which may be due to an additional elastic scattering channel as proposed recently by Maslov *et al.* [121]. Furthermore, the Fermi liquid characteristic can be also observed in the raw reflectivity and phase spectra as shown in Figure 6.13. In the thermal regime, $1-R(\omega)$ is approximately proportional to M_2 [125], and thus rise quadratically with energy. Correspondingly, the phase ϕ follows $\phi \propto M_1$ and has a linear frequency dependence. The same analysis is applied to the other two materials, κ -(BEDT-TTF)₂Cu[N(CN)₂Br_xCl_{1-x}] and κ -(BEDT-STF)₂Cu₂(CN)₃ (see Figure 6.13 (a-f)). The low-energy ω^2 and ω behaviour is indeed observed in $1-R(\omega)$ and $\phi(\omega)$, respectively.

A more direct evidence of the Fermi liquid signatures can be found in the complex optical conductivity. In the formalism of local Fermi liquid theory suggested by Berthod *et al.* [122], the optical conductivity exhibits non-Drude feature, a shoulder in a log-log plot around the thermal energy range, $\hbar\omega \sim 2\pi k_B T$. To make an accurate comparison of the experimental results with theory, we have to subtract the interband components from the total conductivity σ_1 . The optical conductivity spectra are first fitted using Drude-Lorentz-Fano model: Two Drude modes are used to reflect the quasi-particle response at zero energy, the mid-infrared Hubbard bands and high energy interbands are accounted for by several Lorentzians, the EMV-type A_g vibrations are fitted by Fano terms. The results of the intra-

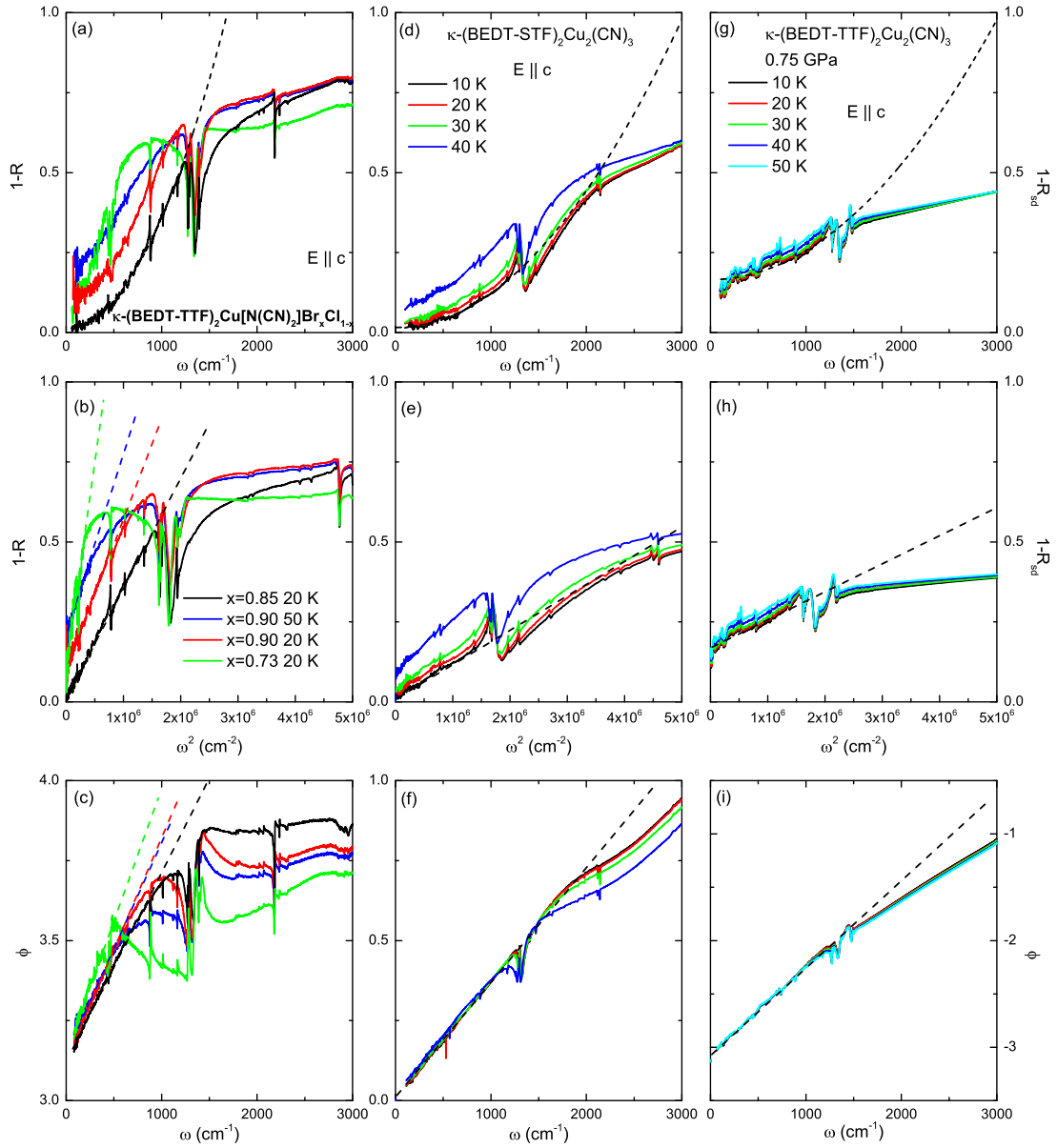


Figure 6.13.: Reflectivity data of (a,b) $\kappa\text{-(BEDT-TTF)}_2\text{Cu}[\text{N}(\text{CN})_2]\text{Br}_x\text{Cl}_{1-x}$ ($x = 0.73, 0.85$ and 0.9), (d,e) $\kappa\text{-(BEDT-STF)}_2\text{Cu}_2(\text{CN})_3$ and (f,h) $\kappa\text{-(BEDT-TTF)}_2\text{Cu}_2(\text{CN})_3$ ($p = 0.75$ GPa) for $E||c$ plotted as $1-R(\omega)$ versus ω and ω^2 at selected temperatures as indicated. The data can be well fitted using power law $1-R(\omega) \propto \omega^2$ (dashed lines). Phase ϕ as a function of frequency. At the low-energy region, it exhibits a linear-like dependence on ω (dashed lines). Note that the data under pressure is normalized to $n_{\text{dia}}^{1/2}$ ($n_{\text{dia}} = 2.4$ is the index of the diamond). The negative value of the phase ϕ is attributed to an additional phase shift induced by the diamond. The raw data of $\kappa\text{-(BEDT-TTF)}_2\text{Cu}[\text{N}(\text{CN})_2]\text{Br}_x\text{Cl}_{1-x}$ and $\kappa\text{-(BEDT-STF)}_2\text{Cu}_2(\text{CN})_3$ are taken from Refs. [39, 74].

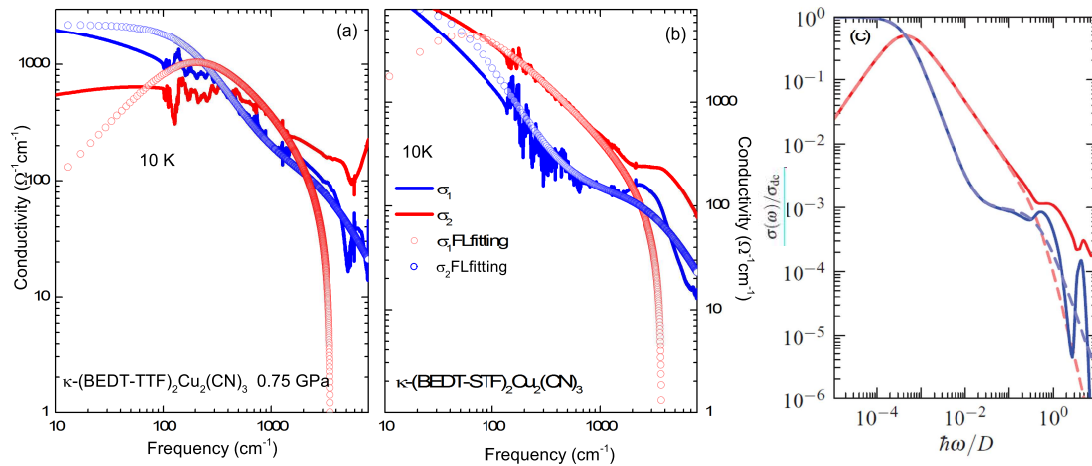


Figure 6.14.: Real and imaginal part of optical conductivity of (a) κ -(BEDT-TTF)₂Cu₂(CN)₃ and (b) κ -(BEDT-STF)₂Cu₂(CN)₃ at 10 K and the corresponding Fermi-liquid scaling fits. (c) Theoretical calculations of the optical conductivity for the doped Hubbard model obtained from DMFT calculations (solid lines). D stands for the half-bandwidth of the system. The intraband contributions are fitted by the universal FL-scaling form (dashed lines). The σ_1 (blue) and σ_2 (red) are plotted on a log-log scale

band contributions and the fits based on universal Fermi-liquid model are shown in Figure 6.14. We can clearly observe the foot structure at around 500 cm⁻¹ in both κ -(BEDT-TTF)₂Cu₂(CN)₃ ($p = 0.75$ GPa) and κ -(BEDT-STF)₂Cu₂(CN)₃ compounds, which is the key feature of the Fermi liquid theory, instead of signature of non-Fermi liquid physics. In Figure 6.14 (c), we plot the complex optical conductivity of the hole-doped Hubbard model based on DMFT predictions. The overall shape of the spectra is in good agreement with the our experimental findings: The peak structure shows up at mid-infrared regime as a result of the transitions between two Hubbard bands; at lower frequencies, the intraband component can be very well described according to Equation 2.62. However, we found out that the Equation 2.62 can only qualitatively mimic our results. In the general case of $p \neq 2$, we would expect that the non-Drude foot feature shows up at around $\hbar\omega \sim f(p)\pi k_B T$, whose exact form has not been derived *et al.* yet.

6.5. Bad-metallic behaviour

In this section, we will discuss the optical response of the anomalous metal near the quantum critical region. Due to technical difficulties, we failed to measure the pressure-dependent optical spectra in the region very close to the Mott boundary. Instead, we will mainly focus on the optical properties of the STF-substituted sample. Though the optical data shown here have been briefly discussed in the thesis of Pustogow [74], we will present new and detailed analysis based on the recently developed density-wave (DW) theory [5].

When the system is tuned into the Mott transition from the metallic side, an unique electronic state is expected due to the stronger electron-electron correlations. As can be seen in Figure 6.15 (a), three characteristic temperature regions can be well identified: (1) at very low temperatures, the resistivity exhibits T^2 Fermi-liquid behaviour; with rising temperature further, it remains still metallic like ($d\rho/dT > 0$), but changes to approximately T -linear dependence until a maximum is reached; above $T = 150$ K the resistivity shows a downturn ($d\rho/dT < 0$), indicating a typical semiconducting behaviour. On the contrary, the resistivity of 100% STF-substituted κ -(BEDT-STF)₂Cu₂(CN)₃ compound decreases continuously as the temperature is reduced. Such T -linear temperature dependence present

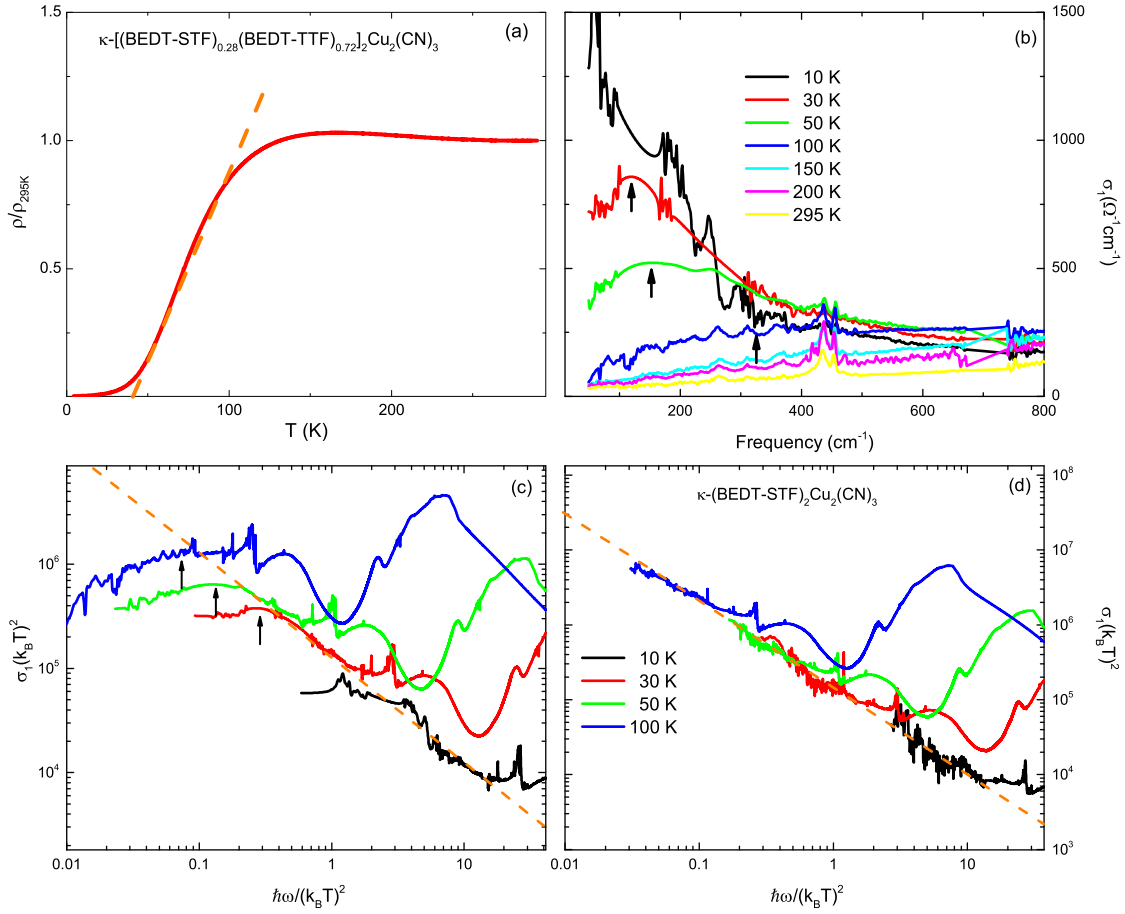


Figure 6.15.: (a) Temperature dependence of the in-plane dc resistivity of the 28% STF- substituted $\kappa\text{-}(\text{BEDT-TTF})_2\text{Cu}_2(\text{CN})_3$. Before entering the Fermi-liquid regime below 20K, the system exhibits a T -linear behaviour (denoted by dashed orange line) at the intermediate temperature regime (b) Temperature evolution of the optical conductivity spectra of $\kappa\text{-}[(\text{BEDT-STF})_{0.28}(\text{BEDT-TTF})_{0.72}]_2\text{Cu}_2(\text{CN})_3$ with $E||b$ below 800 cm^{-1} . With decreasing temperature, the finite energy peak (indicated by black arrow) narrows and shifts to $\omega = 0$. Data collapse in $\kappa\text{-}[(\text{BEDT-STF})_{0.28}(\text{BEDT-TTF})_{0.72}]_2\text{Cu}_2(\text{CN})_3$ (c) and $\kappa\text{-}(\text{BEDT-STF})_2\text{Cu}_2(\text{CN})_3$ (d). The optical conductivity σ_1 is replaced by rescaled quantity $\hbar\sigma_1/(k_B T)^2$. The low-temperature data collapses to a function of the single variable $\hbar\omega/(k_B T)^2$ according to the Drude formalism of the Fermi-liquid state. The deviation of the power-law scaling at very low-frequency in $\kappa\text{-}[(\text{BEDT-STF})_{0.28}(\text{BEDT-TTF})_{0.72}]_2\text{Cu}_2(\text{CN})_3$ is denoted by black arrow. The dashed orange lines correspond to the power law ω^{-2} .

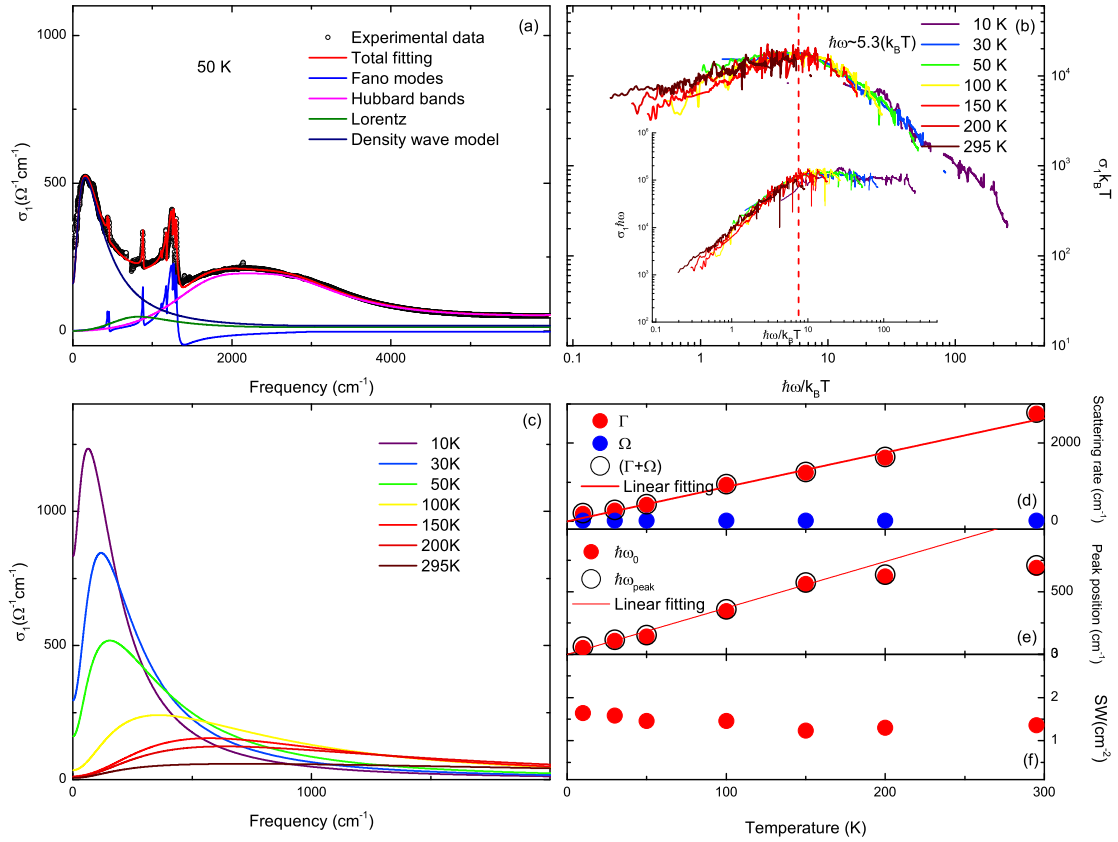


Figure 6.16.: (a) Experimental optical conductivity measured at 50 K and density-wave model (far-IR peak) + two Lorentz terms (mid-IR Hubbard bands) + Fano modes (vibrational features) fitting. A very weak Lorentz-like contribution centered at 800 cm^{-1} is added to obtain a good fitting. (b) The rescaled optical conductivity spectra ($\sigma_1 k_B T$), after the vibrational features and high energy bands are subtracted, follow a universal scaling law as a function of dimensionless ratio $\hbar\omega/k_B T$ for various temperatures as indicated. Inset: $\sigma_1 \hbar\omega$ as a function of $\hbar\omega/k_B T$ (c) Temperature-dependent optical conductivity spectra obtained from the fits using density-wave model (see Equation 2.57). Accordingly, temperature dependence of (d) the peak position (ω_0 and $\omega_{peak} = [\frac{\omega_0(\Gamma + \Omega) \sqrt{\omega_0^2 + \Gamma\Omega} - \Omega(\omega_0^2 + \Gamma\Omega)}{\Gamma}]^{1/2}$, when $\Omega \approx 0$, $\omega_{peak} \approx \omega_0$), (e) the scattering rate (Γ, Ω and $\Gamma + \Omega$) and (f) the spectra weight (SW) extracted from the fits are shown. Solid red lines indicate the linear temperature dependence of Γ and ω_0 .

in dc resistivity of κ -[(BEDT-STF)_{0.28}(BEDT-TTF)_{0.72}]₂Cu₂(CN)₃ clearly demonstrates that the system behaves as a bad metal inbetween insulator and good metal. Very similar behaviour has been extensively discussed in the quantum critical region of other strongly correlated systems, such as high- T_c cuprate [205], iron-pnictide superconductors [206] and heavy-fermion systems [207].

Now we move to the discussion of the frequency-dependent optical response of the above mentioned bad metal. In Figure 6.15 (b), we plot the temperature-dependent optical conductivity spectra along the b-axis, focusing on the far-infrared energy region, as a representative. Surprisingly, we observe a finite energy peak, instead of a Drude-like response centered at zero frequency. With increasing temperature, the peak broadens with likely loss of spectral weight and shifts to higher frequencies, seemly saturating at elevated temperatures. The absence of a zero energy Drude peak in κ -[(BEDT-STF)_{0.28}(BEDT-TTF)_{0.72}]₂Cu₂(CN)₃ clearly manifests the anomalous metallic state at finite energy region. Let's make a direct comparison of the above behaviour with that of a good metal. As we have shown in the previous section, the electronic state of κ -(BEDT-STF)₂Cu₂(CN)₃ can be well identified as Fermi-liquid state with long-lived quasi-particles. At low frequency $\hbar\omega \ll 2\pi k_B T$, the conductivity follows the Drude model with a frequency-independent scattering rate Γ . This also means the following equation

$$\sigma_1(\omega, T)\hbar\Gamma = \frac{e^2 n}{m} \frac{1}{1 + (\omega/\Gamma)^2} \quad (6.1)$$

is satisfied. Since $\Gamma \propto T^2$ is fulfilled in the Fermi-liquid state, the quantity $\sigma_1(k_B T)^2$ is expressed as a function of single parameter $\hbar\omega/(k_B T)^2$ and decreases as ω^{-2} at very high frequencies. This scaling behaviour indeed holds for κ -(BEDT-STF)₂Cu₂(CN)₃ as shown in Figure 6.15 (d). Despite the low-energy optical conductivity of κ -[(BEDT-STF)_{0.28}(BEDT-TTF)_{0.72}]₂Cu₂(CN)₃ strongly deviates from the ω^{-2} , the scaling behaviour is still observed in the high-energy tail. Apparently the simple Drude model based on the momentum relaxation mechanism fails to account for the low-energy peak observed here. The strongly temperature-dependent soft-mode-like behaviour seems to originate from a collective mode, implying some kind of symmetry breaking occurred in the system. Recently a new theory based on the hydrodynamics of phase-fluctuating incommensurate density-wave order has attracted a lot of attention [5, 117], since it can very well describe both the optical spectra and dc resistivity of bad metal. Thus, we will use this model to fit our

experimental data in order to clarify the microscopic nature of our results. The formular of the deduced optical conductivity can be found in theoretical section (see Equation 2.57). The fit are shown in Figure 6.16 (a) for 50 K as a representative. The broad features above 2000 cm^{-1} is assigned to the Hubbard bands, which can be best fitted by two Lorentz oscillators. Fano models are used to describe several peak structures centered around 400 cm^{-1} , 800 cm^{-1} and 1400 cm^{-1} . The far-infrared peak is modeled according to Equation 2.57. In addition, a weak Lorentzian peaked at around 800 cm^{-1} is used to improve the overall fitting. The temperature dependence of the density-wave fits and the extracted parameters are shown in Figure 6.16 (c,d). Upon cooling, the spectral weight increases slightly, which is a typical behaviour found in other organic metals. In contrast, both the pinning frequency ω_0 and width Γ exhibits temperature-dependent blueshift, and possesses a linear temperature dependence below around $T = 200\text{ K}$. A linear fit gives rise to $\hbar\omega_0 \approx 5.3k_B T$ and $\hbar\Gamma \approx 12.4k_B T$ as demonstrated in Figure 6.16 (d,e). The scattering rate, corresponding to the phase fluctuation, is relatively small and shows almost no temperature dependence. This finding is consistent with density-wave scenario, in which the peak structure shows up only when the condition $\omega_0^2 > \Omega^3/(\Gamma + 2\Omega)$ is fulfilled. On the other hand, the non-vanishing of phase relaxation rate ($\Omega \neq 0$) can account for the metallic behaviour of the dc conductivity σ_{DC} , which is defined as

$$\sigma_{DC} = \frac{e^2 n}{m} \frac{\Omega}{\Omega\Gamma + \omega_0^2} \quad (6.2)$$

It is the mobile dislocations induced by the phase gradients that is responsible for the non-zero dc conductivity. Thus, it is essential to take into account the phase fluctuation effect in the hydrodynamic analysis. According to the theoretical prediction by Sachdev *et al.* [208], the optical conductivity follows scaling laws as

$$\sigma_1(\omega, T) = T^{-\mu} f(\omega, T) \quad (6.3)$$

in a quantum critical state of matter. Such scaling law has been indeed verified in cuprate superconductors with optimal doping by van der Marel *et al.* [209]. Here, we also performed the scaling analysis. Surprisingly, all temperature-dependent curves down to the frequencies we have measured collapse on a single curve with $\mu = 1$ as depicted in Figure 6.16 (b). In addition, we found out that $\sigma_1(\omega, T)\hbar\omega$ also

shows universal dependence on $\hbar\omega/k_B T$ as demonstrated in the inset of Figure 6.16 (b). The above findings can be easily understood in the context of density-wave model. When $\Omega \approx 0$, at finite frequencies the real part of the optical conductivity of Equation 2.57 can be approximately expressed as a Lorentz model. Thus, the following relation holds

$$\sigma_1(\omega, T)\Gamma = \frac{\omega_p^2}{4\pi} \frac{(\omega/\Gamma)^2}{((\omega_0/\Gamma)^2 - (\omega/\Gamma)^2)^2 + (\omega/\Gamma)^2} \quad (6.4)$$

If we have the following relation, $\hbar\omega_0 \sim \alpha k_B T$ and $\hbar\Gamma \sim \beta k_B T$, then $\sigma_1(\omega, T)\hbar\Gamma$ is solely determined by $\hbar\omega/k_B T$ with a peak structure at around $\alpha = \hbar\omega_0/k_B T$. We should keep in mind that the Lorentz approximation does not work in the energy regime, $\omega \sim \Gamma$.

Furthermore, we can estimate the time and length scale of the fluctuating density wave from our experimental results. In the framework of hydrodynamics, the spatial correlation is determined as $l \sim \nu_F/\omega_0$, where ν_F is the Fermi velocity. For instance, the pinning frequency is about 350 cm^{-1} at $T = 100 \text{ K}$. This results in a length scale of 10 nm , if we use a typical Fermi velocity $\nu_F \sim 10^5 \text{ m/s}$ ($\text{eV}\text{\AA}$) taken from ARPES measurement [123]. Correspondingly, the Γ and Ω are about 950 cm^{-1} and 350 cm^{-1} , indicating that the magnitude and phase of the fluctuating charge density wave dissipate at time scale of 35 fs and 1.3 ps , respectively. To confirm the estimated value of time and length scale, future experiments based on local probes such as STM [83] and near-field optical nanoscopy [210] are strongly desired.

6.6. Conclusion

To summarize, we have performed temperature-dependent infrared spectroscopic measurements on spin-liquid candidate compound $\kappa\text{-(BEDT-TTF)}_2\text{Cu}_2(\text{CN})_3$ under various pressures up to 1.1 GPa . Based on our far-infrared data, we clearly identified the first-order transition occurring at around $p=0.3 \text{ GPa}$ and $T = 20 \text{ K}$, which is in line with the findings obtained from dc transport measurements. Furthermore, from the analysis of the vibrational modes, we have observed the multiple splitting of the C-S vibrations induced by the local STF-substitution. This is in strongly contrast to the results under high pressures, where blueshift of these modes

were observed. We also demonstrated that the physical pressure have less effect on the electronic properties in the insulating state in contrast to the STF-doping case, where strong intragap absorption was observed possibly due to the Anderson localization effect. In the highly metallic state, we have successfully revealed the universal optical signatures of the Fermi liquid state, both in the pristine sample under pressure and STF-doped one, using the Fermi scaling form. The optical scattering rate was found obey the single parameter scaling and the low-energy optical conductivity display a non-Drude foot at the thermal regime. Additionally, we observed a far-infrared peak in the optical conductivity spectra for the 28% STF-doped material, which is located very close to the Mott transition. The observed T -linear behaviour of the collective mode, together with the T -linear dc resistivity, suggests that the driving mechanism may be explained as a fluctuating density wave pinned by the disorder potential of the doped BEDT-STF molecules.

7. High-pressure vibrational spectroscopy of

β'' -(ET)₂SF₅CHF₂CF₂SO₃

In this chapter we will discuss the results obtained on β'' -(BEDT-TTF)₂SF₅CHF₂CF₂SO₃, in terms of its vibrational evolution under external pressure.

7.1. Background

Similar to other types of ET-based organic salts, the organic conductor β'' -(BEDT-TTF)₂SF₅CHF₂CF₂SO₃ consists of alternating layers of BEDT-TTF donor molecules and layers of organic SF₅CHF₂CF₂SO₃ anions, as shown in Figure 7.1 (a-c). According to the X-ray data, it was found that in the anionic layers, the SF₅CHF₂CF₂SO₃ molecules are disordered [70, 71]. This is due to the competition between the short hydrogen bonds C-H \cdots O and C-H \cdots S, which are formed by the ethylene (CH₂) hydrogen atoms of ET layers with oxygen atoms and fluorine atoms of the terminal SF₅CHF₂CF₂SO₃ groups, respectively. Within the conducting layers, the BEDT-TTF molecules are arranged in β'' -type packing motif with tilted stacks along the a-axis. Thus, β'' -(BEDT-TTF)₂SF₅CHF₂CF₂SO₃ is considered to be a quarter-filled electronic system.

Transport and ESR measurements on β'' -(BEDT-TTF)₂SF₅CHF₂CF₂SO₃ have been performed by Schlueter *et al.* [70]. As depicted in Figure 7.1 (d), they found that the system undergoes a metal-insulator phase transition at 190 K, above which it

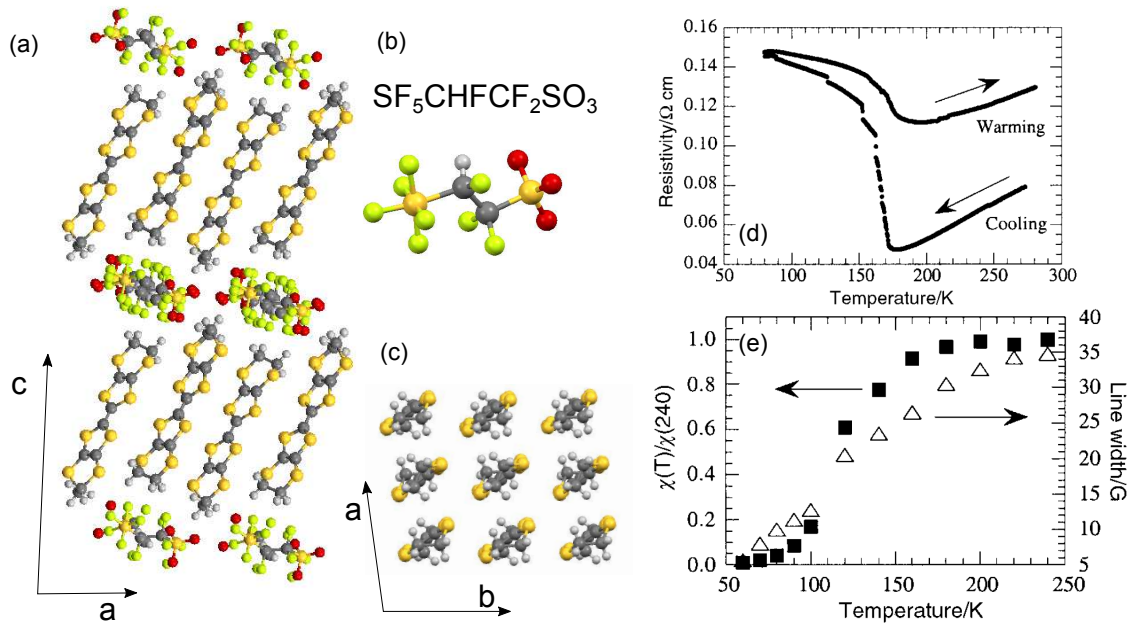


Figure 7.1.: (a) Crystal structure of β'' -(BEDT-TTF)₂SF₅CHF₂CF₂SO₃ viewed along the crystallographic *b*-axis (b) SF₅CHF₂CF₂SO₃ anion. The electronegative oxygen (red) and fluorine atoms (yellowish green) form short hydrogen bonding with the hydrogen atoms of ET molecules. (c) Packing pattern of the ET donor layer viewed along the *c*-axis. *a*- and *b*-axis denote the stacking and interstack axis. (d) Temperature dependence of resistivity measured in the conducting (*ab*)-plane for cooling and heating cycles. (e) Temperature dependence of the relative spin susceptibility (filled squares) and linewidth (open triangles) of β'' -(BEDT-TTF)₂SF₅CHF₂CF₂SO₃. Panel (d) and (e) are adapted from Ref. [70]

remains metallic. Additionally, a strong hysteresis was observed for the cooling and heating cycles. This gives a clear indication that the structural transition may be involved in the metal-insulator transition. In Figure 7.1 (e), the relative spin susceptibility and linewidth are plotted as a function of temperature. Both quantities exhibit a pronounced drop below 120 K, indicating a non-magnetic insulating ground state associated with a spin gap opening. These findings are in accord with the resistivity measurements.

In order to clarify the role of the lattice degrees of freedom in the metal-insulator transition, low-temperature (150 K) X-ray measurements on β'' -(BEDT-TTF)₂SF₅CHF₂CF₂SO₃ have been performed [70]. As illustrated in Figure 7.2, the con-

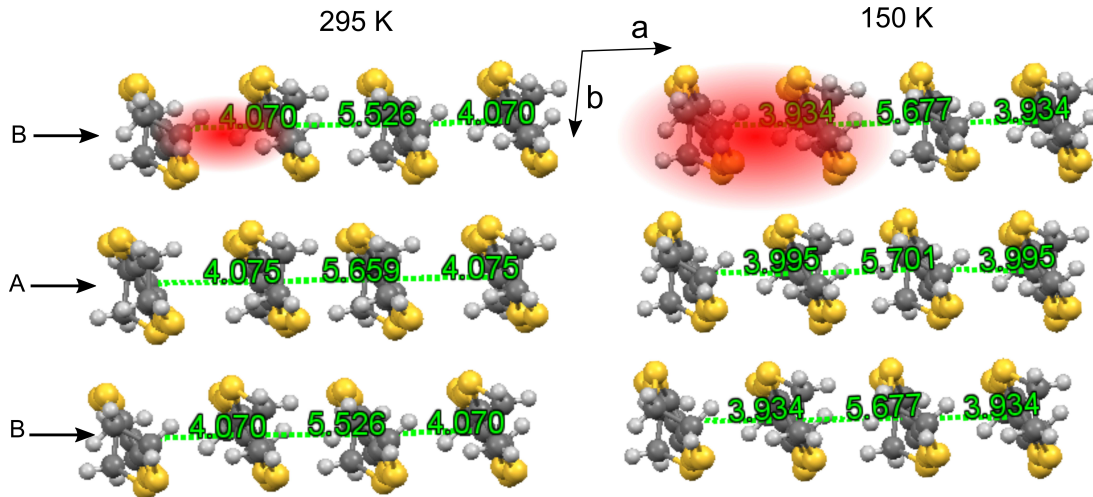


Figure 7.2.: Crystallographic data of conducting (ab) -plane for β'' -(BEDT-TTF) $_2$ SF $_5$ CHFCF $_2$ SO $_3$ at 295 K and 150 K. A and B denote two types of crystallographically nonequivalent ET molecules. Molecule A and B are alternately stacked along the b -axis. The numbers (green) correspond to the inter-molecular distance along the stacking a -axis in units of Å. The size of the red ellipse illustrates the degree of dimerization. X-ray data are taken from Ref. [70]

ducting plane of BEDT-TTF molecules consists of alternating stacks of molecules A and B. A and B are two crystallographically non-equivalent BEDT-TTF molecules with slightly different structures of the TTF fragments. At room temperature, both stacks of A and B have a weak structural dimerization. At 150 K, the occurrence of a more prominent structural transition leads to a strong dimerization in both stacks, and thus, a vanishing interaction between adjacent dimers within each stack. Since the transfer integral along the interstack does not change substantially, the low-temperature electronic state can be considered to be quasi-1D with conducting chain along the b -axis. As a result, the spins sitting on adjacent dimers form singlet pairs along the interstack direction. This gives rise to a non-magnetic ground state. Furthermore, the insulating state was identified as a charge-ordered state. The charge disproportionation between molecule A and B was estimated to be around $0.1e$ at 150 K through an analysis of the lengths of C–S and C=C bonds [70].

The charge-ordering instability is normally expected to arise from the strong intersite Coulomb repulsion. The underlying physics can be well described by

extended Hubbard model [46, 58, 66]. It was predicted that the charge-ordered insulating state can be tuned to metallic state by increasing the bandwidth via applying high pressure. For instance, dc resistivity measurements revealed that the metal-insulator transition is gradually suppressed when pressure is applied on quarter-filled organic salt α -(BEDT-TTF)₂I₃ [147], as shown in Figure 7.3 (b). The vanishing of charge-ordered state and the emergence of semi-metallic state under pressure were confirmed by infrared [147] and NMR measurements [57] as well. However, in strong contrast to the case of α -(BEDT-TTF)₂I₃, the charge order transition in β'' -(BEDT-TTF)₂SF₅CHF₂SO₃ is enhanced with increasing pressure, as seen in Figure 7.3 (a). In order to identify the optical properties of the anomalous states under high pressures, we have performed pressure-dependent vibrational spectroscopy on β'' -(BEDT-TTF)₂SF₅CHF₂SO₃.

7.2. Vibrational modes at ambient condition

High quality black rod-like single crystals of β'' -(BEDT-TTF)₂SF₅CHF₂SO₃ were prepared by standard electrochemical oxidation of the BEDT-TTF molecules as described elsewhere [70]. At ambient pressure condition, temperature-dependent infrared measurements have been performed with light polarized along all three principal axes, i.e., $E||a, b, c$, by Pustogow *et al.* [74]. Here, we will redraw the data and mainly focus on the new analysis of the charge sensitive vibrations.

Figure 7.4 (a) shows the temperature evolution of the optical conductivity spectra for ν_{27} measured with a polarized light ($E||c$). At room temperature, a very broad band around 1440 cm⁻¹ can be well resolved. It corresponds to the asymmetric ν_{27} mode associated with the C=C vibrations. The observed large linewidth indicates that the charge-order fluctuations occur at high temperatures, which is quite common for other β'' compounds. The weak bands shown up around 1410 cm⁻¹ are assigned to ν_{28} vibrations [211], which are not sensitive to charge disproportion. With decreasing temperature, the single mode gets narrower and shifts towards higher frequencies, which is accompanied by the development of a very weak side peak around 1475 cm⁻¹. Upon further cooling below the phase transition at 180 K, the single mode clearly splits into multiple peaks, indicating the appearance

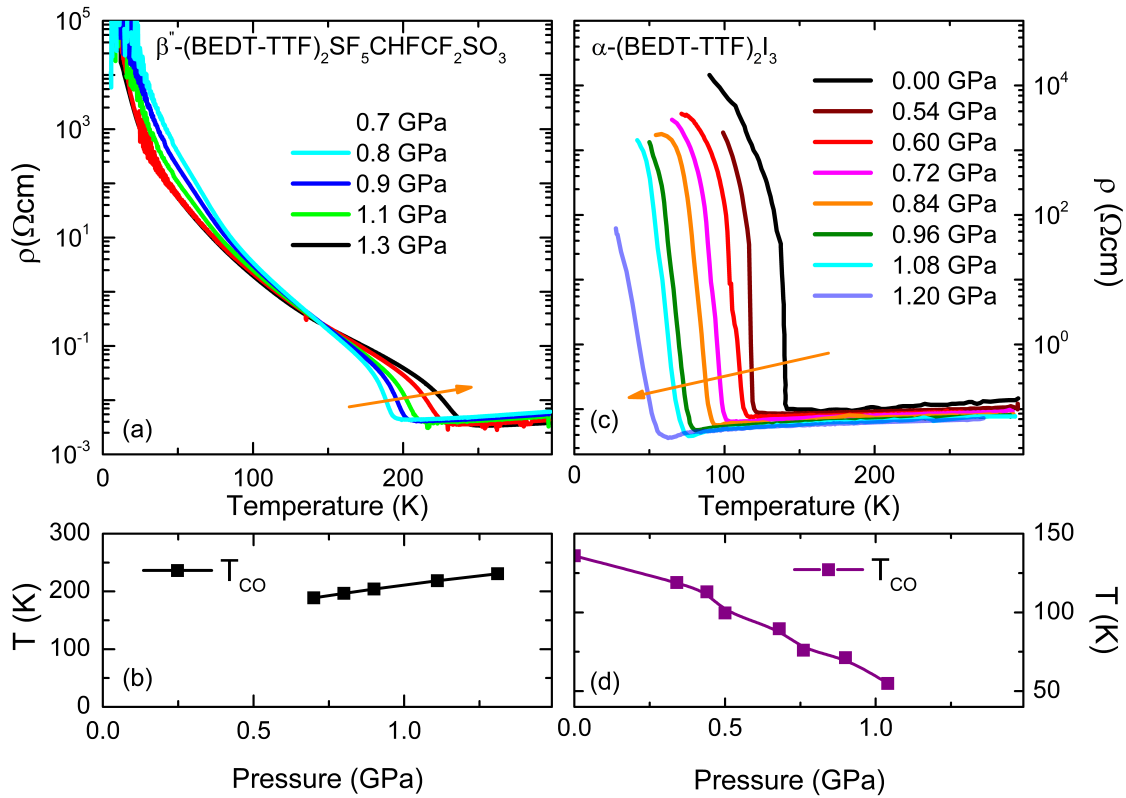


Figure 7.3.: Temperature-dependent dc resistivity of quarter-filled charge-ordered organic salts $\beta''-(\text{BEDT-TTF})_2\text{SF}_5\text{CHF}_2\text{CF}_2\text{SO}_3$ (a) and $\alpha-(\text{BEDT-TTF})_2\text{I}_3$ (c) under various pressures. With increasing pressure the charge order transition in $\beta''-(\text{BEDT-TTF})_2\text{SF}_5\text{CHF}_2\text{CF}_2\text{SO}_3$ gets enhanced, while it becomes gradually suppressed for $\alpha-(\text{BEDT-TTF})_2\text{I}_3$. The orange arrows are guides for eye. Panel (b) and (d) describe the metal-insulator transition temperature T_{CO} as a function of pressure for $\beta''-(\text{BEDT-TTF})_2\text{SF}_5\text{CHF}_2\text{CF}_2\text{SO}_3$ and $\alpha-(\text{BEDT-TTF})_2\text{I}_3$, respectively. Redrawn from Refs. [74, 147]

of charge-ordered insulating state. According to Equation 2.49, the amplitude of the charge ordering is calculated to be $2\delta = 0.3e$, which is three times the value estimated from X-ray diffraction [70].

Around 880 cm^{-1} for the same polarization, i.e., $E||c$, we can identify another asymmetric vibration mode $\nu_{49}(\text{B}_{2u})$, which involves the motion of the four carbon atoms of the inner rings. Thus, this mode is known to be sensitive to charge imbalance and structure dimerization [103, 198]. The single broad mode splits

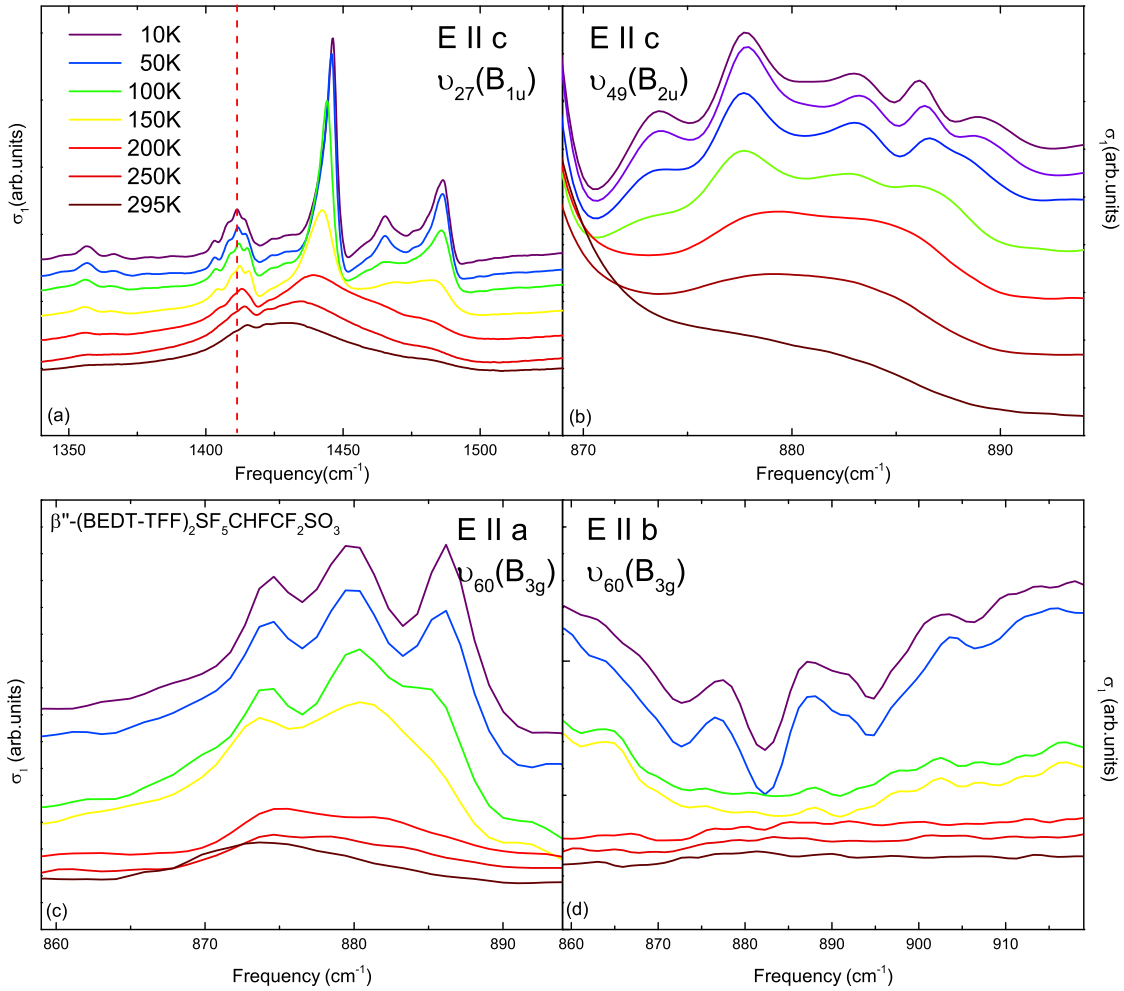


Figure 7.4.: (a) Temperature-dependent optical conductivity of β'' -(BEDT-TTF)₂SF₅CHFCF₂SO₃ for $E \parallel c$ at ambient pressure condition. The charge sensitive vibrational mode $\nu_{27}(B_{1u})$ splits into three bands below $T_{CO} = 180$ K, indicating the development of a pronounced charge-ordered state at low temperature. The red dashed line indicates the charge-insensitive CH₂ bending mode $\nu_{28}(B_{1u})$. (b) Temperature dependence of the charge sensitive $\nu_{49}(B_{2u})$ vibration, which is a normally IR-active mode. Multiple modes are observed in the charge-ordered state. At the same frequency range, the EMV-activated ring-breathing vibration $\nu_{60}(B_{3g})$ displays a Fano shape along the stacking axis (c), but shows up as a strong dip for the interstack direction (d). All the spectra are shifted for clarity. The original data are taken from Ref. [74]

into several peaks below the transition temperature $T_{CO}=180$ K and the intensity becomes much stronger with lowering the temperature, as shown in Figure 7.4 (b). The corresponding symmetric Raman mode $\nu_{60}(B_{3g})$ involving the same inner rings appear in the same frequency range in the in-plane infrared spectra due to the strong coupling to the charge transfer band. As shown in Figure 7.4 (c) and (d), while the $\nu_{60}(B_{3g})$ can be hardly detected at elevated temperatures, multiple strong modes develop when entering the charge-ordered insulating state.

7.3. Vibrational modes under high pressures

Thanks to the relatively large size of the out-of-plane of the sample, we can perform pressure-dependent vibrational spectroscopy on the single crystal instead of powder. High-pressure experiments were conducted mainly for E perpendicular to the conducting layers, i.e., $E||c$. Figure 7.5 (a) exhibits the normal-incidence optical reflectivity of β'' -(BEDT-TTF)₂SF₅CHF₂CF₂SO₃ measured under 0.82 GPa and at selected temperatures for $E||c$ and $E||b$.

Within the conducting plane ($E||b$), the reflectivity increases slightly upon cooling. However, it drops significantly in the energy range of $\omega < 1000$ cm⁻¹ as the temperature is reduced further below $T_{CO}=180$ K, indicating the opening of the optical gap. In comparison to the 10 K spectrum obtained at ambient condition, we observed additional features, which are assigned to the influence from the oil, as indicated by red dashed lines and arrows. These artefacts show up for $E||c$ as well, which obscure the precise analysis of the ν_{27} mode. For $E||c$, the reflectance is relatively low and remains almost unchanged in the frequency range investigated. In Figure 7.5 (b), we plot the 10 K reflectivity spectra under 0.82 GPa along with the spectra under ambient condition for comparison. Despite the rather low intensity of the vibrational modes observed under pressure, the total number and peak positions of these modes are very similar to those at ambient pressure. The detailed discussion of the temperature and pressure dependence of the vibrational features will be given below.

The temperature evolutions of charge sensitive mode ν_{27} around 1450 cm⁻¹ under pressures, ranging from 0.15 GPa to 1.1 GPa, are plotted in Figure 7.6. At 0.15 GPa,

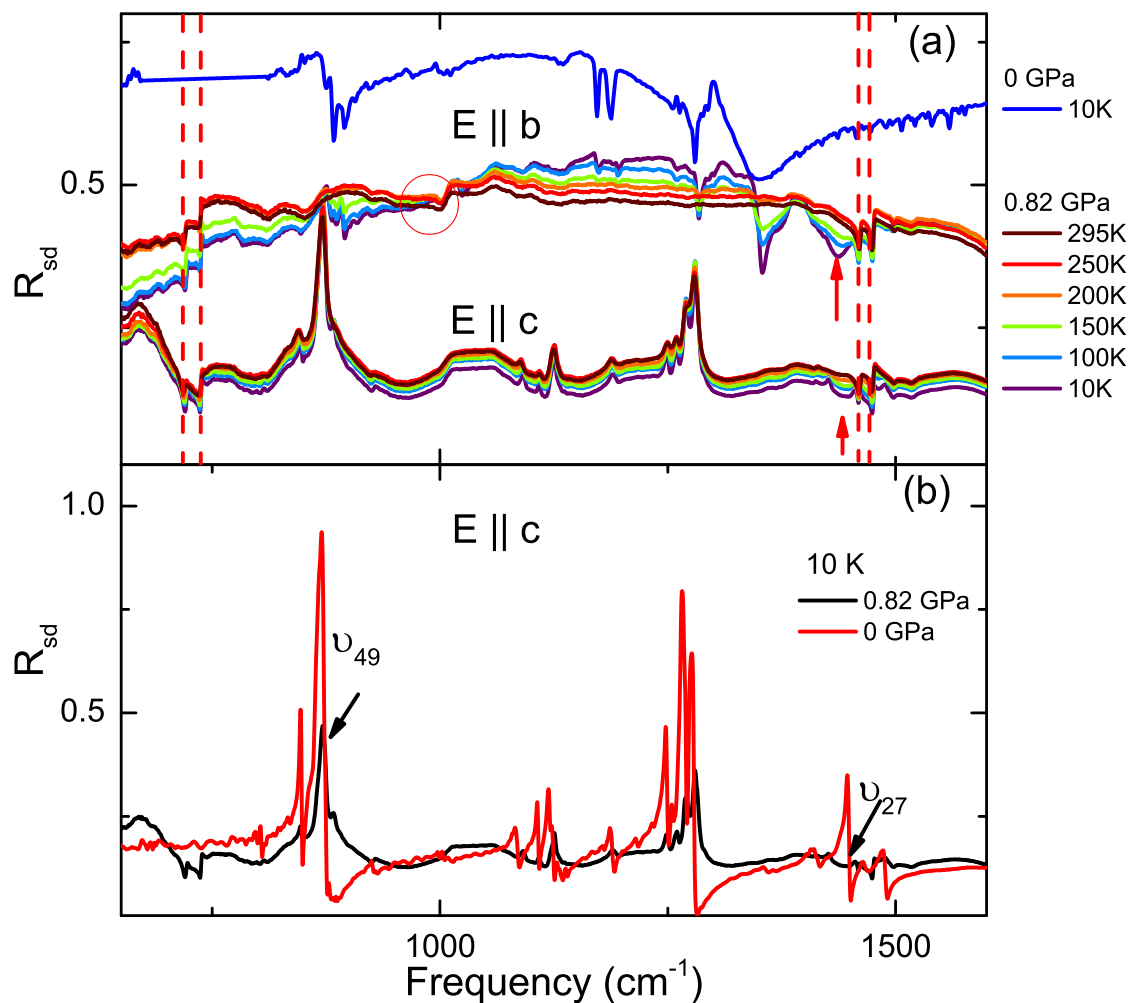


Figure 7.5.: (a) Optical reflectivity spectra measured at 0.85 GPa in the temperature range from 295 K to 10 K with light polarized along the interlayer and interstack direction, i.e., $E||c$ and $E||b$. The charge-ordered phase transition below 180 K results in a drastic suppression of the reflectivity below around 1000 cm^{-1} (red circle). Red dashed lines denote the oil absorption bands. Red arrows correspond to the oil-induced artefacts, which are absent in the spectrum (blue) at ambient condition. (b) Comparison between the reflectivity spectra obtained at 0.82 GPa and ambient pressure for 10 K. Despite the relatively low intensity of the vibrational modes observed at high pressure, the two charge sensitive modes ν_{49} and ν_{27} can be clearly identified as indicated by arrows.

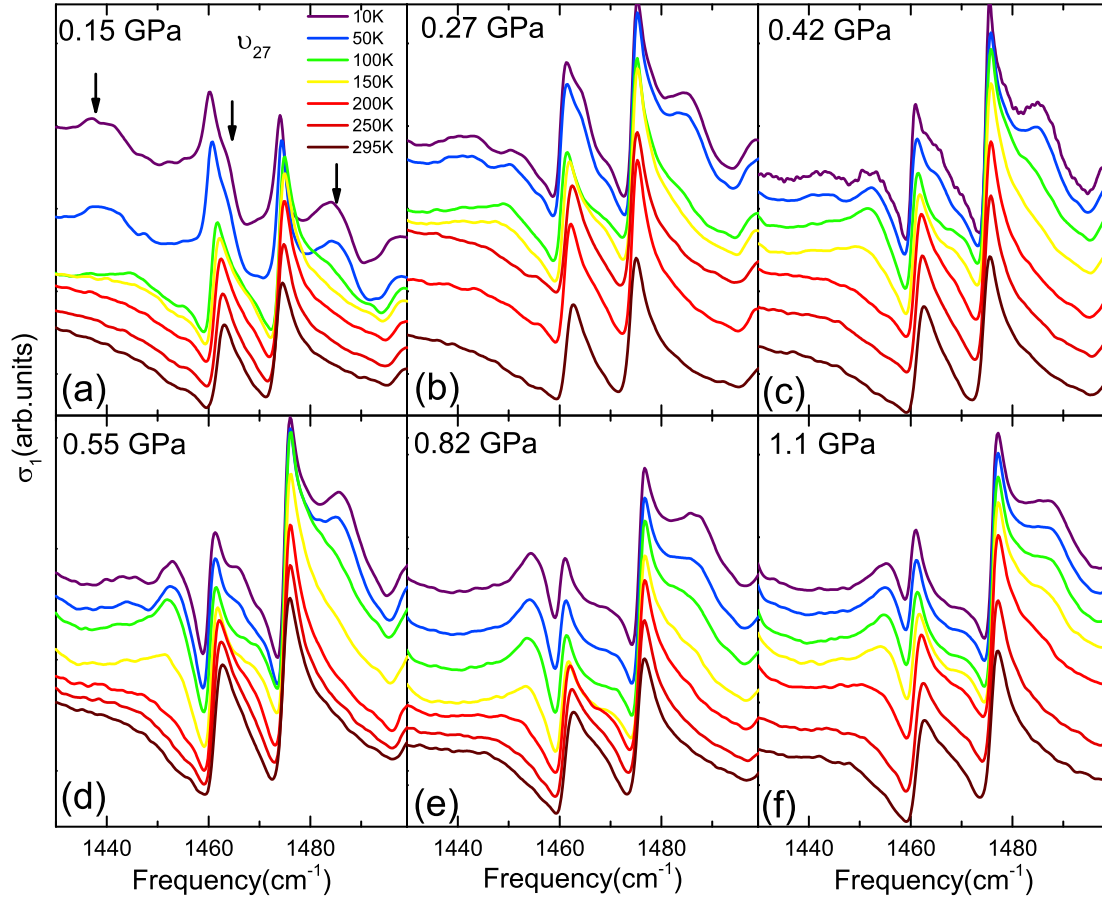


Figure 7.6.: Temperature-dependent mid-infrared optical conductivity spectra of β'' -(BEDT-TTF) $_2$ SF $_5$ CHFCF $_2$ SO $_3$ as a function of pressure as indicated. All spectra are offset for clarity. Due to the influence of the oil absorptions and artefact-like dip features, the single broad band of ν_{27} can not be resolved at high temperatures. At lowest temperature $T = 10$ K, the appearance of three bands (black arrows) strongly indicates the emergence of the charge-ordered ground state. The splitting of the ν_{27} mode is still clearly observed under highest pressure of $p=1.1$ GPa, showing that the CO instability in β'' -(BEDT-TTF) $_2$ SF $_5$ CHFCF $_2$ SO $_3$ is quite robust against external pressure.

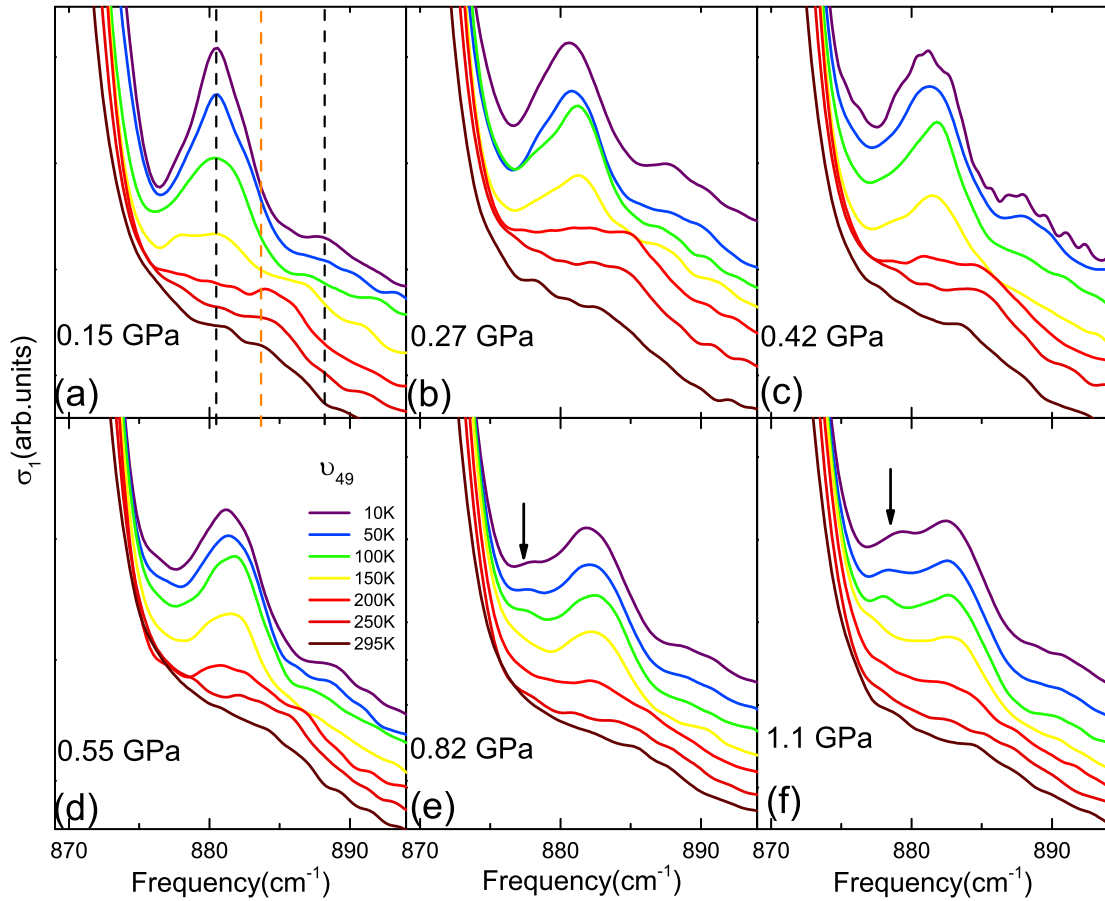


Figure 7.7.: Temperature evolution of the in-plane vibrational modes ν_{49} of β'' -(*BEDT-TTF*)₂SF₅CHFCF₂SO₃ at various pressures. All spectra are shifted for clarity. At high temperatures, the spectra are dominated by one single broad mode around 885 cm^{-1} (orange dashed line), while at least two modes (black dashed line) show up upon cooling. At 0.82 GPa and 1.1 GPa, a weak side peak (black arrow) becomes visible due to the blueshift of its frequency, which is hidden by the tail of the intense mode around 870 cm^{-1} in the low pressure regime.

three new vibrational modes appear during cooling down, indicating appearance of the charge-ordered ground state. The overall developments of ν_{27} mode for all studied pressures are quite the same as those at ambient pressure, except the strong Daphne oil absorptions around 1460 cm^{-1} and 1470 cm^{-1} . Accordingly, the charge order survives up to 1.1 GPa, which is consistent with the resistivity measurements under pressure. The same conclusion can be drawn from the analysis of ν_{49} mode as depicted in Figure 7.7. When temperature is reduced, the ν_{49} mode splits into several peaks and substantially gains infrared spectral weight, giving strong evidence that both charge order and structural dimerization coexist under pressure. Unfortunately it is not possible to give a precise determination of the pressure-dependent transition temperature T_{CO} from our measurements, because of the few temperature steps measured between 200 K and 250 K. Nevertheless, our findings are in strong contrast to the case of α -(BEDT-TTF) $_2$ I $_3$ and β'' -(BEDT-TTF) $_3$ Cl $_2$ ·2H $_2$ O, where charge disproportionation is gradually suppressed with decreasing metal-insulator transition temperature, when external pressure is applied [49, 147].

To demonstrate the pressure effect on the charge order more clearly, we plot the pressure evolution of the ν_{27} and ν_{49} modes at selected temperatures in Figure 7.8. At 10 K, the frequency of the multiplets for both modes monotonically increase with increasing pressure. This pressure-induced blueshift of frequency is partially attributed to the hardening of the lattice. When the suppression of metal-insulator transition occurs, the mode, corresponding to the charge poor site, principally should redshift due to the decrease of the charge inhomogeneity with increasing pressure. In our case, the corresponding one of ν_{27} mode located at around 1490 cm^{-1} (ν_{27}^3) hardens continuously as shown in Figure 7.9. Thus, it strongly indicates that the charge order get enhanced under pressure in comparison with the case of α -(BEDT-TTF) $_2$ I $_3$ and β'' -(BEDT-TTF) $_3$ Cl $_2$ ·2H $_2$ O. Similar behaviour is also observed at 100 K. When temperature is raised up to 200 K, a remarkable spectral changes can be found between 0.15 GPa and 0.55 GPa. This clearly demonstrates that the charge-ordered state emerges above 200 K under higher pressures, i.e., $p \geq 0.55$ GPa.

Now we turn to the discussions of underlying physical mechanism for such unusual pressure effect. In the purely electronic picture, the driving force of the charge ordering, occurred in quarter-filled organic system, originates from the strong in-

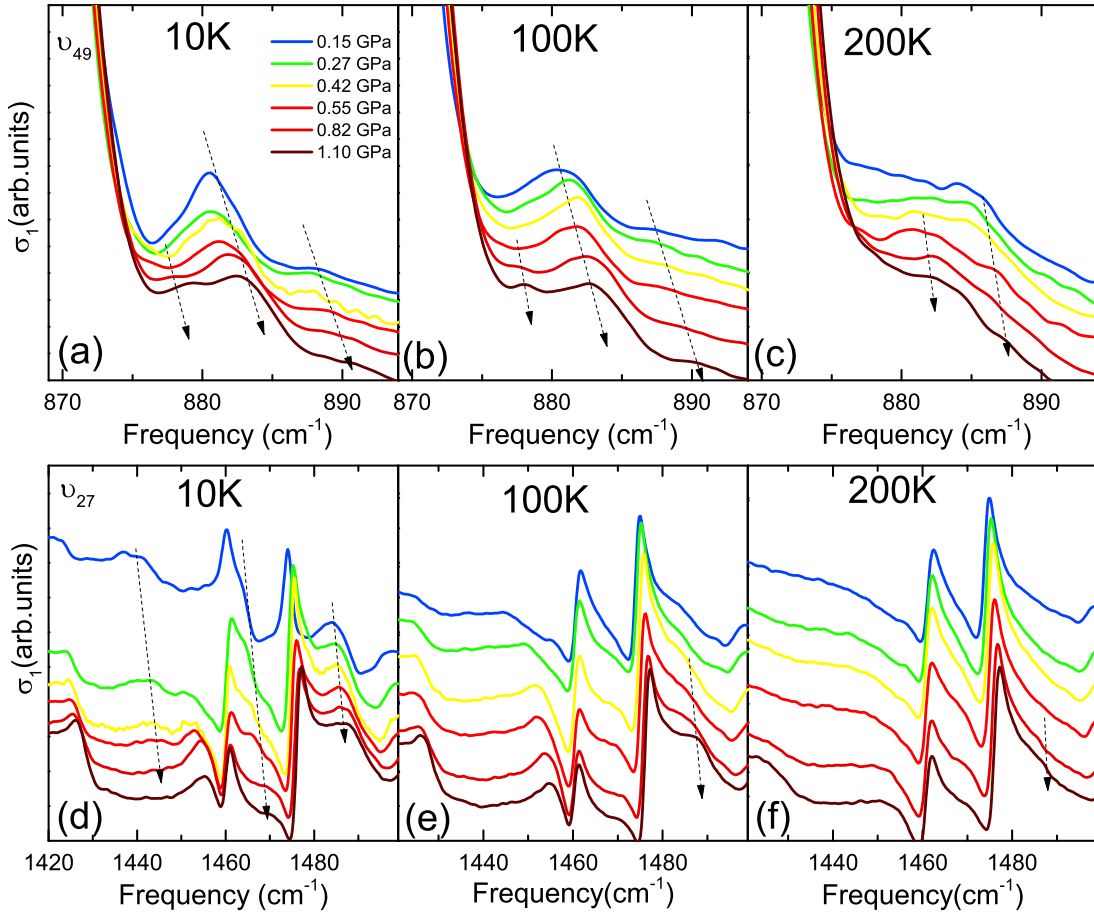


Figure 7.8.: Pressure evolution of optical conductivity spectra of β'' -($BEDT$ - TTF) $_2$ $SF_5CHFCF_2SO_3$ for modes ν_{49} and ν_{27} measured at (a,d) $T = 10$ K, (b,e) $T = 100$ K and (c,f) $T = 200$ K. The vibrations show a frequency upshift as illustrated by the dashed arrows.

tersite Coulomb repulsion V . When the external pressure is applied, the lattice constants are reduced, leading to an increase in the transfer integrals, and thus enhancement of bandwidth W . If we assume that the V remains unchanged, the effective correlation strength V/W decreases with increasing pressure, giving rise to a suppression of charge ordering [46]. This scenario is indeed successfully verified in the case of β'' -($BEDT$ - TTF) $_3Cl_2 \cdot 2H_2O$, where charge ordering appears without lattice distortion. And the charge-ordered state is completely suppressed and accompanied with the appearance of superconductivity at around 1.6 GPa [49]. This picture seems to be also valid in the chemical substitution case for the family of β'' -(ET) $_2$ SF_5RSO_3 salts with $R = CH_2, CH_2CF_2, CHF$ and $CHFCF_2$. It was observed

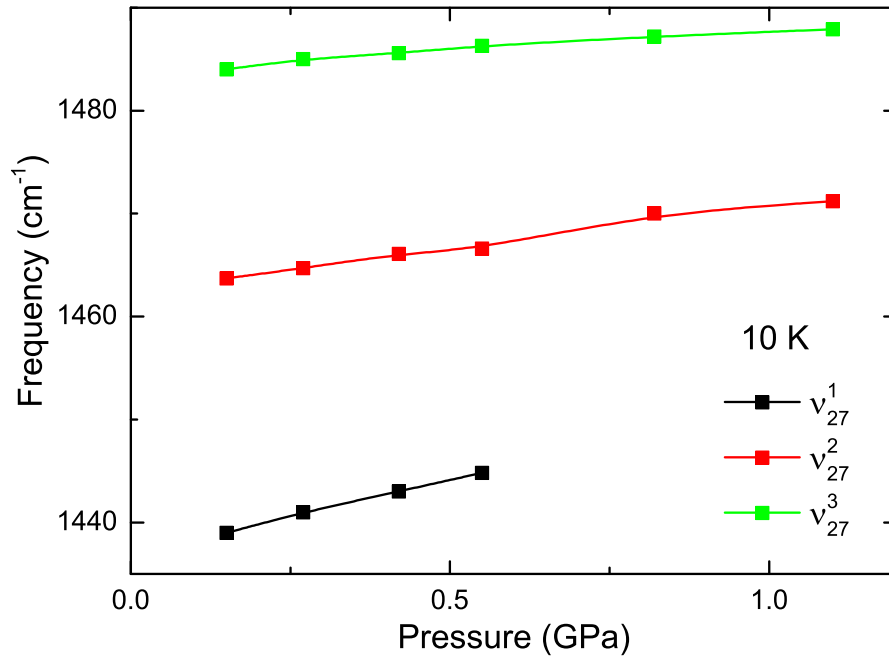


Figure 7.9.: Frequencies of the three ν_{27} modes at 10 K plotted against pressure. Above 0.55 GPa, the frequency of the charge rich site can not be resolved due to the influence of the oil absorptions.

Table 7.1.: Comparison of the electronic states of several charge-ordered organic salts at ambient and high pressure. β'' -(BEDT-TTF) $_2$ Hg(SCN) $_2$ Cl is a new discovered organic salts and exhibits charge ordering phase below $T_{CO}=75$ K. Transport measurements on this compound will be performed in near future.

Material	Band filling	CO	Structural transition	Under pressure	Ref.
β'' -(BEDT-TTF) $_2$ Hg(SCN) $_2$ Cl	1/4	Yes	Yes	under investigation	[211]
β'' -(BEDT-TTF) $_2$ SF $_5$ CHFCF $_2$ SO $_3$	1/4	Yes	Yes	CO	This work
θ -(BEDT-TTF) $_2$ RbM'(SCN) $_4$ [M'=Co,Zn]	1/4	Yes	Yes	CO	[212]
β' -Me $_4$ P[Pt(dmit) $_2$] $_2$	1/2	Yes	Yes	CO	[213]
α -(BEDT-TTF) $_2$ I $_3$	1/4	Yes	Yes(weak)	Semimetal	[139, 147]
β'' -(BEDT-TTF) $_3$ Cl $_2 \cdot 2$ H $_2$ O	1/4	Yes	No	Metal	[49]
κ -(BEDT-TTF) $_2$ Hg(SCN) $_2$ Cl	1/2	Yes	No	Metal	[214, 215]

that the insulating ground state of β'' -(BEDT-TTF)₂SF₅CHF₂CF₂SO₃ can be tuned to superconducting state and metal, when CHF₂CF₂ was replaced with CH₂CF₂ and CHF, respectively [69].

On the other hand, it was suggested in the case of θ -(BEDT-TTF)₂MM'(SCN)₄(M= Tl, Rb, Cs, M'=Co, Zn) that a structural transition can stabilize charge ordering via the electron-lattice coupling, and thus, the metal-insulator transition temperature tends to get enhanced with applied pressure [212]. According to the theoretical investigations of the extended Hubbard model on triangular lattices [216], the larger anisotropy of the triangular lattice can cause stronger charge ordering instability. Thus, we suggest that in our case the application of pressure promotes the structural phase transition, which leads to the enhancement of the anisotropy of the triangular lattice, and thus, the stronger charge-order transition. The importance of the lattice distortion on the stabilization of charge-ordered state has also been pointed out from the investigation of the photoinduced phase transition in β'' -(BEDT-TTF)₃X₂[X=ReO₄, ClO₄] [217]. It is also interesting to note that the interaction of the BEDT-TTF molecules with the anionic layers can also play a crucial role in the charge disproportionation as predicted by Alemany *et al.* [59]. In Table 7.1, we summarize the electronic states of several charge-ordered organic salts under pressure and at ambient pressure to clearly illustrate the crucial role of the lattice degrees of freedom for the unusual pressure dependence observed here.

7.4. Conclusions

In summary, we carried out temperature- and pressure-dependent optical measurements on β'' -(BEDT-TTF)₂SF₅CHF₂CF₂SO₃ for E||c. At ambient pressure, the metal-insulator transition in β'' -(BEDT-TTF)₂SF₅CHF₂CF₂SO₃ was identified as charge ordering transition accompanied with strong lattice dimerization. This leads to the splitting of ν_{49} and ν_{27} modes. However, the charge-ordered state was observed to survive under pressure of up to 1.1 GPa and get enhanced upon increasing pressure. This is in distinct contrast to the chemical substitution case. The observed opposite effect between chemical substitution and hydrostatic pressure on the transport and vibrational properties strongly indicates that lattice degrees of freedom are responsible for the stabilization of charge ordering. Thus, new theory beyond ex-

tended Hubbard model is desired to account for the anomalous pressure-dependent behaviour in the quarter-filled organic salts β'' -(BEDT-TTF)₂SF₅CHFCF₂SO₃.

8. Conclusions and Outlook

Conclusions

The experimental results shown in the framework of this thesis demonstrate that pressure-dependent infrared spectroscopy is a uniquely powerful technique able to examine not only the electron-electron correlations but also the electron-phonon coupling, and provide deep insight into the low-energy electrodynamics of the quasi-particles in strongly correlated organic system.

In chapter 4, we investigate the electrodynamic response of the Dirac electrons in the quasi-two-dimensional organic conductor α -(BEDT-TTF)₂I₃ under high pressure. At room temperature, the applied pressure cause a significant spectral weight transfer in optical conductivity over a wide energy range, up to 0.5 eV. This can be well understood within the Mott-Hubbard picture. At around 90 K, we observe a flat universal constant conductivity, which is in good agreement with the theoretical prediction of the optical properties of 2D Dirac quasi-particles. This implies that the band edge is strongly modified and accompanied with the development of linear band dispersions upon cooling. At the lowest temperature of 6 K, the Drude spectral weight is transferred to finite energies, giving rise to local peaks in $\sigma_1(\omega)$, which strongly indicates the appearance of pseudogap with states piling up at the band edges. Furthermore, we discuss our results in the framework of correlation effect and compare the gap value quantitatively to the theoretical predictions given by Khveshchenko [166]. The good agreement between our optical data and theory yields strong evidence of the gap, arising from the long-range Coulomb repulsion between the massless Dirac electrons. With rising pressure, the correlation gap is found to be suppressed and likely disappear above 4 GPa. Our results demonstrate that the electronic correlation strength between the Dirac electrons can be tuned

by temperature and pressure.

In chapter 5, we elucidate the electrodynamics of β' -EtMe₃Sb[Pd(dmit)₂]₂ at the Mott insulator-metal transition in detail. The results unambiguously confirm the realization of the purely bandwidth-controlled phase transition by applying an external hydrostatic pressure. The high-temperature electronic state can be characterized as a rather poor metallic state with only a small amount of free charge carriers. When cooled down at ambient and weak pressure ($p < p_c$), the system becomes insulating at the quantum Widom line, i.e., the spectral weight shifts to higher energies due to the opening of Mott gap in the optical spectrum. The Mott-Hubbard gap of β' -EtMe₃Sb[Pd(dmit)₂]₂ is found to decrease linearly with pressure and vanish at $p_c = 0.6$ GPa. Due to the electron-phonon coupling, we also reveal the rapid changes in frequency and Fano constant of the EMV- vibrational modes. Additionally, the anisotropy of the in-plane optical response becomes inverted across the insulator-metal transition. With $p > p_c$, a metallic ground state is established at reduced temperatures with a zero-frequency Drude-like component. When the Mott transition is approached from the metallic side, we observe the enhancement of the effective mass m^* at p_c due to the increase of the correlations strength. From the analysis of our optical conductivity at 10 K based on the Drude-Lorentz model we estimate values for the onsite Coulomb repulsion U and the bandwidth W . We find a continuous suppression of the effective correlations U/W with increasing pressure. The determined parameters of T/W and U/W are in good agreement with DMFT calculations.

In chapter 6, we discuss the pressure-dependent optical response of spin-liquid candidate compound κ -(BEDT-TTF)₂Cu₂(CN)₃. From the analysis of the ν_{10} mode, we reveal the hardening of this vibrational mode under high pressure. In contrast, the substitution of S atoms by Se atoms gives rise to a multiple splitting of ν_{10} mode. The local disorder effects observed in STF-doped case seem to be closely related with the intragap absorption seen in the optical conductivity spectra. Furthermore, we reveal the occurrence of first order insulator-metal transition at around $p=0.3$ GPa and $T = 20$ K, which is in good agreement with the dc transport measurements. In the high-pressure metallic state, we apply the local Fermi liquid theory to our optical data and reveal the universal optical signatures of the Fermi liquid state.

The optical scattering rate is found to follow the single parameter scaling law. In addition, we observe a non-Drude foot in the low-energy optical conductivity at the thermal regime. Similar universal behaviour is also identified in STF-doped sample. In the 28% STF-doped crystal, which is located very close to the Mott transition, we observe a far-infrared collective mode in the optical conductivity spectra. Both, the peak position and the width of this mode exhibit T -linear behaviour, which can be well understood in the framework of pinned fluctuating density wave theory.

The results of temperature- and pressure-dependent optical measurements on β'' -(BEDT-TTF)₂SF₅CHF₂SO₃ are presented in chapter 7. At ambient pressure, we identify the nature of the metal-insulator transition as charge ordering with strong lattice dimerization. The charge-ordered state is found to be very robust against external pressure and still survive under pressure of up to 1.1 GPa. Additionally, from the vibrational spectroscopy we reveal the enhancement of the charge ordering transition with increasing pressure. This finding is in opposite to the decrease of the amplitude of charge disproportionation observed in the chemical substitution case. The distinct effects of chemical substitution and hydrostatic pressure on the charge-order transition imply that structural transition may play an important role in the realization of the charge-ordered state in β'' -(BEDT-TTF)₂SF₅CHF₂SO₃ salt.

Outlook

Despite the extensive temperature- and pressure-dependent optical investigations on the phase transitions in this thesis, there are a number of questions that need to be resolved in future. For example, in the case of α -(BEDT-TTF)₂I₃, it has been theoretically predicted that both, the Fermi velocities and the velocity anisotropy, have strong influence on the dynamic gap [218]. Thus, we call for NMR studies on this compound in order to provide complementary information about the pressure-evolution of these parameters. For β' -EtMe₃Sb[Pd(dmit)₂]₂, future pressure-dependent Hall measurements should be performed to obtain more information about the electron-hole asymmetry of the Fermi surface, and thus, a deeper understanding of the anisotropy inversion as a function of pressure. In contrast to the upturn ob-

served in the dc resistivity of β' -EtMe₃Sb[Pd(dmit)₂]₂, NMR measurements exhibit signature of presumably a Fermi-liquid state [172]. To clarify this contradiction, measurements at lower temperature and energy scales are required. In order to extract the bare mode frequencies of these charge sensitive vibrations, it would be of interest to perform Raman investigations on κ -(BEDT-TTF)₂Cu₂(CN)₃ under physical and chemical pressure. In the STF-doped case, we suggest that further experiments with spatial and temporal resolution need to be carried out to investigate the possible phase separation across the metal-insulator transition. For the β'' -(BEDT-TTF)₂SF₅CHF₂CF₂SO₃ salt, future pressure-dependent x-ray studies could provide a better understanding of the interplay of electronic and lattice degrees of freedom in β'' -family.

A. Acknowledgements

Here, I want to thank all the people who supported me during my PhD time at the 1.Physikalisches Institut in many different ways.

First of all, I would like to thank to my supervisor Prof. Dr. Martin Dressel, for your guidance and support in this thesis work. Without your continuous support, I would not successfully accomplish my thesis in time. Your advices and discussions are valuable for me. I am also grateful to you for careful reading and revising of this thesis.

I also would like to thank Jun.-Prof. Dr. Stefan Kaiser for kindly agreeing to co-referee this thesis and thank Prof. Dr. Hans Peter Büchler for agreeing to be examination chairperson

I also appreciated useful conversations with Artem V. Pronin and Yuan Yan for sharing your inspiring thoughts in the field of Dirac physics and general physics. Many thanks to Marc Scheffler for sharing the knowledge and expertise about Fermi liquid physics.

I would like to thank Prof. Dr. Christine A Kuntscher for kindly enabling my visits at your lab to perform infrared measurements on α -(ET)₂I₃ under high pressure. Many thanks to Ece Uykur for the technical assistance with high-pressure setup and your collaborations and efforts on the project of α -(ET)₂I₃.

I also would like to thank Tomislav Ivek for introducing me to the pressure-dependent infrared lab and for your kind advices during the experiments.

I am very grateful to my colleagues, Andrej Pustogow, Yohei Saito, Roland Rösslhuber and Micha B. Schilling for your fruitful discussions and valuable suggestions in the field of organic and inorganic physics. It was always great fun with all of you in daily life. I wish you much success in your further career.

I would like to thank Alexej Pashkin for kindly sharing the matlab codes, without which I can not proceed all my analysis so smoothly. Thanks also to Prof. István Kézsmárki and Takuya Iizuka, with whom I have learned many technical knowledge about the pressure cell.

I would like to thank Gabriele Untereiner for continuous experimental support. Most of my experiments would not go smooth without your perfect technical works. Furthermore, I would like to thank Agnieszka Cienkowska-Schmidt for all your friendly help in my daily life.

I also want to acknowledge all collaborators, people who provided some samples and supported my work:

I would like to thank D. Schweitzer for providing the single crystals of α -(ET)₂I₃, thank Dr. John Schlueter for providing the κ -(ET)₂Cu₂(CN)₃ and β'' -(ET)₂SF₅CH₂FCF₂SO₃ crystals, thank Svetlana A. Torunova, Elena I. Zhilyaeva and Rimma N. Lyubovskaya for the growth of β'' -(ET)₂Hg(SCN)₂Cl samples, and finally thank Prof. Dr. Reizo Kato for grow high-quality β' -EtMe₃Sb[Pd(dmit))₂]₂ crystals.

I would like to thank Xiaoyu Deng for the detailed explanations of the Fermi liquid theory. Many thanks also to Luca V. Delacrétaz and Prof. Sean A. Hartnoll for the fruitful discussions about the density-wave theory for the bad metals. I also appreciated the communication with Michihiro Hirata, who helped me correctly use Khveshchenko's formula for the calculation of the correlation gap.

Many thanks to Guilherme Gorgen. Lesseux and Minh Vu. Tran for the ESR measurements. Thanks also to Mamoun Hemmida and Björn Miksch for valuable discussions about ESR data. I would like to thank Ralph Hübner and Wolfgang

Frey for collection and analysis of the X-ray data. Thanks Eva Rose and Roland Rösslhuber for the support of dc resistivity measurements.

I am very grateful to Prof. Roman Świetlik for allowing me to perform Raman measurements at Institute of Molecular Physics in Poznan. Many thanks also to Andrzej Lapiński for your assistance with the measurements and for your hospitality during my visits. I also appreciated collaborations with Arkadiusz Frackowiak during his research stay in Stuttgart.

I also would like to thank my bachelor students Julia Wecker, Konstantin Riegel and master student Tobias Biesner. Thank you for all your questions which made me think. Especially, I appreciated intensive discussions with Tobias on topics ranging from general physics to social issues. All the best with your PhD research.

It was also a pleasure to have fun conversations with Andrea Rohwer, Anja Löhle, David Neubauer, Sascha Polatkan and Mehmet Ali. Nebioglu during the coffee times in the kitchen. I would like to thank our current, previous and new infrared lab members, Andreas Baumgartner, Yuk Tai Chan, Olga Iakutkina, Lucky Maulana, Fabian Pfister, Ievgen Voloshenko, Seulki Roh, Richard Kemmler and Di Liu *etc.* for a nice working atmosphere. Thanks also to all other people from the institute, Helga Kumrić, Bruno Gompf, Markus Thiemann, Marian Blankenhorn and Vasily Artemov for all your on- and off-topic conversations.

Special acknowledgements to Sascha Polatkan, Ece Uykur, Atem V. Pronin, Di Liu, Mehmet Ali. Nebioglu, Seulki Roh and Tobias Biesner for proofreading this thesis and many fruitful suggestions.

I want to thank all the people who supported and accompanied me over the years:

Thanks to all my friends for balancing my life. In particular, I would like to thank Natalie Schiebl, Chenfei Wang, Jue Wang, Wenjin Sun, Yuan Yan's family, Meng Wang's family, Qi Ai's family, Qi Guo's family, Shiyu Yang's family, Yongxiang Wu's family, Yuanshen Wang, Tianhua Zhou, Bosen Wang, Xueyi Cai, all other friends from NKU, THU, PKU and BUAA for having a lot of fun.

Finally, I want to thank my parents and family for their endless encouragement and care. Thanks a lot for the possibility of such a long way of education and for the freedom, which allows me to freely pursue my own goals abroad.

Bibliography

- [1] D. Basov, R. Averitt, and D. Hsieh, *Nat. Mater.* **16**, 1077 (2017).
- [2] M. Dressel, *J. Phys. Condens. Matter* **23**, 293201 (2011).
- [3] R. Beyer and M. Dressel, *Rev. Sci. Instrum.* **86**, 053904 (2015).
- [4] S.-i. Kimura and H. Okamura, *J. Phys. Soc. Jpn.* **82**, 021004 (2013).
- [5] L. V. Delacrétaz, B. Goutéraux, S. A. Hartnoll, and A. Karlsson, *SciPost Phys.* **3**, 025 (2017).
- [6] T. Mori, *Electronic Properties of Organic Conductors* (Springer, 2016).
- [7] *The Physics of Organic Superconductors and Conductors*, Vol. 110, Springer Series in Materials Science, edited by A. Lebed (Springer-Verlag, Berlin, 2008).
- [8] T. Ishiguro, K. Yamaji, and G. Saito, *Organic Superconductors*, 2nd (Springer-Verlag, Berlin, 1998).
- [9] N. Toyota, M. Lang, and J. Müller, *Low-Dimensional Molecular Metals*, Vol. 154, Springer Series in Solid-State Sciences (Springer-Verlag, Berlin, 2007).
- [10] J. M. Williams, J. R. Ferraro, R. J. Thorn, K. D. Carlson, U. Geiser, H. H. Wang, A. M. Kini, and M. H. Whangbo, *Organic Superconductors (Including Fullerenes : Synthesis, Structure, Properties, and Theory)* (Prentice Hall, Englewood Cliffs, NJ, 1992).
- [11] *Organic Conductors*, edited by J.-P. Farges (Marcel Dekker, New York, 1994).
- [12] <https://de.wikipedia.org/wiki/Benzol>.
- [13] D. Jerome and S. Yonezawa, *Comptes Rendus Physique* **17**, 357–375 (2016).
- [14] M. Dressel, *Naturwissenschaften* **94**, 527–541 (2007).

- [15] D. Jérôme and H. J. Schulz, *Adv. Phys.* **51**, 293–479 (2002).
- [16] Jérôme, D., Mazaud, A., Ribault, M., and Bechgaard, K., *J. Physique Lett.* **41**, 95–98 (1980).
- [17] G. Saito, T. Enoki, K. Toriumi, and H. Inokuchi, *Solid State Commun.* **42**, 557–560 (1982).
- [18] K. Oshima, T. Mori, H. Inokuchi, H. Urayama, H. Yamochi, and G. Saito, *Phys. Rev. B* **38**, 938–941 (1988).
- [19] K. Medjanik, A. Chernenkaya, S. A. Nepijko, G. Öhrwall, P. Foury-Leylekian, P. Alemany, E. Canadell, G. Schönhense, and J.-P. Pouget, *Phys. Chem. Chem. Phys.* **17**, 19202–19214 (2015).
- [20] A. Pustogow, T. Peterseim, S. Kolatschek, L. Engel, and M. Dressel, *Phys. Rev. B* **94**, 195125 (2016).
- [21] T. Mori, *Bull. Chem. Soc. Jpn.* **71**, 2509–2526 (1998).
- [22] H. Seo, C. Hotta, and H. Fukuyama, *Chem. Rev.* **104**, 5005–5036 (2004).
- [23] R. Clay and S. Mazumdar, *Phys. Rep.* **788**, 1–89 (2019).
- [24] B. J. Powell and R. H. McKenzie, *Rep. Progr. Phys.* **74**, 056501 (2011).
- [25] K. Miyagawa, K. Kanoda, and A. Kawamoto, *Chem. Rev.* **104**, 5635–5654 (2004).
- [26] K. Kanoda and R. Kato, *Annu. Rev. Condens. Matter Phys.* **2**, 167–188 (2011).
- [27] J. M. Williams, A. M. Kini, H. H. Wang, K. D. Carlson, U. Geiser, L. K. Montgomery, G. J. Pyrka, D. M. Watkins, and J. M. a. Komers, *Inorg. Chem.* **29**, 3272–3274 (1990).
- [28] R. H. McKenzie, *Science* **278**, 820–821 (1997).
- [29] B. J. Powell and R. H. McKenzie, *Phys. Rev. Lett.* **94**, 047004 (2005).
- [30] S. Lefebvre, P. Wzietek, S. Brown, C. Bourbonnais, D. Jérôme, C. Mézière, M. Fourmigué, and P. Batail, *Phys. Rev. Lett.* **85**, 5420–5423 (2000).
- [31] P. Limelette, P. Wzietek, S. Florens, A. Georges, T. A. Costi, C. Pasquier, D. Jérôme, C. Mézière, and P. Batail, *Phys. Rev. Lett.* **91**, 016401 (2003).

- [32] D. Fournier, M. Poirier, M. Castonguay, and K. D. Truong, *Phys. Rev. Lett.* **90**, 127002 (2003).
- [33] F. Kagawa, K. Miyagawa, and K. Kanoda, *Nature* **436**, 534 (2005).
- [34] F. Kagawa, K. Miyagawa, and K. Kanoda, *Nat. Phys.* **5**, 880 (2009).
- [35] E. Gati, M. Garst, R. S. Manna, U. Tutsch, B. Wolf, L. Bartosch, H. Schubert, T. Sasaki, J. A. Schlueter, and M. Lang, *Sci. Adv.* **2**, e1601646–e1601646 (2016).
- [36] T. Furukawa, K. Miyagawa, H. Taniguchi, R. Kato, and K. Kanoda, *Nat. Phys.* **11**, 221 (2015).
- [37] T. Sasaki and N. Yoneyama, *Sci. Technol. Adv. Mater.* **10**, 024306 (2009).
- [38] D. Faltermeier, J. Barz, M. Dumm, M. Dressel, N. Drichko, B. Petrov, V. Semkin, R. Vlasova, Mézière, and P. Batail, *Phys. Rev. B* **76**, 165113 (2007).
- [39] M. Dumm, D. Faltermeier, N. Drichko, M. Dressel, C. Mézière, and P. Batail, *Phys. Rev. B* **79**, 195106 (2009).
- [40] M. Dressel, D. Faltermeier, M. Dumm, N. Drichko, B. Petrov, V. Semkin, R. Vlasova, C. Mézière, and P. Batail, *Physica B* **404**, 541–544 (2009).
- [41] S. Yasin, M. Dumm, B. Salameh, P. Batail, C. Mézière, and M. Dressel, *Eur. Phys. J. B* **79**, 383–390 (2011).
- [42] T. Sasaki, N. Yoneyama, Y. Nakamura, N. Kobayashi, Y. Ikemoto, T. Moriwaki, and H. Kimura, *Phys. Rev. Lett.* **101**, 206403 (2008).
- [43] T. Sasaki, *Crystals* **2**, 374–392 (2012).
- [44] N. Yoneyama, T. Sasaki, N. Kobayashi, Y. Ikemoto, T. Moriwaki, and H. Kimura, *Solid State Commun.* **149**, 775–777 (2009).
- [45] S. H. Pan, J. O’neal, R. Badzey, C. Chamon, H. Ding, J. Engelbrecht, Z. Wang, H. Eisaki, S. Uchida, A. Gupta, et al., *Nature* **413**, 282 (2001).
- [46] J. Merino and R. H. McKenzie, *Phys. Rev. Lett.* **87**, 237002 (2001).
- [47] M. Dressel, N. Drichko, J. Schlueter, and J. Merino, *Phys. Rev. Lett.* **90**, 167002 (2003).
- [48] S. Kaiser, M. Dressel, Y. Sun, A. Greco, J. A. Schlueter, G. L. Gard, and N. Drichko, *Phys. Rev. Lett.* **105**, 206402 (2010).

- [49] S. Nagata, T. Ogura, A. Kawamoto, and H. Taniguchi, *Phys. Rev. B* **84**, 035105 (2011).
- [50] K. Kajita, Y. Nishio, N. Tajima, Y. Suzumura, and A. Kobayashi, *J. Phys. Soc. Jpn.* **83**, 072002 (2014).
- [51] N. Tajima and K. Kajita, *Sci. Technol. Adv. Mater.* **10**, 024308 (2009).
- [52] T. Kakiuchi, Y. Wakabayashi, H. Sawa, T. Takahashi, and T. Nakamura, *J. Phys. Soc. Jpn.* **76**, 113702 (2007).
- [53] T. Ivek, B. Korin-Hamzić, O. Milat, S. Tomić, C. Clauss, N. Drichko, D. Schweitzer, and M. Dressel, *Phys. Rev. B* **83**, 165128 (2011).
- [54] Y. Yue, K. Yamamoto, M. Uruichi, C. Nakano, K. Yakushi, S. Yamada, T. Hiejima, and A. Kawamoto, *Phys. Rev. B* **82**, 075134 (2010).
- [55] K. Yakushi, *Crystals* **2**, 1291–1346 (2012).
- [56] R. Wojciechowski, K. Yamamoto, K. Yakushi, M. Inokuchi, and A. Kawamoto, *Phys. Rev. B* **67**, 224105 (2003).
- [57] K. Ishikawa, M. Hirata, D. Liu, K. Miyagawa, M. Tamura, and K. Kanoda, *Phys. Rev. B* **94**, 085154 (2016).
- [58] J. Merino, H. Seo, and M. Ogata, *Phys. Rev. B* **71**, 125111 (2005).
- [59] P. Alemany, J.-P. Pouget, and E. Canadell, *Phys. Rev. B* **85**, 195118 (2012).
- [60] Y. Ihara, K. Noda, and A. Kawamoto, *Phys. Rev. B* **90**, 041107 (2014).
- [61] D. Andres, M. V. Kartsovnik, W. Biberacher, K. Neumaier, E. Schuberth, and H. Müller, *Phys. Rev. B* **72**, 174513 (2005).
- [62] H. Mori, S. Tanaka, M. Oshima, G. Saito, T. Mori, Y. Maruyama, and H. Inokuchi, *Bull. Chem. Soc. Jpn.* **63**, 2183–2190 (1990).
- [63] H. Mori, S. Tanaka, K. Oshima, M. Oshima, G. Saito, T. Mori, Y. Maruyama, and H. Inokuchi, *Solid State Commun.* **74**, 1261–1264 (1990).
- [64] T. Mori, H. Mori, and S. Tanaka, *Bull. Chem. Soc. Jpn.* **72**, 179–197 (1999).
- [65] N. Drichko, M. Dressel, C. A. Kuntscher, A. Pashkin, A. Greco, J. Merino, and J. Schlueter, *Phys. Rev. B* **74**, 235121 (2006).

-
- [66] J. Merino, A. Greco, R. H. McKenzie, and M. Calandra, *Phys. Rev. B* **68**, 245121 (2003).
- [67] T. Hiejima, S. Yamada, M. Uruichi, and K. Yakushi, *Physica B* **405**, S153–S156 (2010).
- [68] U. Geiser, J. A. Schlueter, H. H. Wang, A. M. Kini, J. M. Williams, P. P. Sche, H. I. Zakowicz, M. L. VanZile, J. D. Dudek, P. G. Nixon, et al., *J. Am. Chem. Soc.* **118**, 9996–9997 (1996).
- [69] B. H. Ward, J. A. Schlueter, U. Geiser, H. H. Wang, E. Morales, J. P. Parakka, S. Y. Thomas, J. M. Williams, P. G. Nixon, R. Winter, et al., *Chem. Mater.* **12**, 343–351 (2000).
- [70] J. A. Schlueter, B. H. Ward, U. Geiser, H. H. Wang, A. M. Kini, J. Parakka, E. Morales, H.-J. Koo, M.-H. Whangbo, R. W. Winter, J. Mohtasham, and G. L. Gard, *J. Mater. Chem.* **11**, 2008–2013 (2001).
- [71] A. D. Garlach, J. L. Musfeldt, J. M. Pigos, B. R. Jones, I. Olejniczak, A. Graja, M.-H. Whangbo, J. A. Schlueter, U. Geiser, Winter, and Gard, *Chem. Mater.* **14**, 2969–2976 (2002).
- [72] N. Drichko, S. Kaiser, Y. Sun, C. Clauss, M. Dressel, H. Mori, J. Schlueter, E. I. Zhyliaeva, S. A. Torunova, and R. N. Lyubovskaya, *Physica B* **404**, 490–493 (2009).
- [73] A. Girlando, M. Masino, J. A. Schlueter, N. Drichko, S. Kaiser, and M. Dressel, *Phys. Rev. B* **89**, 174503 (2014).
- [74] A. Pustogow, „Unveiling Electronic Correlations in Layered Molecular Conductors by Optical Spectroscopy“ (1. Physikalisches Institut, Uni Stuttgart, Stuttgart, 2017).
- [75] R. Kato, *Chem. Rev.* **104**, 5319–5346 (2004).
- [76] M. Tamura and R. Kato, *Sci. Technol. Adv. Mater.* **10**, 024304 (2009).
- [77] R. Kato, *Bull. Chem. Soc. Jpn.* **87**, 355–374 (2014).
- [78] T. Peterseim and M. Dressel, *Crystals* **7** (2017).
- [79] T. Peterseim, „Organic conductors in equilibrium and nonequilibrium states“ (1. Physikalisches Institut, Uni Stuttgart, Stuttgart, 2016).
-

- [80] T. Itou, A. Oyamada, S. Maegawa, M. Tamura, and R. Kato, *Phys. Rev. B* **77**, 104413 (2008).
- [81] Y. Shimizu, H. Akimoto, H. Tsujii, A. Tajima, and R. Kato, *Phys. Rev. Lett.* **99**, 256403 (2007).
- [82] M. Dressel and G. Grüner, *Electrodynamics of Solids* (Cambridge University Press, Cambridge, 2002).
- [83] Ø. Fischer, M. Kugler, I. Maggio-Aprile, C. Berthod, and C. Renner, *Rev. Mod. Phys.* **79**, 353–419 (2007).
- [84] A. Damascelli, Z. Hussain, and Z.-X. Shen, *Rev. Mod. Phys.* **75**, 473–541 (2003).
- [85] T. P. Devereaux and R. Hackl, *Rev. Mod. Phys.* **79**, 175–233 (2007).
- [86] A. Pustogow, M. Bories, A. Löhle, R. Rösslhuber, E. Zhukova, B. Gorshunov, S. Tomic, J. A. Schlueter, R. Hübner, T. Hiramatsu, Y. Yoshida, G. Saito, R. Kato, T.-H. Lee, V. Dobrosavljevic, S. Fratini, and M. Dressel, *Nat. Mater.* **17**, 773–777 (2018).
- [87] D. N. Basov, R. D. Averitt, D. van der Marel, M. Dressel, and K. Haule, *Rev. Mod. Phys.* **83**, 471–541 (2011).
- [88] M. Dressel and N. Drichko, *Chem. Rev.* **104**, 5689–5716 (2004).
- [89] P. Drude, *Ann. Phys.* **306**, 566–613 (1900).
- [90] A. Sommerfeld, *Z. Phys.* **47**, 1–32 (1928).
- [91] H. A. Lorentz, *Ann. Phys.* **245**, 641–665 (1880).
- [92] U. Fano, *Phys. Rev.* **124**, 1866–1878 (1961).
- [93] P. B. Allen, *Phys. Rev. B* **3**, 305–320 (1971).
- [94] D. N. Basov and T. Timusk, *Rev. Mod. Phys.* **77**, 721–779 (2005).
- [95] J. Hwang, T. Timusk, and G. D. Gu, *Nature* **427**, 714–717 (2004).
- [96] A. Girlando, *J. Phys. Chem. C* **115**, 19371–19378 (2011).
- [97] T. Yamamoto, M. Uruichi, K. Yamamoto, K. Yakushi, A. Kawamoto, and H. Taniguchi, *J. Phys. Chem. B* **109**, 15226–15235 (2005).

- [98] K. Yamamoto, K. Yakushi, K. Miyagawa, K. Kanoda, and A. Kawamoto, *Phys. Rev. B* **65**, 085110 (2002).
- [99] T. Yamamoto, M. Uruichi, K. Yakushi, J.-i. Yamaura, and H. Tajima, *Phys. Rev. B* **70**, 125102 (2004).
- [100] T. Yamamoto, M. Uruichi, K. Yakushi, and A. Kawamoto, *Phys. Rev. B* **73**, 125116 (2006).
- [101] T. Yamamoto, H. M. Yamamoto, R. Kato, M. Uruichi, K. Yakushi, H. Akutsu, A. Sato-Akutsu, A. Kawamoto, S. S. Turner, and P. Day, *Phys. Rev. B* **77**, 205120 (2008).
- [102] R. Bozio, M. Meneghetti, C. Pecile, and F. Maran, *Synth. Met.* **19**, 309–316 (1987).
- [103] J. L. Musfeldt, Świetlik, I. Olejniczak, J. E. Eldridge, and U. Geiser, *Phys. Rev. B* **72**, 014516 (2005).
- [104] A. H. Castro Neto, F. Guinea, N. M. R. Peres, K. S. Novoselov, and A. K. Geim, *Rev. Mod. Phys.* **81**, 109–162 (2009).
- [105] S. Das Sarma, S. Adam, E. H. Hwang, and E. Rossi, *Rev. Mod. Phys.* **83**, 407–470 (2011).
- [106] A. B. Kuzmenko, E. van Heumen, F. Carbone, and D. van der Marel, *Phys. Rev. Lett.* **100**, 117401 (2008).
- [107] V. P. Gusynin, S. G. Sharapov, and J. P. Carbotte, *New J. Phys.* **11**, 095013 (2009).
- [108] P. Hosur, S. A. Parameswaran, and A. Vishwanath, *Phys. Rev. Lett.* **108**, 046602 (2012).
- [109] Á. Bácsı and A. Virosztek, *Phys. Rev. B* **87**, 125425 (2013).
- [110] M. B. Schilling, „Optical Studies on Dirac and Weyl Semimetals“ (1. Physikalisches Institut, Uni Stuttgart, Stuttgart, 2018).
- [111] M. B. Schilling, L. M. Schoop, B. V. Lotsch, M. Dressel, and A. V. Pronin, *Phys. Rev. Lett.* **119**, 187401 (2017).
- [112] A. F. Ioffe and A. R. Regel, *Prog. Semicond.* **4**, 237–291 (1960).

- [113] N. E. Hussey, K. Takenaka, and H. Takagi, *Philos. Mag.* **84**, 2847–2864 (2004).
- [114] S. A. Hartnoll, *Nat. Phys.* **11**, 54 (2014).
- [115] A. Donos and S. A. Hartnoll, *Nat. Phys.* **9**, 649 (2013).
- [116] G. Grüner, *Rev. Mod. Phys.* **60**, 1129–1181 (1988).
- [117] L. V. Delacrétaz, B. Goutéraux, S. A. Hartnoll, and A. Karlsson, *Phys. Rev. B* **96**, 195128 (2017).
- [118] M. Dressel and M. Scheffler, *Ann. Phys.* **15**, 535–544 (2006).
- [119] L. D. LANDAU, *J. Exptl. Theoret. Phys.* **30**, 1058–1064 (1956).
- [120] A. V. Chubukov and D. L. Maslov, *Phys. Rev. B* **86**, 155136 (2012).
- [121] D. L. Maslov and A. V. Chubukov, *Phys. Rev. B* **86**, 155137 (2012).
- [122] C. Berthod, J. Mravlje, X. Deng, Žitko, D. van der Marel, and A. Georges, *Phys. Rev. B* **87**, 115109 (2013).
- [123] T. Kiss, A. Chainani, H. M. Yamamoto, T. Miyazaki, T. Akimoto, T. Shimojima, K. Ishizaka, S. Watanabe, C.-T. Chen, A. Fukaya, R. Kato, and S. Shin, *Nat. Commun.* **3**, 1089 (2012).
- [124] R. Gurzhi, *Sov. Phys. JETP* **35**, 673–675 (1959).
- [125] D. Stricker, J. Mravlje, C. Berthod, R. Fittipaldi, A. Vecchione, A. Georges, and D. van der Marel, *Phys. Rev. Lett.* **113**, 087404 (2014).
- [126] N. F. MOTT, *Rev. Mod. Phys.* **40**, 677–683 (1968).
- [127] J. Hubbard and B. H. Flowers, *Proc. Royal Soc. Lond. A* **276**, 238–257 (1963).
- [128] M. Imada, A. Fujimori, and Y. Tokura, *Rev. Mod. Phys.* **70**, 1039–1263 (1998).
- [129] A. Georges, G. Kotliar, W. Krauth, and M. J. Rozenberg, *Rev. Mod. Phys.* **68**, 13–125 (1996).
- [130] G. Kotliar and D. Vollhardt, *Phys. Today* **57**, 53 (2004).
- [131] G. Kotliar, S. Y. Savrasov, K. Haule, V. S. Oudovenko, O. Parcollet, and C. A. Marianetti, *Rev. Mod. Phys.* **78**, 865–951 (2006).

- [132] R. Ulbricht, E. Hendry, J. Shan, T. F. Heinz, and M. Bonn, *Rev. Mod. Phys.* **83**, 543–586 (2011).
- [133] C. A. Kuntscher, A. Huber, and M. Hückler, *Phys. Rev. B* **89**, 134510 (2014).
- [134] H. K. Mao, J. Xu, and P. M. Bell, *J. Geophys. Res.* **91**, 4673–4676 (1986).
- [135] D. D. Ragan, R. Gustavsen, and D. Schiferl, *J. Appl. Phys.* **72**, 5539–5544 (1992).
- [136] A. Pashkin, M. Dressel, and C. A. Kuntscher, *Phys. Rev. B* **74**, 165118 (2006).
- [137] H. Okamura, *J. Phys. Conf. Ser.* **359**, 012013 (2012).
- [138] M. K. Tran, J. Levallois, A. Akrap, J. Teyssier, A. B. Kuzmenko, F. Lévy-Bertrand, R. Tediosi, M. Brandt, P. Lerch, and D. van der Marel, *Rev. Sci. Instrum.* **86**, 105102 (2015).
- [139] E. Uykur, W. Li, C. A. Kuntscher, and M. Dressel, *npj Quantum Materials* **4**, 19 (2019).
- [140] K. Bender, K. Dietz, H. Endres, H. W. Helberg, I. Hennig, H. J. Keller, H. W. Schäfer, and D. Schweitzer, *Mol. Cryst. Liq. Cryst.* **107**, 45–53 (1984).
- [141] N. Tajima, S. Sugawara, M. Tamura, R. Kato, Y. Nishio, and K. Kajita, *EPL* **80**, 47002 (2007).
- [142] A. Kobayashi, S. Katayama, Y. Suzumura, and H. Fukuyama, *J. Phys. Soc. Jpn.* **76**, 034711 (2007).
- [143] A. Kobayashi, S. Katayama, and Y. Suzumura, *Sci. Technol. Adv. Mater.* **10**, 024309 (2009).
- [144] Y. Suzumura and A. Kobayashi, *Crystals* **2**, 266–283 (2012).
- [145] S. Katayama, A. Kobayashi, and Y. Suzumura, *J. Phys. Soc. Jpn.* **75**, 054705 (2006).
- [146] D. Liu, K. Ishikawa, R. Takehara, K. Miyagawa, M. Tamura, and K. Kanoda, *Phys. Rev. Lett.* **116**, 226401 (2016).
- [147] R. Beyer, A. Dengl, T. Peterseim, S. Wackerow, T. Ivek, A. V. Pronin, D. Schweitzer, and M. Dressel, *Phys. Rev. B* **93**, 195116 (2016).

- [148] M. Hirata, K. Ishikawa, K. Miyagawa, M. Tamura, C. Berthier, D. Basko, A. Kobayashi, G. Matsuno, and K. Kanoda, *Nat. Commun.* **7**, 12666, 12666 (2016).
- [149] M. Hirata, K. Ishikawa, G. Matsuno, A. Kobayashi, K. Miyagawa, M. Tamura, C. Berthier, and K. Kanoda, *Science* **358**, 1403–1406 (2017).
- [150] R. Keller and W. B. Holzapfel, *Rev. Sci. Instrum.* **48**, 517–523 (1977).
- [151] M. Dressel, G. Grüner, J.P. Pouget, A. Breining, and D. Schweitzer, *J. Phys. (Paris) I* **4**, 579–594 (1994).
- [152] R. Kondo, S. Kagoshima, N. Tajima, and R. Kato, *J. Phys. Soc. Jpn.* **78**, 114714 (2009).
- [153] M. Rozenberg, G. Kotliar, H. Kajueter, G. Thomas, D. Rapkine, J. Honig, and P. Metcalf, *Phys. Rev. Lett.* **75**, 105 (1995).
- [154] A. Perucchi, L. Degiorgi, and R. E. Thorne, *Phys. Rev. B* **69**, 195114 (2004).
- [155] D. Ohki, G. Matsuno, Y. Omori, and A. Kobayashi, *Crystals* **8** (2018).
- [156] K. F. Mak, M. Y. Sfeir, Y. Wu, C. H. Lui, J. A. Misewich, and T. F. Heinz, *Phys. Rev. Lett.* **101**, 196405 (2008).
- [157] A. Mori, M. Sato, T. Yajima, T. Konoike, K. Uchida, and T. Osada, *Phys. Rev. B* **99**, 035106 (2019).
- [158] K. Kishigi and Y. Hasegawa, *Phys. Rev. B* **96**, 085430 (2017).
- [159] M. Monteverde, M. O. Goerbig, P. Auban-Senzier, F. Navarin, H. Henck, C. R. Pasquier, C. Mézière, and P. Batail, *Phys. Rev. B* **87**, 245110 (2013).
- [160] T. Peterseim, T. Ivek, D. Schweitzer, and M. Dressel, *Phys. Rev. B* **93**, 245133 (2016).
- [161] Y. Suzumura, I. Proskurin, and M. Ogata, *J. Phys. Soc. Jpn.* **83**, 094705 (2014).
- [162] S. Verma, A. Mawrie, and T. K. Ghosh, *Phys. Rev. B* **96**, 155418 (2017).
- [163] P. Foury-Leylekian, J.-P. Pouget, Y.-J. Lee, R. M. Nieminen, P. Ordejón, and E. Canadell, *Phys. Rev. B* **82**, 134116 (2010).

- [164] D. Neubauer, A. Yaresko, W. Li, A. Löhle, R. Hübner, M. B. Schilling, C. Shekhar, C. Felser, M. Dressel, and A. V. Pronin, *Phys. Rev. B* **98**, 195203 (2018).
- [165] D. V. Khveshchenko, *J. Phys. Condens. Matter* **21**, 075303 (2009).
- [166] D. V. Khveshchenko, *Phys. Rev. Lett.* **87**, 246802 (2001).
- [167] H. Kino and T. Miyazaki, *J. Phys. Soc. Jpn.* **75**, 034704 (2006).
- [168] W. Li, A. Pustogow, R. Kato, and M. Dressel, *Phys. Rev. B* **99**, 115137 (2019).
- [169] K. Ueda, T. Tsumuraya, and R. Kato, *Crystals* **8** (2018).
- [170] A. Pustogow, Y. Saito, E. Zhukova, B. Gorshunov, R. Kato, T.-H. Lee, S. Fratini, Dobrosavljević, and M. Dressel, *Phys. Rev. Lett.* **121**, 056402 (2018).
- [171] P. Lazić, M. Pinterić, D. R. Góngora, A. Pustogow, K. Treptow, T. Ivek, O. Milat, B. Gumhalter, N. Došlić, M. Dressel, et al., *Phys. Rev. B* **97**, 245134 (2018).
- [172] T. Itou, E. Watanabe, S. Maegawa, A. Tajima, N. Tajima, K. Kubo, R. Kato, and K. Kanoda, *Sci. Adv.* **3**, e1601594 (2017).
- [173] K. Reizo, F. Takeo, Y. H. M., U. Kohei, and H. Cui, *Phys. Status Solidi B* **249**, 999–1003.
- [174] T. Yamamoto, Y. Nakazawa, M. Tamura, T. Fukunaga, R. Kato, and K. Yakushi, *J. Phys. Soc. Jpn.* **80**, 074717 (2011).
- [175] T. Yamamoto, T. Fujimoto, T. Naito, Y. Nakazawa, M. Tamura, K. Yakushi, Y. Ikemoto, T. Moriwaki, and R. Kato, *Sci. Rep.* **7**, 12930 (2017).
- [176] T. Yamamoto, Y. Nakazawa, M. Tamura, A. Nakao, Y. Ikemoto, T. Moriwaki, A. Fukaya, R. Kato, and K. Yakushi, *J. Phys. Soc. Jpn.* **80**, 123709 (2011).
- [177] J. Merino, M. Dumm, N. Drichko, M. Dressel, and R. H. McKenzie, *Phys. Rev. Lett.* **100**, 086404 (2008).
- [178] T. Senthil, *Phys. Rev. B* **78**, 045109 (2008).
- [179] T. Furukawa, K. Kobashi, Y. Kurosaki, K. Miyagawa, and K. Kanoda, *Nat. Commun.* **9**, 307 (2018).

- [180] A.-K. Klehe, R. D. McDonald, A. F. Goncharov, V. V. Struzhkin, H.-k. Mao, R. J. Hemley, T. Sasaki, W. Hayes, and J. Singleton, *J. Phys. Condens. Matter* **12**, L247 (2000).
- [181] R. McDonald, A. Klehe, J. Singleton, and W. Hayes, *J. Phys. Condens. Matter* **15**, 5315 (2003).
- [182] Y. Kawasugi, K. Seki, Y. Edagawa, Y. Sato, J. Pu, T. Takenobu, S. Yunoki, H. M. Yamamoto, and R. Kato, *Nat. Commun.* **7**, 12356 (2016).
- [183] T. Sasaki, N. Yoneyama, A. Matsuyama, and N. Kobayashi, *Phys. Rev. B* **65**, 060505 (2002).
- [184] R. Rösslhuber, E. Uykur, and M. Dressel, *Rev. Sci. Instrum.* **89**, 054708 (2018).
- [185] S. Fujiyama and R. Kato, *Phys. Rev. B* **97**, 035131 (2018).
- [186] M. Dressel, P. Lazić, A. Pustogow, E. Zhukova, B. Gorshunov, J. Schlueter, O. Milat, B. Gumhalter, and S. Tomić, *Phys. Rev. B* **93**, 081201 (2016).
- [187] Y. Shimizu, K. Miyagawa, K. Kanoda, M. Maesato, and G. Saito, *Phys. Rev. Lett.* **91**, 107001 (2003).
- [188] K. Sedlmeier, S. Elsässer, D. Neubauer, R. Beyer, D. Wu, T. Ivek, S. Tomić, J. A. Schlueter, and M. Dressel, *Phys. Rev. B* **86**, 245103 (2012).
- [189] I. Kézsmárki, Y. Shimizu, G. Mihály, Y. Tokura, K. Kanoda, and G. Saito, *Phys. Rev. B* **74**, 201101 (2006).
- [190] S. Elsässer, D. Wu, M. Dressel, and J. A. Schlueter, *Phys. Rev. B* **86**, 155150 (2012).
- [191] T.-K. Ng and P. A. Lee, *Phys. Rev. Lett.* **99**, 156402 (2007).
- [192] Y. Kurosaki, Y. Shimizu, K. Miyagawa, K. Kanoda, and G. Saito, *Phys. Rev. Lett.* **95**, 177001 (2005).
- [193] Y. Saito, T. Minamidate, A. Kawamoto, N. Matsunaga, and K. Nomura, *Phys. Rev. B* **98**, 205141 (2018).
- [194] U. Geiser, H. H. Wang, K. D. Carlson, J. M. Williams, H. A. Charlier, J. E. Heindl, G. A. Yaconi, B. J. Love, M. W. Lathrop, and . et al., *Inorg. Chem.* **30**, 2586–2588 (1991).

- [195] T. Komatsu, N. Matsukawa, T. Inoue, and G. Saito, *J. Phys. Soc. Jpn.* **65**, 1340–1354 (1996).
- [196] *Private communication with Dr. Saito.*
- [197] Y. Shimizu, T. Hiramatsu, M. Maesato, A. Otsuka, H. Yamochi, A. Ono, M. Itoh, M. Yoshida, M. Takigawa, Y. Yoshida, and G. Saito, *Phys. Rev. Lett.* **117**, 107203 (2016).
- [198] K. Kornelsen, J. E. Eldridge, H. H. Wang, and J. M. Williams, *Phys. Rev. B* **44**, 5235–5245 (1991).
- [199] J. Eldridge, Y. Xie, J. A. Schlueter, J. M. Williams, D. Naumann, and T. Roy, *Solid State Commun.* **99**, 335–340 (1996).
- [200] J. Eldridge, Y. Xie, Y. Lin, C. Homes, H. Wang, J. Williams, A. Kini, and J. Schlueter, *Spectrochimica Acta Part A: Molecular and Biomolecular Spectroscopy* **53**, 565–573 (1997).
- [201] H. Shinaoka and M. Imada, *J. Phys. Soc. Jpn.* **78**, 094708 (2009).
- [202] D. Heidarian and N. Trivedi, *Phys. Rev. Lett.* **93**, 126401 (2004).
- [203] N. D. Patel, A. Mukherjee, N. Kaushal, A. Moreo, and E. Dagotto, *Phys. Rev. Lett.* **119**, 086601 (2017).
- [204] E. Lahoud, O. N. Meetei, K. B. Chaska, A. Kanigel, and N. Trivedi, *Phys. Rev. Lett.* **112**, 206402 (2014).
- [205] N. E. Hussey, J. Buhot, and S. Licciardello, *Rep. Prog. Phys.* **81**, 052501 (2018).
- [206] P. Phillips, *Philos. Trans. Royal Soc. A* **369**, 1574–1598 (2011).
- [207] Q. Si and F. Steglich, *Science* **329**, 1161–1166 (2010).
- [208] K. Damle and S. Sachdev, *Phys. Rev. B* **56**, 8714–8733 (1997).
- [209] D. v. d. Marel, H. J. A. Molegraaf, J. Zaanen, Z. Nussinov, F. Carbone, A. Damascelli, H. Eisaki, M. Greven, P. H. Kes, and M. Li, *Nature* **425**, 271–274 (2003).
- [210] D. A. Bonnelli, D. N. Basov, M. Bode, U. Diebold, S. V. Kalinin, V. Madhavan, L. Novotny, M. Salmeron, U. D. Schwarz, and P. S. Weiss, *Rev. Mod. Phys.* **84**, 1343–1381 (2012).

- [211] W. Li, E. Rose, M. V. Tran, R. Hübner, A. Lapiński, R. Świetlik, S. A. Turunova, E. I. Zhilyaeva, R. N. Lyubovskaya, and M. Dressel, *J. Chem. Phys.* **147**, 064503 (2017).
- [212] H. Mori, S. Tanaka, and T. Mori, *Phys. Rev. B* **57**, 12023–12029 (1998).
- [213] <http://www2.riken.jp/lab-www/molecule/nenpo/16nenpo-e.html>.
- [214] N. Drichko, R. Beyer, E. Rose, M. Dressel, J. A. Schlueter, S. A. Turunova, E. I. Zhilyaeva, and R. N. Lyubovskaya, *Phys. Rev. B* **89**, 075133 (2014).
- [215] A. Löhle, E. Rose, S. Singh, R. Beyer, E. Tafra, T. Ivek, E. I. Zhilyaeva, R. N. Lyubovskaya, and M. Dressel, *J. Phys. Condens. Matter* **29**, 055601 (2017).
- [216] C. Hotta and N. Furukawa, *Phys. Rev. B* **74**, 193107 (2006).
- [217] N. Takubo, N. Tajima, H. M. Yamamoto, H. Cui, and R. Kato, *Phys. Rev. Lett.* **110**, 227401 (2013).
- [218] J.-R. Wang and G.-Z. Liu, *Phys. Rev. B* **89**, 195404 (2014).

Declaration of Originality

I hereby declare that this thesis and the work reported herein was composed by and originated entirely from me. Information derived from the published and unpublished work of others has been acknowledged in the text and references.

Weiwu Li

